School of Civil and Environmental Engineering

Addis Ababa University

Spatio-Temporal Variability of Historical and Future Climate Extremes and Their Impacts on Hydroclimatic Extremes in Ethiopia

By

Daniel Berhanu Afrasso

Supervisors: Dr Tena Alamirew and Dr Solomon Gebreyohannis

A Ph.D. dissertation submitted to the School of Civil and Environmental Engineering, Addis Ababa University, in partial fulfillment of the requirements for the Degree of Doctor of Philosophy in Water Resource Engineering and Management (Surface Water Engineering and Management)

School of Civil and Environmental Engineering
Addis Ababa University
School of Graduate Studies

Spatio-Temporal Variability of Historical and Future Climate Extremes and Their Impacts on Hydroclimatic Extremes in Ethiopia

By

Daniel Berhanu Afrasso

Supervisors: Dr Tena Alamirew and Dr Solomon Gebreyohannis

A Ph.D. dissertation submitted to the School of Civil and Environmental Engineering, Addis Ababa University, in partial fulfillment of the requirements for the Degree of Doctor of Philosophy in Water Resource Engineering and Management (Surface Water Engineering and Management)

February 9, 2026

Addis Ababa, Ethiopia

Declaration

I, **Daniel Berhanu Afrasso (GSR/4029/12)**, hereby declare that the work presented in this thesis, entitled *"Spatio-Temporal Variability of Historical and Future Climate Extremes and Their Impacts on Hydroclimatic Extremes in Ethiopia"*, is my original research carried out under the supervision of Dr. Tena Alamirew and Dr. Solomon Gebreyohannis.

I further confirm that this thesis has not been submitted, either in whole or in part, to any other university or institution for the award of any degree, diploma, or other qualification. All sources of information and references used in this study have been properly acknowledged. I understand that plagiarism in any form is a serious academic offense, and I affirm that this thesis complies with the academic integrity regulations of Addis Ababa University.

Parts of this dissertation (the first two) have already been published in peer-reviewed journals, while others are currently under review:

1. *Evaluation of CMIP6 models in reproducing observed rainfall over Ethiopia*
2. *Evaluation of CMIP6 models in simulating seasonal extreme precipitation over Ethiopia*
3. *Historical trends and future projections of extreme seasonal precipitation over Ethiopia, East Africa*
4. *Historical trends and future changes of hydroclimate extremes in the Awash Basin, Ethiopia*

Ph.D. Candidate's Name	Signature	Date
Daniel Berhanu Afrasso		February 9, 2026

Spatio-Temporal Variability of Historical and Future Climate Extremes and Their Impacts on Hydroclimatic Extremes in Ethiopia

By:

Daniel Berhanu Afrasso Signature Date February 9, 2026

A Ph.D. Dissertation Submitted to the School of Civil and Environmental Engineering, Addis Ababa University

Approved by the Board of Examiners

This is to certify that we have read this Ph.D. dissertation and that in our opinion; it is fully adequate, in scope and quality, as a Ph.D. dissertation for the Degree of Doctor of Philosophy in Water resource engineering and management (Surface water engineering and management).

	Name	Signature	Date
Main Advisor	Dr. Tena Alamirew		February 9, 2026
Co-Advisor	Dr.Solomon Gebreyohannis		February 9, 2026
External examiner	Professor Tsegaye Tadesse	TSEGAYE TADESSE	February 9, 2026
Internal examiner	Professor Yilma Seleshi		February 9, 2026
Chairperson	Dr. Yenesew Mengiste		February 9, 2026

Dedication

This dissertation is dedicated to the cherished memory of my father, Ato Berhanu Afrasso, whose guidance and values continue to inspire me, and to my beloved mother, Zerishwork Debella, whose love, prayer, and support have been my strength throughout this journey.

Acknowledgments

First and foremost, I am deeply grateful to God Almighty for blessing me with the strength, health, and perseverance to bring this Ph.D. journey to completion.

I extend my sincere gratitude to my supervisor, Dr. Tena Alamirew, whose invaluable guidance, encouragement, and constructive feedback have shaped both my academic work and professional growth. I am also thankful to my co-supervisor, Dr. Solomon Gebreyohannis, for his support throughout my doctoral studies.

My heartfelt gratitude also goes to Dr. Gete Zeleke for providing me with the opportunity to pursue my PhD, financial support, and resources that enabled me to do so. I am also grateful to Addis Ababa University for providing me with the opportunity to study and grow over the past six years. Without such support, it would not have been possible to pursue my research and focus fully on it.

Above all, I am profoundly indebted to my beloved wife, Tsion Dagne, and my children, Rin Daniel and Nebyou Daniel, for their unconditional love, patience, and unwavering support. My deepest gratitude also goes to my mother, brothers, and sisters for their constant prayers and encouragement, which sustained me throughout.

Special thanks are due to my colleagues and friends, whose companionship, discussions, and encouragement kept me motivated through the challenges of this journey.

Finally, I extend my gratitude to all co-authors, both named and unnamed, whose contributions have played a part in this achievement. Your support has been truly invaluable.

List of Publications During PhD Study

1. Berhanu, D., Alamirew, T., Bewket, W., Tarkegn, T.G., Zeleke, G., Haileslassie, A., O'Donnell, G., Walsh, C.L. and Gebrehiwot, S., 2025. Evaluation of CMIP6 models in simulating seasonal extreme precipitation over Ethiopia. Weather and Climate Extremes. https://doi.org/10.1016/j.wace.2025.100752.

2. Berhanu, D., Alamirew, T., Taye, M.T., Tibebe, D., Gebrehiwot, S., Zeleke, G., 2023. Evaluation of CMIP6 models in reproducing observed rainfall over Ethiopia. J. Water Clim. Chang. 14, 2583–2605. https://doi.org/10.2166/wcc.2023.502.

3. Berhanu, D., Tarkegn, T. G., Haileslassie, A., Alamirew, T., Mekuria, W., Zeleke, G.; Lemann, T.; Hurni, H.; Feyisa, G. L. 2025. Hydrological dynamics in various agroecological zones and impacts of soil and water conservation measures on runoff and sediment yields in the Bale Eco-Region, Ethiopia. Journal of Water and Climate Change, 16(6):2032-2052. https://doi.org/10.2166/wcc.2025.755

4. Legass, A.M., Alamirew, T., Gebrehiwot, S.G., Haro-Monteagudo, D. and Berhanu, D., 2025. Spatiotemporal climate change projection and trend analysis using selected downscaled CMIP6 models for water action over awash River Basin, Ethiopia. Environmental Challenges, 18, p.101059. https://doi.org/10.1016/j.envc.2024.101059

TABLE OF CONTENTS

List of Tables

List of Figures

Abstract

Climate variability and change have profound impacts on the livelihoods and economies of the East African region, including Ethiopia due to its strong reliance on rain-fed agriculture, high population exposure, and limited adaptive capacity. Ethiopia has historically experienced recurrent droughts and floods, and these extremes are expected to intensify under climate change. This study evaluated model performance, addressed biases, and assessed future projections of precipitation and hydroclimatic extremes across Ethiopia. Together, these studies highlight both the potential and the limitations of CMIP6 models for supporting climate impact assessments and adaptation planning in the country.

An assessment of 45 CMIP6 models against ENACTS rainfall data revealed that while most models successfully captured the spatial distribution of mean and extremes, they could not reproduce the magnitude of indices, especially in highland regions such as the northwest, west and southwest. Many models introduced a pronounced dry bias in high-elevation areas that typically receive substantial rainfall during the June–September (JJAS) main rainy season. Extreme indices such as consecutive dry days (CDD), total wet-day precipitation (PRCPTOT), heavy precipitation days (R10), very heavy precipitation days (R20), simple daily intensity index (SDII), very wet days (R95pTOT), extremely wet days (R99pTOT), maximum consecutive five-day precipitation (Rx5day), and maximum one-day precipitation (Rx1day) were generally underestimated. However, consecutive wet days (CWD) were often overestimated in highland and high-rainfall areas, particularly in the western parts of tropical, subtropical, temperate, and alpine agro-ecological zones (AEZs). Conversely, in lowland and drier areas such as east and northeast parts of desert and tropical AEZs, model biases were smaller. Evident seasonal and regional differences in model skill suggest that model performance depends heavily on the choice of indices, and metrics, as well as on the season and geographic context.

Using Taylor Skill Scores (TSS) and Comprehensive Rating Metrics (CRM), the most reliable models for Ethiopia during the JJAS season were identified as CESM2-WACCM-FV2, NESM3, NorESM2-LM, NorESM2-MM, CMCC-ESM2, IPSL-CM6A-INCA, and E3SM-1-0. Of the 45 models evaluated against the observed dataset, NorESM2-MM performed best during the FMAM season. The next best performers were HadGEM3-GC31-MM, GFDL-CM4, NorESM2-LM,

GFDL-ESM4, BCC-ESM1-MR, and MPI-ESM-1-2-HAM. Nevertheless, ensembles of those top-ranking models consistently provided better alignment with observed indices compared to either individual models or the full model ensemble. These results emphasize that model weighting and sub-ensemble selection are critical steps in applying CMIP6 outputs to climate risk assessments.

Projections of future precipitation extremes offer a more detailed view of potential risks. Using bias-corrected outputs from top-performing CMIP6 models under SSP245 and SSP585 scenarios, studies indicate that, by the 2050s and 2080s, there will be an increase in PRCPTOT and an intensification of extremes such as R10, R20, R95p, R99p, and SDII in northwest, west, and southwest Ethiopia during the JJAS period. In FMAM, however, the historical declining trend in rainfall may persist in some regions, particularly in the northeast and the Awash basin, though increases are projected in the north (Tekeze basin). The northeast is projected to face more intense extremes during JJAS but decreased rainfall during FMAM. These divergent patterns highlight growing intra-annual and regional variability in precipitation.

At the basin scale, the Awash basin illustrates the severity of these challenges. Historical analyses reveal distinct spatial contrasts, with relatively stable precipitation in the upper basin but greater variability downstream. Using bias-corrected outputs from seven top-performing CMIP6 models, hydrological modeling with SWAT+ demonstrates significant changes in precipitation, streamflow, and extremes across the basin. Projections suggest increases in JJAS rainfall and CWD, particularly in the lower basin, but declines in FMAM rainfall and streamflow in the Mojo catchment, where flows may decrease by 80–100%. Meanwhile, JJAS streamflow is expected to rise by up to 70% in response to increased rainfall. Temperature increases of about +2 °C by the 2080s will further exacerbate evapotranspiration pressures. Both drought severity (+36%) and flood frequency (+48%) are projected to rise, underscoring a dual challenge of managing water deficits and surpluses. These findings highlight the urgent need for integrated climate change resilience water resource management strategies that can accommodate both extremes within the same basin.

The findings of these studies emphasize the following important conclusions. First, while CMIP6 models are valuable tools, they require careful evaluation, bias correction, and selective ensemble construction to provide actionable insights. Second, Ethiopia’s climate future will likely be

characterized by heightened variability and intensification of extremes. Third, adaptation and resilience strategies must be informed by both the potential for increased rainfall and flooding in some regions and declining rainfall and water stress in others. Finally, uncertainty in climate model projections must be explicitly recognized in planning. Acknowledging these uncertainties allows for the adoption of flexible and adaptive management strategies that remain robust under a range of possible futures.

Chapter 1. Introduction

1.1 Background

Climate variability and change have profound impacts on the livelihoods and economies of populations in the Horn of Africa, including Ethiopia. This region is highly sensitive to climate fluctuations due to its heavy reliance on rain-fed agriculture, limited adaptive capacity, and fragile socio-economic systems (Omondi et al., 2014; Endris et al., 2013). In Ethiopia in particular, the consequences of climate variability manifest through recurrent droughts, floods, and hydroclimatic extremes. These events threaten water, food, and energy security, thereby undermining socio-economic development. Climate change has been recognized globally as one of the most pressing challenges of the 21st century, but its effects are particularly severe in developing regions like East Africa, where adaptive capacity is low and vulnerability is high (Nicholson, 2017; Ongoma et al., 2018). Climate extremes in the region disrupt livelihoods, destroy property, and claim lives, often pushing already vulnerable communities deeper into poverty. In Ethiopia, these challenges are exacerbated by rapid population growth, limited infrastructure, and dependence on agriculture, which together amplify the impacts of climate extremes on rural communities (Viste et al., 2013; Maidment et al., 2015).

The effects of climate extremes such as droughts and floods are particularly devastating for Ethiopia. Historical evidence demonstrates that the country has faced repeated climate shocks in the past decades. Severe droughts in 1983–1985, 1988, 2000, 2002–2003, 2006, 2011, and 2015 have led to widespread food insecurity, livestock deaths, and long-term socio-economic impacts (Viste et al., 2013; Mera, 2018; Cherinet et al., 2022). The drought of 1983–1985 is remembered as one of the most severe disasters in Ethiopian history, while the El Niño-induced drought of 2015 left 10.2 million people in urgent need of food assistance (Gummadi et al., 2018; Lewis, 2017; Philip et al., 2018). More recently, the prolonged drought of 2022, the worst in 50 years, resulted in the death of 2.2 million livestock, massive crop failures, and the displacement of numerous families, bringing millions to the brink of destitution (FEWS NET, 2022). In addition to droughts, floods also pose a severe threat, with eleven major flood events recorded in the last two decades, causing substantial loss of human life, property damage, and displacement (Cherinet et al., 2022). These recurrent extremes highlight Ethiopia's vulnerability to climate variability and the urgent need for effective adaptation strategies.

Recognizing the critical threat posed by climate change, the Ethiopian government has developed a policy framework to enhance resilience and adaptation. The National Adaptation Plan (NAP-ETH), embedded within the broader Climate Resilient Green Economy (CRGE) strategy, is designed to mitigate climate impacts, enhance resilience, and promote sustainable growth (FDRE, 2019). The NAP-ETH emphasizes the need to integrate adaptation strategies proactively and iteratively into development planning across all sectors of the economy. Its success, however, depends heavily on access to reliable climate projections that can inform national planning and sector-specific adaptation strategies. Since the Ethiopian economy is highly vulnerable to climate change due to its heavy reliance on rainfed agriculture, developing reliable projections of precipitation extremes and understanding their potential impacts on the country is therefore essential. Accurate climate information is vital for anticipating future risks, prioritizing investments, and implementing effective measures to safeguard vulnerable communities. This underscores the importance of evaluating the reliability of available climate models, particularly in simulating mean and climate extremes, before applying their projections in policy and planning.

Global Climate Models (GCMs) serve as the principal tools for generating future climate scenarios and assessing the impacts of climate change across temporal and spatial scales. They provide insights into past and future changes in temperature, rainfall, and associated extremes, and are widely used in detection and attribution studies as well as in adaptation and mitigation planning (Stouffer et al., 2017; Wainwright et al., 2019; Flato et al., 2014). Historical simulations allow researchers to evaluate the skill of climate models in reproducing observed conditions, including extreme events, which is critical for establishing confidence in future projections (Eyring et al., 2016). The outputs of these models thus form the foundation for climate impact assessments in multiple sectors, including agriculture, energy, and water resources. However, uncertainties persist due to differences in model structures, spatial resolutions, boundary conditions, and parameterization schemes (Akinsanola et al., 2021; Chen et al., 2020; Eyring et al., 2016; Kim et al., 2020). These differences influence GCMs' ability to accurately simulate local and regional climates.

Earlier generations of GCMs, particularly those included in the Coupled Model Intercomparison Project phase 5 (CMIP5), provided important advances in climate science but exhibited significant limitations in reproducing regional climate characteristics over Africa, including Ethiopia. Several

studies evaluating CMIP5 performance over East Africa have reported that, although the models capture the broad seasonal cycles, they exhibit large biases (Yang et al., 2015; Jury, 2015; Li et al., 2016; Dyer et al., 2020). These shortcomings limited their usefulness for planning adaptation at finer scales, such as local scale or agro-ecological zones. The subsequent phase, CMIP6, introduced higher spatial resolution, more advanced representations of physical processes, improved parameterization schemes, and larger ensembles, with the aim of addressing some of these deficiencies (Eyring et al., 2016; Kim et al., 2020). In addition, CMIP6 incorporates Shared Socioeconomic Pathways (SSPs), which provide a more comprehensive framework for analyzing future climate under different development and emissions scenarios. These advancements suggest that CMIP6 offers improved potential for simulating regional climates, although model performance remains highly variable across regions and indices.

Recent studies have evaluated the performance of CMIP6 models across different regions of Africa. These studies show that, although CMIP6 models have improved in their ability to capture large-scale climate dynamics and extremes, they still exhibit substantial biases (Srivastava et al., 2020; Feng et al., 2023; Donat et al., 2023). In East Africa, CMIP6 models have been used to study mean precipitation trends, yet relatively few analyses have focused on extremes indices (Akinsanola et al., 2021; Ayugi et al., 2021; Klutse et al., 2021; Omay et al., 2023). Within Ethiopia, only a limited number of studies have assessed and applied CMIP6 models in simulating mean precipitation at basin scale (Alaminie et al., 2021; Dyer et al., 2022; Fetene et al., 2022; Gebisa et al., 2023). Additionally, only a handful have investigated extreme precipitation events at the national scale (Rettie et al., 2023) and at the basin scale (Bulti et al., 2021; Teshome et al., 2022) in relation to their future projections. Moreover, most of these studies relied on fewer than 20 models and often used global satellite products like CHIRPS and GPCP, rather than high-resolution datasets specifically tailored for Ethiopia (ENACTS). This reliance limits the robustness of the findings because global datasets may not adequately capture the spatial heterogeneity of precipitation across Ethiopia's diverse agro-ecological zones. ENACTS dataset, with its high spatial resolution of 4 km and specific calibration for Ethiopian conditions, offers a significant opportunity to overcome this limitation (Dinku et al., 2014; 2018). Additionally, there remains a knowledge gap in previous studies concerning the analysis of extreme rainfall trends using high-resolution climate data, as well as the projection of precipitation extremes under the latest CMIP6 scenarios at the national and basin scale. By combining historical observations with future

projections, this study seeks to offer a comprehensive understanding of the evolving climate dynamics in Ethiopia.

Hydroclimatic extremes, including both droughts and floods, pose direct threats to Ethiopia's water resources, agriculture, and energy systems. Climate change is expected to alter the frequency, intensity, and timing of hydrological processes such as river flows, groundwater recharge, and streamflow variability (Jiménez Cisneros et al., 2014; Zhao et al., 2024). These shifts will have serious implications for water security, agriculture, ecosystems, and hydropower generation. The Awash basin, one of Ethiopia's most economically and socially critical basins, is already experiencing acute water insecurity due to recurrent droughts, floods, and increasing water demand (Adeba et al., 2015; Gedefaw et al., 2018; Mulugeta et al., 2019). With its importance for agriculture, industry, and urban water supply, understanding hydroclimatic variability and extremes in the Awash basin is crucial for designing basin-wide adaptation strategies. The Mojo catchment, a tributary of the Awash river basin in Ethiopia, plays a critical role in the hydrology of the larger basin, influencing local ecosystems and agricultural activities. The catchment is particularly vulnerable to meteorological and hydrological drought due to its heavy reliance on rainfall. Meteorological drought is driven by prolonged deficits in precipitation, while hydrological drought is characterized by reduced streamflow and water availability (Alemu et al., 2023). Understanding and analyzing droughts and floods in this catchment is therefore essential for effective water resource management and agricultural planning. Yet most previous research in Ethiopia has focused on mean rainfall or relied on CMIP5 models, with limited analysis of hydroclimatic extremes at the basin scale (Alemu et al., 2022; Emiru et al., 2021; Taye et al., 2018). A few recent studies have attempted to use CMIP6 models, but these remain scarce in integrating climate extremes with hydrological impacts using the updated SWAT+ hydrological model.

This study addresses a contextual gap by evaluating the spatio-temporal variability of climate extremes, assessing historical trends and future projections of climate extremes and their impacts on hydroclimatic extremes across Ethiopia. Specifically, we analyze the performance of 45 CMIP6 models in simulating mean and extremes seasonal precipitation during the main rainy season (June–September, JJAS) and the short rainy season (February–May, FMAM), which together account for about 90% of Ethiopia's annual rainfall (Philip et al., 2018). Using the high-resolution

ENACTS dataset as a reference, we assess the models' ability to reproduce observed mean and extremes at both national and agro-ecological zone scales. We further compare different ensembles of top-performing models to identify the ensembles of the top-performing models and apply ensembles of these models to generate robust future projections. To our knowledge, this study is the first to evaluate multiple CMIP6 models and to use the top-performing models to develop an ensemble to provide robust evidence for projections of future extreme climate conditions during the JJAS and FMAM seasons across Ethiopia. Therefore, by adopting a skill-based model ranking and ensemble selection approach, this study strengthens the reliability of future climate projections. Beyond analyzing rainfall extremes, this study integrates hydrological modeling using SWAT+ to assess the potential impacts of climate change on hydrological extremes in the Upper Awash basin, specifically within the Mojo catchment. By analyzing both historical trends (1981–2010) and future projections (2015–2100), it provides a comprehensive assessment of evolving climate and hydroclimatic extremes.

The findings of this study provide robust evidence to support the implementation of the CRGE and NAP-ETH frameworks, inform integrated water resource management, and contribute to Ethiopia's long-term national plan. More broadly, the results will serve policymakers and stakeholders across East Africa in developing effective adaptation measures to address the risks posed by climate variability and change. By filling critical knowledge gaps in the understanding of spatio-temporal climate extremes and hydroclimatic impacts, this research enhances the scientific basis for designing resilient strategies that safeguard livelihoods and promote sustainable development in the face of climate change.

1.2 Problem statement

Rain-fed agriculture accounts for the majority of food production and rural livelihoods, while water resources are indispensable for energy generation, irrigation, and industrial development (Moges and Bhat 2021). This dependence on rainfall and hydrological systems makes the country acutely vulnerable to climate extremes such as droughts, floods, and prolonged dry spells. Historical evidence highlights that recurrent droughts have triggered devastating humanitarian crises, crop failures, and widespread food insecurity. For example, between 1980 and 2019, droughts displaced over 10 million people, led to the loss of millions of hectares of cropland, and

contributed to chronic food insecurity affecting more than 15% of the population at peak periods (World Bank, 2019; FEWS NET, 2020). Between 1991 and 2019, floods resulted in 3,000 deaths, displaced 1.3 million people, and caused the loss of 250,000 cattle and 500,000 hectares of cropland (World Bank, 2019). Ethiopia faces escalating risks to water, food, and energy security, as climate change projected to increase the frequency and severity of such events, thereby undermining its socio-economic development trajectory.

In recognition of these challenges, the Government of Ethiopia has developed national climate strategies, including the Climate Resilient Green Economy (CRGE) and the National Adaptation Plan (NAP-ETH). Existing studies largely emphasize mean climate trends, while extremes, such as droughts, floods, and extreme rainfall events, pose the most serious risks to Ethiopia's hydroclimatic systems, agriculture, and energy production. The absence of robust projections of historical-to-future extremes at national and regional scales hinders the design of evidence-based adaptation strategies. Addressing this gap is critical for aligning scientific projections with Ethiopia's CRGE vision and ensuring sustainable, climate-resilient development.

Previous generations of climate models, notably those from CMIP5, provided valuable insights into regional climate futures but exhibited substantial limitations in Ethiopia. Several studies have shown that CMIP5 models have struggled to reproduce seasonal rainfall cycles, the timing of rainy-season onset and cessation, and the variability of precipitation. They also exhibited large magnitude biases, which may further undermine their reliability for developing climate adaptation strategies (Yang et al., 2015; Jury, 2015; Li et al., 2016). The advent of CMIP6 introduced updates to deep convective schemes, cloud microphysics, aerosol contributions to cloud formation, and higher model resolution (Eyring et al., 2016; Kim et al., 2020). These improvements have slightly reduced model bias in capturing precipitation characteristics and offer an opportunity for a better understanding of future climate (Kim et al., 2020; Akinsanola et al., 2021). Yet, despite these advances, systematic evaluations of CMIP6 model performance in simulating mean climate and extreme events for future climate projection across Ethiopia remain limited.

Research on CMIP6 models in Ethiopia has primarily focussed on long-term averages of precipitation at the basin scale (Alaminie et al., 2021; Fetene et al., 2022; Dyer et al., 2022; Gebisa et al., 2023; Omay et al., 2023). Only a few studies have evaluated the ability of these models to

simulate precipitation extremes or seasonal rainfall characteristics for East Africa (Akinsanola et al., 2021) and Ethiopia (Rettie et al., 2023). Moreover, most of these studies have relied on a limited subset of models (often fewer than 20) and observational datasets such as CHIRPS or GPCP, which, although useful, may not adequately capture the fine-scale heterogeneity of Ethiopian rainfall. Evaluations of seasonal performance, particularly for the main rainy season (JJAS) and the short rainy season (FMAM), remain limited. The central problem this study addresses is therefore the absence of a comprehensive, Ethiopia-specific evaluation of CMIP6 models in simulating both mean climate conditions and extremes for future climate projection. Consequently, to the best of our knowledge, there is still a lack of information on projections of precipitation extremes at both the national and basin scales under the new CMIP6 scenarios. Moreover, much of the existing literature either relies on using all-model ensembles, which dilute predictive skill by including poorly performing models, or individual models, which cannot represent the full range of variability.

Furthermore, little attention has been given to linking climate extremes using CMIP6 models to hydroclimatic systems, despite their critical influence on river flows, groundwater recharge, and water availability. For instance, the Awash basin, Ethiopia's most heavily utilized basin, faces increasing stress due to recurrent droughts, floods, and rising demand (Adeba et al., 2015; Gedefaw et al., 2018). Despite growing interest in climate change impacts on hydrology, many studies rely on earlier CMIP5 projections and primarily analyze mean rainfall trends, which overlook the more critical hydroclimatic extremes such as droughts and floods. The limited focus on extremes creates an incomplete picture of climate risks, particularly in vulnerable basins like the Awash. Additionally, hydrological modeling efforts often fail to integrate updated tools like SWAT+, which provide better representation of basin-scale processes and extremes.

Ultimately, addressing these knowledge gaps is essential for reducing uncertainty in climate risk assessments, enhancing national adaptation planning, and safeguarding Ethiopia's socio-economic development in the face of a changing climate.

1.3 Research questions

Based on the problems identified, the following key research questions are formulated:

1. How well do CMIP6 models reproduce the mean precipitation pattern over Ethiopia, particularly during the main rainy season (JJAS) and the short rainy season (FMAM), when evaluated against the ENACTS observational dataset? How can the optimum number of models be selected to generate an ensemble of CMIP6 simulations for future climate projection impact studies over Ethiopia?

2. To what extent do CMIP6 models capture the spatial and temporal variability of 10 extreme precipitation indices at both national and agro-ecological zone levels?

3. What are the historical trends and projected future changes in precipitation extremes using ensembles from the best-performing CMIP6 models at national and basin level under different SSPs?

4. How will projected climate change affect hydroclimatic extremes, such as droughts, and floods, in key basin like the Upper Awash basin (Mojo catchment), when simulated using the SWAT+ hydrological model?

1.4 Research objectives

To address the issues identified in the preceding research questions, the main objective of this study is to evaluate the performance of CMIP6 climate models in simulating mean and extreme precipitation across Ethiopia and to generate robust, ensemble-based hydroclimate projections that can inform water resources management and climate adaptation planning. To achieve this overarching aim, the specific objectives are:

1. To evaluate the performance of CMIP6 models in simulating mean precipitation across Ethiopia for the main rainy season (JJAS) and short rainy season (FMAM), using the ENACTS dataset as a reference. It also selects the optimum number of models for generating an ensemble of CMIP6, which can be used for future climate projection impact studies over Ethiopia.

2. To assess the performance of 45 CMIP6 models in simulating 10 extreme precipitation indices at the national level and across Ethiopia's five agro-ecological zones.

3. To generate historical trends and projections of future precipitation extremes using the ensembles of top-ranking CMIP6 models under different emission scenarios at the national and basin scales.

4. To assess the potential impacts of climate change on hydroclimatic extremes (droughts and floods) in critical basins such as the Upper Awash basin (Mojo catchment) by employing updated CMIP6 projections in conjunction with the SWAT+ hydrological model.

1.5 Scope of the study

This study focuses on the spatio-temporal variability of climate extremes and the impacts of climate change on hydroclimatic systems in Ethiopia. The scope is defined by the following aspects:

1. Geographical Scope: The research covers the entire national territory of Ethiopia, including the five major agro-ecological zones. For hydrological impact analysis, the Upper Awash basin, specifically Mojo catchment, is selected as a case study due to its economic, social, and ecological significance and its vulnerability to climate extremes such as droughts and floods.

2. Temporal Scope: The study analyzes historical climate data from 1981 to 2010 to assess trends and variability in precipitation extremes. Future projections of climate and hydroclimatic extremes are conducted for the period 2015–2100 SSPs scenarios of CMIP6 models. Seasonal analysis is performed for the main rainy season (JJAS) and the short rainy season (FMAM), which account for approximately 90% of Ethiopia's annual rainfall.

3. Data Scope: High-resolution observational climate data from ENACTS dataset (0.0375° × 0.0375°) are used to evaluate the performance of CMIP6 models in simulating precipitation extremes. Forty-five CMIP6 models are assessed for their ability to reproduce historical climate characteristics, with ensemble analyses conducted using top-performing models. Hydroclimatic impacts, including streamflow, drought, and flood indices, are modeled using the SWAT+.

4. Variable Scope: The study focuses on precipitation and hydrological extremes, including heavy rainfall, drought frequency, and intensity. Other climate variables such as evapotranspiration are considered indirectly in relation to hydrological modeling.

1.6 Limitations of the study

Despite its comprehensive scope, this study has the following limitations:

1. Model uncertainties: While CMIP6 models represent an improvement over previous generations, uncertainties remain due to differences in model structures, parameterization schemes, and spatial resolutions. These uncertainties may affect the precision of projected precipitation extremes and hydrological impacts.

2. Hydrological modeling constraints: The SWAT+ model relies on observed and simulated climate inputs and may not capture all local-scale hydrological processes, such as groundwater-surface water interactions or localized flooding events, especially in urban areas or regions with limited hydrometeorological data.

3. Focus on select basin: Although the study assesses the future projection of climate extremes at the national and basin level, detailed hydroclimatic impact assessment is restricted to the Mojo catchment. Results from this catchment may not fully represent conditions in Upper basins and other basins with different hydrological characteristics or land-use practices.

4. Temporal trends: Historical trends are analyzed using data from 1981–2010, and future projections cover 2015–2100. The findings may be sensitive to the selection of these time periods, and changes outside these ranges are not considered. Another limitation arises from focusing only on two rainfall seasons (FMAM and JJAS), which may not fully represent the substantial seasonal variability observed across different regions of Ethiopia.

Despite these limitations, the study provides a robust and comprehensive assessment of climate extremes and hydroclimatic impacts in Ethiopia, offering valuable insights for adaptation planning, water resource management, and climate-resilient development strategies.

1.7 Significance of the study

The findings of this study hold substantial scientific, practical, and policy relevance for Ethiopia and the broader East African region. From a scientific perspective, this research provides a comprehensive evaluation of 45 CMIP6 models in simulating the historical mean and precipitation extremes, offering insights into model performance at both national and agro-ecological zone scales. By integrating high-resolution ENACTS observational data, updated CMIP6 models, and advanced hydrological modeling using SWAT+, the study advances understanding of the spatio-temporal variability of climate and hydroclimatic extremes. This contributes to the existing body of knowledge on climate modeling, extreme event analysis, and the interaction between climate and hydrology in regions with complex topography and heterogeneous rainfall patterns.

From a practical standpoint, the study addresses critical information gaps for water resource management, agriculture, energy, and disaster risk reduction. By assessing the impacts of climate change on hydrological extremes such as droughts, floods, and streamflow variability in the Upper Awash basin, the study provides actionable information for basin-specific adaptation strategies. These insights can guide the design and implementation of climate-resilient infrastructure, irrigation schemes, water allocation strategies, and early warning systems, enhancing the capacity of local and national institutions to respond effectively to climate-induced hazards.

Policy-wise, the study supports Ethiopia's national development and climate adaptation initiatives, including the Climate Resilient Green Economy (CRGE) strategy, and the National Adaptation Plan (NAP-ETH). By providing reliable projections of climate extremes and associated hydrological impacts, the research offers evidence-based guidance for formulating policies that integrate climate risk management into national and regional planning. The findings also have broader relevance for East African countries facing similar climate vulnerabilities, offering insights into how robust modeling and ensemble approaches can inform adaptation strategies and enhance resilience to climate variability and change.

Furthermore, this study contributes to reducing uncertainties in climate and hydrological projections by comparing an ensemble of top-performing CMIP6 models against the full ensemble, providing a methodological framework that can be replicated in other regions. By linking historical observations with future climate projections, the research enables a better understanding of

evolving climate dynamics and their potential impacts on socio-economic systems, ecosystems, and water security. Overall, the study's findings have the potential to inform scientific research, policy development, resource management, and long-term climate adaptation planning, making it highly significant for Ethiopia and the East African region. The significance of this research lies not only in advancing scientific understanding of climate model performance in complex topographic regions but also in generating information for policy and planning to support climate-resilient development, disaster risk reduction, and sustainable water and agricultural management.

1.7 Structure of the dissertation

This dissertation is organized into seven chapters. Chapter 1 introduces the study by presenting the background and problem statement, research objectives and questions, scope and limitations, and significance of the research. Chapter 2 outlines the overall methodological framework adopted in the study, describing the datasets, analytical tools, and approaches used. Chapters 3–6 address the four specific objectives of the research. Each chapter follows a consistent structure, comprising an introduction, materials and methods, results, discussion, and conclusions. Chapter 3 evaluates CMIP6 models in capturing Ethiopia's rainfall patterns during JJAS and FMAM using ENACTS and identifies an optimal ensemble. Chapter 4 assesses their ability to simulate 10 extreme precipitation indices at national and agro-ecological levels. Chapter 5 generates historical trends and future projections of precipitation extremes under different emission scenarios using top-performing models at national and basin scale. Chapter 6 assesses climate change impacts on streamflow, droughts, and floods in key basins, particularly the Upper Awash (Mojo catchment), using the SWAT+ model. Chapter 7 synthesizes the main findings of the study, presents an overall summary, conclusions, and highlights recommendations for policy, practice, and future research directions.

Chapter 2. Overall Methodology and Conceptual Framework

2.1 Overall methodology of the study

The overall methodology of the study was designed to comprehensively evaluate multiple recent CMIP6 models in simulating mean and extreme precipitation for projecting future climate and hydroclimate extremes at the national and basin levels. Model performance was assessed using spatial rainfall patterns and statistical metrics, including Pearson Correlation Coefficient (PCC), mean bias (MB), Percent bias (Pbias), Root-Mean-Square Error (RMSE), Taylor Skill Score (TSS), Portrait, and Taylor diagrams.

The first part of the study evaluated the ability of 37 CMIP6 models to represent the spatiotemporal distribution of mean rainfall in Ethiopia from 1981 to 2014, using ENACTS and CHIRPS as reference datasets. The CMIP6 models were assessed for their ability to represent mean monthly and seasonal precipitation cycles. All data were regridded to a uniform 1°×1° resolution, and model performance was assessed using MB, RMSE, PCC, TSS, and Taylor diagrams. Individual models were ranked based on TSS for mean monthly, JJAS, and FMAM rainfall, and an overall rank was calculated using a comprehensive rating metric. Seven different ensembles were then compared against observations to identify the optimal set of CMIP6 models for generating ensembles for future climate projections and impact studies across Ethiopia.

The second part of the study conducted a comprehensive evaluation of 45 CMIP6 models in simulating seasonal precipitation extremes (JJAS and FMAM) across Ethiopia, using the ENACTS dataset as a reference. Ten extreme precipitation indices were computed at native model resolution and regridded to a common 1°×1° grid for spatial and statistical analysis. Model performance was assessed using metrics including PCC, Pbias, normalized root-mean-square error (NRMSE), TSS, Portrait and Taylor diagrams. Individual models were ranked for each extreme index using TSS, and an overall ranking was derived using a comprehensive rating metric (RM). Ensembles (EnseMean) were then generated using the top-ranking models with RM_TSS > 0.70, while EnseMean_ALL was created using all 45 models. The EnseMean was compared against EnseMean_ALL, and individual models through spatial patterns, statistical metrics, and graphical assessments. Finally, the performance of the top-ranking ensemble was evaluated across Ethiopia's five agro-ecological zones to assess its ability to simulate extreme precipitation indices regionally.

The third part of the study examined the spatial and temporal variability of extreme precipitation in Ethiopia over recent decades (1981–2010) and future periods (2041–2100), integrating historical observations with CMIP6 projections. To improve reliability, CMIP6 data were bias-corrected using the quantile mapping (QM) technique, and the ensemble mean of top-ranking models (EnseMean) was generated for each season. Ten extreme precipitation indices from the Expert Team on Climate Change Detection and Indices (ETCCDI) were used to analyze patterns, trends, and future changes under SSP245 and SSP585 scenarios. Long-term averages for the mid-future (2041–2070) and far-future (2071–2100) periods were computed, and relative changes in indices were determined by comparing projected values to the baseline period. Seasonal trends in extreme precipitation were assessed using the Mann–Kendall test and Sen's slope estimator.

The fourth part of the study assessed the impacts of future climate extremes on the Awash Basin and corresponding hydrological responses in the Mojo Catchment using SWAT+ hydrological model. Historical data from 1981–2010 served as a reference to evaluate changes in precipitation, maximum, and minimum temperatures for the 2020s (2014–2040), 2050s (2041–2070), and 2080s (2071–2100) under SSP245 and SSP585 scenarios. Five ETCCDI extreme indices, PRCPTOT, CDD, CWD, Rx5day, and R95pTOT, were used to assess flooding and drought risks. Bias correction was applied using quantile mapping for precipitation and variance scaling for temperature before generating ensemble means of top-performing models. These ensembles were used to drive SWAT+, with sensitivity analysis, calibration, and validation conducted via SWAT+ Toolbox v2.2, to evaluate future hydrological changes, including mean streamflow, floods, and droughts in the Mojo Catchment.

Generally, the methodology integrated a comprehensive evaluation of CMIP6 models for simulating mean and extreme precipitation over Ethiopia, using ENACTS (1981–2014) as reference datasets. Statistical and graphical analyses were applied to rank models and generate optimal ensembles, which were further assessed across Ethiopia's five agro-ecological zones. Historical observations and bias-corrected CMIP6 projections were combined to examine the spatial and temporal variability of extreme precipitation using ten ETCCDI indices under SSP245 and SSP585 scenarios for mid- and late-century periods. Trends were evaluated using the Mann–Kendall test and Sen's slope estimator. At the basin scale, bias-corrected ensembles and the

SWAT+ model were applied in the Mojo catchment to project changes in streamflow, floods, and droughts.

2.2 Conceptual framework of the study

The conceptual framework integrates methodological steps that include evaluating CMIP6 models against ENACTS to identify the most skillful models and producing bias-corrected ensembles. Subsequently, ETCCDI indices are applied to analyze historical variability and project future extremes under SSP245 and SSP585 scenarios. These projections are then linked with basin-scale hydrological modeling using SWAT+ to assess impacts on streamflow, floods, and droughts. Figure 2.1 presents the overall conceptual framework and highlights the interconnections among the study objectives.

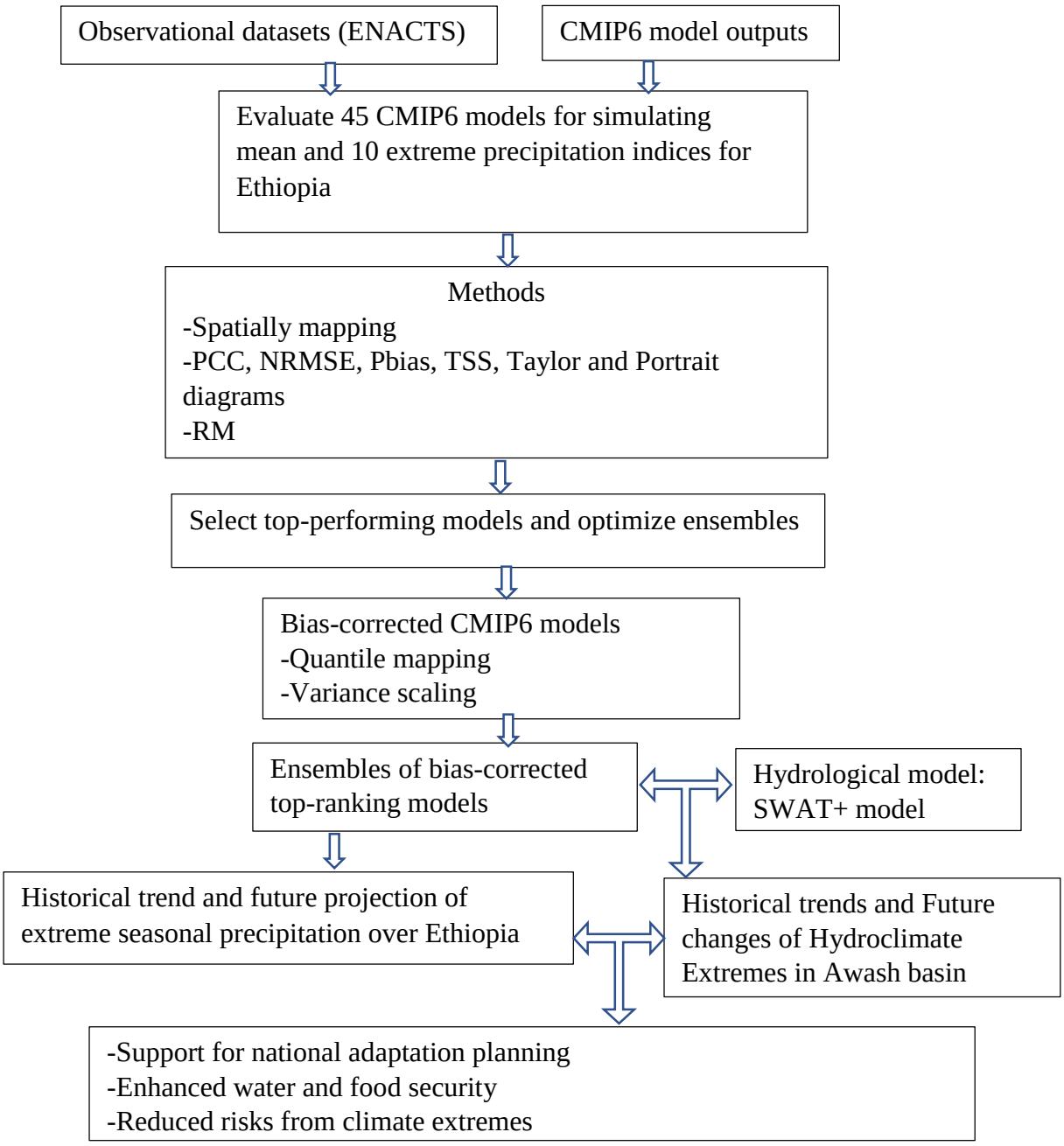

Figure 2.1: Overall conceptual framework of the study

Chapter 3. Evaluation of CMIP6 models in Reproducing observed Rainfall over Ethiopia

Abstract

Ethiopia is highly susceptible to the effects of climate change and variability. This study evaluated the performances of 37 CMIP6 models against the gridded rainfall product of Ethiopia known as Enhancing National Climate Services (ENACTS) in simulating the observed rainfall from 1981 to 2014. Taylor Skill Score was used to rank the performance of individual models for mean monthly, June–September, and February–May seasonal rainfall. Comprehensive rating metrics (RM) were used to derive the overall ranks of the models. Results show that the performances of the models were not consistent in reproducing rainfall distributions at different statistical metrics and timeframes. More than 20 models simulated the largest dry bias on high topographic and rainfall-receiving areas of the country during the June–September season. The RM-based overall ranks of CMIP6 models showed that GFDL-CM4 is the best-performing model, followed by GFDL-ESM4, NorESM2-MM, and CESM2 in simulating rainfall over Ethiopia. The ensemble of these four Global Climate Models showed the best performance in representing the spatiotemporal patterns of the observed rainfall relative to the ensembles of all models. Generally, this study highlighted the existence of dry bias in climate model projections for Ethiopia, which requires bias adjustment of the models for impact assessment.

Key words: CMIP6, Ethiopia, FMAM, JJAS, model evaluation, rainfall

3.1 Introduction

Climate variability and change have a substantial impact on the livelihood and economy of people in the Horn of Africa, including Ethiopia (Reinman 2012). To address the impacts of climate change, the Ethiopian Government implements a National Adaptation Plan (NAP) by developing a Climate Resilient Green Economy (CRGE) strategy as the country's development policy framework. The country aims to pursue further integration of climate change adaptation proactively and iteratively into development policies and strategies (FDRE 2019). It is, therefore, important to have a reliable future climate projection for the country to build a successful NAP, devise efficient CRGE strategies, and prevent setbacks associated with climate change.

The coupled model intercomparison project phase 6 (CMIP6) models show improvements in the spatial resolution and the representation of physical processes relative to the previous CMIP5 models (Eyring *et al.* 2016). Various studies ,therefore, utilized CMIP6 models to study climate characteristics of observed datasets over different parts of the globe (Zhu & Yang 2020; Ayugi *et al.* 2021; Babaousmail *et al.* 2021; Ngoma *et al.* 2021; Faye & Akinsanola 2022; Makula & Zhou 2022). The above-mentioned authors reported that CMIP6 had both better and poorer performance than earlier versions of CMIP5 in simulating climate characteristics in different regions. Moreover, most of those studies indicate that the performance of models in reproducing the observed climate can vary over regions and across CMIP6 models.

Few studies have evaluated the CMIP5 models in Ethiopia (Jury 2015; Li *et al.* 2016; Dyer *et al.* 2020), and they indicated that CMIP5 models are still prone to substantial biases in simulating seasonal and annual rainfall over the country. Few studies have evaluated and utilized CMIP6 models in Ethiopia (Alaminie *et al.* 2021; Dyer *et al.* 2022; Fetene *et al.* 2022). Despite the high importance of assessing the performances of different CMIP6 models in replicating the mean monthly and seasonal rainfall both spatially and temporally, there is no national study that investigates the performance of different CMIP6 models. This study aimed to fill that knowledge gap using the most reliable gridded dataset of Enhancing National Climate Services (ENACTS) produced specifically for Ethiopia to evaluate the CMIP6 models.

This study evaluates the capability of CMIP6 models in their representation of the spatiotemporal rainfall distribution before employing them in future climate projections for building adaptation

capacity and climate resilient strategies at the national scale. It also selects the optimum number of models for generating an ensemble of CMIP6 which can be used for future climate projection impact studies over Ethiopia. Spatial and temporal evaluation of CMIP6 rainfall products were conducted for mean monthly, long rainy season during June–September (JJAS), and short rainy season during February–May (FMAM). The two seasons account for about 90% of the total rainfall over the country (Philip *et al.* 2018).

3.2 Study area, datasets, and methods

3.2.1 Study area description

Ethiopia is located between latitudes of 3°N to14°N and longitude of 33°E to 48°E. The country is characterized by complex topography, with marked contrasts in relief and altitudes ranging from about 155 m below sea level in the Northeast to about 4,533 m above sea level in the Northern highlands (Figure 3.1). The climate of Ethiopia is characterized by three distinct seasons locally named as *Belg, Kiremt*, and *Bega* (Gissila *et al.* 2004; Korecha & Barnston 2007). *Belg* season is the short rainy season from February to May (FMAM). Much of the Northeastern, Central, Southern, Southwestern, Eastern, and Southeastern parts of the country receive a modest rainfall amount during this season (Gissila *et al.* 2004). *Kiremt* season is the long rainfall season from June to September for most parts of the country except for the lowlands of Southern and Southeastern Ethiopia. This season (JJAS) contributes 65–90% of Ethiopia's annual rainfall and is responsible for 80–95% of the production of food crops in the country (Gissila *et al.* 2004). The *Bega* season is mostly a dry season from October to January, for most parts of the country except for Southwestern as well as the lowlands of Southern and Southeastern Ethiopia.

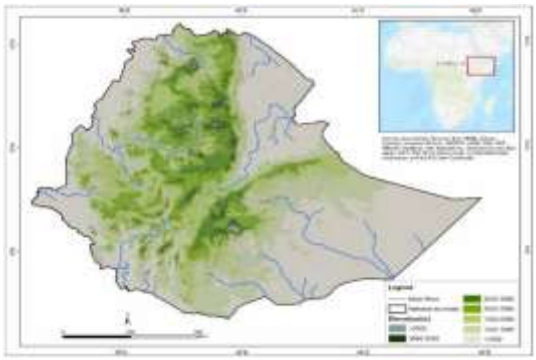

Figure 3.1: Location map of Ethiopia in the African continent. The color scale shows elevation in meters and the blue line shows main river.

3.2.2 Datasets

3.2.2.1 ENACTS and CHIRPS

Rainfall measurements from ground-based rain gauge observations in Ethiopia cannot provide adequate and timely information due to insufficient spatial coverage, poor representation, and many missing records (Dinku *et al.* 2014). Thus, ENACTS has been developed by a three-track approach that involved the Ethiopian Meteorological Institute (EMI), the International Research Institute for Climate and Society (IRI), and the University of Reading in order to produce high-resolution gridded climate data time series (Dinku *et al.* 2014).

ENACTS climate dataset derives from two main kinds of data. The first dataset is station rainfall data from the national weather stations managed by NMHS. The Ethiopian NMHS contributed high-quality-controlled ground-based station data from more than 600 rain gauge stations. The second dataset is satellite rainfall estimates from the European Organization for the Exploitation of Meteorological Satellites. TAMSAT satellite rainfall data were calibrated over Ethiopia using over 600 high-quality-controlled station data to generate the best possible satellite rainfall estimates. Station rainfall data were used to evaluate and correct the errors in the spatially complete products, which in turn are used to fill spatial and temporal gaps in station observations. The combined station and satellite products were generated at a daily or decadal time scale for all available stations, and the final products are datasets with over 40 years of rainfall time series produced at nominal 4-km grids across the country. Most global satellite products use 17 stations through Global Telecommunications System (GTS), stations while the ENACTS data incorporate over 600 stations. The result is a distinctive, high-quality, and more reliable dataset than any other long-term, satellite-based time series dataset (Dinku *et al.* 2014). ENACTS products are a 'gold standard' binding of the best local datasets and global data and can be produced sustainably so that new data can be regularly added to the historical archive (Dinku *et al.* 2018). Despite its strengths, ENACTS has limitations, including uneven spatial coverage of ground-based observations—particularly in data-sparse regions—dependence on the quality and continuity of national station networks, and potential uncertainties in areas with complex topography. Furthermore, regular updates rely on sustained institutional capacity and effective data-sharing arrangements, which may constrain long-term consistency in some countries. ENACTS has a spatial resolution of $0.0375° \times 0.0375°$ from 1981 to 2020 across Ethiopia. Hence, in this study,

ENACTS gridded dataset was used as an observation reference in order to evaluate the performance of CMIP6 models in simulating rainfall characteristics for the period 1981–2014 over Ethiopia.

In addition, monthly Climate Hazards Group InfraRed Precipitation with Station (CHIRPS) data for the period 1981–2014 were used as an additional observed dataset to evaluate the climate models. CHIRPS v2.0 is a quasi-global (50°S–50°N) gridded product and has a spatial resolution of $0.05° \times 0.05°$ at daily, pentad, decadal, and monthly temporal resolution (Funk *et al.* 2015). CHIRPS v2.0 is available online at http://chg.geog.ucsb.edu/data/chirps. A detailed description of CHIRPS satellite rainfall products is available in Funk *et al.* (2015).

3.2.2.2 CMIP6 model data

This study used the monthly precipitation data of historical simulation of 37 CMIP6 model outputs from 1981 to 2014 for the same period as observed reference gridded datasets. The rainfall simulated data from 37 CMIP6 models were obtained from Earth System Grid Federation archives (https://esgf-node.llnl.gov/ search/cmip6). The details of CMIP6 models regarding the modeling groups, countries, and horizontal resolution are presented in Table 3.1. To establish a time series from a NetCDF (.nc) file in R, first load the file using packages like ncdf4 or raster and identify the variable of interest (e.g., daily precipitation) along with the time, latitude, and longitude dimensions. Next, convert the time variable to standard dates based on the file's reference date. Then, extract data for a specific location or area of interest. Once extracted, the data can be aggregated to the desired time scale, such as daily, monthly, or seasonal totals for Kiremt (June–September) and Belg (March–May) seasons in Ethiopia. Finally, the resulting time series can be saved or used to calculate seasonal mean for multiple years.

Table 3.1: List of 37 CMIP6 models used in the current study over Ethiopia

No	Model	Country	Resolution (lon × lat)
1	ACCESS-CM2	Australia	1.9 × 1.3
2	ACCESS-ESM1-5	Australia	1.9 × 1.3
3	BCC-CSM2-MR	China	1.13 × 1.13
4	BCC-ESM1	China	2.81 × 2.81
5	CAMS-CSM1-0	China	1.13 × 1.13
6	CanESM5	Canada	2.81 × 2.81
7	CESM2	USA	1.25 × 0.94
8	CESM2-WACCM	USA	1.25 × 0.94

9	CESM2-WACCM-FV2	USA	2.5 × 1.9
10	CMCC-CM2-HR4	Italy	1.25 × 0.94
11	CMCC-CM2-SR5	Italy	1.25 × 0.94
12	CMCC-ESM2	Italy	1.3 × 0.9
13	CNRM-CM6- 1	France	1.4 × 1.4
14	CNRM-CM6-1-HR	France	0.5 × 0.5
15	CNRM-ESM2-1	France	1.4 × 1.4
16	E3SM-1-0	USA	1.0 × 1.0
17	EC-Earth3	Europe	0.7 × 0.7
18	EC-Earth3-Veg	Europe	0.7 × 0.7
19	EC-Earth3-Veg-LR	Europe	1.1×1.1
20	FGOALS-f3-L	China	1.25 × 1.0
21	FGOALS-g3	China	2.0 × 2.5
22	GFDL-CM4	USA	2.50 × 2.00
23	GFDL-ESM4	USA	1.25 × 1.00
24	HadGEM3-GC31-LL	UK	1.9×1.3
25	IITM-ESM	India	1.9 × 1.9
26	INM-CM4-8	Russia	2.0 × 1.5
27	INM-CM5-0	Russia	2.0 × 1.5
28	IPSL-CM6A-LR	France	2.5 × 1.3
29	MIROC6	Japan	1.41 × 1.41
30	MPI-ESM1-2-HR	Germany	0.94 × 0.94
31	MPI-ESM1-2-LR	Germany	1.9 × 1.9
32	MRI-ESM2-0	Japan	1.13 × 1.13
33	NESM3	China	1.9 × 1.9
34	NorESM2-MM	Norway	1.25 × 0.94
35	SAM0-UNICON	Republic of Korea	1.25 × 0.94
36	TaiESM1	Taiwan	1.25 × 0.94
37	UKESM1-0-LL	UK	1.88 × 1.25

3.2.3 Evaluation methods

3.2.3.1 Quantitative statistical measures

The models were first evaluated by observing their ability to capture the annual rainfall cycle and mean seasonal climatology (FMAM and JJAS seasons). The abilities of the CMIP6 models to replicate the climate properties of the study area were assessed using spatial comparisons. Since the resolutions are different for most models and observations, all data were re-gridded to a common grid of $1° \times 1°$ resolution using the bilinear interpolation method to confirm uniform resolution (Makula & Zhou 2022). The performance of each model in simulating rainfall was also evaluated using statistical metrics. Statistical metrics used for this study included mean bias (MB), root-mean-squared error (RMSE), and Pearson correlation coefficient (PCC) for the period 1981–2014. These quantitative metrics have been employed in many studies in Africa (Dyer *et al.* 2020; Akinsanola *et al.* 2021; Alaminie *et al.* 2021; Ngoma *et al.* 2021; Makula & Zhou 2022) and are summarized in Table 3.2 along with their equations.

Table 3.2: Description of quantitative statistical measures

Statistics	Formula	Range	unit	Best value
Mean bias	$MB = \frac{\sum_{i=1}^{n} m}{n} - \frac{\sum_{i=1}^{n} r}{n}$ (1)	-∞ to ∞	mm	0
Root-mean-squared error	$RMSE = \sqrt{\frac{\sum_{i=1}^{n}(m-r)^2}{n}}$ (3)	0 to ∞	mm	0
Pearson correlation coefficient	$PCC = \frac{\sum_{i=1}^{n}[(r-\bar{r})(m-\bar{m})]}{(\sigma_r * \sigma_m)}$ (4)	-1 to 1	none	1

where 'r' is the rainfall value acquired from ENACTS: the *'m'* represents the assessed value obtained from the CMIP6 rainfall dataset: while $\bar{r}$ *and* $\bar{m}$ are mean of ENACTS and models, respectively. σ_r and σ_m are the standard deviations of ENACTS and models, respectively: and *'n'* is the number of data pairs.

3.2.3.2 Ranking of CMIP6

The spatial performance of CMIP6 models has been further assessed based on the Taylor diagrams and Taylor Skill Score (TSS) (Taylor 2001). Taylor diagrams are used to measure the performance of the models by indicating the spatial similarity of each model with respect to the observations in terms of the PCC, the RMSE, and the standard deviation (SD).

TSS is a statistical summary of PCC, RMSE, and SD (Taylor 2001). It has been used for assessing and ranking individual CMIP6 models in reproducing mean monthly and seasonal spatial patterns of observed rainfall with respect to ENACTS and CHIRPS. Successful application of this approach has been employed in various recent studies in Africa and East Africa regions in ranking model capability (Dyer *et al.* 2020; Ayugi *et al.* 2021; Makula & Zhou 2022). TSS is calculated using the following equation (Taylor 2001):

$$TSS = \frac{4(1+PCC)^2}{(\frac{\sigma_m}{\sigma_r}+\frac{\sigma_r}{\sigma_m})^2(1+PCC_o)^2} \quad (3.1)$$

where PCC is the Pearson correlation coefficient between reference and model outputs; σ_m and σ_r are the model and reference standard deviations, respectively; and PCC_0 is the highest achievable correlation coefficient set at 1. The closer the value of TSS is to 1, the better the agreement

between the simulation and observation.

Rank was computed for the individual models using TSS for mean monthly, JJAS, and FMAM with respect to ENACTS and CHIRPS. The comprehensive rating metric (RM) was then used to obtain the overall ranks of CMIP6 models over the entire study area (Chen *et al.* 2019). An RM value closer to 1 refers to a better-performing CMIP6 model whereas an RM closer to 0 refers to a poorly performing model. The overall ranks (RM) of Global Climate Models (GCMs) were calculated using the following equation:

$$RM = 1 - \frac{1}{nm}\sum_{i=1}^{n} rank_i \qquad (3.2)$$

Where *n* and *m* represent number of GCMs and timeframe, respectively and *i* represent the rank of GCMs in the mean monthly, JJAS and FMAM seasons.

Steps to calculate RM:

1. Select models and timeframes: Identify the number of GCMs (n) and the timeframes or seasons (m) to evaluate (e.g., mean monthly, JJAS, FMAM).
2. Rank each GCM: For each timeframe/season, rank the GCMs based on their performance compared to observations.
3. Sum the ranks: Add up the ranks of each GCM across all timeframes/seasons.
4. Compute RM: Apply the formula.
5. Interpret the results: A higher RM value indicates better overall performance across seasons and metrics; GCMs can then be ordered from best to worst.

3.2.3.3 Generating ensembles of CMIP6

Identification and selection of an ensemble of better-performing GCMs are important in the projection of climate in order to reduce the uncertainty associated with future climate projection (Philip *et al.*, 2018). In this study, seven different ensembles were produced based on RM values:

I. Ensembles mean of CMIP6 models with RM values ≥ 0.85
II. Ensembles mean of CMIP6 models with RM values ≥ 0.75
III. Ensembles mean of CMIP6 models with RM values ≥ 0.65

IV. Ensembles mean of CMIP6 models with RM values ≥ 0.55

V. Ensembles mean of CMIP6 models with RM values ≥ 0.45

VI. Ensembles mean of CMIP6 models with RM values ≥ 0.35

VII. Ensembles mean of all 37 CMIP6 models

Finally, seven different ensembles were compared and evaluated against ENACTS using the spatial distribution of rainfall, quantitative statistical measures, and TSS in order to select the optimum number of models for generating ensembles. The weighted average (WA) and simple average (SA) methods were employed to generate different ensembles based on RM values using Equations (3.3) and (3.4), respectively. The performance of ensembles was compared relative to two methods (WA and SA).

The formula for computing a weighted average is as follows:

$$WA=\sqrt{\frac{\sum_{i=1}^{n} m_i * RM_i}{\sum_{i=1}^{n} RM_i}} \tag{3.3}$$

Simple average based ensembles was calculated as follows:

$$SA = \frac{1}{n}\sum_{i=1}^{n} mi \tag{3.4}$$

where $\bar{m}$ is weighted average of models, m_i represents the assessed value obtained from the CMIP6 rainfall dataset, RM_i represent values of overall rank CMIP6 with respect to ENACTS; and *'n'* is the number of data pairs.

3.3 Results

3.3.1 Mean annual and seasonal cycle precipitation

ENACTS reproduces a bimodal rainfall pattern, with a peak in August and May for JJAS and FMAM seasons, respectively, over Ethiopia (Figure 3.2). CHIRPS was able to capture these bimodal rainfall patterns and rates very well. Nevertheless, compared to ENACTS, it underestimated rainfall amounts ranging between 1.2 mm in January and 24 mm in August. A high degree of spread was observed among different CMIP6 models in capturing the annual and seasonal rainfall distributions (Figure 3.2). Six models (15%) (E3SM-1-0, HadGEM3-GC31-LL, MPI-ESM1-2-HR, MPI-ESM1-2-LR, MIROC6, and UKESM1-0-LL) represented the shape of

the observed annual cycle more correctly, even though they showed some discrepancy in the amount of rainfall. MIROC6 simulated the highest rainfall amount in all months whereas E3SM-1-0, HadGEM3-GC31-LL, MPI- ESM1-2-LR, and UKESM1-0-LL reproduced the observed rainfall rates and patterns of the annual cycle more accurately.

Out of the 37 CMIP6 models, 13 (35%) captured the general pattern of the long rainy season (JJAS). On the other hand, 18 models (49%) simulated rainfall peaks in September and October rather than in August during the long rainy season. Thirteen models, except for FGOALS-f3-L and MPI-ESM1-2-LR, simulated more rainfall compared to a seasonal peak during the JJAS season. The pattern of the short rainy season (FMAM) was adequately replicated with reasonable skill by all the 37 CMIP6 models except for three models (CAMS-CSM1-0, CNRM-CM6-1, and CNRM-CM6-1-HR). However, seven models reduced the peak for FMAM while 27 models increased the peak. UKESM1-0-LL and MPI-ESM1-2-LR showed better JJAS seasonal rainfall patterns and peaks with a slight difference of +2 and -2.8 mm/month, respectively. IITM-ESM model represented the FMAM peak value accurately with a slight difference of 0.7 mm to observed peak rainfall, followed by NESM3, IPSL- CM6A-LR, and UKESM1-0-LL.

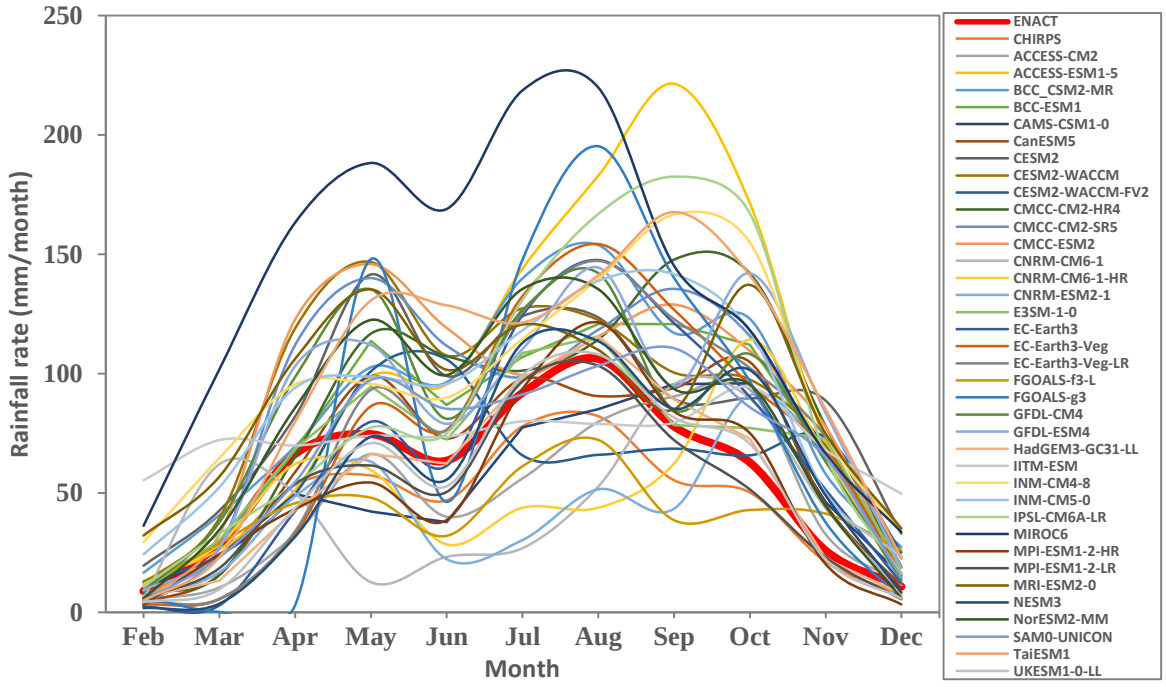

Figure 3.2: Mean monthly and seasonal cycle of rainfall over Ethiopia for 1981-2014 based on ENACTS, 37 CMIP6 models and 7 ensembles

3.2.2 Spatially distribution of seasonal rainfall

Figure 3.3 shows that the maximum amount of rainfall occurs in the West and Northwest, followed by the Central, South, and Southeast parts of the country during the JJAS season. CHIRPS and most CMIP6 models could generally capture the observed geographical distribution of rainfall over Ethiopia (Figure 3.3). However, more than 25 models were unable to simulate the maximum seasonal rainfall amount in the West and Northwest and they reproduced the low rainfall amount in the Southeast and South lowlands of the country. Out of the 37 CMIP6 models, 20 (54%) underestimated the observed seasonal rainfall over high rainfall receiving areas of the country (West and Northwest), with the highest underestimation by FGOALS-f3-L, CNRM-CM6-1, CNRM-CM6-1-HR, and CNRM-ESM2-1 models. On the contrary, six models (ACCESS-ESM1-5, BCC- CSM2-MR, CESM2-WACCM, CESM2, MIROC6, and NorESM2-MM) overestimated the observed seasonal rainfall over the aforementioned areas of the country during the JJAS season. GFDL-CM4, GFDL-ESM4, and E3SM-1-0 showed greater performance in replicating the spatial distribution of observed JJAS rainfall, while CNRM-CM6-1, CNRM-CM6-1-HR, CNRM- ESM2-1, FGOALS-g3-L, and INM-CM4-8 poorly reproduced the seasonal rainfall pattern.

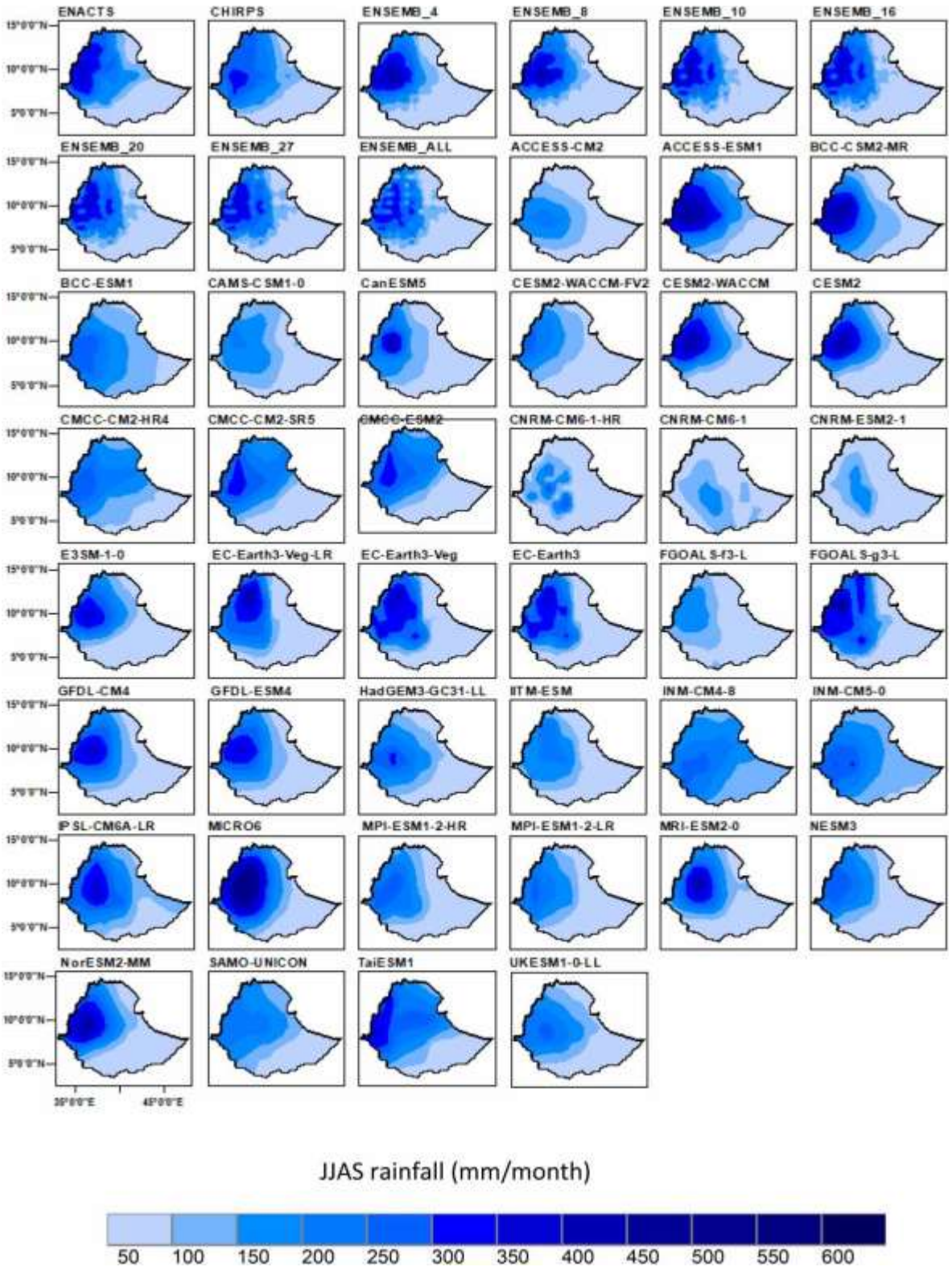

Figure 3.3: Spatial distribution of JJAS seasonal rainfall for ENACTS, CHIRPS, 37 CMIP6 models, and seven ensembles over Ethiopia for the period 1981–2014. The CHIRPS, individual models, and ensembles are labeled in the top of the panels.

The highest amount of FMAM rainfall was received over the Southwest and Southeast highlands of the country, followed by Central Ethiopia, but it decreased towards the North, Northeast, and Southeast parts of the country (Figure 3.4). CHIRPS showed better performance in capturing the spatial pattern of rainfall during the FMAM season compared to the JJAS season. However, most of the models could not generally capture such a geographical distribution of observed rainfall over the country during the FMAM season compared to the JJAS season. Moreover, more than 30 CMIP6 models were incapable of capturing observed rainfall over the Southwest and Southeast highland parts of the country, where the highest FMAM rainfall is observed.

Out of 37 models, 24 (65%) underestimated the maximum observed rainfall, with the highest underestimation by ACCESS-CM2 and FGOALS-f3-L models over the Southwest and Southeast highland parts of the country. In contrast, six models (ACCESS-ESM1-5, BCC_CSM2-MR, CESM2-WACCM, CESM2, MIROC6, MRI-ESM2-0) displayed an overestimation of the observed rainfall, with the highest overestimation by MIROC6 models over the above-mentioned areas during the FMAM season. BCC-ESM1 and NorESM2-MM were more capable of simulating the spatial variations of the observed FMAM rainfall than other models. On the contrary, ACCESS-CM2, ACCESS-ESM1-5, CAMS-CSM1-0, FGOALS-f3-L, NESM3, SAM0-UNICON, and UKESM1-0-LL were unable to accurately represent the spatial distribution of the observed FMAM rainfall, especially in high rainfall-receiving areas.

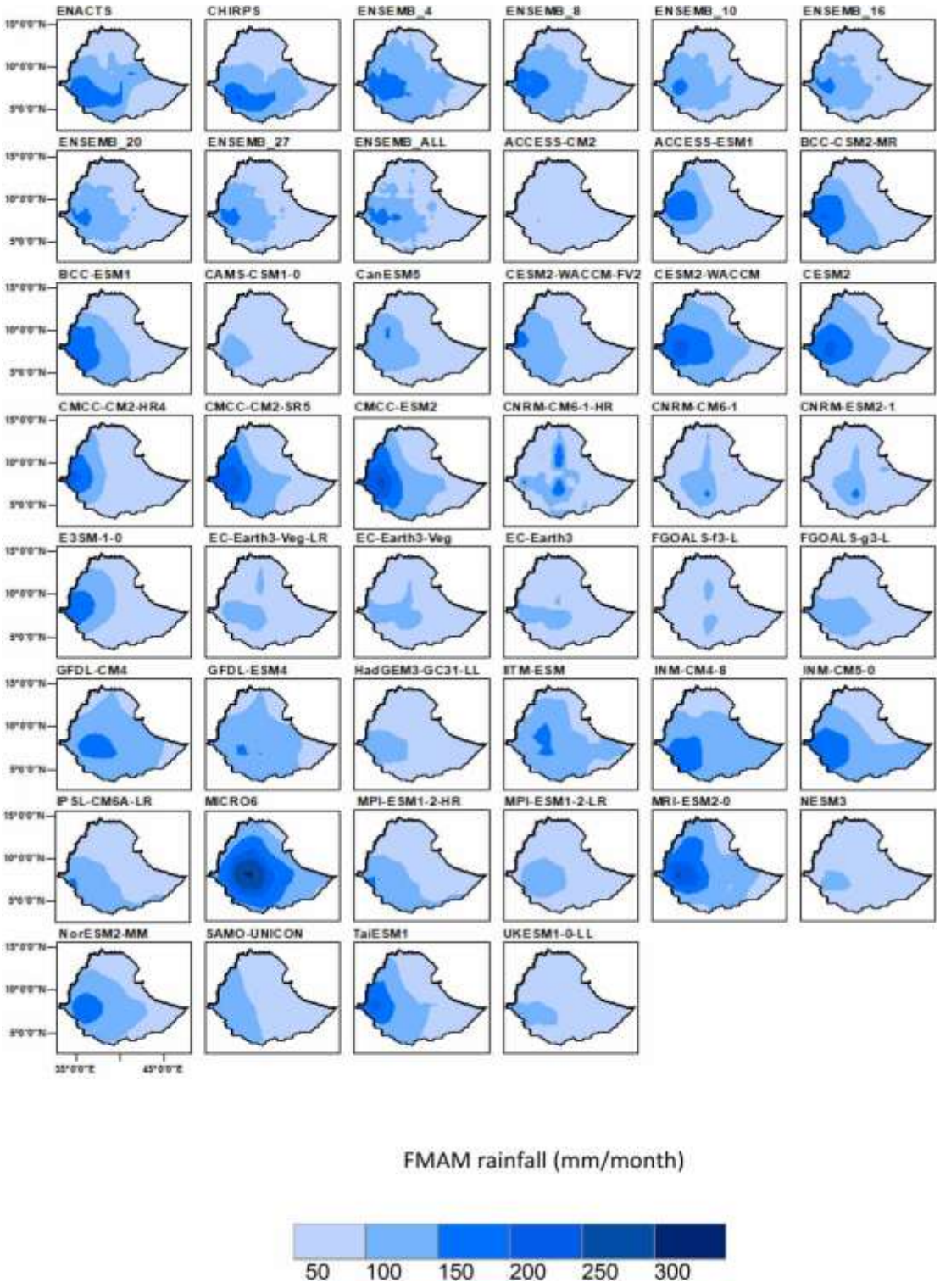

Figure 3.4: Spatial distribution of FMAM seasonal rainfall for ENACTS, CHIRPS,37 CMIP6 models, and seven ensembles over Ethiopia for the period 1981–2014. The CHIRPS, individual models, and ensembles are labeled in the top of the panels.

CHIRPS showed rainfall bias in the range -50 to 50 mm in most parts of the country during the JJAS season (Figure 3.5). CMIP6 models revealed a varying performance in reducing the error of simulating the JJAS seasonal rainfall. Eight of the models (ACCESS-ESM1-5, BCC-CSM2-MR, CanESM5, CESM2-WACCM, CESM2, MIROC6, MRI-ESM2-0, and NorESM2-MM) depicted the highest wet bias >100 mm over high rainfall and topographic areas of the country. On the contrary, CNRM-CM6-1, CNRM-CM6-1-HR, FGOALS-f3-L, and CNRM-ESM2-1 depicted the highest dry bias , which ranges from -100 mm to -326 mm over the above-mentioned area during the JJAS season. Generally, out of the 37 models, 13(35%) portrayed a wet bias of the observed JJAS rainfall ranging from 37 to 350 mm at most grid points of the country, while 17 models (46%) showed a dry bias of seasonal rainfall in the range -40 to -330 mm. CESM2-WACCM-FV2, E3SM-1-0, GFDL-CM4, GFDL-ESM4, MPI-ESM1-2-HR, and NESM3 performed well in simulating the JJAS rainfall with a relatively lower bias of less than 50 mm in most parts of the country, with the exception of highly wet and dry biases in some parts of the country.

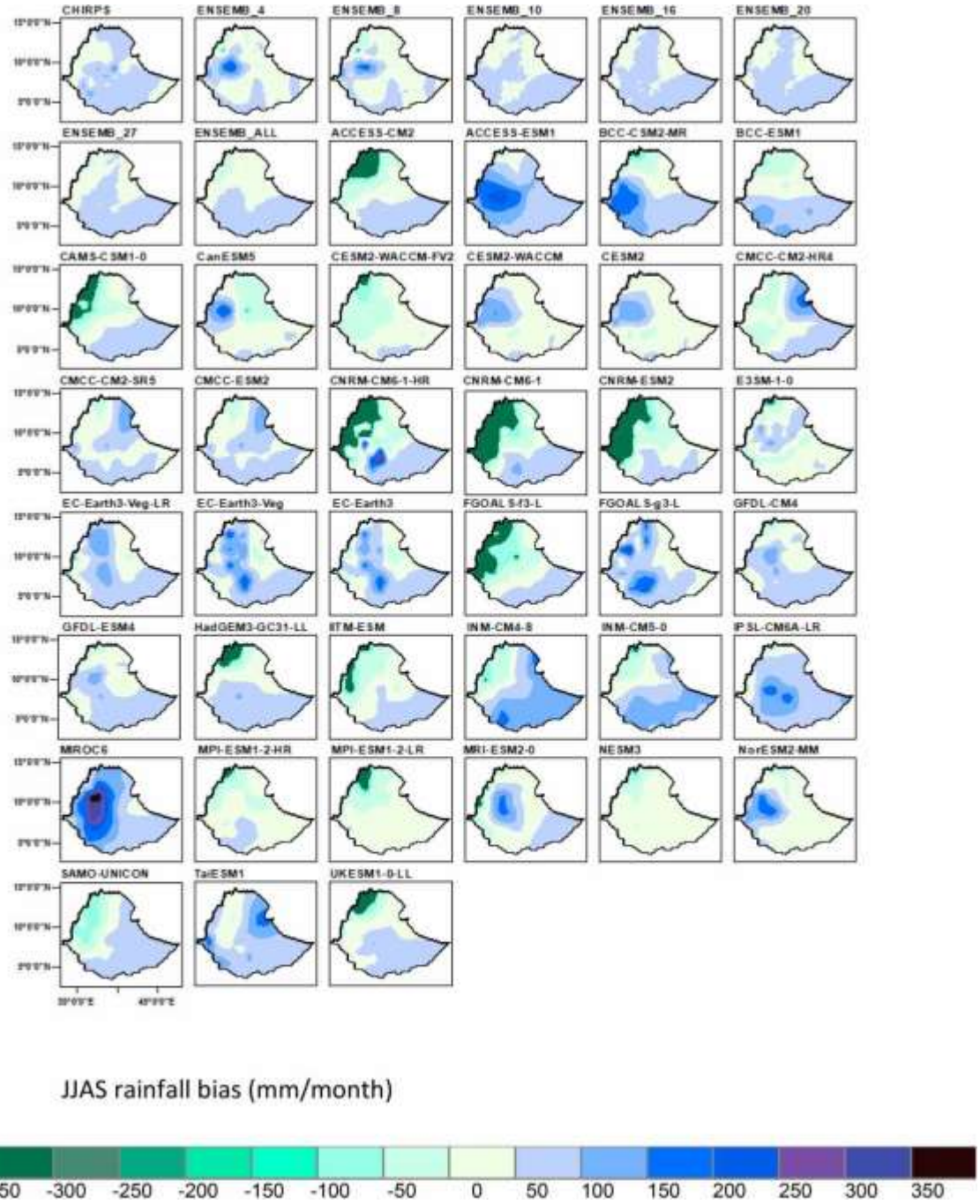

Figure 3.5: Spatial bias of rainfall (mm/month) of 37 CMIP6 models, seven ensembles, and CHIRPS with respect to ENACTS during the JJAS season over Ethiopia for the period 1980–2014. The CHIRPS, individual models, and ensembles are labeled in the top of the panels.

The models and CHIRPS were evaluated for bias of FMAM rainfall during 1981–2014 (Figure 3.6). Out of the 37 models, 21 (57%) showed a dry bias of observed rainfall from 80

to 110 mm over most parts of the country, with higher dry bias by 12 models (ACCESS-CM2, ACCESS-ESM1-5, CAMS-CSM1-0, CMCC-CM2-HR4, E3SM-1-0, EC-Earth3, EC-Earth3-Veg, EC-Earth3-Veg-LR, HadGEM3-GC31-LL, MPI-ESM1-2-HR, NESM3, and UKESM1-0-LL) in rainfall-receiving areas of the country (southern parts of the country) during the FMAM season (Figure 3.6). On the contrary, 10 models (ACCESS-ESM1-5, BCC-CSM2-MR, CESM2-WACCM, CESM2, CMCC-CM2-HR4, CMCC-CMS-SR5, CMCC-ESM2, MIROC6, MRI-ESM2-0, and NorESM2-MM) (27%) revealed a wet bias of seasonal rainfall in the range 50 to 97 mm over rainfall-receiving areas of the country. MIROC6 revealed the highest wet bias across most regions of the country, with values ranging from with greater than 70 mm to less than 200 mm during the JJAS and FMAM seasons. On the contrary, BCC-ESM1, GFDL-CM4, GFDL-ESM4, INM-CM5-0, and NorESM2-MM performed relatively well in simulating the FMAM rainfall with a lower bias of less than 40 mm in most parts of the country.

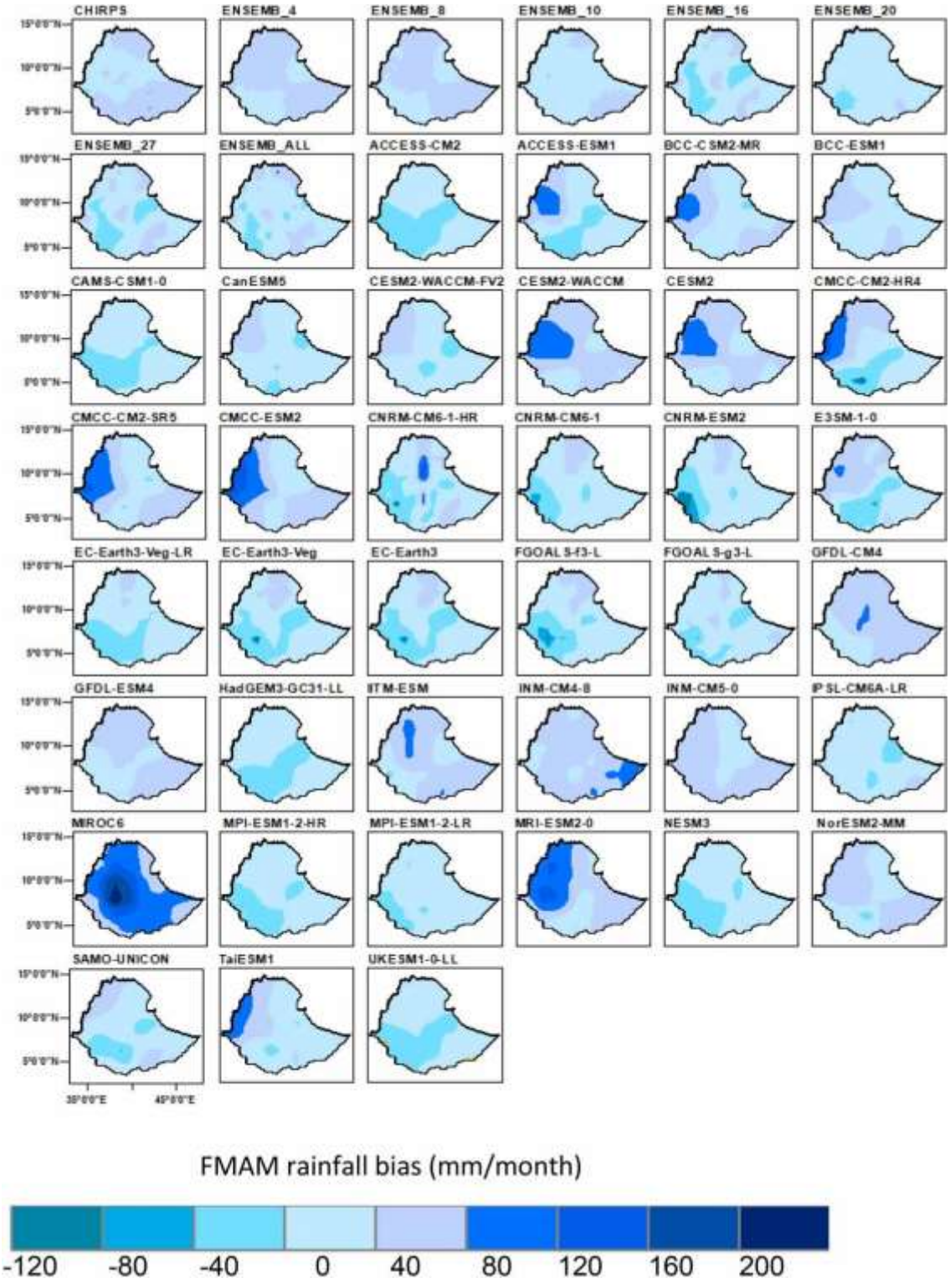

Figure 3.6: Spatial bias of rainfall (mm/month) of 37 CMIP6 models, seven ensembles, and CHIRPS with respect to ENACTS during the FMAM season over Ethiopia for the period 1981–2014. The CHIRPS, ensembles, and individual models are labeled at the top of the panels.

3.3.2 Statistical analysis of CMIP6 models

Results of statistical analysis of the MB for the 37 CMIP6 models and CHIRPS with respect to the ENACTS showed that CHIRPS exhibited little bias in mean monthly (-1.8 mm), JJAS (5.3 mm), and FMAM (1.8 mm) seasons (Figure 3.7(a)). The MB in mean monthly simulated rainfall was between -36.62 and 52.71 mm while JJAS and FMAM rainfall biases were in the range of -79.58 to 71.78 mm and -31.69 to 60.61mm, respectively. More than half of the models revealed wet bias in mean monthly rainfall, whereas many of the models simulated dry bias in both seasons. Twenty-five (close to 68%) of the models reflected more dry bias during the FMAM season than the JJAS season (20 models); however, the magnitude of dry bias was larger in the JJAS season (22 models) compared to the FMAM season (15 models) (Figure 3.7(a)). FGOALS g3 exhibited the lowest simulation bias of 0.48 mm for mean monthly, while BCC-CSM2-MR, and EC-Earth3 revealed the lowest bias of 0.70 and 0.30 mm for the FMAM and JJAS seasons, respectively. Further analyses of JJAS seasonal rainfall bias for some models' time series are presented in Appendix A1. Rainfall bias was changed significantly from one year to another year in most models during the JJAS season (Appendix A1). The simulated rainfall bias for GFDL-CM4, CESM2-WACCM-FV2, and MPI-E3SM1-2-HR was in the range of -24.6% (1992) to 91.7% (1981), -51% (2002) to 65% (1984) and -42.1% (1993) to 64.9% (1981), respectively, during the JJAS season. The biases in GFDL-ESM4, ESM-1-0, NESM3, CESM2, CESM2 WACCM, MPI-ESM1-2-LR, and BCC-CSM2-MR also varied over time as shown in Appendix A1.

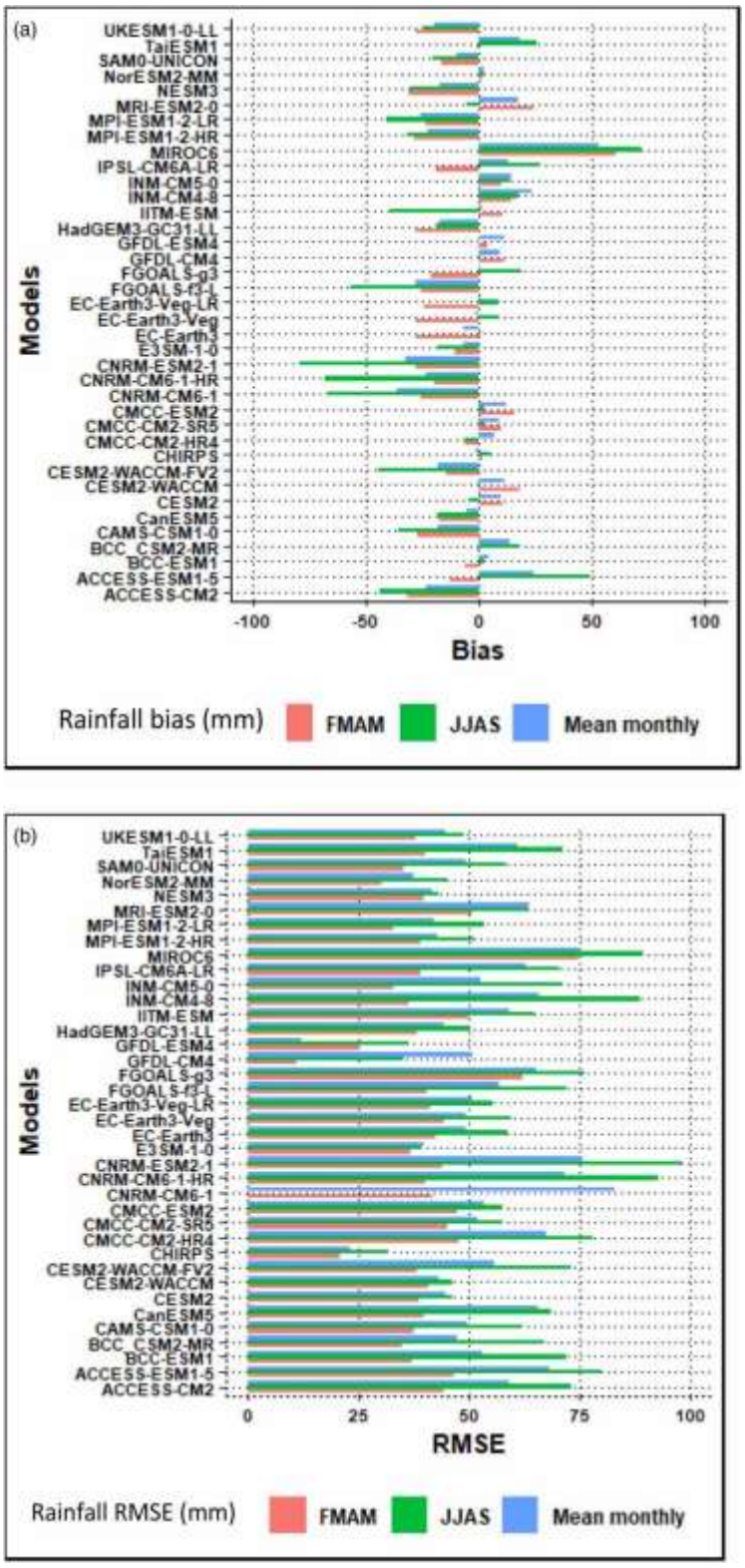

Figure 3.7: Rainfall bias (a) and RMSE (b) of 37 CMIP6 models and CHIRPS with respect to observations (ENACTS) over Ethiopia during 1981– 2014 for mean monthly, FMAM, and JJAS rainfall.

The RMSE results show that CHIRPS exhibited a larger error in JJAS (31.74 mm) compared to mean monthly (22.89 mm) and FMAM (20.65 mm) (Figure 3.7(b)). The general distribution of RMSE varied across models and time frames. The simulated error in mean monthly rainfall was in the range of 11.88 mm (GFDL-ESM4) to 83.06 mm (CNRM-CM6-1). The simulated rainfall of RMSE distribution for all the models during JJAS and FMAM were in the range of 35.01 mm (GFDL-CM4) to 114.78 mm (CNRM-CM6-1) and 11 mm (GFDL-ESM4) to 74.7 mm (MIROC6), respectively. Most of the models exhibited higher RMSE when simulating rainfall for the JJAS season than for the FMAM season. Three and 30 CMIP6 models exhibited RMSEs exceeding 50 mm for simulating observed rainfall during the FMAM and JJAS seasons, respectively. GFDL-CM4 showed a lower RMSE value of 11.9 mm in mean monthly rainfall while GFDL-ESM4 revealed low RMSE values of 11 and 35 mm for FMAM and JJAS seasons, respectively.

The 37 CMIP6 models and CHIRPS of PCC were evaluated for mean monthly and two seasons relative to the ENACTS dataset. Results indicated that CHIRPS showed the best correlation with PCC values of 0.92 and 0.91 when simulating JJAS and FMAM rainfall, respectively (Figure 3.8). All models revealed a positive correlation with observed rainfall patterns throughout the period. The models had varied PCC values ranging between 0.154 and 0.91 in JJAS, 0.31 and 0.88 in FMAM season while the corresponding mean monthly value ranged from 0.17 to 0.89. CESM2-WACCM, and NorESM2-MM revealed the highest correlation with PCC values of more than 0.8 in the whole period. MPI-ESM1-2-LR, NorESM2-MM, GFDL-CM4, and NESM3 showed the highest correlation with PCC values of over 0.85 when simulating mean monthly observed rainfall. NESM3, GFDL-CM4, GFDL-ESM4, and E3SM-1-0 were models that best captured the spatial distribution of observed JJAS rainfall, with the highest PCC values of greater than 0.9. GFDL-ESM4, MPI-ESM1-2-LR, GFDL-CM4, and NorESM2-MM performed relatively well, with higher PCC values of greater than 0.8 during FMAM. On the other hand, CNRM-CM6-1 showed the lowest skill with a low correlation coefficient with PCC value of less than 0.3 in the whole period. The fine resolution model, CNRM-CM6-1-HR, had a lower PCC value of less than 0.5 in mean monthly and JJAS while it had a higher PCC value of 0.65 during the FMAM season compared to the JJAS season over Ethiopia.

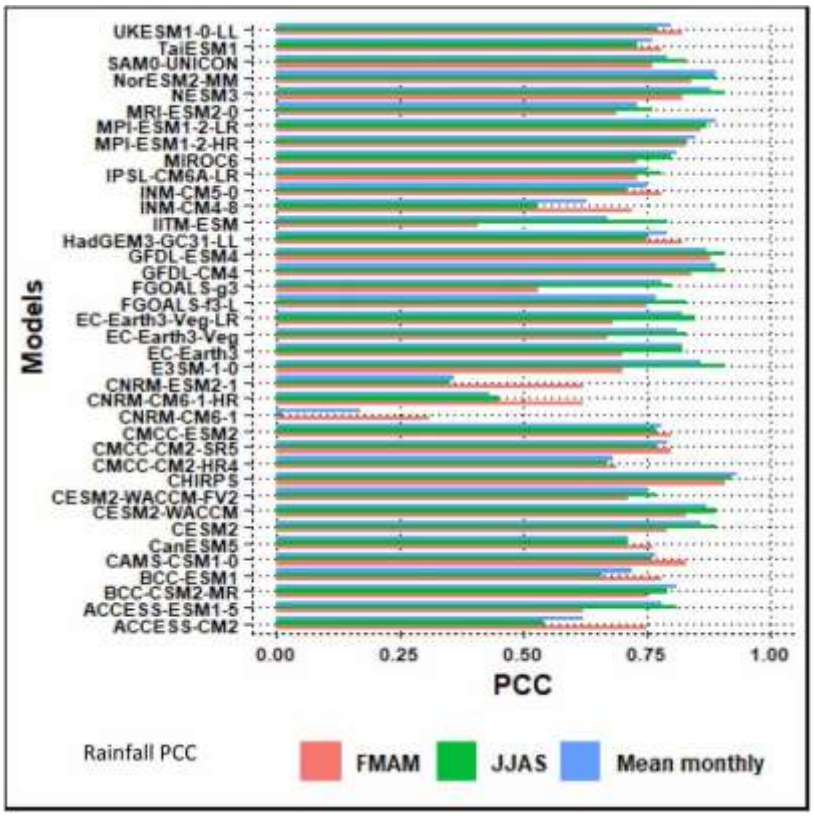

Figure 3.8: Rainfall PCC of 37 CMIP6 models and CHIRPS with respect to observations (ENACTS) over Ethiopia during 1981–2014 for mean monthly, JJAS, and FMAM rainfall. FMAM is represented by red, JJAS is represented by green, and the mean monthly is represented by blue.

3.3.3 Model ranking

Taylor diagrams were plotted to summarize the performance of the models in correlating with the observed patterns for mean monthly and two seasons (Figure 3.9). The reference point (REF) represents the observed dataset (here, ENACTS). It is always located at Correlation = 1 and Normalized standard deviation = 1. Even though the actual precipitation varies seasonally, the REF is always normalized in this diagram (standard deviation = 1, correlation = 1). The curved contours (0.5, 1, 1.5) on the diagram represent the Root Mean Square Difference (RMSD) between each model and the reference. CNRM-CM6-1, CNRM-ESM2-1, CNRM-CM6-1-HR, and MIROC6 had variations that are much larger than the observed pattern in the whole period, while GFDL-CM4, GFDL-ESM4, NESM3, E3SM-1-0, NorESM2- MM, CESM2-WACCM, and CESM2 had little spatial variability (Figure 3.9). Most models showed spatial correlations ranging from 0.6 to 0.9. Overall, most models

exhibited better performance for reproducing JJAS seasonal rainfall compared to FMAM seasonal rainfall (Figure 3.9). Seven of the models (GFDL-CM4, GFDL-ESM4, NESM3, E3SM-1-0, NorESM2-MM, CESM2-WACCM, and CESM2) performed best with higher PCC (.0.8), lower RMSE (0.5), and SD (close to 1) during the JJAS season. In contrast, only one model (GFDL-ESM4) showed relatively better performance during the FMAM season.

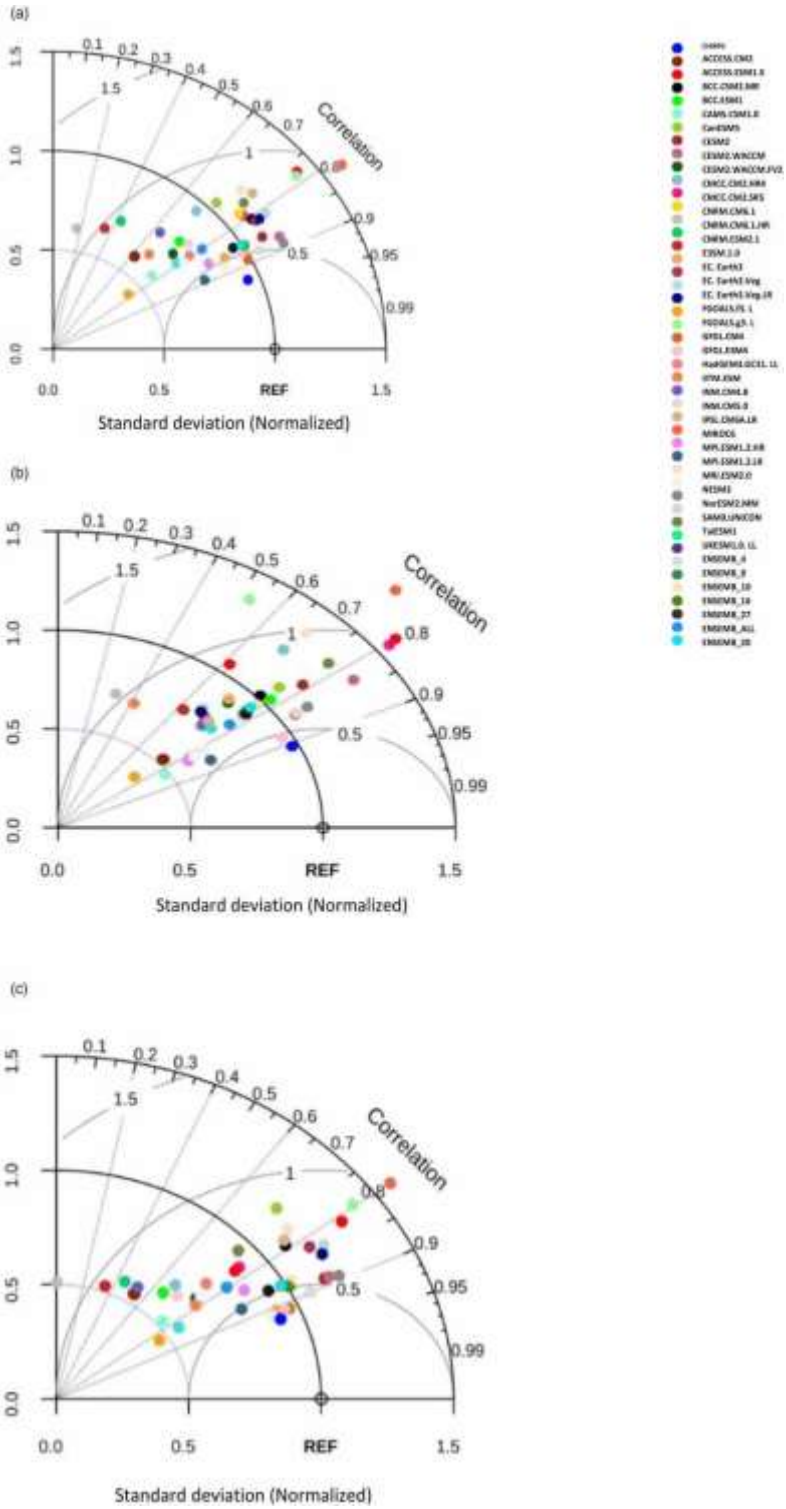

Figure 3.9: Taylor diagram of mean monthly (a), FMAM (b), and JJAS (c) simulated rainfall with respect to ENACTS over Ethiopia for the period 1981–2014.

TSS was used to rank CMIP6 models for simulating mean monthly, FMAM, and JJAS rainfall

over the country (Table 3.3). A large variation was found in the TSS of simulated rainfall among different models and time scales (Table 3.3). TSS values of the models for simulating mean monthly rainfall ranged from 0.27 to 0.89. For FMAM and JJAS seasons, the variations ranged from 0.35 to 0.8 and 0.17 to 0.91, respectively. Thirteen of the models depicted more than 0.8 TSS in mean monthly, 11 of the models in JJAS, and three of the models in FMAM. GFDL-CM4, GFDL-ESM4, NorESM2-MM, NESM3, and CESM2-WACCM were the best-performing models, with the highest TSS values of greater than 0.85 during the mean monthly. GFD-LCM4, GFDL-ESM4, NESM3, CESM2, CESM2-WACCM, and Nor-ESM2-MM showed the best JJAS rainfall representation, with TSS exceeding 0.85. During the FMAM season, GFDL-ESM4, GFDL-CM4, and NorESM2- MM adequately replicated the observed seasonal rainfall, with higher TSS values of more than 0.80. CNRM-CM6-1 and CNRM-ESM2-1 were the least skilled models in simulating the observed mean monthly and JJAS rainfall, with lower TSS values of less than 0.4, while CNRM-CM6-1 and FGOALS-f3-L poorly simulated the FMAM rainfall patterns.

Table 3.3: TSS values for mean monthly, JJAS, and FMAM, and overall ranks of CMIP6 models based on RM of TSS values (RM_TSS) for 37 CMIP6 models with respect to ENACTS for the period 1981–2014

Models	TSS			RM value (RM_TSS)	Overall ranks of models based on RM_TSS values
	Mean Monthly	JJAS	FMAM		
GFDL-CM4	0.89(1)	0.91(1)	0.85(2)	0.96	1
GFDL-ESM4	0.87(2)	0.91(2)	0.88(1)	0.95	2
NorESM2-MM	0.87(3)	0.87(7)	0.83(3)	0.88	3
CESM2	0.85(7)	0.87(5)	0.78(6)	0.85	4
CESM2-WACCM	0.86(5)	0.87(6)	0.7 6(7)	0.84	5
NESM3	0.87(4)	0.90(3)	0.71(15)	0.80	6
E3SM-1-0	0.85(6)	0.90(4)	0.72(13)	0.79	7
MPI-ESM1-2-LR	0.83(8)	0.84(8)	0.74(10)	0.77	8
BCC-CSM2-MR	0.81(12)	0.79(13)	0.77(9)	0.69	9
EC-Earth3	0.81(10)	0.81(11)	0.68(18)	0.65	10
EC-Earth3-Veg-LR	0.81(11)	0.83(9)	0.67(23)	0.61	11
TaiESM1	0.76(16)	0.74(19)	0.73(11)	0.60	12
EC-Earth3-Veg	0.80(13)	0.81(12)	0.67(22)	0.59	13
MPI-ESM1-2-HR	0.82(9)	0.82(10)	0.64(28)	0.58	14
IPSL-CM6A-LR	0.74(18)	0.78(14)	0.70(16)	0.57	15

Models	TSS			RM value (RM_TSS)	Overall ranks of models based on RM_TSS values
	Mean Monthly	JJAS	FMAM		
CMCC-CM2-SR5	0.79(14)	0.77(15)	0.67(20)	0.56	16
CanESM5	0.73(22)	0.71(22)	0.77(8)	0.54	17
INM-CM5-0	0.74(20)	0.61(27)	0.78(5)	0.53	18
CMCC-ESM2	0.78(15)	0.77(16)	0.66(25)	0.50	19
BCC-ESM1	0.70(26)	0.55(30)	0.79(4)	0.46	20
HadGEM3-GC31-LL	0.75(17)	0.71(21)	0.66(24)	0.44	21
UKESM1-0-LL	0.74(19)	0.70(23)	0.67(21)	0.43	22
CESM2-WACCM-FV2	0.68(28)	0.68(25)	0.73(12)	0.42	23
MRI-ESM2-0	0.73(21)	0.76(17)	0.65(27)	0.39	24
SAM0-UNICON	0.71(23)	0.61(28)	0.72(14)	0.37	25
ACCESS-ESM1-5	0.70(27)	0.76(18)	0.65(26)	0.36	26
CMCC-CM2-HR4	0.70(25)	0.60(29)	0.68(190	0.35	27
FGOALS-g3	0.71(24)	0.72(20)	0.53(32)	0.32	28
INM-CM4-8	0.62(30)	0.44(33)	0.69(17)	0.28	29
MIROC6	0.66(29)	0.66(26)	0.55(31)	0.23	30
IITM-ESM	0.58(32)	0.68(24)	0.44(35)	0.18	31
CAMS-CSM1-0	0.59(31)	0.53(31)	0.52(34)	0.14	32
CNRM-CM6-1-HR	0.46(34)	0.39(35)	0.61(29)	0.12	33
ACCESS-CM2	0.51(33)	0.42(34)	0.52(33)	0.10	34
CNRM-ESM2-1	0.39(36)	0.31(36)	0.61(30)	0.08	35
FGOALS-f3-L	0.42(35)	0.49(32)	0.35(37)	0.06	36
CNRM-CM6-1	0.27(37)	0.17(37)	0.38(36)	0.01	37

The overall ranks were assigned for each model based on the RM values (RM_TSS) to indicate their performance in representing the spatial characteristics of rainfall (Table 3.3). It is noted that the value of the RM_TSS metric varied between 0.01 (last rank) and 0.96 (first preferred) over the 37 ranks (Table 3.3). GFDL-CM4, GFDL-ESM4, NorESM2-MM, CESM2, CESM2- WACCM, and NESM3 were occupying the first six positions with RM_TSS values greater than 0.80 and hence regarded as the most skillful CMIP6 models in terms of TSS. It was observed that GFDL-CM4 and GFDL-ESM4 were the only CMIP6 models that were able to perform well for all timeframes with respect to TSS. On the other hand, CNRM-ESM2-1 FGOALS-f3-L, CNRM-CM6-1, ACCESS-CM2, and CNRM-CM6–1–HR were the last five models with RM_TSS values below 0.2 and can be regarded as the least-performing CMIP6 models for Ethiopia. It is important to note that the finest resolution CMIP6 model (CNRM-CM6–1–HR) showed the least

skill for simulating rainfall, signifying that reducing the resolution is not a guarantee for better performance.

Two CMIP6 GCMs (GFDL-CM4 and GFDL-ESM4), which were developed by the same modeling center (Geophysical Fluid Dynamics Laboratory (GFDL), USA), ranked first and second in the overall ranking of the models (Table 3.3), whereas most of the CMIP6 models showed different performances by ranks even though they were developed by the same modeling center. For example, CESM2, CESM2-WACCM, and CESM2-WACCM-FV2, which were developed by the same institution (National Center for Atmospheric Research, USA) ranked 4th, 5th, and 23rd, respectively. Similarly, differences in rank among models developed by the same modeling centers were also depicted between the models: INM-CM5-0 and INM-CM5-0; BCC-ESM1 and BCC-CSM2-MR; CMCC-CM2-HR4 and CMCC-CM2-SR5; ACCESS-CM2 and ACCESS-ESM1- 5; CESM2, CESM2-WACCM, and CESM2-WACCM-FV2; MPI-ESM1-2-LR and MPI-ESM1-2-HR; and FGOALS-f3-L and FGOALS-g3 (Table 3.3).

3.3.4 Comparison of different ensembles

WA and SA methods for generating ensembles were compared and presented in Appendix A2-A5. All ensembles showed better improvement in bias (Appendix A2) and RMSE (Appendix A3) in WA relative to the SA method. They revealed minimum bias (>7 mm) and RMSE (<40 mm) in all timeframes in WA-based ensembles relative to SA-based ensembles. The highest TSS value (.0.75) is found in WA-based ensembles relative to SA-based ensembles in all timeframes (Appendix A4). Thus, WA generated better-performing ensembles compared to SA and was therefore used in comparing ensembles in this study.

Spatially, a high amount of rainfall over the Northwest and West parts of the country was well acquired by all ensembles during the JJAS season (Figure 3.3). Furthermore, ENSEMB_4 and ENSEMB_8 outperformed all the 37 CMIP6 individual models and other ensembles in capturing the spatial distribution of JJAS (Figure 3.3) and FMAM (Figure 3.4) seasonal rainfall. All seven ensembles showed relatively weaker simulation bias ranging between -50 and 50 mm and between -40 and 40 mm in most parts of the country during the JJAS (Figure 3.5) and FMAM seasons (Figure 3.6), respectively.

All ensembles showed wet and dry bias in mean monthly and JJAS seasons, respectively (Table 3.4). Except for ENSEMB_4 and ENSEMB_8, they showed dry bias during the FMAM season. The simulated rainfall of RMSE for all ensembles was in the range between 16.12 mm (ENSEMB_4) and 29.06 mm (ENSEMB_ALL) during the FMAM season and 25.09 mm (ENSEMB_4) and 50.41 mm (ENSEMB_ALL) during the JJAS season. ENSEMB_4 and ENSEMB_8 exhibited lower RMSE values of greater than 30 mm in simulating observed rainfall during the whole period. The error was larger during the JJAS season than during the FMAM season across all ensembles. TSS values of the ensembles for simulating rainfall in mean monthly were in the range of 0.82–0.88, while during FMAM and JJAS seasons they were 0.78–0.84 and 0.81–0.91, respectively. ENSEMB_4 showed the best performance in representing the spatial distribution of seasonal rainfall with the highest TSS value of greater than 0.84, while ENSEMB_ALL revealed the lowest performance compared to other ensembles.

Appendix A5 presented the estimated value of RM and overall ranks of 37 models, and seven ensembles with respect to bias, RMSE, PCC, and TSS. Compared to individual CMIP6 models, ENSEMB_4, ENSEMB_10, ENSEMB_20, ENSEMB_8, ENSEMB_27, and ENSEMB_16 occupied the first six positions in the RM_BIAS values, while NorESM2-MM, BCC-ESM1, CMCC-CM2-HR4, and GFDL-ESM4 ranked 7, 8, 9, and 10, respectively. ENSEMB_4, ENSEMB_8, GFDL-ESM4, ENSEMB_10, ENSEMB_16, ENSEMB_20, and ENSEMB_27 were occupying the first seven positions in the RM_RMSE values, while MIROC6, CNRM-ESM2-1, and CNRM-CM6-1 attained the last three ranks in the RM_BIAS and RM_ RMSE values. GFDL-CM4 was occupying the first position in the RM_PCC value, followed by GFDL-ESM4, MPI-ESM1-2-LR, and ENSEMB_4, whereas CNRM-CM6-1, CNRM-ESM2-1, and CNRM-CM6-1-HR were occupying the last three positions with the lowest RM_PCC value in that order. Compared to individual CMIP6 models, Appendix A5 shows that ENSEMB_4, ENSEMB_8, ENSEMB_16, ENSEMB_20, ENSEMB_10, ENSEMB_27, and ENSEMB_ALL ranked 3rd, 4th, 6th, 7th, 8th, 12th, and 15th positions in the RM_TSS values, respectively.

Table 3.4: Bias, RMSE, and TSS values for mean monthly, FMAM, and JJAS for seven ensembles with respect to ENACTS for the period 1981– 2014 over Ethiopia

Ensembles	TSS			Bias			RMSE		
	Mean monthly	JJAS	FMAM	Mean monthly	JJAS	FMAM	Mean monthly	JJAS	FMAM
ENSEMB_4	0.88	0.9	0.84	1.81	-0.16	1.49	20.23	25.09	16.12
ENSEMB_8	0.88	0.91	0.82	0.59	-2.43	0.01	22.45	27.55	19.47
ENSEMB_10	0.86	0.87	0.78	-0.3	-1.79	-4.7	30.26	39.52	26.32
ENSEMB_16	0.86	0.88	0.78	-0.72	-1.08	-6.96	30.52	38.93	27.65
ENSEMB_20	0.86	0.87	0.78	-0.51	-1.09	-6.55	31.02	39.94	27.76
ENSEMB_27	0.85	0.86	0.79	-0.56	-1.73	-6.84	31.7	40.51	27.88
ENSEMB_ALL	0.82	0.81	0.78	-1.95	-6.64	-6.85	36.74	50.41	29.06

3.3.5 Evaluation of models with CHIRPS

The performance of the model was further evaluated using CHIRPS as the reference dataset with respect to TSS and the results are presented in Table 3.5. Thirteen of the models illustrated more than 0.8 TSS in mean monthly, nine models in JJAS, and eight models in FMAM. CanESM5 showed a better skill, with a TSS value of 0.9 in simulating mean monthly rainfall followed by BCC-ESM1, GFDL-CM4, NESM3, and MPI-ESM1-2-LR. MPI-ESM1-2-LR revealed the best performance in reproducing the JJAS rainfall pattern, with the highest TSS value of 0.91, followed by NESM3, BCC-CSM2-MR, and MPI- ESM1-2-HR. CanESM5 showed the best skill in representing FMAM rainfall, with a TSS value of 0.98 followed by BCC- ESM1, GFDL-CM4, GFDL-ESM4, and NESM3.

Based on comparative rating metrics of RM_TSS values (Table 3.5), six models (NESM3, GFDL-ESM4, MPI-ESM1-2-LR, GFDL-CM4, BCC_CSM2-MR, and E3SM-1-0) outperformed the other individual models against CHIRPS, with RM_TSS values greater than 0.8 in that order. CNRM-CM6-1 revealed the lowest RM_TSS value (0.00) preceded by FGOALS-f3-L, CMCC-CM2-HR4, IPSL-CM6A-LR, and CNRM-CM6-1-HR. Some models, such as NESM3, GFDL-CM4, and GFDL-ESM4 showed higher RM_TSS values, with greater than 0.8 in both CHIRPS (Table 3.5) and ENACTS (Table 3.3) even though their position is different. The fine resolution model, CNRM-CM6-1-HR, showed the least performance in simulating rainfall from the CHIRPS and ENACTS datasets.

Table 3.5: TSS values for mean monthly, JJAS, and FMAM, and overall ranks of CMIP6 models based on RM of TSS values (RM_TSS) for 37 CMIP6 models for the period 1981–2014 over Ethiopia with respect to CHIRPS

Models	TSS			RM value based on TSS (RM_TSS)	Overall ranks based on RM_TSS value
	Mean monthly	JJAS	FMAM		
NESM3	0.53	0.89	0.84	0.90	1
GFDL-ESM4	0.69	0.88	0.89	0.89	2
MPI-ESM1-2-LR	0.60	0.91	0.80	0.88	3
GFDL-CM4	0.70	0.87	0.90	0.86	4
BCC_CSM2-MR	0.90	0.89	0.76	0.78	5
E3SM-1-0	0.74	0.86	0.74	0.76	6
CanESM5	0.90	0.54	0.98	0.72	7
HadGEM3-GC31-LL	0.68	0.75	0.77	0.70	8
EC-Earth3-Veg-LR	0.71	0.84	0.75	0.69	9
UKESM1-0-LL	0.34	0.72	0.80	0.69	9
BCC-ESM1	0.90	0.48	0.96	0.68	11
EC-Earth3	0.72	0.78	0.73	0.68	11
MPI-ESM1-2-HR	0.61	0.89	0.67	0.67	13
EC-Earth3-Veg	0.71	0.78	0.72	0.64	14
ACCESS-ESM1-5	0.90	0.80	0.82	0.61	15
NorESM2-MM	0.50	0.70	0.77	0.59	16
INM-CM5-0	0.67	0.68	0.73	0.55	17
MRI-ESM2-0	0.54	0.76	0.71	0.52	18
CESM2	0.89	0.73	0.70	0.50	19
CESM2-WACCM	0.88	0.71	0.70	0.48	20
CMCC-CM2-SR5	0.82	0.75	0.59	0.47	21
CMCC-ESM2	0.81	0.75	0.57	0.42	22
FGOALS-g3	0.70	0.68	0.57	0.37	23
SAM0-UNICON	0.48	0.64	0.65	0.35	24
INM-CM4-8	0.67	0.53	0.71	0.34	25
TaiESM1	0.48	0.68	0.63	0.32	26
ACCESS-CM2	0.95	0.47	0.67	0.30	27
CESM2-WACCM-FV2	0.86	0.63	0.66	0.27	28
IITM-ESM	0.68	0.71	0.46	0.25	29
MIROC6	0.64	0.67	0.53	0.25	29
CAMS-CSM1-0	0.90	0.66	0.53	0.23	31
CNRM-ESM2-1	0.77	0.49	0.62	0.19	32
CNRM-CM6-1-HR	0.79	0.42	0.61	0.12	33
IPSL-CM6A-LR	0.64	0.46	0.58	0.12	33
CMCC-CM2-HR4	0.85	0.46	0.52	0.10	35
FGOALS-f3-L	0.70	0.58	0.40	0.10	35

CNRM-CM6-1	0.81	0.28	0.33	0.00	37

3.3.6 Trend analysis

Table 3.6 presents mean rainfall, Sen's Slope, and P-values for the four top-ranking models, including ENACTS and CHIRPS during 1981–2014. The four top-ranking models are GFDL-ESM4, GFDL-CM4, NorESM2-MM, and ENSEMB_4. ENACTS depicts the insignificant increasing trend in rainfall at the rate of 0.10 and 0.59 mm/year for mean monthly and FMAM seasons at a 5% significance level, respectively. On the contrary, the JJAS rains exhibit an insignificant trend with a decrease at the rate of -0.49 mm/year. The CHIRPS trend has a smaller magnitude than the ENACTS trend in both the mean monthly and seasonal trends. According to CHIRPS, significant and insignificant positive trends were observed at the rate of 0.33 and 0.14 mm/year at JJAS and mean monthly rains, respectively. An insignificant negative trend at the rate of -0.11 mm/year was depicted in FMAM rainfall. All four models were consistent in showing positive insignificant trends over Ethiopia for mean monthly and both seasons and they have the lowest absolute trend magnitudes compared to ENACTS in both seasons. GFDL-ESM4, GFDL-CM4, NorESM2-MM, and ENSEMB_4 slightly overestimated the observed rainfall for JJAS rainfall, while they moderately overestimated for FMAM and mean monthly.

Table 3.6: Mean rainfall (RF), Sen's Slope, and P-value of mean monthly, JJAS, and FMAM over Ethiopia during the 1981–2014 using ENACTS, CHIRPS, and four top-ranked models

Model	Mean monthly			JJAS			FMAM		
	RF mm	Sen's Slope mm/year	P-value	RF mm	Sen's Slope mm/year	P-value	RF mm	Sen's Slope mm/year	P-value
ENACTS	58.72	0.10	0.45	111.69	-0.49	0.20	41.61	0.59	0.08
CHIRPS	46.87	0.09	0.14	75.23	0.33	0.02*	40.67	-0.11	0.43
GFDL-CM4	77.24	0.09	0.29	114.89	0.27	0.15	70.15	0.11	0.64
GFDL-ESM4	79.21	0.06	0.79	113.51	0.09	0.61	63.27	0.08	0.81
NorESM2-MM	73.27	0.16	0.18	119.17	0.17	0.53	62.85	0.23	0.51
ENSEMB_4	77.51	0.18	0.09	114.73	0.19	0.19	67.40	0.20	0.17

Bold and* indicate significant trend at 5% significant level.

3.4 Discussion

The main focus of this study was to evaluate the performance of CMIP6 models in reproducing the mean monthly and seasonal observed rainfall over Ethiopia from 1981 to 2014 using ENACTS data. ENACTS reveals a bimodal rainfall pattern with two peaks at the national scale. This is due to the north–south movement of the Intertropical Convergence Zone (ITCZ), or tropical rain belt which oscillates from 15°S to 15°N throughout the year (Nicholson 2018). More than 30 models showed better performance in capturing the short rainy seasonal cycle (FMAM) relative to the long rainy seasonal cycle (JJAS). This is because most models (22) cannot simulate August rainfall peaks during the JJAS season, as they produce peak rainfall in September and October. This may be related to the large East African rainfall pattern, which has two rainfall seasons in MAM and OND. However, the JJAS seasonal rainfall is of great significance to the rain-fed agricultural economy of the Northwest part of Ethiopia. This season accounts for 80–95% of the production of food crops in the country (Gissila *et al.* 2004). This emphasizes the need for improved simulation of the long rainy seasonal cycle of JJAS rainfall.

Majority of CMIP6 models showed a better spatial correlation in the long rainy JJAS season relative to the short rainy FMAM season over most parts of the country. This may be due to higher rainfall variability during FMAM compared to JJAS (Bekele *et al.* 2017) which is often difficult to capture in climate models (Kamruzzaman *et al.* 2022). However, more than 15 and 20 CMIP6 models simulated dry bias over most parts of the country in JJAS and FMAM seasons, respectively. This was more pronounced in high topographic and rainfall-receiving areas (Northwest and Central parts of the country). The dry bias that is reported in the previous version of CMIP5 models over the study area (Jury 2015; Li *et al.* 2016; Dyer *et al.* 2020) has not been significantly improved in CMIP6 models. Similar dry bias is reflected in the long rainy season in CMIP5 and CMIP6 models in East Africa (Ayugi *et al.* 2021). This might be related to weak Hadley circulation (Chadwick *et al*. 2013) and associated with large-scale dynamics and southward shifts of the ITCZ over East Africa (Yang *et al.* 2015). Dyer *et al.* (2022) demonstrate that biases in CMIP5 and CMIP6 are related to Southern Ocean warm biases and Western Indian Ocean warm biases, respectively.

Moreover, the fine resolution model, CNRM-CM6-1-HR, highly underestimated the observed JJAS seasonal rainfall, whereas medium and coarse resolution models such as BCC-ESM1, E3SM-1-0, GFDL-CM4, and NESM3 showed a better simulation of JJAS rainfall over the study area. This indicates that the underestimation of observed rainfall in this study may not be improved by simply increasing the models' horizontal resolution. This is mainly due to the challenges related to the complex topography, especially in the East African region, which is related to model physical parameterization (Ayugi et al. 2021). Once the representation of microphysical parameterizations is improved, increases in model resolution are also likely to contribute to more accurate simulation of precipitation especially in mountainous regions (Champion et al. 2011). Our results indicate a wide range of model performance in simulating observed rainfall across different time scales and statistical metrics, leading to different model rankings.

Based on the overall ranks of CMIP6 models using RM_TSS values (RM_TSS), GFDL-CM4 showed the best performance, followed by GFDL-ESM4, NorESM2-MM, CESM2, CESM2 WACCM, NESM3, E3SM-1-0, MPI-ESM1-2-LR, and BCC-CSM2-MR in simulating rainfall over Ethiopia with respect to ENACTS (Table 5). Generally, the best-performing models, considering all the metrics values (RM_BIAS, RM_RMSE, RM_PCC, and RM_TTS), were observed for the GFDL-ESM4, NorESM2-MM, and ENSEMB_4, while the worst performance was observed for the CNRM-CM6-1, CNRM-ESM2-1, and CNRM-CM6-1-HR models. These results are consistent with other previous studies over Ethiopia (Dyer et al. 2020; Alaminie et al. 2021), Uganda (Ngoma et al. 2021), North Africa (Babaousmail et al. 2021), and East Africa (Makula & Zhou 2022). The failure of individual models to capture the observed spatial patterns of precipitation might be due to the complex dynamics of the temporal and spatial properties of precipitation over the East African region, differences in initial and boundary conditions (Makula & Zhou 2022), and poor representation of convective schemes and model parametrization (Ongoma et al., 2019). CHIRPS showed the best performance in representing the reference observed rainfall (ENACTS) based on spatial analysis, quantitative statistics metrics, and TSS.

Furthermore, CMIP6 models were compared with CHIRPS using TSS to assess their performance across different observed datasets. Some models such as NESM3, GFDL CM4,

and GFDL-ESM4 were the most skillful models while CNRM-CM6-1, CNRM-ESM2-1, and CNRM-CM6-1-HR were the poorest models in both CHIRPS and ENACTS. However, most models exhibited distinct skill across ENACTS and CHIRPS, although some showed similar performance on both gridded datasets. Thus, the relative performances of the CMIP6 models may depend on the choice of the reference gridded dataset as the different gridded observation datasets revealed substantial differences (Akinsanola et al. 2021; Faye & Akinsanola 2022). Various studies use the different numbers of top-ranked GCMs for generating ensembles since there is no standard on the selection of the maximum number of the top-ranked of GCMs (Alaminie et al. 2021; Babaousmail et al. 2021; Makula & Zhou 2022; Ngoma et al. 2022). We found that the WA method showed better skill compared to the SA method in reducing errors as it gives more weight to higher performing models.

Overall, all ensembles outperformed most individual models in representing the temporal and spatial rainfall distribution. Six ensembles (ENSEMB_4, ENSEMB_8, ENSEMB_10, ENSEMB_16, ENSEMB_20, and ENSEMB_27) showed better performance in most of the statistical metrics relative to the weighted average of all models. Nevertheless, the weighted average of the four top-ranked models (ENSEMB_4) can best reproduce spatial and temporal rainfall variations while the weighted average of all models (ENSEMB_ALL) revealed the least skill. Moreover, ENSEMB_4 was the only ensemble that showed the most skills in all metrics compared to other ensembles and individual models. This indicated the importance of choosing models for climate change impact assessment for a given region. A similar result was observed in the earlier version of CMIP5 model over Ethiopia (Jury 2015; Dyer et al. 2020). Dyer et al. (2020) showed that the ensemble averages of 30 CMIP5 models revealed weak bimodal seasonality in the Awash basin due to large discrepancies in individual models. An average of better models may provide more confident guidance than an average of all models as it is prone to dry bias (Jury 2015). Kang et al. (2014) stated that the predictive capabilities of the ensembles do not significantly improve after a certain number of GCMs. A model that cannot properly represent the current climate system may not add value to the ensemble.

3.5 Conclusion and Recommendation

This study evaluated the performance of 37 CMIP6 models in reproducing observed national-scale rainfall for the period 1981–2014. Most of the CMIP6 models revealed lower performance over high topographic and rainfall-receiving areas of the Northwest and Central parts of the country, while they performed well in low topographic and rainfall-receiving areas of the Southeast. This indicates that the effect of high topography on precipitation is remains a challenge for climate modeling. Overall, CMIP6 models revealed a similarly poor capability with producing a dry bias simulation of rainfall as CMIP5 models over the study area. The four top-ranked models (GFDL-CM4 GFDL-ESM4, NorESM2-MM, and CESM2) and their weighted average of those models (ENSEMB_4) can be applied in the projection of climate using CMIP6 under different Shared Socioeconomic Pathways (SSPs) for Ethiopia.

The findings of this study provide important information to model producers and end-users of the datasets. More research and detailed studies are still crucial for improving the poor performance of models that lead to sources of dry biases since the future projection of its likelihood will be of great importance to the country's economy. This calls for the modeling groups to improve the simulation of the seasonal rainfall through a better understanding of the complex dynamics of the seasonal rainfall over Ethiopia. For climate model output users, caution is needed when employing the models in seasonal climate change studies as dry bias exists in seasonal rainfall simulation, and hence bias correction is important before employing models for future climate projection and impact studies.

Despite the robust findings of this study, there are some limitations. One of the limitations is the choice of the two seasonal rainfall (FMAM and JJAS) for different regions of the country since large seasonal variations are observed in different regions of Ethiopia. Thus, this study recommends evaluating the different CMIP6 models based on different homogeneous rainfall zones in the country to make further detailed studies of the performance of models. The results offer useful information about the different performances of CMIP6 models over the whole country and can serve as a reference for the new phase of climate models over the continent.

Chapter 4. Evaluation of CMIP6 Models in Simulating Seasonal Extreme Precipitation over Ethiopia

Abstract

Historically, Ethiopia has experienced recurrent droughts and floods, which may intensify due to climate change. This study has evaluated the performance of 45 models from the Coupled Model Intercomparison Project Phase 6 (CMIP6) in simulating ten extreme precipitation indices against corresponding indices from the Enhancing National Climate Services (ENACTS) during short rainy (February–May, FMAM) and main rainy (June–September, JJAS) seasons for the period 1981–2014 over Ethiopia. Ensemble mean of the top-ranking models are also evaluated against ENACTS in reproducing extreme indices over five Agro-ecological zones (AEZs) of the country. The Taylor Skill Score (TSS) was used to rank the performance of the individual CMIP6 models for JJAS and FMAM seasons with respect to ENACTS while Comprehensive Rating Metrics (RM) were used to compute the overall ranks of the models. Our results show that most CMIP6 models reasonably captured the spatial distribution of the seasonal extreme precipitation indices even though they could not reproduce the magnitude of indices, especially in the highland and high rainfall areas of the country such as Northwest and west parts of the country. However, the biases in lowland and low-rainfall regions, such as the eastern and northeastern parts of the country, are smaller compared to other areas. More than 30 CMIP6 models underestimated the extreme indices with the exception of consecutive wet days which are grossly overestimated in the highland and high rainfall areas specifically in the western parts of the country.

Additionally, EnseMean in the tropical and desert AEZs performs particularly better in simulating extreme indices compared to other AEZs. The ensemble mean of the top-ranking models (EnseMean) generally outperformed both individual models and the ensemble of all models in representing observed extreme indices across all metrics and seasons. Moreover, the performance of individual models is subject to variation based on the season, and the selected extreme indices. It is also noteworthy that their performance is relatively less influenced by horizontal resolution. Further evaluation, focusing on teleconnections such as ENSO and IOD, is a crucial next step in assessing models and constructing a sub-ensemble.

Keywords:

Extreme precipitation indices, CMIP6, Model evaluation, ENACTS, Agro-ecological zones, Ethiopia

4.1 Introduction

Climate extremes that cause droughts and floods have devastating impacts on society and the environment by causing property damage, injury, crop failure, poverty, and loss of life (Kim et al., 2020; Akinsanola et al., 2021; IPCC, 2022). The effects of climatic extremes are more severe in many areas of Africa, including East Africa, due to low adaptive capacity and high dependence on the agricultural sector (Nicholson, 2017; Ongoma et al., 2018; Bedasa and Bedemo, 2023). Like many East African countries, Ethiopia also suffers from climate change-related disaster risks, such as drought, flooding, and intense rainfall resulting in several damages (Viste et al., 2013; Mera, 2018; Cherinet et al., 2022). For instance, the country experienced seven significant drought occurrences over the last 30 years in 1983–1985, 1988, 2000, 2002–2003, 2006, 2011, and 2015 with the drought in 1983–1985 was among the worst that the country has ever faced. The severe El Ni˜no-induced drought of 2015 caused significant food insecurity for 10.2 million people (Gummadi et al., 2018; Lewis, 2017; Philip et al., 2018; Tegegne et al., 2021). The prolonged 2022 drought was the worst that Ethiopia has experienced in 50 years; three consecutive failed rainy seasons, resulted in the death of 2.2 million livestock, the failure of crops, and the displacement of numerous children with their families on the verge of destitution (FEWS, NET, 2022). In addition to drought, the country is also affected by floods. There have been eleven major floods that have caused substantial loss of both human life and property over the past two decades (Cherinet et al., 2022). Climatic extremes and associated impacts are projected to become frequent and severe over most parts of Ethiopia, which will increase food insecurity (Gebrechorkos et al., 2019; Tegegne et al., 2021; Rettie et al., 2023).

Recognizing this, the government of Ethiopia is presently implementing the National Adaptation Plan (NAP-ETH) as part of a broader Climate Resilient Green Economy (CRGE) strategy to mitigate the impacts of climate change, including extreme events, and enable the growth of the country's economy (FDRE-Federal Democratic Republic of Ethiopia, 2019). The National Adaptation Plan (NAP-ETH) further elaborates on how Ethiopia will adapt to climate change and the country aims to actively and continuously incorporate climate change adaptation into its development policies and strategies. However, the effectiveness of implementing appropriate local

adaptation and mitigation strategies for the future depends on the skill of GCMs outputs to simulate rainfall patterns and extreme events (Akinsanola et al., 2020; Omay et al., 2023).

Global Climate Models (GCMs) generally provide reliable information on the characteristics of past and future climate change, including droughts and floods (Stouffer et al., 2017; Wainwright et al., 2019). Historical simulations play a crucial role in evaluating model performance, not only in simulating mean climate conditions but also in capturing extreme weather and climate events (Flato et al., 2014). They serve as essential tools for assessing the consistency of climate model forcing and sensitivity against observational records. Additionally, they act as benchmarks, alongside control simulations, for conducting detection and attribution studies (Eyring et al., 2016). Furthermore, these simulations are considered the "entry card" for all models participating in the CMIP6 project.

Based on a few available studies on the performance of the CMIP5 models over East Africa (Yang et al., 2015; Zebaze et al., 2019) and Ethiopia (Jury, 2015; Li et al., 2016; Dyer et al., 2020), CMIP5 are still susceptible to substantial biases in simulating precipitation characteristics although they revealed generally good performance. Nowadays, a new coordinated series of climate experiments has recently been carried out under the umbrella of phase 6 of CMIP (CMIP6) which includes higher spatial resolution, the addition of new physical processes, refined parameterization schemes, and large ensemble members relative to CMIP5 (Eyring et al., 2016; Kim et al., 2020). Various studies have so far evaluated the accuracy of CMIP6 models in reproducing climate extremes in many regions (Srivastava et al., 2020; Feng et al., 2023; Donat et al., 2023; Reddy and Saravanan, 2023; Bala et al., 2023; Akinsanola et al., 2021; Ayugi et al., 2021; Klutse et al., 2021; Omay et al., 2023). The summary of the above studies indicates that model performance varies over regions, countries, and across CMIP6 models in reproducing extreme indices at temporal and spatial scales, as there are variations in how different CMIP6 models represent largescale dynamics, physical processes, spatial resolutions, and their initial and boundary conditions. This indicates the necessity to extend evaluation of GCMs to the national level before applying for future projections of climate extreme impact analysis and planning climate change adaptation measures.

Various studies have assessed the performance of CMIP6 models in reproducing the mean rainfall over Ethiopia (Alaminie et al., 2021; Fetene et al., 2022; Dyer et al., 2022; Berhanu et al., 2023; Gebisa et al., 2023; Omay et al., 2023). However, very few studies have been conducted in the evaluation of extreme precipitation indices for CMIP6 simulations (Rettie et al., 2023; Akinsanola et al., 2021). The above-mentioned studies evaluated only a limited number (less than 20) of CMIP6 models against various satellite-gridded datasets. The analysis on a seasonal basis such as the main rainy season (JJAS) and the short rainy season (FMAM) over Ethiopia, is rarely assessed using CMIP models simulations. Additionally, most of the above-mentioned studies evaluate different CMIP6 models using global satellite data from CHIRPS and GPCP rainfall products over Ethiopia.

To fill this knowledge gap, this paper conducts a more comprehensive evaluation of 45 CMIP6 models in simulating seasonal precipitation extremes using different statistical metrics for JJAS and FMAM seasons over Ethiopia through comparison with the recently implemented dataset (ENACTS) that is generated specifically for Ethiopia. This study also analyzed extreme indices across the five agro-ecological zones of Ethiopia using the ensemble mean of top-ranking models and compared the performance of an ensemble of top-performing models against the full ensemble of models. This comparison was used to assess discrepancies between the two ensembles and to determine whether the top-performing models offer significantly better or different insights than the full ensemble. This approach aids in refining model selection for more reliable future projections, potentially providing more accurate information for decision-making and policy development.

4.2 Data and methodology

4.2.1 Study area

Ethiopia is located between 3°N and 15°N latitudes and 33°E and 48°E longitudes (Figure 4.1). The amount and distribution of rainfall are highly variable in both time and space (Gummadi et al., 2018; Van den Hende et al., 2021). The highland regions (> 1500 m a.s.l.) in the center, north, south, and southwest of the country are characterized by high rainfall and humidity, while lowlands region in the northeast, east, and southeast (< 1500 m a.s.l.) receive low rainfall and have semi-arid and arid agro-ecology (Gummadi et al., 2018). Ethiopia has three rainfall seasons (Diro et al.,

2011). The main rainy season, *Kiremt*, occurs from June to September and accounts for 50–80% of the annual rainfall. The short rainy season, *Belg*, often has considerably less rainfall from February to May in central, northern, and southern parts of Ethiopia. The *Bega* season is from October to December, and it is a dry and relatively cold season.

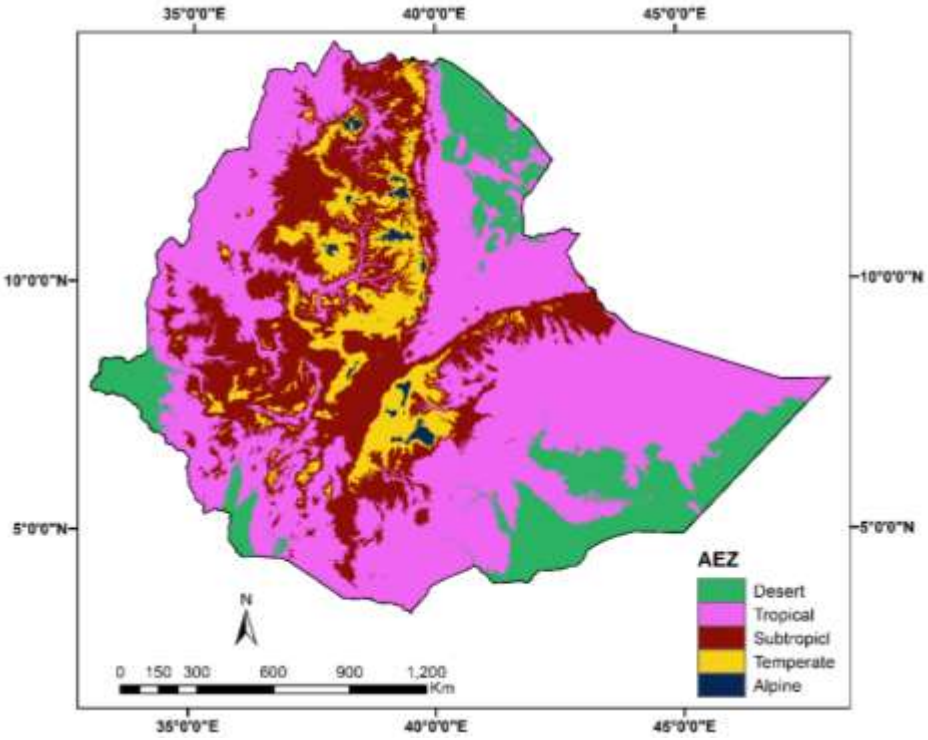

Figure 4.1: Location map of Ethiopia and its agro-ecological zones (MOA, 1998).

Ethiopia has diverse agro-ecology, ranging from desert to alpine climatic conditions. Ethiopia is divided into five agro-ecological zones (AEZs) based on altitude and climate (MOA, 1998): Desert (hot arid), Tropical (Kolla), Sub-Tropical (Dega), Temperate (Weyna Dega), and Alpine (Wurch) (Figure 4.1). Each of these regions has distinct environmental conditions that influence the types of vegetation, agricultural practices, and lifestyles of the people living there.

4.2.2 Data

This study used the daily precipitation of CMIP6 models from the Earth System Grid (ESG) data portal (https://esgf-node.llnl.gov/search/cmip6/). We studied the performance of 45 CMIP6 models in reproducing extreme precipitation over Ethiopia. The lists of the models considered, along with their country and spatial resolution are provided in Table 4.1.

Table 4.1: List of 45 CMIP6 models used for extreme indices over Ethiopia

No	Models	Country	Resolution (lon × lat)
1	ACCESS-CM2	Australia	1.90 × 1.30
2	ACCESS-ESM1-5	Australia	1.9 × 1.3
3	AWI-ESM-1-1-LR	Germany	0.93 × 0.93
4	BCC-CSM2-MR	China	1.13 × 1.13
5	BCC-ESM1	China	2.81 × 2.81
6	CAMS-CSM1-0	China	1.13 × 1.13
7	CanESM5	Canada	2.81 × 2.81
8	CESM2	USA	1.25 × 0.94
9	CESM2-FV2	USA	2.5 × 1.9
10	CESM2-WACCM	USA	1.25 × 0.94
11	CESM2-WACCM-V2	USA	2.5 × 1.9
12	CMCC-CM2-HR4	Italy	1.25 × 0.94
13	CMCC-ESM2	Italy	1.3 × 0.9
14	CNRM-CM6- 1	France	1.4 × 1.4
15	CNRM-CM6-1-HR	France	0.5 × 0.5
16	CNRM-ESM2-1	France	1.4 × 1.4
17	E3SM-1-0	USA	1.0 × 1.0
18	EC-Earth3	Europe	0.7 × 0.7
19	EC-Earth3-Veg	Europe	0.7 × 0.7
20	EC-Earth3-Veg-LR	Europe	1.1×1.1
21	FGOALS-f3-L	China	1.25 × 1.0
22	FGOALS-g3	China	2.5 × 2.0
23	GFDL-CM4	USA	2.50 × 2.00
24	GFDL-ESM4	USA	1.25 × 1.00
25	GISS-E2-2-G	USA	2.5 × 2.0
26	HadGEM3-GC31-LL	UK	1.9×1.3
27	IITM-ESM	India	1.9 × 1.9
28	INM-CM4-8	Russia	2.0 × 1.5
29	INM-CM5-0	Russia	2.0 × 1.5
30	IPSL-CM5A2-INCA	France	3.75 × 1.87
31	IPSL-CM6A-LR	France	2.5 × 1.3
32	IPSL-CM6A-LR- INCA	France	2.5 × 1.3
33	KACE-1-0-G	Korea	1.9 × 1.3
34	KIOST-ESM	Korea	1.9 × 1.3
35	MIROC6	Japan	1.41 × 1.41
36	MPI-ESM-1-2-HAM	Germany	1.9 × 1.9
37	MPI-ESM1-2-HR	Germany	0.94 × 0.94

No	Models	Country	Resolution (lon × lat)
38	MPI-ESM1-2-LR	Germany	1.9 × 1.9
39	MRI-ESM2-0	Japan	1.13 × 1.13
40	NESM3	China	1.9 × 1.9
41	NorESM2-LM	Norway	2.5 × 1.9
42	NorESM2-MM	Norway	1.25 × 0.94
43	SAM0-UNICON	Republic of Korea	1.25 × 0.94
44	TaiESM1	Taiwan	1.25 × 0.94
45	UKESM1-0-LL	UK	1.88 × 1.25

Since model evaluations are highly sensitive to the choice of the observational dataset, it is important to select reference gridded dataset which incorporates a high number of ground stations and has been demonstrated to perform reliably in validation (Kim et al., 2020; Akinsanola et al., 2021). The majority of global satellite products incorporate fewer than 50 stations from Global Telecommunications System (GTS). However, the ENACTS data product incorporates over 500 stations from the national network managed by Ethiopian Meteorological Institute, which are integrated with satellite rainfall estimations (Dinku et al., 2014; Dinku et al., 2019). On this basis, ENACTS was selected as the main reference dataset to evaluate CMIP6 models. This product has a spatial resolution of $0.0375^{o} \times 0.0375^{o}$ and covers the time period between 1981 and 2020, inclusive, at a daily resolution.

The gridded product produced as part of the ENACTS project (Dinku et al., 2014) is similar to CHIRPS, but it incorporates a significantly larger number of observation stations. Consequently, ENACTS is expected to provide rainfall observations that are closer to the "true" values. To estimate observational uncertainty, precipitation indices from CHIRPS are evaluated against ENACTS. CHIRPS v2.0 provides free daily climate data with spatial resolution $0.05^{o} \times 0.05^{o}$ and a quasi-global coverage (50S–50N) (Funk et al., 2015). CHIRPS v2.0 is available online at http://chg.geog.ucsb.edu/data/chirps.

ENACTS is herein referred to as the ‘‘observational dataset’’. ENACTS has been used for evaluating climate models over Ethiopia (Alaminie et al., 2021; Dyer et al., 2022; Berhanu et al., 2023). Detailed descriptions of ENACTS and CHIRPS are available in Dinku et al., (2014), and Funk et al., (2015), respectively.

4.2.3 Methodology

The performance of 45 CMIP6 models in simulating 10 extreme precipitation indices over Ethiopia is evaluated using the spatial distribution of rainfall and statistical metrics such as PCC, Pbias, RMSE, TSS, Portrait, and Taylor diagram.

4.2.3.1 Precipitation Extreme Indices

We assessed the capability of the CMIP6 models to accurately represent extreme precipitation indices defined by the Expert Team on Climate Change Detection and Indices (ETCCDI) (Zhang et al., 2011). Ten ETCCDI precipitation indices were selected for this study (Table 4.2). This set of extreme precipitation has been extensively used for climate model evaluation, trend analysis, and projection of changes in climate extremes over Africa (Gebrechorkos et al., 2019; Bala et al., 2023; Akinsanola et al., 2021) and Ethiopia (Mohammed et al., 2022; Tegegne et al., 2021; Gummadi et al., 2018). The indices were computed on the native resolution for each grid cell for the CMIP6 models, CHIRPS and the observational dataset. The indices were calculated for two seasons (JJAS and FMAM) using RClimDex graphical interface in the R software (Zhang and Yang, 2004) for the period 1981–2014.

Table 4.2: List of detailed precipitation extreme indices used in the study (Zhang et al., 2011).

Index	Description	Definition	Unit
PRCPTOT	Total wet-day precipitation	Seasonal total precipitation during wet days	mm/season
SDII	Simple daily intensity index	Seasonal precipitation during wet days	mm/days
CDD	Consecutive dry days	Maximum number of consecutive days with precipitation <1 mm in season	Days/season
CWD	Consecutive wet days	Maximum number of consecutive days with precipitation >1 mm in season	Days/season
R10	Heavy precipitation days	Seasonal number of days with precipitation ≥10 mm	Days/season
R20	Very heavy precipitation days	Seasonal number of days with precipitation ≥20 mm	Days/season

R95pTOT	Very wet days	Seasonal total precipitation exceeding the 95th percentile	mm/season
R99pTOT	Extremely wet days	Seasonal total precipitation exceeding the 99th percentile	mm/season
Rx5day	Maximum consecutive five-day precipitation	Seasonal maximum 5-day precipitation amount	mm/season
Rx1day	Maximum one-day precipitation	Seasonal maximum 1-day precipitation amount	mm/season

PRCPTOT is the total seasonal precipitation accumulated on wet days, where a wet day is typically defined as a day with rainfall ≥ 1 mm. To calculate it, first identify the wet days within the season of interest, then sum the precipitation amounts for those days. This provides a measure of the seasonal rainfall occurring only on days with measurable precipitation. SDII (Simple Daily Intensity Index) is calculated as the total precipitation on wet days (≥1 mm) divided by the number of wet days, reflecting rainfall intensity. CDD (Consecutive Dry Days) is the maximum number of consecutive days with precipitation <1 mm, while CWD (Consecutive Wet Days) is the maximum number of consecutive days with precipitation ≥1 mm, indicating dry and wet spell lengths. R10 and R20 are counts of days with precipitation ≥10 mm and ≥20 mm, representing heavy and very heavy rainfall events. Extreme precipitation totals are quantified as R95pTOT and R99pTOT, which sum daily rainfall exceeding the 95th and 99th percentiles of the daily precipitation distribution. Short-term extremes are described by Rx1day, the maximum daily precipitation, and Rx5day, the maximum total precipitation over any consecutive five-day period. These indices together provide a comprehensive assessment of seasonal rainfall amount, intensity, spell length, and extremes, which are critical for understanding climate variability and its impacts on agriculture and water resources.

Prior to the statistical analysis, indices computed on native resolution of CMIP6 data and observational dataset were re-gridded to a common 1°×1° using bilinear interpolation for analysis of spatial distribution and statistical metrics (Kim et al., 2020; Ayugi, et al., 2021; Berhanu et al., 2023; Ali et al., 2023). This step ensured a uniform resolution for analyzing spatial distributions and statistical metrics. The performance of the CMIP6 models was further assessed and presented

graphically using a portrait diagram for the ten extreme precipitation indices. The assessment metrics included Percentage Bias (Pbias), Normalized Root Mean Square Error (NRMSE), and Pattern Correlation Coefficient (PCC), based on the observational ENACTS dataset (Akinsanola et al., 2021; Srivastava et al., 2020). The Pbias, NRMSE, and PCC of the models relative to observational dataset were computed using Equations 4.1– 4.3. These metrics are calculated over the whole country and five agro-ecological zones (AEZs).

$$Pbias = 100\frac{\sum_{i=1}^{n}(m_i - r_i)}{\sum_{i=1}^{n} r_i} \tag{4.1}$$

$$NRMSE = 100\frac{\sqrt{\frac{1}{n}\sum_{i=1}^{n}(m_i - r_i)^2}}{\sigma_r} \tag{4.2}$$

$$PCC = \frac{\sum_{i=1}^{n}(r_i - \bar{r})(m_i - \bar{m})}{(\sigma_r * \sigma_m)} \tag{4.3}$$

where m and r are model and observational dataset, respectively, σ_r and σ_m are the standard deviations of observational dataset and models, and n represents the number of observations.

4.2.3.2 Overall ranks of CMIP6

Taylor skill score (TSS) is a statistical summary of Pattern Correlation Coefficient (PCC), Root Mean Square Error (RMSE), and SD (standard deviations) (Taylor, 2001). TSS was used in assessing and ranking individual CMIP6 models relative to the observational dataset in reproducing the spatial patterns of each extreme index for the JJAS and FMAM seasons. The successful implementation of this approach has been utilized in several recent studies conducted in the African and East African regions to evaluate the capability of ranking models (Dyer et al., 2020; Babaousmail et al., 2021; Ayugi et al., 2021; Makula & Zhou 2022). TSS is calculated using Equation (4.4) (Taylor, 2001).

$$TSS = \frac{4(1+PCC)^2}{(\frac{\sigma_m}{\sigma_r} + \frac{\sigma_r}{\sigma_m})^2(1+PCC_o)(1+PCC_o)^2} \tag{4.4}$$

Where PCC is the Pattern Correlation Coefficient between the observational dataset and model outputs; σ_m and σ_r are the standard deviations of the model and observational dataset, respectively; and PCC_0 is the highest achievable correlation coefficient, set at 1. The closer the value of TSS to 1, the better is the agreement between the simulation and observational dataset.

ENACTS is a distinctive, high-quality, and more reliable dataset than any other long-term, satellite-based time series dataset (Dinku et al., 2014). Thus, the ranking of the individual models was determined by calculating the TSS for each extreme index for the JJAS and FMAM seasons with respect to the ENACTS. The overall ranks of CMIP6 models considering all the extreme indices for each season were then computed using the comprehensive rating metric (RM) (Jiang et al., 2015; Rivera & Arnould, 2020; Berhanu et al., 2023). An RM value close to 1 indicates a better-performing CMIP6 model, whereas an RM closer to 0 refers to a poorly performing model. The overall ranks (RM) of GCMs were computed using Equation (4.5).

$$RM = 1 - \frac{1}{nm}\sum_{i=1}^{n} rank_i \tag{4.5}$$

where m and n represent the number of CMIP6 models and metrics, respectively, calculated separately for the JJAS and FMAM seasons.

4.2.3.3 Ensemble mean of CMIP6 models

Identification and selection of an ensemble of better-performing GCMs is important in order to reduce biases in the individual model members and the uncertainty associated with projection of future climates (Akinsanola & Zhou, 2019; Pour et al., 2018). Numerous studies have developed ensemble mean of models based on the first three to ten top-ranked GCMs (Ahmed et al., 2020; Salman et al., 2020; Omay et al., 2023). In this study, the ensemble mean (EnseMean) was developed based on the RM values of TSS (RM_TSS) of the CMIP6 models. CMIP6 models, with RM_TSS values greater than 0.70 were included in the input set to produce EnseMean for the JJAS and FMAM seasons, separately. On the other hand, EnseMean_ALL was generated using a weighted average of all 45 models. The EnseMean of the top-ranking models was compared with EnseMean_ALL and individual models by analysing the spatial distribution of rainfall, portrait diagram, Taylor diagram and TSS using the observational dataset. Additionally, the performance of the EnseMean of the top-ranking models for simulating ten extreme indices was further assessed across five agro-ecological zones of Ethiopia (AEZs) using Pbias, NRMSE, PCC and TSS.

In this study, the performance of top-ranking models, EnseMean, and EnseMean_ALL in simulating extreme precipitation indices has been further evaluated based on the Taylor diagrams and trend analysis by comparing them with an observational dataset (ENACTS). Taylor diagrams

are a graphical tool commonly used in climate science to assess the similarity between model simulations and observational datasets. They display statistical measures such as correlation coefficient (PCC), root mean square error (RMSE), and standard deviation (SD) in a concise format (Taylor 2001). Taylor diagrams were created using R in the taylor.diagram function from the plotrix package.

Trend analysis of extreme climate indices was conducted to evaluate the performance of top-ranking models, EnseMean, and EnseMean_ALL in simulating extreme precipitation indices with respect to observational dataset. Mann–Kendall (MK) test and Sen's slope estimator were utilized to identify and quantify potential trends in the time series data for observational dataset, top ranking models, EnseMean, and EnseMean_ALL at national level. These analyses were conducted using the "trend" package within the R statistical software (Pohlert, 2016). The analysis presented covers the spatial averages across the entire country for the ENACTS dataset, as well as the EnseMean and EnseMean_ALL datasets. The analysis utilized box-and-whisker plots to visually represent the distribution, variability, and trends of these indices for two seasonal periods, JJAS (June–September) and FMAM (February–May), over the historical period of 1981–2014. This approach provided insights into the central tendency, range, and consistency of model simulations compared to observational data, facilitating a robust evaluation of model performance in capturing extreme precipitation patterns across Ethiopia.

4.3 Results

4.3.1 Spatial distribution of extreme precipitation indices

The spatial distribution of CWD, R10, R95pTOT, PRCPTOT and Rx5day, for the observational dataset, CHIRPS, 45 models, and EnseMean during JJAS and FMAM seasons are shown in Figures 4.2-4.11. The spatial distribution of CDD, R20, R99pTOT, and Rx1day are presented in the Appendix (Appendix B1-B8). Table 4.3 revealed the comparison between ENACTS and CHIRPS with respect to extreme indices for JJAS and FMAM seasons.

Table 4.3: Comparison of observational dataset (ENACTS) and CHIRPS with respect to extreme indices for JJAS and FMAM seasons

Metric	JJAS (Min-median-Max)		FMAM (Min-Median-Max)	
	ENACTS	CHIRPS	ENACTS	CHIRPS
CWD (days/season)	0 - 5 -51	0 - 4 - 21	1 – 5 - 16	3 - 5- 11
CDD (days/season)	2 - 26 - 119	4 - 24 - 122	17 - 52 - 106	17 - 34 - 95
R10 (days/season)	0 - 11 - 76	0 - 13 - 68	0 - 6 - 33	0 - 8 - 35
R20 (days/season)	0 - 3 - 39	0 - 5 - 29	0 - 2 - 16	0 - 3 - 15
R95pTOT (mm/season)	0 - 59 - 310	0 - 59 - 256	2- 36 - 176	7 - 41- 134
R99pTOT (mm/season)	0 - 31 - 117	0 - 45 - 106	1 - 30 - 81	7 - 37 - 96
PRCPTOT (mm/season)	2 - 310 - 2060	3 - 334 - 1560	4 - 177 - 903	7 - 220 - 906
SDII (mm/day)	1 - 10 - 24	1 - 12 - 32	2 - 12 - 24	3 - 13 – 27
Rx5day (mm/season)	3 – 61 - 205	0 – 50 - 234	3 – 56 - 173	7-61-224
Rx1day (mm/season)	2 – 31 - 77	0 – 24 - 114	2 – 30 - 82	4 – 33 - 120

4.3.1.1 Consecutive wet days (CWD)

Based on the observational dataset, the north, northwest, west and central parts of Ethiopia experiences the highest number in CWD during the JJAS season while the northeast, and most parts in the south experiences the lowest number. The ENACTS and CHIRPS showed broadly similar patterns of CWD during both seasons but with a discrepancy in the number of CWD. CHIRPS has lower CWD (up to 51 days/season) over the northwest and central parts of the country than the ENACTS (up to 21 days/season) (Table 4.3 and Figure 4.2) during JJAS season while both datasets showed similar spatial pattern and magnitude of CWD in the FMAM season (Table 4.3 and Figure 4.3).

The majority of models captured the spatial pattern of the observational dataset of CWD reasonably well but with much higher magnitudes over the highland and topography areas of northwest, west and central parts of the country during JJAS season (Figure 4.2). However, they were capable of capturing the spatial pattern and simulating the magnitude of the ENACTS of CWD over the east and south parts of the country where low rainfall occurs for the JJAS season. The model exceptions to overestimation, in the observational dataset were BCC-ESM1-MR, FGOALS-f3-L, CNRM-ESM2-1, CNRM-CM6-1, CNRM-CM6-1-HR, UKESM1-0-LL, and BCC-ESM1-MR. INM-CM4-8, INM-CM5-0, CESM2, CESM2-WACCM, EC-Earth3, EC-

Earth3-Veg-LR, EC-Earth3-Veg, IPSL-CM6A-INCA, IPSL-CM6A-LR, IPSL-CM5A2-INCA, E3SM-1-0, and MIROC6 grossly overestimated CWD (up to 120 days/season) in the abovementioned areas. NESM3, MPI-ESM-1-2-HAM, CESM2-WACCM-FV2, MPI-ESM1-2-LR, and NorESM2-MM reproduced the observed number of CWD relatively well.

Similar to JJAS, more than 40 models overestimated the observed CWD (up to 32 days/season) over the west and southwest parts of the country where high rainfall occurs for the FMAM season (Figure 4.3). CMCC-ESM2, INM-CM4-8, INM-CM5-0, HadGEM3-GC31-LL, KIOST-ESM, and UKESM1-0-LL grossly overestimated CWD over west and southwest parts of the country (> 30 days/season). BCC-ESM1-MR, GFDL-CM4, and NorESM2-MM revealed higher skill in representing the CWD observational dataset during the FMAM season (Figure 4.3). Based on the observed dataset, the south and southeast lowlands of Ethiopia record the highest number of CDD for the JJAS season (Appendix B1). A majority of models often overestimated the CDD of the observed dataset with large amount at locations of low rainfall and lowland areas of Ethiopia where they tend to underestimate the CWD by large amount (Appendix B1 and B2).

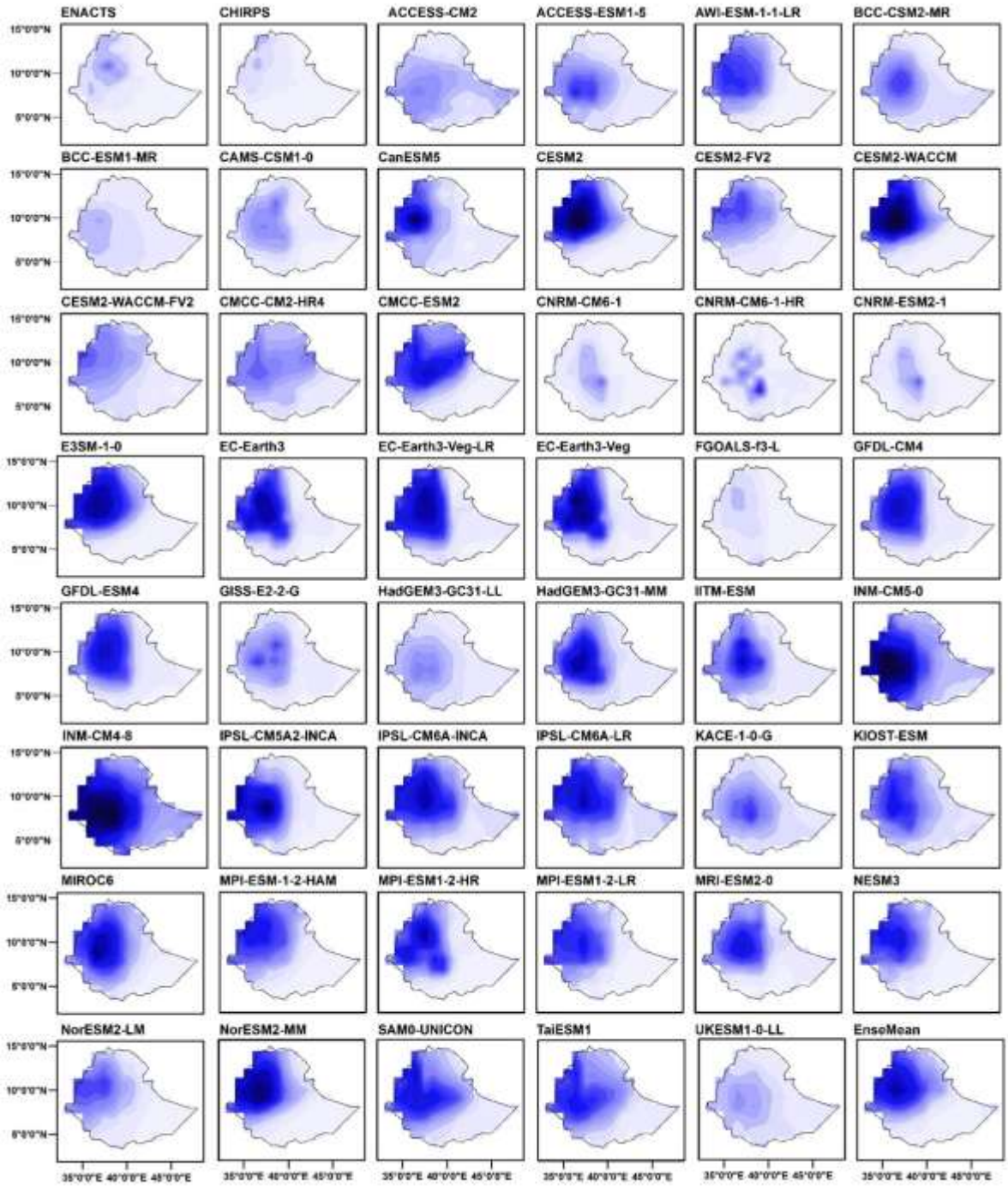

JJAS CWD (days/season)

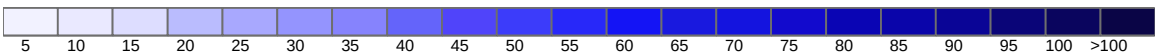

Figure 4.2: Mean consecutive wet days (CWD) (days/season) from observational dataset, CHIRPS, 45 CMIP6 models, and EnseMean over Ethiopia for JJAS season from 1981–2014.

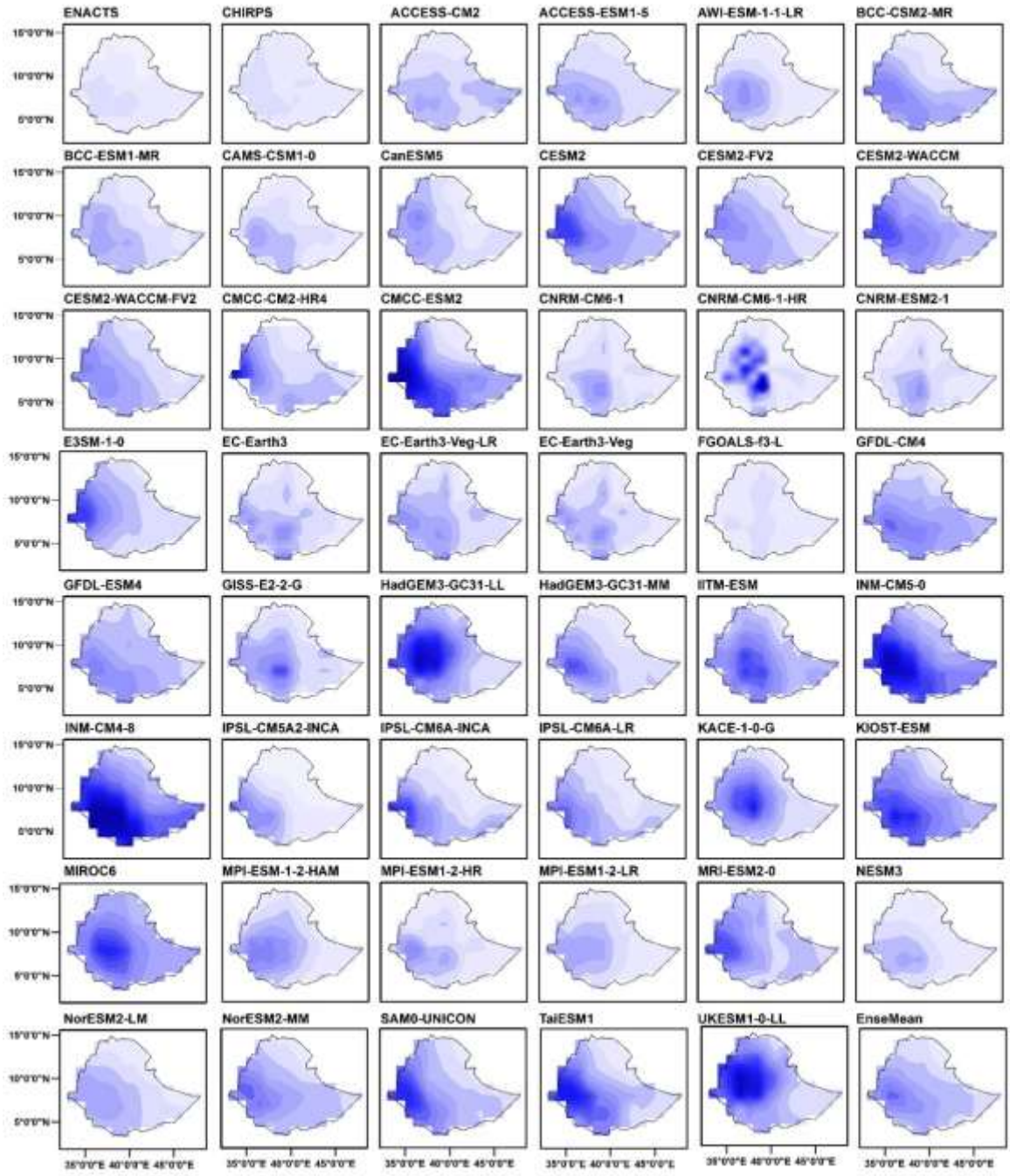

FMAM CWD (days/season)

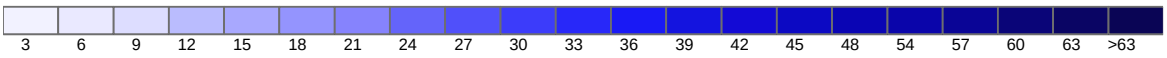

Figure 4.3: Mean consecutive wet days (CWD) (days/season) from observational dataset, CHIRPS, 45 CMIP6 models, and EnseMean over Ethiopia for FMAM season from 1981–2014

4.3.1.2 Heavy precipitation days (R10)

ENACTS and CHIRPS show good agreement in representing the spatial pattern and magnitude of the heavy precipitation days (R10) during JJAS and FMAM seasons (Table 4.3). CHIRPS overestimated the ENACTS R10 in some central parts of the country during the JJAS season. The median of heavy precipitation days (R10) for ENACTS and CHIRPS were 11 days/season and 13 days/season, respectively, during the JJAS season and 6 day/season and 8 days/season during FMAM (Table 4.3).

More than 25 models underestimated the spatial distribution of the R10 over the high rainfall and highland areas of the country including west and northwest of the country (< 55 days/season) during the JJAS season (Figure 4.4). In particular, CAMS-CSM1-0, CNRM-ESM2-1, CNRM-CM6-1, CNRM-CM6-1-HR, KIOST-ESM, UKESM1-0-LL, SAMO-UNICON, and HadGEM3-GC31-LL highly underestimated the observed R10 (< 10 days/season). On the other hand, 16 models overestimated the R10 (> 90 days/season) over the abovementioned areas during the JJAS season. However, most models showed better performance in simulating the magnitude of R10 over the east and southeast of the country compared to other parts of the country. NESM3, CESM2-WACCM-FV2, CMCC-ESM2, GFDL-ESM4, MPI-ESM-1-2-HAM, and MPI-ESM1-2-HR outperformed other models, with less deviation from R10 of the observational dataset. Out of 45 models, 35 showed a substantial bias of underestimating the R10 (< 16 days/season) over west and southwest of the country during the FMAM season (Figure 4.5). In contrast, 10 models overestimated the observed R10 (> 40 days/season) over the aforementioned areas. CMCC-ESM2, MIROC6, MRI-ESM2-0, CESM2-WACCM, CESM2, TaiESM1, and NorESM2-MM are the models that overestimated the R10 over west and southwest of the country in both seasons. UKESM1-0-LL, GFDL-CM4, and CESM2-FV2 reproduced the spatial distribution of the R10 reasonably well during FMAM season.

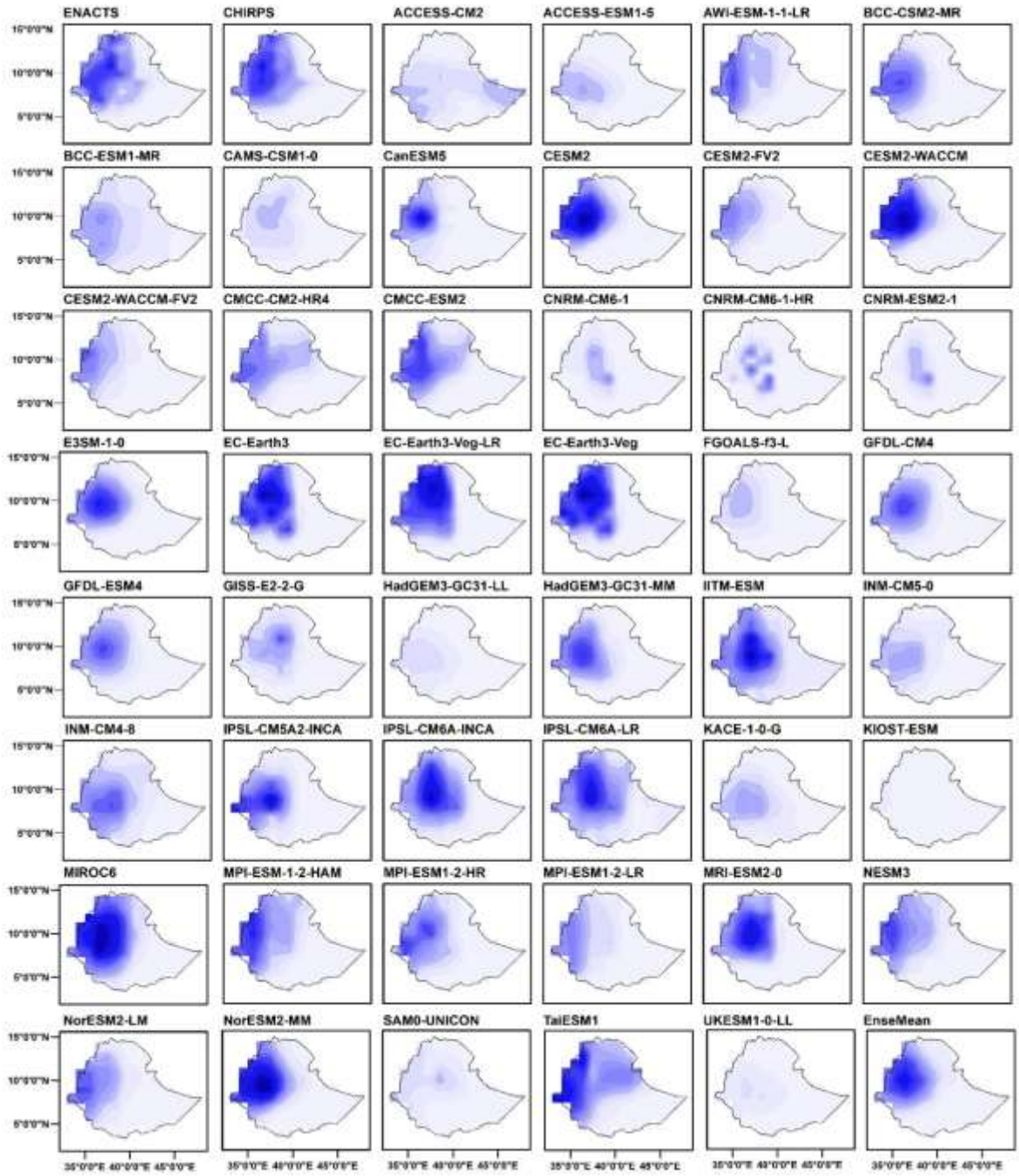

Figure 4.4**:** Mean heavy precipitation days (R10) (days/season) from observational dataset, CHIRPS, 45 CMIP6 models, and EnseMean over Ethiopia for JJAS season from 1981–2014.

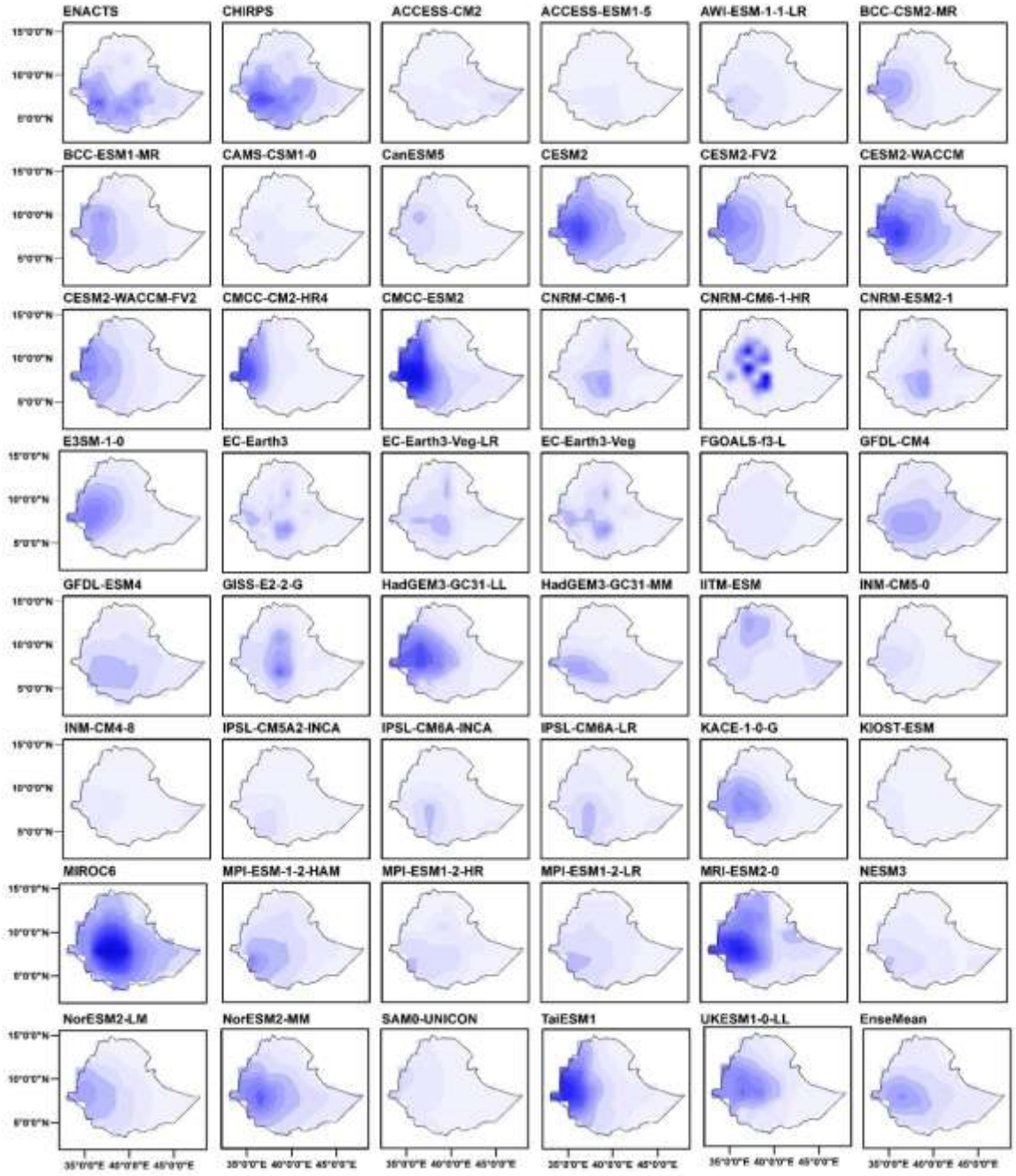

FMAM R10 (days/season)

Figure 4.5**:** Mean heavy precipitation days (R10) (days/season) from observational dataset, CHIRPS, 45 CMIP6 models, and EnseMean over Ethiopia for FMAM season from 1981–2014.

The median R20 in the JJAS season for ENACTS and CHIRPS were 3 days/season and 5 days/season, respectively, and 2 days/season and 3 days/season during FMAM (Table 4.3). For R20 (Appendix B3 and B4), all models except MIROC6, BCC-CSM2-MR, and MRI-ESM2-0 underestimated the observational dataset of the R20 (< 15 days/season) over north, northwest, and west of the country during the JJAS season (Appendix B3). During the FMAM season, all models except CESM2-WACCM, MIROC6, and MRI-ESM2-0 underestimated the R20 of the observational dataset (< 5 days/season). MIROC6 greatly overestimated over all parts of the country in the range of 8-39 days/season during the FMAM season (Appendix B4).

4.3.1.3 Seasonal total precipitation over very wet days (R95pTOT)

ENACTS and CHIRPS had R95pTOT between 0 – 310 mm/season and 0-256 mm/season for the JJAS season, respectively. For the FMAM season, ENACTS and CHIRPS of R95pTOT ranged from 2-176 mm/season and 7-134 mm/season, respectively (Table 4.3). CHIRPS reasonably captured the spatial pattern and magnitude of observed R95pTOT across most parts of the country. The models captured the key characteristics of the R95pTOT patterns,although their magnitudes were inaccurate. Out of 45 models, 30 underestimated the spatial distribution of R95pTOT (< 240 mm/season), with ACCESS-ESM1-5, CNRM-ESM2-1, CNRM-CM6-1, CNRM-CM6-1-HR, and EC-Earth3-Veg showing the highest underestimation (< 10 mm/season) over high rainfall and highland areas of the country (north, northwest, west, and central) during the JJAS season (Figure 4.6). Ten models overestimated the observed R95pTOT over the abovementioned areas. GFDL-CM4, GFDL-ESM4, MIROC6, and CanESM5 tended to produce the highest R95pTOT over the west and southwest parts of the country during the JJAS season. Generally, CMCC-ESM2, CESM2-WACCM-FV2, CESM2-WACCM, CESM2, E3SM-1-0, and NorESM2-MM showed relatively strong capabilities in simulating the spatial distribution of R95pTOT over the country during the JJAS season (Figure 4.6).

More than 25 models underestimated R95pTOT relative to the observed dataset for the FMAM simulation in the south and southwest regions of the country, whereas 15 models overestimated R95pTOT (Figure 4.7). ACCESS-ESM1-5, CAMS-CSM1-0, IPSL-CM5A2-INCA, AWI-ESM-1-1-LR, NESM3, MPI-ESM1-2-HAM, MPI-ESM1-2-HR, MPI-ESM1-2-LR, EC-Earth3-Veg-LR, EC-Earth3, and EC-Earth3-Veg considerably underestimated the R95pTOT of the observed

dataset compared to other models over most parts of the country, which ranged from 6 to 66 mm/season. On the other hand, MIROC6, and BCC-CSM2-MR showed the highest overestimation of the R95pTOT, ranging from 27 mm/season to 261 mm/season over the western part of the country during the FMAM season (Figure 4.7). ACCESS-CM2 is the only model that overestimated the R95pTOT over the eastern parts of the country during both seasons.

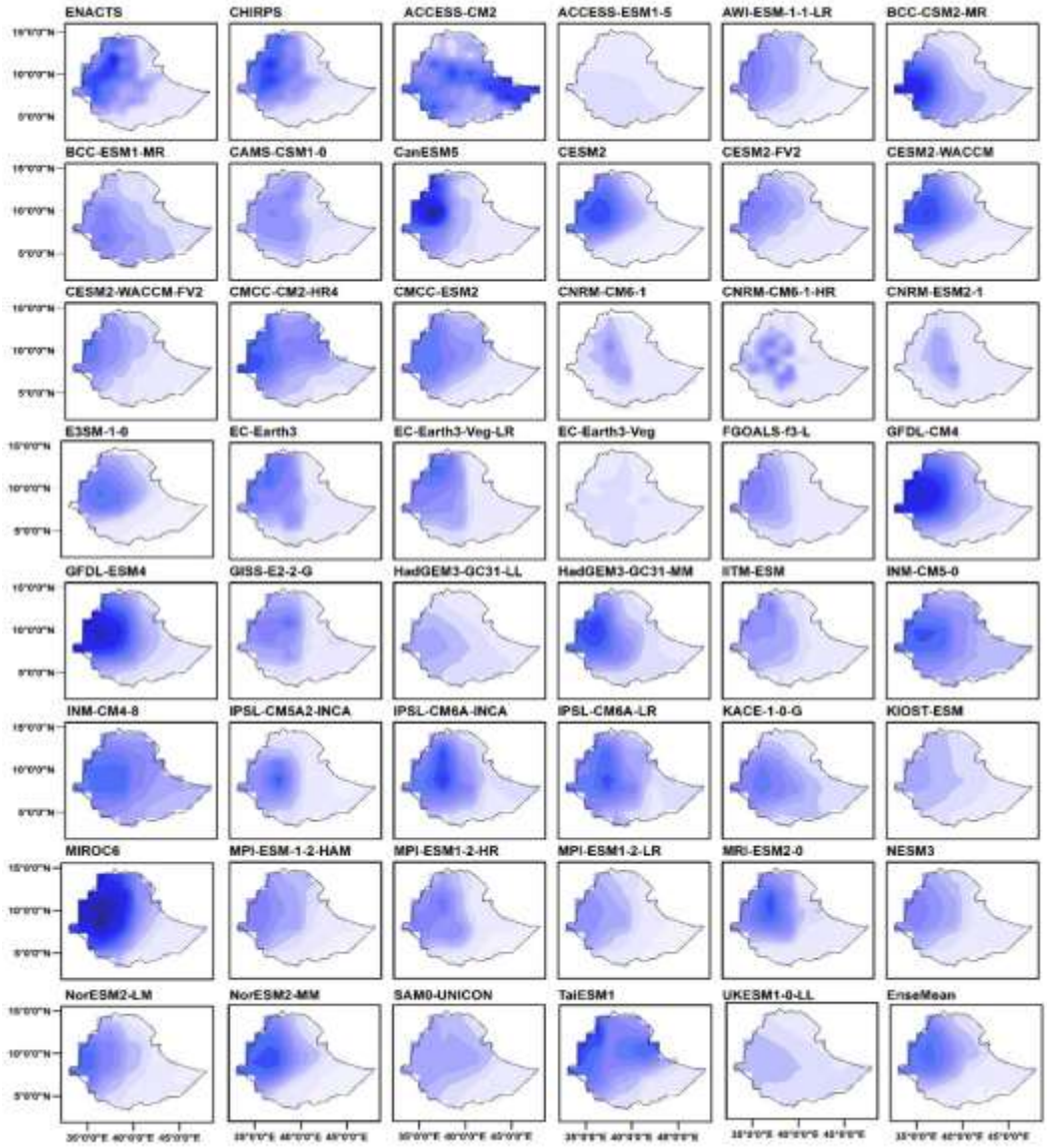

JJAS R95pTOT(mm/season)

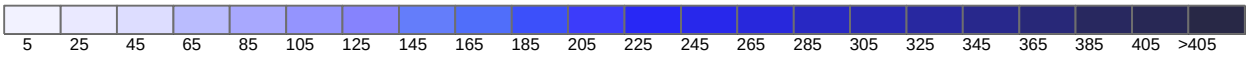

Figure 4.6**:** Mean seasonal precipitation over very wet days (R95pTOT) (mm/season) from observational dataset, CHIRPS, 45 CMIP6 models, and EnseMean over Ethiopia for JJAS season from 1981–2014.

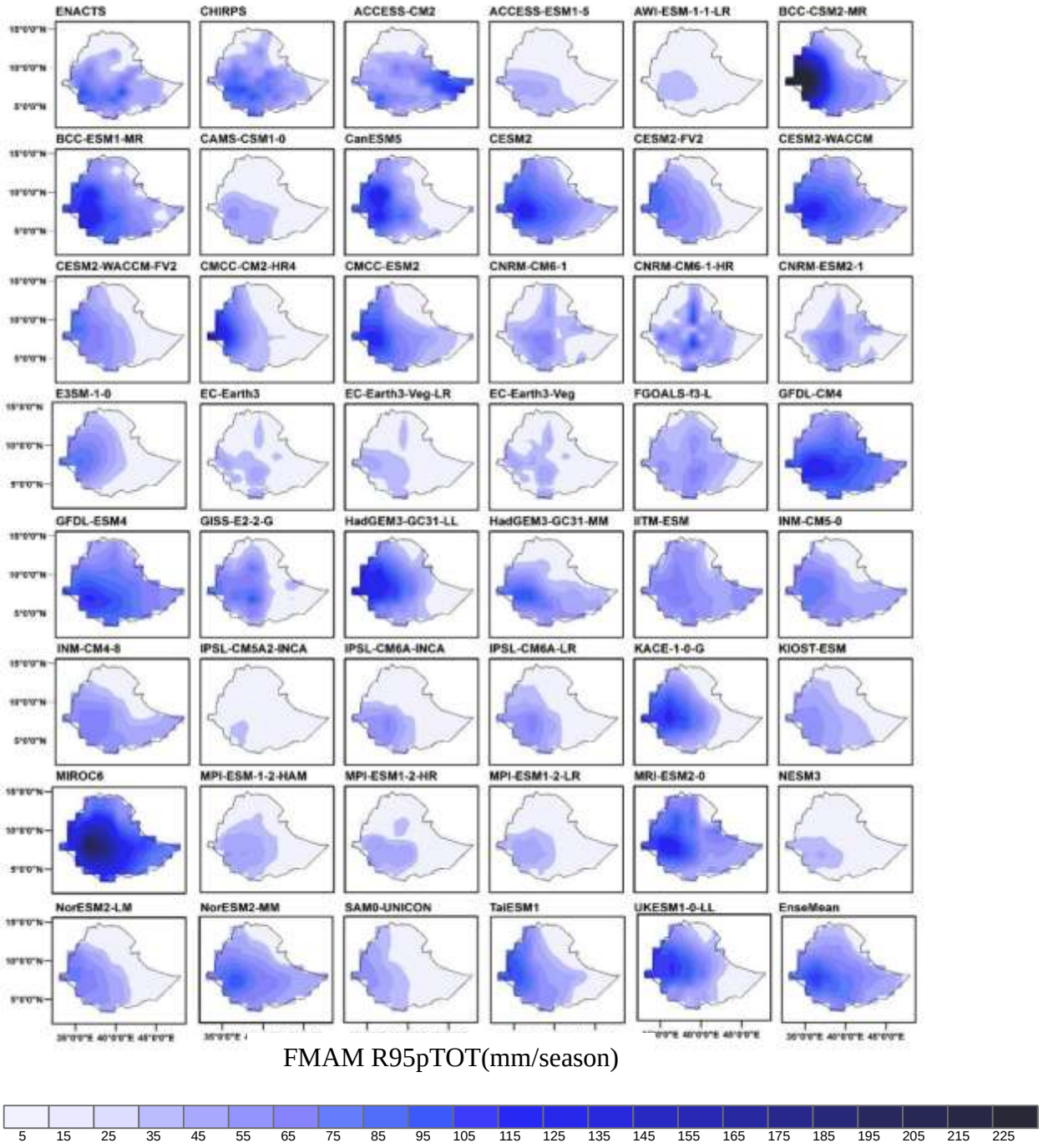

FMAM R95pTOT(mm/season)

Figure 4.7**:** Mean seasonal precipitation over very wet days (R95pTOT) (mm/season) from observational dataset, CHIRPS, 45 CMIP6 models, and EnseMean over Ethiopia for FMAM season from 1981–2014.

For R99pTOT (Appendix B5 and B6), 30 models simulated less intense extreme wet days for seasonal precipitation (< 72 mm/season) during the JJAS season. On the other hand, 15 models simulated more intense extreme wet days over high rainfall receiving and highland areas of west and southwest of the country (Appendix B5). All models except BCC-CSM2-MR, BCC-ESM1-MR, CanESM5, GFDL-CM4, GFDL-ESM4, and MIROC6 under-simulated the R99pTOT over the west and southwest parts of the country (< 42 mm/season) during the FMAM season (Appendix B6). MIROC6 showed the largest overestimation of R99pTOT over the north, west, and northwest of the country (up to 140 mm/season) for both seasons.

4.3.1.4 Total wet-day precipitation (PRCPTOT)

The highest JJAS seasonal total wet-day precipitation occurred in the north, west and southwest parts of the country. This is reduced in the south to a minimum value over the northeast and east of the country. During the JJAS season, the PRCPTOT values for ENACTS and CHIRPS ranged approximately from 2 mm/season to 2060 mm/season and 3 mm/season to 1560 mm/season, respectively. For the observed FMAM season, their PRCPTOT magnitudes ranged between 4 mm/season to 903 mm/season and 7 mm/season to 906 mm/season, respectively (Table 4.3). CHIRPS showed a higher PRCPTOT over the southwestern parts of the country relative to the observational data during the FMAM season.

Most models observed PRCPTOT pattern reasonably well, though with varying degrees of overlap. Out of 45 models, 26 showed lower amount of total wet-day precipitation as compared to observational dataset over rainfall receiving areas of west and northwest of the country during the JJAS season. However, ACCESS-ESM1-5, CAMS-CSM1-0, KIOST-ESM, CNRM-CM6-1, CNRM-ESM2-1, CNRM-CM6-1-HR, FGOALS-f3-L, HadGEM3-GC31-LL and UKESM1-0-LL showed significant negative bias in representing the observed PRCPTOT over the northwest of the country (Figure 4.8). On the other hand, 19 models revealed higher amount of PRCPTOT over north, northwest, and central parts of the country. BCC-ESM1-MR, CanESM5, CESM2, CESM2-WACCM, MRI-ESM2-0, MIROC6, NorESM2-MM, IPSL-CM6A-ICA, IPSL-CM6A-LR, EC-Earth3-Veg-LR, EC-Earth3-Veg, GFDL-CM4, and GFDL-ESM4 exhibited significant positive bias in reproducing the observed PRCPTOT over northwest parts of the country for the JJAS

season. The largest values of PRCPTOT were simulated by MIROC6 (up to 2350 mm/season) over the north and northwest parts of the country.

Out of 45 models, 30 showed lower values than the observed PRCPTOT over the west and southwest parts of the country during the FMAM season while the remaining 15 models revealed higher values. BCC-CSM2-MR, MIROC6, MRI-ESM2-0, CMCC-ESM2, CESM2, CESM2-WACCM, HadGEM3-GC31-LL, INM-CM4-8, INM-CM5-0, KACE-1-0-G, and UKESM1-0-LL highly overestimated the observed PRCPTOT over the abovementioned area during the FMAM season (Figure 4.9).

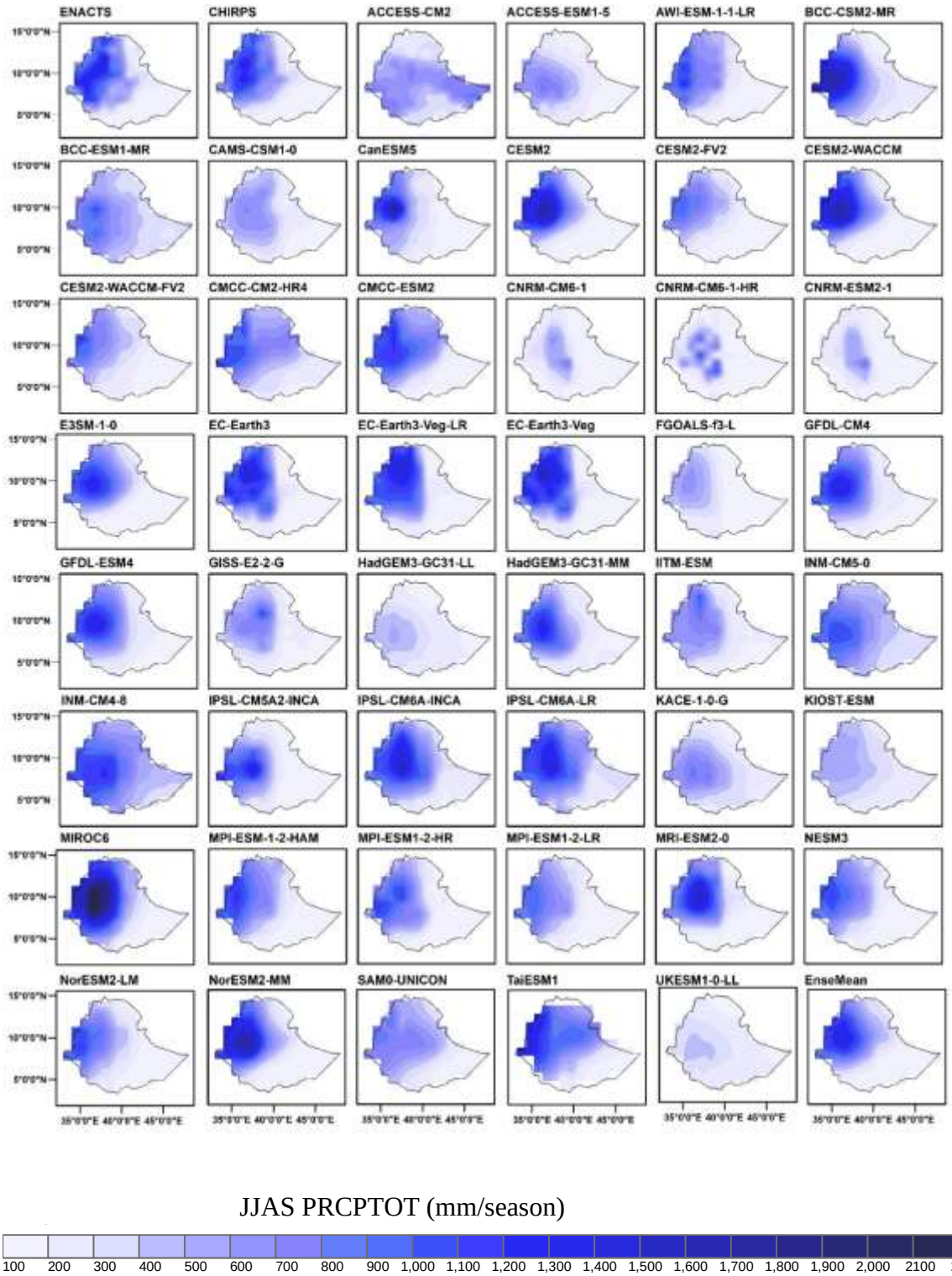

Figure 4.8**:** Mean total wet day rainfall (PRCPTOT) (mm/season) from observational dataset, CHIRPS 45 CMIP6 models, and EnseMean over Ethiopia for JJAS season from 1981–2014.

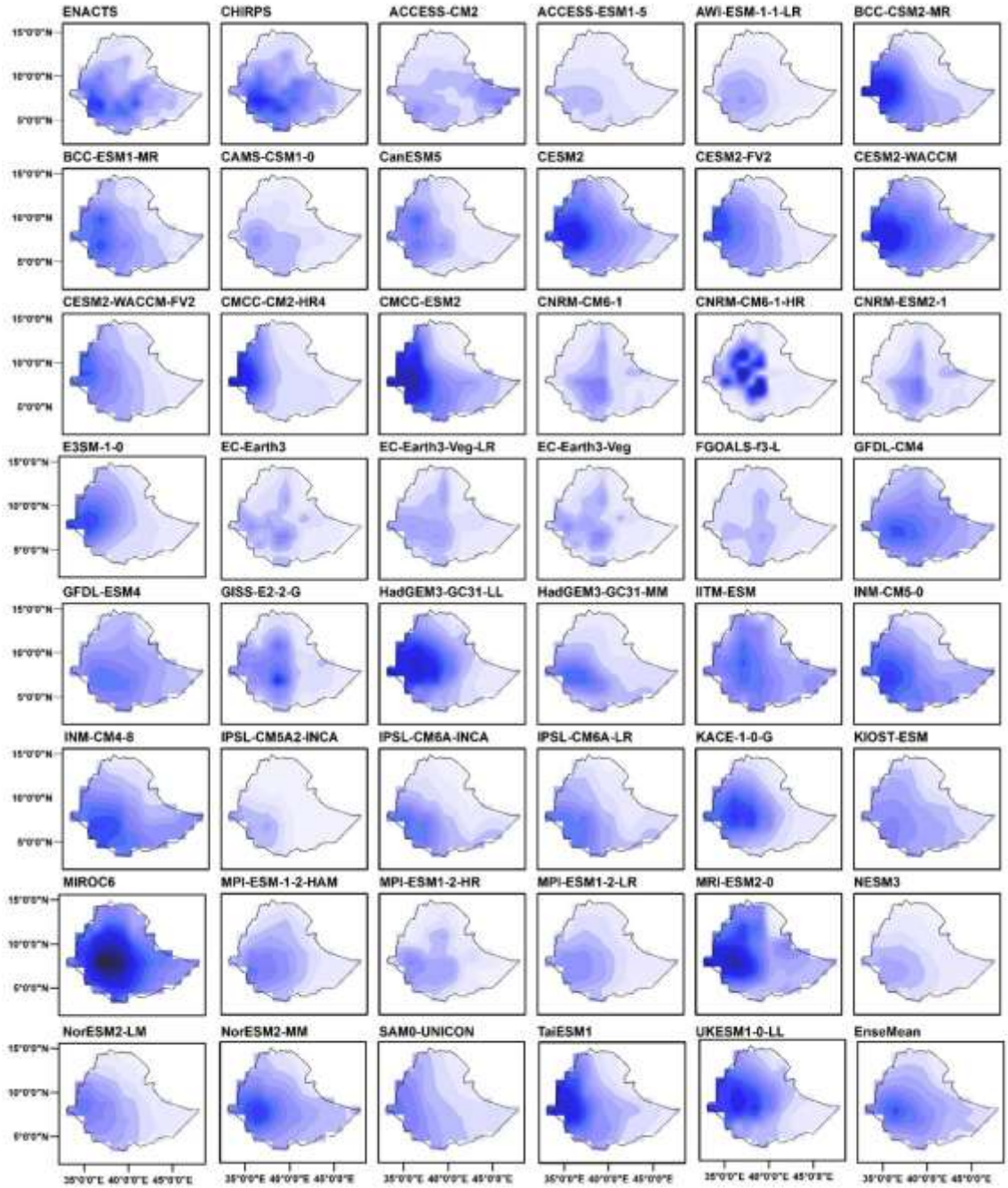

FMAM PRCPTOT (mm/season)

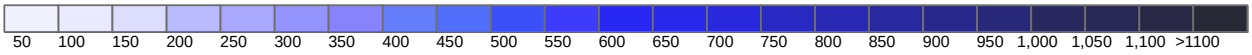

Figure 4.9**:** Mean total wet day rainfall (PRCPTOT) (mm/season) from observational dataset, CHIRPS 45 CMIP6 models, and EnseMean over Ethiopia for FMAM season from 1981–2014.

4.3.1.5 Seasonal maximum of 5-day precipitation (Rx5day)

The Rx5day for the ENACTS and CHIRPS ranged from 3 mm/season to 205 mm/season, and 0 mm/season to 234 mm/season, respectively, during JJAS season (Table 4.3) and from 3 mm/season to 173 mm/season and 7 mm/season to 224 mm/season, respectively, during FMAM season (Table 4.3). CHIRPS overestimated the observed Rx5day over the northwest, and west parts of the country. The majority of the models were able to capture the pattern of the observed Rx5day reasonably well over most parts of the country, but with errors in their magnitudes. Typically, they simulated the Rx5day precipitation amount better over the south and east of the country compared to other parts of the country. Out of 45 models, 6 (BCC-CSM2-MR, BCC-ESM1-MR, MIROC6, MRI-ESM2-0, and CanESM5) overestimated the Rx5day over the north, northwest, and west parts of the country as compared to the observational dataset during the JJAS season (Figure 4.10). More than 25 models underestimated the Rx5day of the observed dataset during JJAS season. KIOST-ESM, CNRM-ESM2-1, CNRM-CM6-1, CNRM-CM6-1-HR, and UKESM1-0-LL strongly underestimated the Rx5day.

Out of 45 models, 10 overestimated the Rx5day precipitation amount over west and southwest parts of the country during the FMAM season while more than of the 30 CMIP6 models underestimated the Rx5day (Figure 4.11). BCC-CSM2-MR, and MIROC6 highly overestimated the observed Rx5day over the eastern parts of the country during FMAM season while INM-CM4-8, INM-CM5-0, and IPSL-CM5A2-INCA strongly underestimated the Rx5day.Out of 45 models, more than 35 simulated a lower amount of Rx1day over the western part of the country during JJAS (Appendix B7) and FMAM season (Appendix B8). BCC-ESM1-MR, BCC-CSM2-MR, GFDL-ESM4, GFDL-CM4 and MIROC6 highly overestimated the observed Rx1day over the abovementioned areas during JJAS and FMAM seasons.

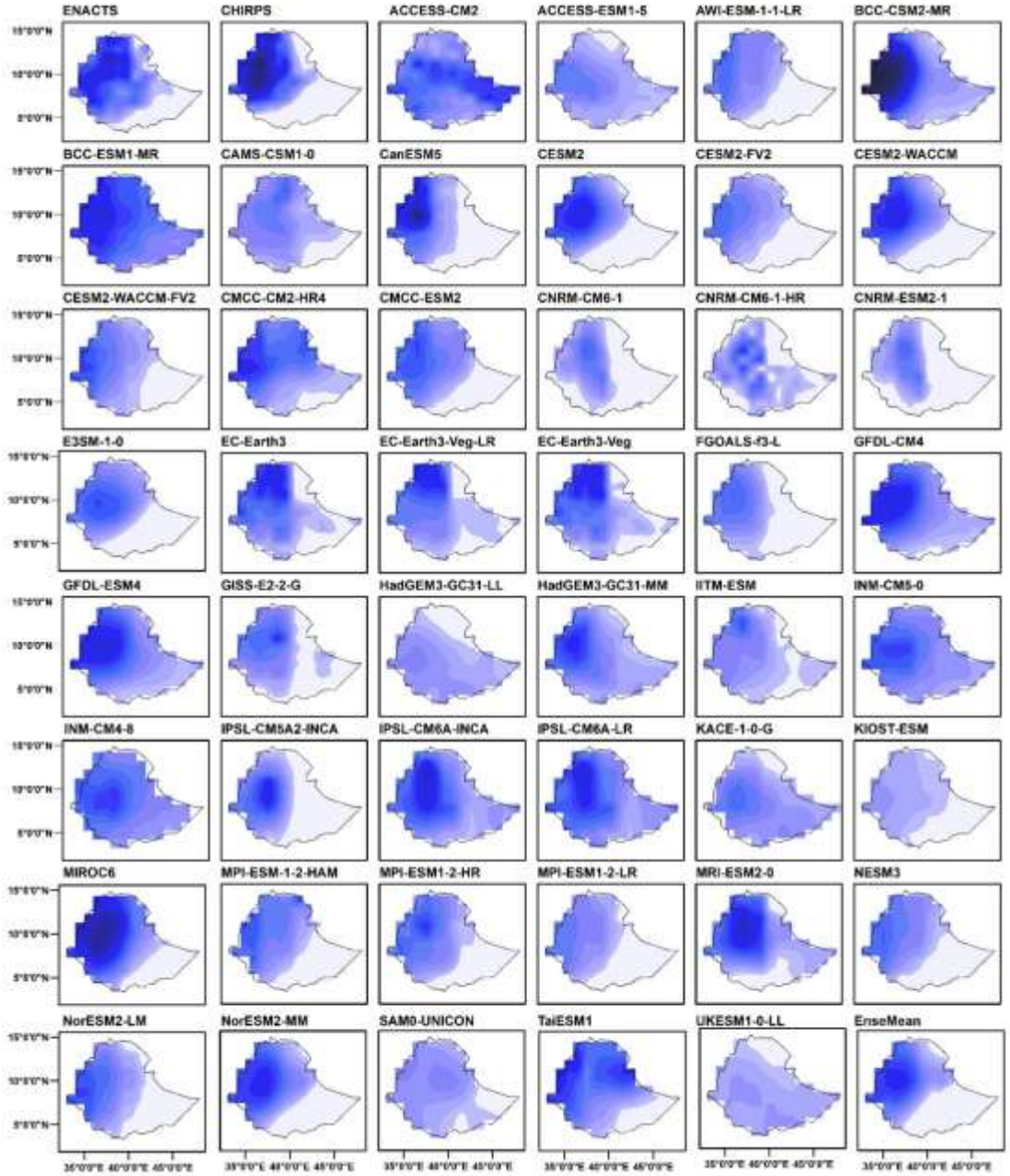

JJAS Rx5day (mm/season)

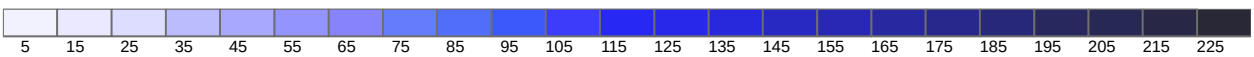

Figure 4.10: Mean maximum five-day rainfall (Rx5day) (mm/season) from observational dataset, CHIRPS, 45 CMIP6 models, and EnseMean over Ethiopia for JJAS season from 1981-2014

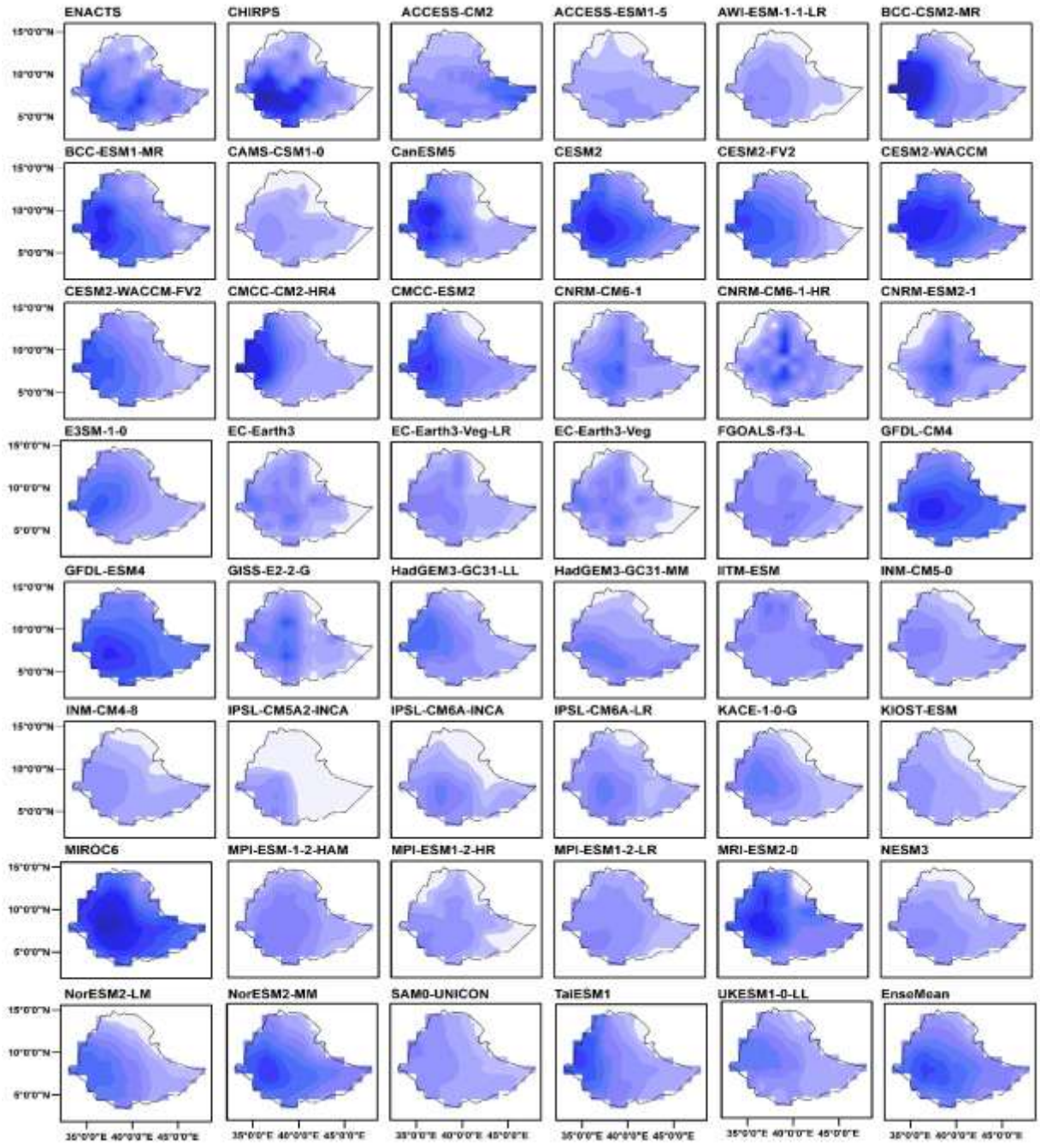

FMAM Rx5day (mm/season)

Figure 4.11: Mean maximum five-day rainfall (Rx5day) (mm/season) from observational dataset, CHIRPS, 45 CMIP6 models, and EnseMean over Ethiopia for FMAM season from 1981-2014

4.3.2 Statistical evaluation of the models

A portrait diagram that gives a summary of performance of all individual models, EnseMean, EnseMean_ALL and CHIRPS in representing the precipitation extremes indices for the JJAS and FMAM seasons with respect to ENACTS are presented in Figures 4.12 (a-f). CHIRPS slightly overestimated all extreme indices except for CDD. All models exhibited high positive CWD bias (blue) which ranges from +2% to +650% and 10% to 457% for JJAS and FMAM seasons, respectively, while they exhibited negative SDII bias (red) that range from -22% to – 90% and -30% to – 70%, respectively. More than half of the models overestimated the CWD by more than 100% with INM-CM4-8, and INM-CM5-0 showing the largest positive bias with greater than 300% for both seasons relative to observational dataset (Figures 4.12a, b). High-resolution models such as CNRM-CM6-1-HR, and AWI-ESM-1-1-LR showed larger Pbias compared to medium and low-resolution models such as NorESM2-MM, GFDL-CM4, NorESM2-LM, and GFDL-ESM4. Generally, the majority of the models revealed negative bias for R10, R20, R95pTOT, R99pTOT, Rx5day, Rx1day and PRCPTOT that ranged from − 5% to − 75% across both seasons relative to the observational dataset.

a) JJAS Pbias

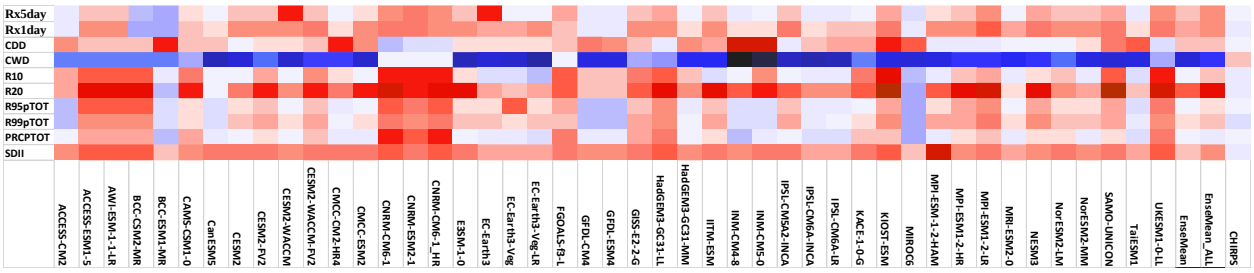

b) FMAM Pbias

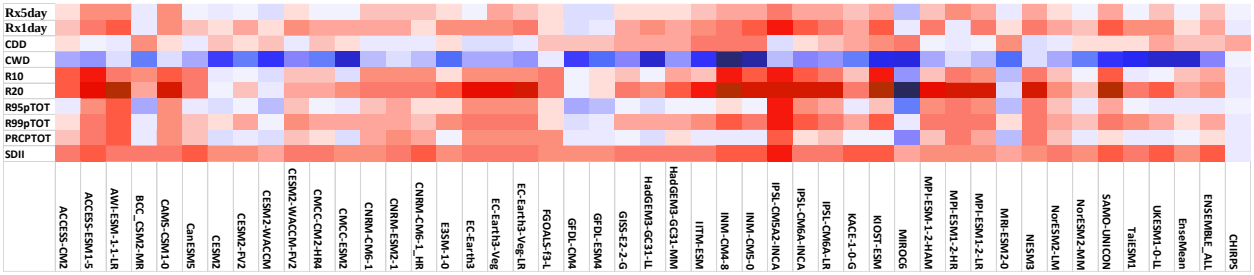

Pbias (%)

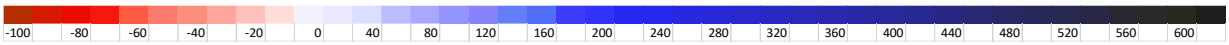

c) JJAS NMSE

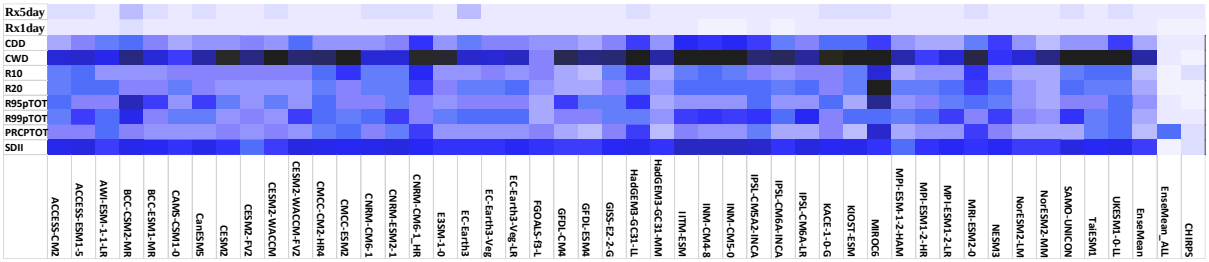

d) FMAM NMSE

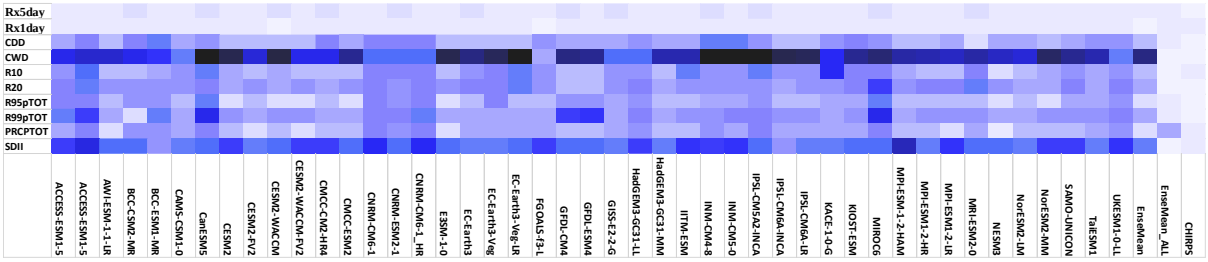

NRMSE

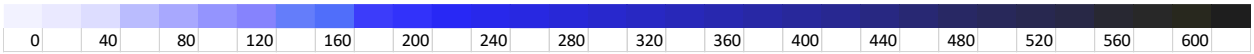

e) JJAS PCC

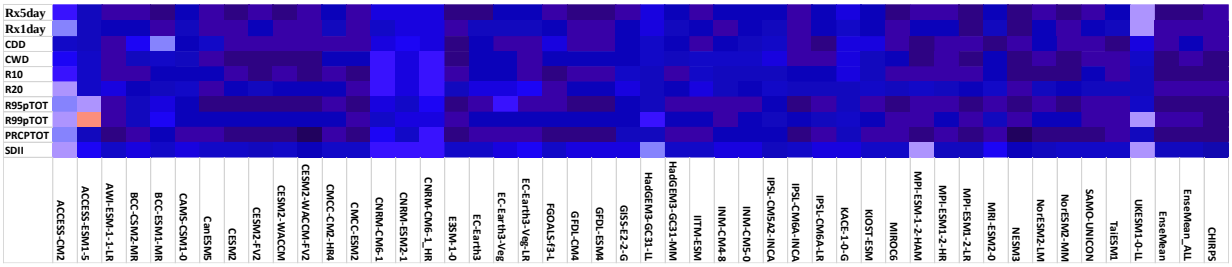

f) FMAM PCC

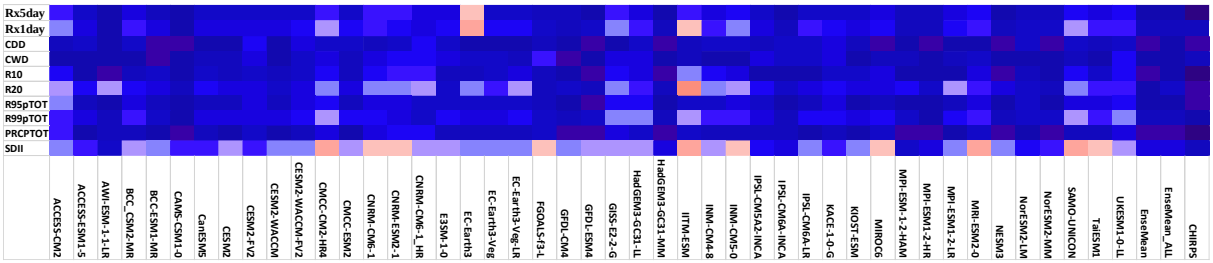

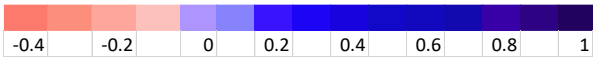

Figure 4.12: Portrait diagrams showing the Pbias (a, b), NRMSE (c, d), and PCC (e, f) of 45 CMIP6 models, CHIRPS, EnseMean_ALL and EnseMean with respect to the observed dataset. The descriptive statistics are for JJAS (a, c, e) and FMAM (b, d, f).

NRMSE has the advantage of being able to consider the impact of spatially compensating errors because it considers the overall magnitude of the errors, as well as their spatial distribution. CHIRPS exhibited lower values of NRMSE across both seasons. The NRMSE is higher for CWD and SDII across most of the models and the two seasons relative to the observational dataset while it is lower for Rx5day and Rx1day (Figures 4.12c, d). The light blue color series indicate lower correlation while the darker blue denotes a model with higher correlation (Figures 4.12e, f). CHIRPS showed higher values of PCC (>0.7) in simulating all extreme indices, with the exception of SDII. More than 30 models obtain better PCC values (> 0.7) for simulating CDD, PRCPTOT, R10, Rx5day, Rx1day and R95pTOT, but lower PCC for SDII (< 0.65), and in between for CWD, R20, and R99pTOT for JJAS season. Overall, most extreme indices showed higher values of PCC, Pbias and NRMSE for JJAS season compared to FMAM season across most models and

observational dataset. Additionally, high-resolution models such as CNRM-CM6-1-HR and AWI-ESM-1-1-LR exhibited larger Pbias and NMSE values, as well as lower PCC values, compared to medium- and low-resolution models like NorESM2-MM, GFDL-CM4, NorESM2-LM, and GFDL-ESM4.

4.3.3 Overall ranks of CMIP6 models

The performance of individual models for each extreme index with respect to ENACTS is presented in the supplementary material (Appendix B9, and B10). The CESM2-WACCM-FV2 model outperformed other models in simulating most metrics (CWD, R10, R95pTOT, R99pTOT, PRCPTOT, and SDII) during the JJAS season, while the GFDL-CM4 model performed better in simulating most extreme indices (R10, R20, R95pTOT, R99pTOT, PRCPTOT, Rx5day, and Rx1day) during the FMAM season. Generally, CWD and SDII showed less skill, with lower TSS values that ranged from 0.03 to 0.57 across most of the models relative to the observational dataset during both seasons. In contrast, CDD showed the highest skill, with TSS values ranging from 0.26 to 0.91. It was followed by Rx5day (0.06 to 0.87), Rx1day (0.05 to 0.82), and PRCPTOT (0.02 to 0.80).

The overall ranks were assigned for each model based on the RM values of TSS (RM_TSS) derived from the observed dataset (Appendix B9 and B10) in order to indicate their performance in representing the spatial characteristics of the ten extreme indices for JJAS and FMAM seasons. The top-ranking models with RM_TSS values greater than 0.7 are described in Table 4.4 (JJAS season) and Table 4.5 (FMAM season).Model ranks vary considerably across the observed datasets. CESM2-WACCM-FV2, NESM3, NorESM2-LM, NorESM2-MM, CMCC-ESM2, IPSL-CM6A-INCA, and E3SM-1-0 occupied the first seven positions with RM_TSS values of greater than 0.70 with respect to the observed dataset during the JJAS season (Table 4.4 and Appendix B9). UKESM1-0-LL, HadGEM3-GC31-LL, KIOST-ESM, ACCESS-CM2, and ACCESS-ESM1-5 were the last five models, with RM_TSS values of less than 0.2, in reproducing the extreme indices of the observed dataset (Appendix B9).

Table 4.1: TSS values for top-ranking CMIP6 models with RM_TSS values of greater than 0.70 for JJAS season for the period 1981-2014 over Ethiopia with respect to observational dataset

Models	TSS Values										RM_ TSS	Over all ranks
	CDD	CWD	R10	R20	R95p TOT	R99p TOT	PRCP TOT	SDII	Rx 5day	Rx 1day		
CESM2-WACCM-FV2	0.76	0.54	0.86	0.5	0.93	0.75	0.94	0.58	0.82	0.69	0.85	1
NESM3	0.76	0.22	0.95	0.23	0.89	0.78	0.96	0.63	0.87	0.6	0.78	2
NorESM2-LM	0.75	0.53	0.83	0.48	0.83	0.70	0.86	0.58	0.78	0.67	0.76	3
NorESM2-MM	0.83	0.14	0.66	0.72	0.88	0.70	0.80	0.59	0.86	0.77	0.75	4
IPSL-CM6A-INCA	0.80	0.23	0.74	0.56	0.86	0.72	0.87	0.53	0.78	0.73	0.74	5
CMCC-ESM2	0.78	0.2	0.86	0.37	0.88	0.78	0.88	0.52	0.81	0.66	0.74	6
E3SM-1-0	0.84	0.11	0.68	0.72	0.88	0.67	0.81	0.58	0.86	0.79	0.73	7

Based on RM values of TSS, the best model from the 45 models with respect to the observed dataset was NorESM2-MM, followed by HadGEM3-GC31-MM, GFDL-CM4, NorESM2-LM, GFDL-ESM4, BCC-ESM1-MR, and MPI-ESM-1-2-HAM in reproducing the FMAM extreme precipitation indices, with RM_TSS values greater than 0.7 (Table 4.5 and Appendix B10). SAMO-UNICON, ACCESS-ESM1-5, INM-CM5-0, and INM-CM4-8 showed lower skill in representing the observed dataset of extreme indices during FMAM season.

Table 4.2: TSS values for top-ranking CMIP6 models with RM_TSS values of greater than 0.70 for FMAM season for the period 1981-2014 over Ethiopia with respect to the observational dataset

MODELS	TSS Values										RM_ TSS	Over all ranks
	CDD	CWD	R10	R20	R95p TOT	R99p TOT	PRCP TOT	SDII	Rx 5day	Rx 1day		
NorESM2-MM	0.69	0.29	0.70	0.61	0.71	0.44	0.76	0.21	0.67	0.45	0.85	1
HadGEM3-GC31-MM	0.70	0.27	0.73	0.37	0.66	0.60	0.80	0.20	0.72	0.59	0.84	2
GFDL-CM4	0.70	0.34	0.68	0.53	0.72	0.53	0.76	0.12	0.64	0.57	0.84	3
NorESM2-LM	0.51	0.34	0.65	0.44	0.60	0.51	0.71	0.39	0.62	0.52	0.80	4
GFDL-ESM4	0.76	0.40	0.58	0.40	0.77	0.43	0.74	0.04	0.62	0.44	0.77	5
BCC-ESM1-MR	0.76	0.41	0.58	0.49	0.41	0.49	0.66	0.25	0.52	0.47	0.76	6
MPI-ESM-1-2-HAM	0.71	0.20	0.75	0.02	0.60	0.37	0.80	0.50	0.63	0.38	0.73	7

4.3.4 Comparison of ensemble with individual models

Weighted average of the top seven models (CESM2-WACCM-FV2, NESM3, NorESM2-LM, CMCC-ESM2, IPSL-CM6A-INCA, E3SM-1-0, and NorESM2-MM) were used to generate ensemble (EnseMean) for JJAS season, while NorESM2-MM, GFDL-CM4, HadGEM3-GC31-MM, NorESM2-LM, BCC-ESM1-MR, GFDL-ESM4, and MPI-ESM-1-2-HAM were used to produce ensemble for FMAM season.

The EnseMean typically reproduced the spatial patterns of most of the extreme precipitation indices better than the individual models in both seasons (Figures 4.2 – 4.11). Similar to individual models, the EnseMean and EnseMean_ALL showed a large positive bias for CWD by more than 100% across both seasons relative to the observed dataset (Figures 4.12 (a-f)) while they revealed negative bias for SDII, R10, R20, R95pTOT, R99pTOT, and PRCPTOT that range from − 4% to − 60%. EnseMean_ALL showed larger Pbias in simulating CDD, R95pTOT, R10, R20, relative to EnseMean_ALL during JJAS season (Figure 4.12a) while it showed lower Pbias in CDD, R95pTOT SDII, and PRCPTOT during FMAM season (Figure 4.12b). The NMSE is higher for EnseMean_ALL in simulating most of extreme indices relative to EnseMean during JJAS and FMAM seasons (Figure 4.12c, d). Generally, the EnseMean outperformed the individual models and EnseMean_ALL by exhibiting a lower Pbias (Figure 4.12a, b), a lower NRMSE (Figure 4.12c, d) and a higher PCC value (Figure 4.12e, f) for the extreme precipitation indices across both seasons.

The TSS values that illustrate the performance of the EnseMean and EnseMean_ALL in simulating extreme precipitation indices of the observational dataset are presented in the supplementary material for JJAS (Appendix B11) and FMAM (Appendix B12) seasons. The TSS for PRCPTOT (0.92), R95pTOT (0.93), R10 (0.86), CDD (0.83), Rx5day (0.86) and R99pTOT (0.77) in the EnseMean depicted better performance relative to most of the individual models and EnseMean_ALL during the JJAS season (Appendix B11). In contrast, EnseMean_ALL showed lower performance with lower TSS values in simulating CDD (0.69), R10 (0.70), R95pTOT (0.76), PRCPTOT (0.77), SDII (0.36), and Rx5day (0.67). Similarly, the EnseMean showed better skill scores for PRCPTOT (0.81), R10 (0.78), and R99pTOT (0.62) compared to individual models for

the FMAM season (Appendix B12), while it revealed better skill scores in all indices except R99P indices when compared to EnseMean_ALL during the FMAM season.

CMIP6 models, EnseMean_ALL and EnseMean are further evaluated using the estimated value of overall ranking (RM) of ten extreme indices with respect to Pbias, NRMSE, PCC, and TSS in the supplementary material for JJAS (Appendix B13) and FMAM (Appendix B14) seasons. MRI-ESM2-0, HadGEM3-GC31-MM, EnseMean_ALL, NorESM2-LM, EnseMean, NorESM2-MM, and CESM2 are the top seven models in terms of the RM_Pbias values (> 0.65) during JJAS season (Appendix B13). On the other hand, NorESM2-MM, EnseMean, CESM2-FV2, EnseMean_ALL, CMCC-CM2-HR4, FGOALS-f3-L, and BCC-ESM1-MR attained the top seven positions the RM_Pbias values during FMAM season (Appendix B14). In the JJAS season, EnseMean, EnseMean_ALL, CESM2-FV2, HadGEM3-GC31-MM, NorESM2-LM, AWI-ESM-1-1-LR, CMCC-ESM2, and NESM3 are the top eight models in terms of RM_NRMSE values (>0.65) (Appendix B13) while EnseMean, EnseMean_ALL, NorESM2-MM, FGOALS-f3-L, HadGEM3-GC31-MM, NorESM2-LM, and MPI-ESM-1-2-HAM, held the top six positions during the FMAM season (Appendix B14). NESM3, ranked first in RM_PCC value during the JJAS season, followed by CESM2-WACCM-FV2, MPI-ESM1-2-LR, EnseMean, CESM2-WACCM, NorESM2-MM and EnseMean_ALL (Appendix B13). In contrast, EnseMean, CAMS-CSM1-0, HadGEM3-GC31-MM, MPI-ESM1-2-HR, NESM3, GFDL-ESM4, NorESM2-MM, and GFDL-CM4 occupied the top eight positions in RM_PCC value, all exceeding 0.80, during the FMAM season (Appendix B14).CESM2-WACCM-FV2, EnseMean, NESM3, NorESM2-LM, NorESM2-MM, IPSL-CM6A-INCA, CMCC-ESM2, CESM2, and E3SM-1-0 are the top seven models in terms of RM_TSS values (> 0.70) during JJAS season (Appendix B13) while EnseMean, NorESM2-MM, HadGEM3-GC31-MM, GFDL-CM4, NorESM2-LM, GFDL-ESM4, BCC-ESM1-MR, and MPI-ESM-1-2-HAM ranked the first 8 positions during FMAM season (Appendix B14). Thus, EnseMean consistently ranked higher across all overall rakings of the ten extreme indices, considering Pbias, NMSE, PCC, and TSS for both seasons.

Taylor diagram is further presented to assess the capability of the statistical features of top-ranked CMIP6 models, EnseMean and EnseMean_ALL in simulating the spatial pattern of extreme precipitation indices with respect to the observation dataset (ENACTS) during JJAS season (Figure 4.13) and FMAM season (Figure 4.14). Among all the climate indices, the top-ranked

CMIP6 models exhibited the greatest spatial variability in CWD, followed by the indices R20 and SDII, during both the JJAS (Figure 4.13 (b, d, h)) and FMAM (Figure 4.14 (b, d, h)) seasons. Compared to the JJAS season, the top-ranked models revealed a relatively poorer performance in simulating the spatial distribution of SDII during the FMAM season, as indicated by lower PCC values (<0.4), larger RMSE, and SD. Five (CMCC-ESM2, IPSL-CM6A-INCA, E3SM-1-0, NESM3, and NorESM2-MM) and one top ranking models (NorESM2-MM) exhibited the largest values of RMSE in representing the reference dataset of CWD and R10, respectively during JJAS season.

The overall spatial variation of the PRCPTOT was well simulated by the top-ranking models, EnseMean and EnseMean_ALL with PCC values exceeding 0.7, RMSE ranging from 0.5 to 1, and SD approaching 1.0 during the FMAM season. On the other hand, all seven top-ranking models and EnseMean showed the best simulation in representing PRCPTOT, and R95pTOT with PCC greater than 0.8, the SD close to 1, and RMSE less than 0.5 during the JJAS season. However, NorESM2-MM exhibited larger RMSE and SD for CWD, R10, R99pTOT, and PRCPTOT during the JJAS season compared to other top-ranking models. Conversely, BCC-ESM1-MR revealed lower skill in simulating CWD, R10, R20, R95pTOT, and R99pTOT during the FMAM season relative to other top-ranking models. In general, the top-ranking models exhibited greater variability in simulating extreme indices during the FMAM season compared to the JJAS season, with the exception of CWD.

Compared with top-ranking models, EnseMean generally performs well in simulating various indices across both seasons, with superior performance on PRCPTOT, R10, and R99pTOT, as indicated by PCC, RMSE and SD. EnseMean showed better performance in simulating CDD, R10, R20, R95pTOT, PRCPTOT, and Rx5day with higher PCC and lower RMSE and SD compared to EnseMean_ALL during JJAS (Figure 4.13) and FMAM (Figure 4.14) seasons. Moreover, EnseMean_ALL revealed higher SD in simulating CDD, PRCPTOT, R10, R20, R95pTOT, and Rx5day compared to top-ranking models and EnseMean during the JJAS season while EnseMean showed lower SD.

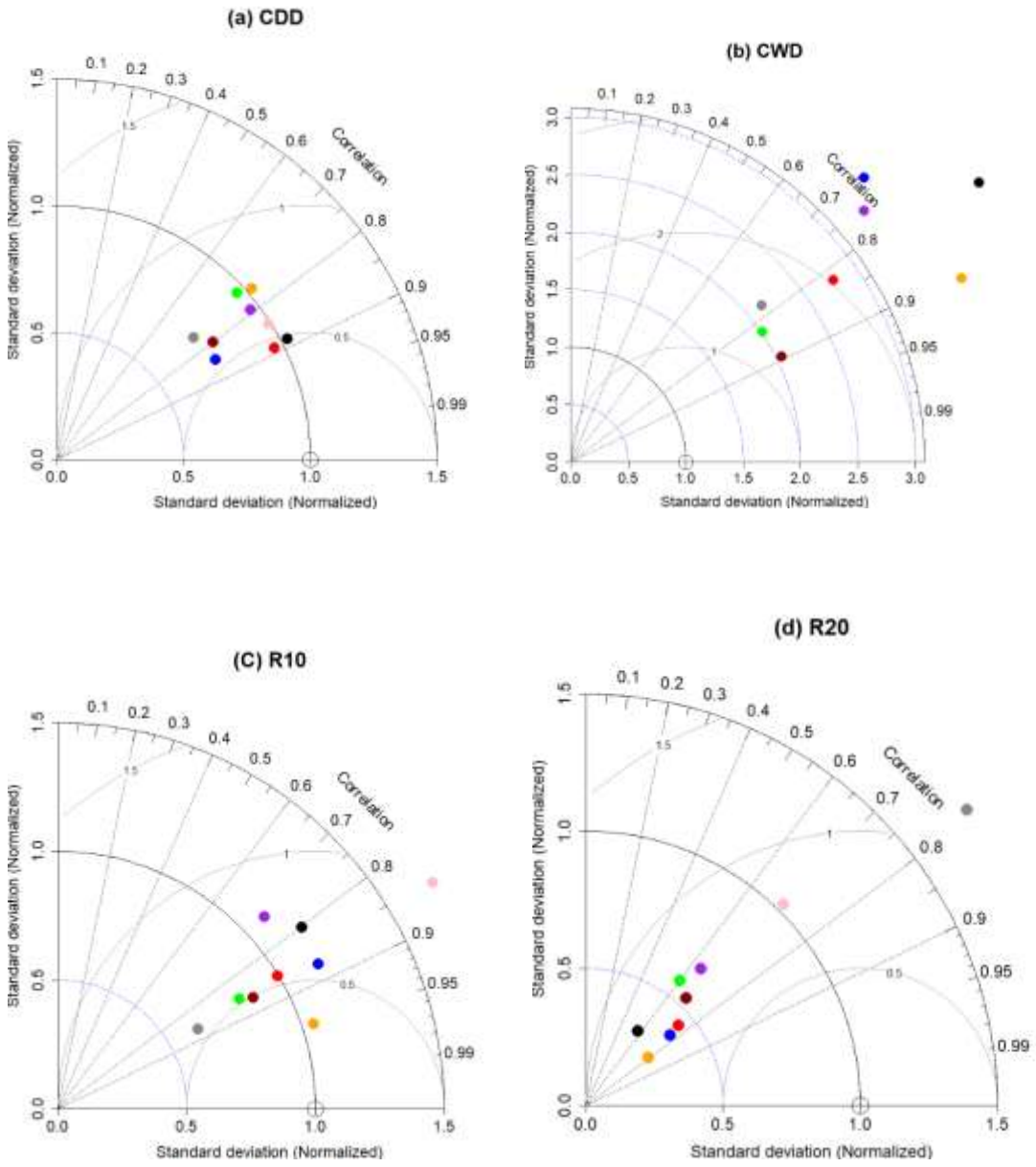
(a) CDD
(b) CWD
(C) R10
(d) R20
Correlation
Standard deviation (Normalized)
Standard deviation (Normalized)

(e) R95pTOT

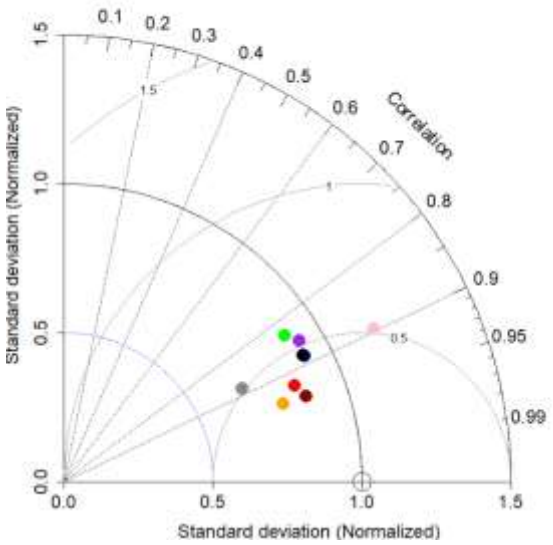

(f) R99pTOT

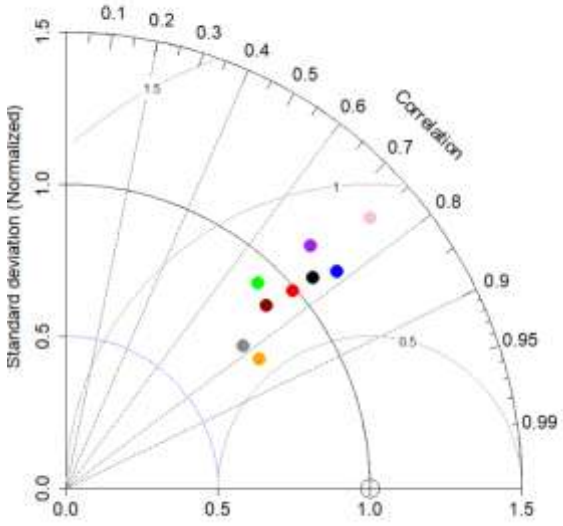

(g) PRCPTOT

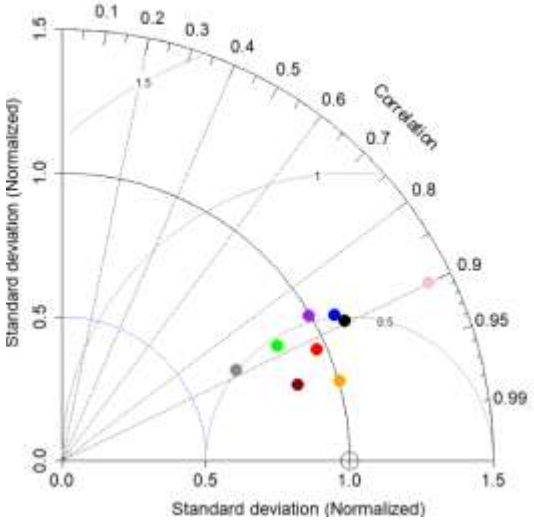

(h) SDII

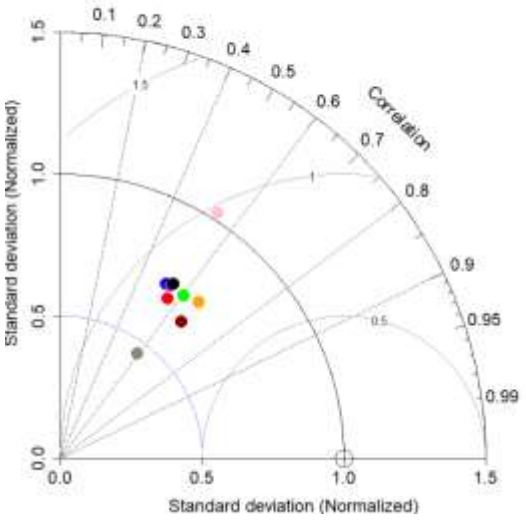

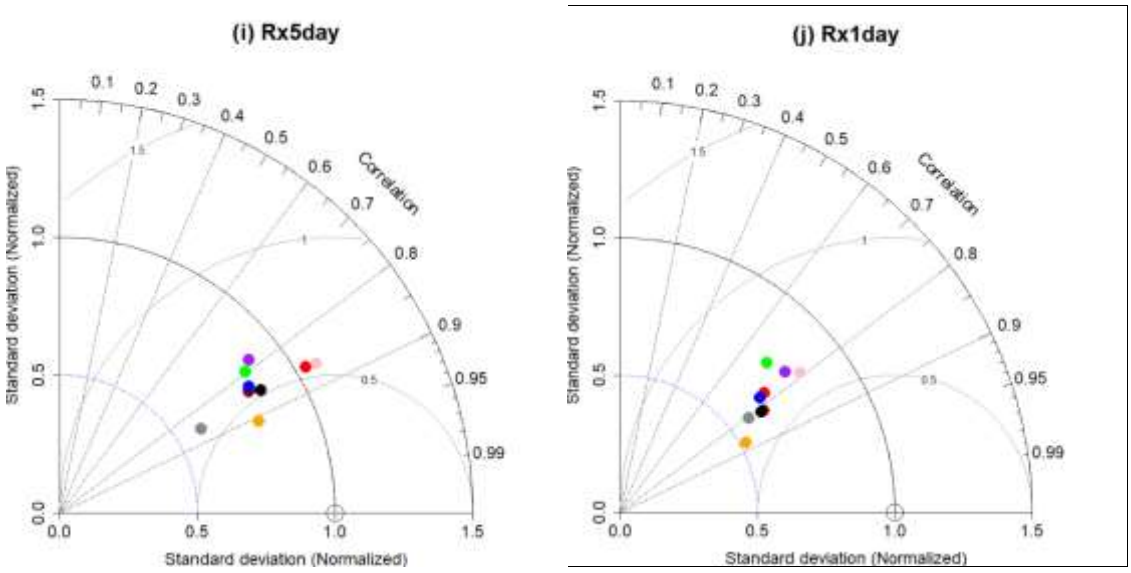

Top ranking models, EnseMean and EnseMean_ALL for JJAS season

Figure 4.13: Taylor diagram (a-j) of the top-ranking models, EnseMean, and EnseMean_ALL in simulating JJAS extreme precipitation indices with respect to ENACTS over Ethiopia for the period 1981–2014.

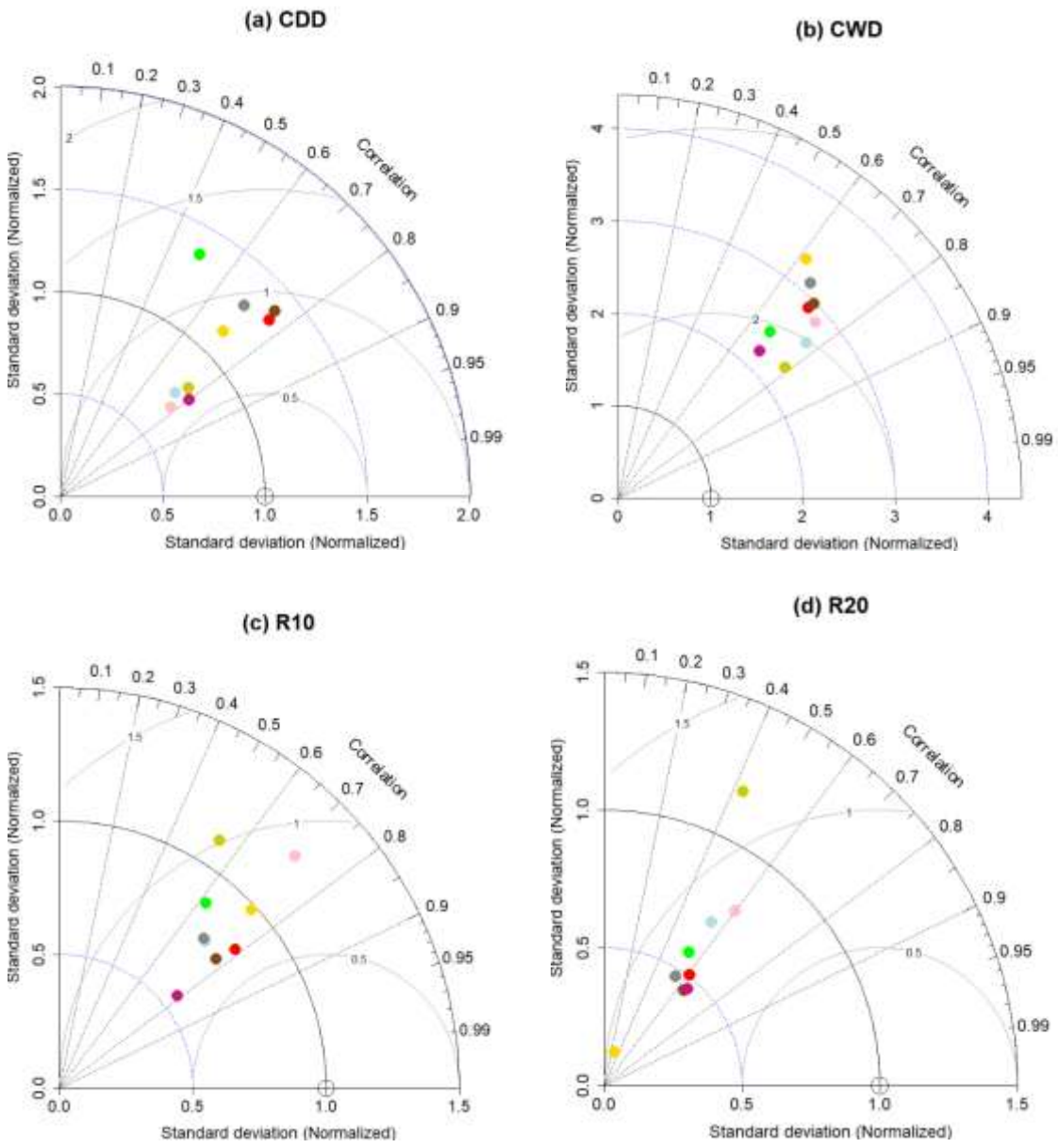
(a) CDD
(b) CWD
(c) R10
(d) R20
Correlation
Standard deviation (Normalized)
0.1
0.2
0.3
0.4
0.5
0.6
0.7
0.8
0.9
0.95
0.99

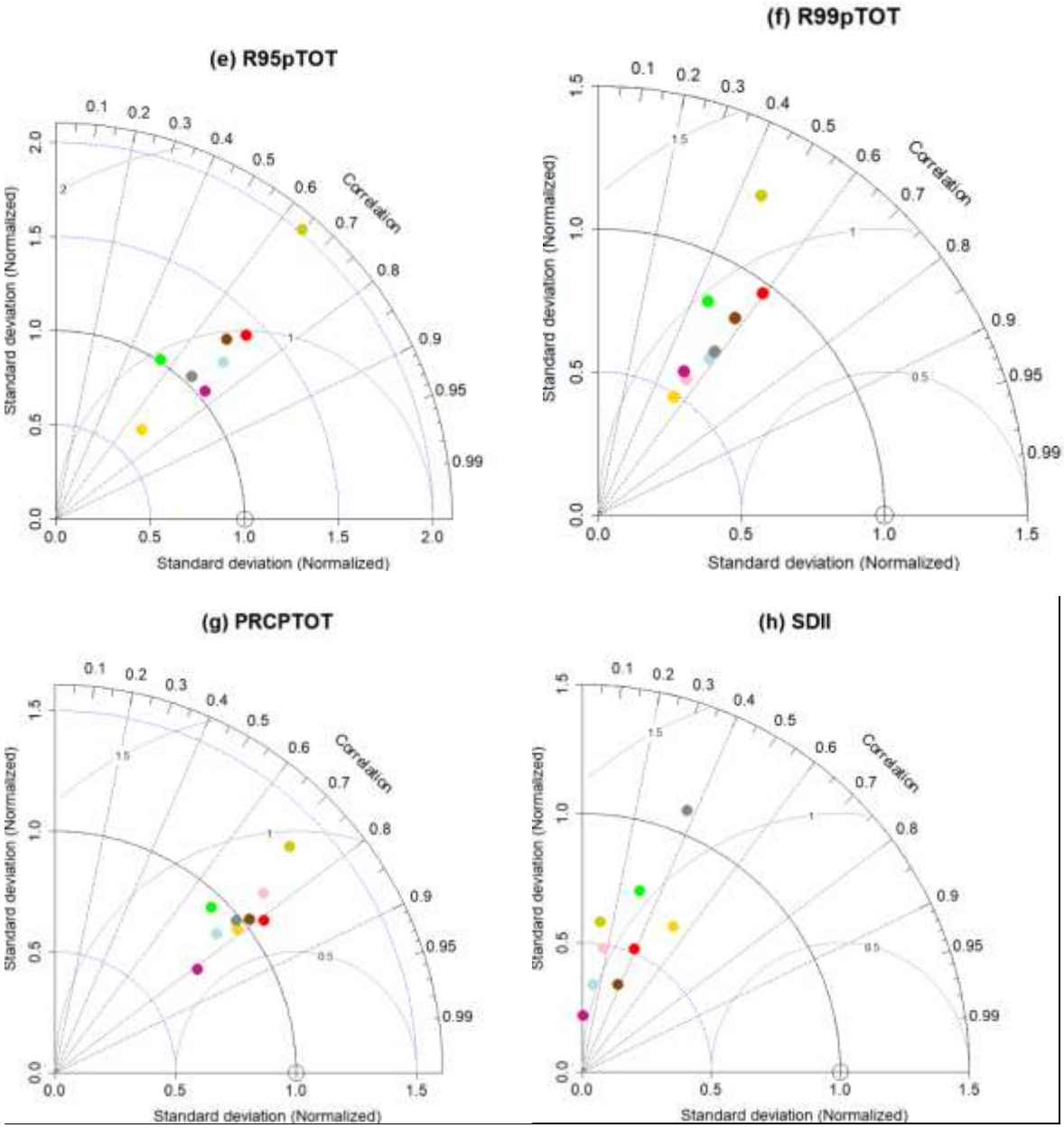
(e) R95pTOT
(f) R99pTOT
(g) PRCPTOT
(h) SDII
Correlation
Standard deviation (Normalized)
Standard deviation (Normalized)

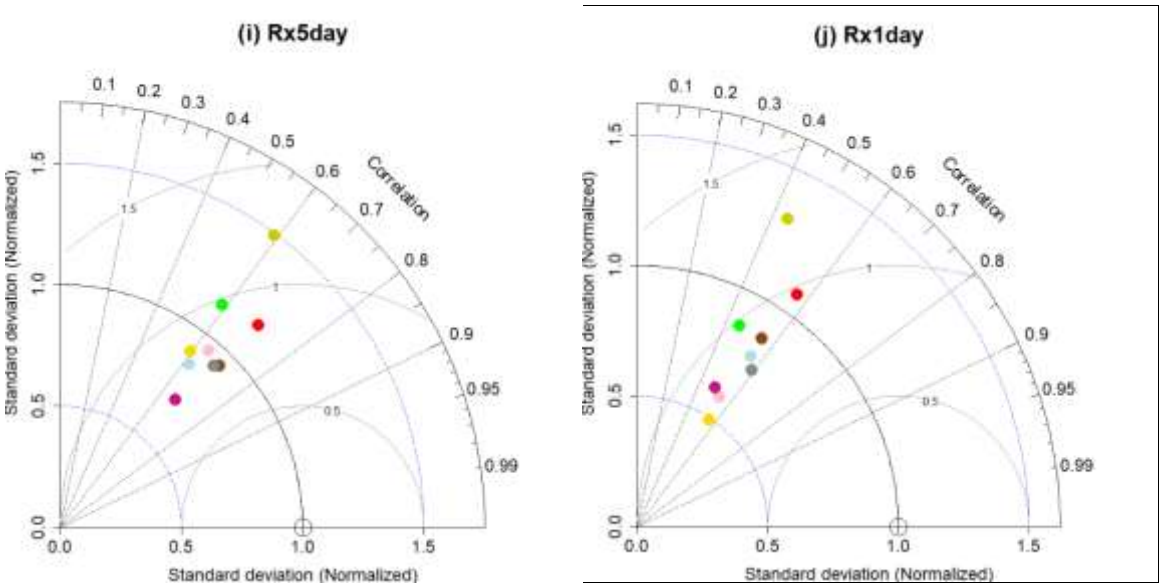

Top ranking models, EnseMean and EnseMean_ALL for FMAM season

Figure 4.14: Taylor diagram (a-j) of the top-ranking models, EnseMean, and EnseMean_ALL in simulating FMAM extreme precipitation indices with respect to ENACTS over Ethiopia for the period 1981–2014.

4.3.5 Regional analysis of climatologies in ensemble (EnseMean)

Table 4.6 presents a summary of the Pbias, NRMSE, PCC, and TSS values for ten extreme indices, comparing with the EnseMean to the observational dataset (ENACTS). The analysis is conducted across the five agro-ecological zones (AEZs) of Ethiopia for the JJAS season. The desert zone exhibited the largest overestimation of CWD, with a Pbias value exceeding 300%. The Pbias for the alpine, temperate, and tropical AEZs indicates that EnseMean underestimated all ten extreme indices, with the exception of CWD. For the desert zone, EnseMean overestimated the CWD, PRCPTOT, R95pTOT, Rx5day, and R10 indices, while it underestimated other indices. Generally, EnseMean highly overestimated CWD, with the range in Pbias across the five zones from 140% to 397%, and underestimated CDD, R99pTOT, Rx1day, R20, and SDII, during the JJAS season.

The NRMSE results show that EnseMean exhibited the largest error for CWD, followed by PRCPTOT over all AEZs relative to other indices with highest error over the desert AEZ while it showed a smaller error for R10, R20, and SDII.

The EnseMean PCC was evaluated for ten extreme indices using the ENACTS dataset during the JJAS season (Table 4.6). The correlation was positive for all extreme indices over the five AEZs. For the tropical zone, the PCC values were greater than 0.8, with the exception of SDII. Alpine and temperate regions typically had the lowest PCC values. Ranks were assigned for simulating the ten extreme indices for each of the five AEZs based on the TSS values for the JJAS season (Table 4.6). TSS values of the EnseMean for simulating the ten extreme indices ranged from 0.16 to 0.92. EnseMean showed the best performance in simulating all extreme indices across tropical and desert AEZs (TSS > 0.75), except for R20 and SDII, which had the lowest skill scores over alpine and temperate AEZs (TSS < 0.40). Generally, TSS values of the EnseMean were lower for simulating R20 and SDII for most AEZs while it was higher for PRCPTOT and R99pTOT. Additionally, tropical occupied the rank first position, followed by desert, sub-tropical, temperate and alpine.

Table 4.3: Rainfall Pbias (%), PCC, NRMSE, and TSS of EnseMean model with respect to observational dataset (ENACTS) for five AEZs over Ethiopia during 1981-2014 for JJAS season.

Indices	Continuous statistical metrics	AEZs				
		Alpine	Desert	Sub-tropical	Temperate	Tropical
CDD	PCC	0.27	0.82	0.80	0.59	0.85
	PBIAS	-15.20	-14.80	-19.40	-18.00	-11.00
	NRMSE	5.66	20.97	10.17	6.78	18.49
	TSS	0.32	0.82	0.62	0.33	0.86
	Rank based on TSS	5	1	3	4	2
CWD	PCC	0.25	0.83	0.75	0.06	0.90
	PBIAS	139.70	396.60	262.00	150.00	257.90
	NRMSE	22.29	10.97	35.43	25.28	23.90
	TSS	0.36	0.15	0.19	0.16	0.23
	RANK based on TSS	1	5	3	4	2
PRCPTOT	PCC	0.54	0.92	0.82	0.13	0.92
	PBIAS	-29.40	94.50	6.00	-15.20	-2.00
	NRMSE	319.28	108.81	225.66	261.51	160.00

Indices	Continuous statistical metrics	AEZs				
		Alpine	Desert	Sub-tropical	Temperate	Tropical
	TSS	0.22	0.92	0.82	0.27	0.93
	Rank based on TSS	5	2	3	4	1
R95pTOT	PCC	0.39	0.93	0.80	0.17	0.93
	PBIAS	-28.70	44.40	-10.70	-27.00	-21.00
	NRMSE	41.03	14.48	32.59	43.64	27.68
	TSS	0.19	0.92	0.80	0.28	0.91
	Rank based on TSS	5	1	3	4	2
R99pTOT	PCC	0.20	0.79	0.46	0.10	0.83
	PBIAS	-46.00	-5.10	-13.60	-31.50	-28.90
	NRMSE	22.63	6.89	16.46	17.17	13.17
	TSS	0.14	0.76	0.50	0.20	0.82
	Rank based on TSS	5	2	3	4	1
Rx1day	PCC	0.56	0.76	0.50	0.02	0.83
	PBIAS	-52.60	-25.80	-38.60	-45.60	-47.40
	NRMSE	24.80	6.24	16.27	19.35	15.91
	TSS	0.07	0.58	0.49	0.20	0.76
	Rank based on TSS	5	2	3	4	1
Rx5day	PCC	0.51	0.91	0.56	0.31	0.87
	PBIAS	-48.30	0.40	-18.80	-27.80	-27.50
	NRMSE	55.43	12.23	32.45	44.53	24.96
	TSS	0.49	0.91	0.60	0.11	0.87
	Rank based on TSS	4	1	3	5	2
R10	PCC	0.31	0.94	0.76	0.02	0.91
	PBIAS	-42.80	63.40	3.10	-30.10	-11.00
	NRMSE	16.27	2.69	12.47	13.69	7.57
	TSS	0.16	0.89	0.71	0.23	0.90
	Rank based on TSS	5	2	3	4	1
R20	PCC	0.44	0.97	0.63	0.16	0.85
	PBIAS	-88.70	-61.90	-59.10	-81.10	-65.40
	NRMSE	10.56	0.90	6.33	7.38	5.31
	TSS	0.01	0.38	0.50	0.07	0.53
	Rank based on TSS	5	3	2	4	1
SDII	PCC	0.76	0.53	0.27	0.03	0.55
	PBIAS	-46.50	-41.80	-35.90	-42.20	-51.50
	NRMSE	5.97	3.26	4.85	5.12	6.01
	TSS	0.27	0.45	0.40	0.21	0.59
	Rank based on TSS	4	2	3	5	1

Table 4.7 presents the statistical performance metrics attained by EnseMean for simulating ten extreme indices with respect to the observational dataset (ENACTS) over five AEZs from 1981 to 2014 for the FMAM season. The Pbias values for the alpine, temperate, and tropical AEZs indicate that EnseMean underestimated all ten extreme indices, except for CWD and Rx5day. On the other hand, EnseMean overestimated all ten extreme indices, except for CDD and SDII, in the desert and sub-tropical AEZs. Overall, EnseMean overestimated CWD, R95pTOT, and Rx5day across all five AEZs, while it underestimated CDD and SDII. Moreover, the Pbias of EnseMean was largest for the CWD compared to other indices across the five AEZs, with a slight underestimation for CDD. The NRMSE values for all zones were highest for CWD. Similar to the JJAS season, EnseMean revealed a positive correlation for all extreme indices across the five AEZs during the FMAM season. PCC was greater than 0.7 for CDD, CWD, PRCPTOT, R95pTOT, and R10 for desert and tropical AEZs, with lower values for the alpine AEZ. Similar to the JJAS season, ranks were assigned for each of the five AEZs based on the TSS values for simulating each of the extreme indices during the FMAM season (Table 4.7). Generally, the TSS values for EnseMean were lower when simulating SDII, and higher when simulating PRCPTOT. EnseMean showed better performance over the desert and tropical AZEs, with lower performance over the alpine and temperate.

Table 4.4: Rainfall bias, PCC, NRMSE, and TSS of EnseMean model with respect to observational dataset (ENACTS) for five AEZs over Ethiopia during 1981-2014 for FMAM season.

Indices	Continuous statistical metrics	AEZs				
		Alpine	Desert	Sub-tropical	Temperate	Tropical
CDD	PCC	0.23	0.71	0.65	0.41	0.80
	PBIAS	-2.70	-14.00	-24.50	-16.10	-10.50
	NRMSE	4.77	11.20	15.39	9.28	9.65
	TSS	0.24	0.58	0.38	0.30	0.70
	Rank based on TSS	5	2	3	4	1
CWD	PCC	0.53	0.81	0.80	0.86	0.70
	PBIAS	109.10	151.50	144.10	122.40	140.70
	NRMSE	68.98	54.61	94.26	83.29	73.76
	TSS	0.58	0.35	0.36	0.46	0.47
	Rank based on TSS	1	5	4	3	2
PRCPTOT	PCC	0.44	0.83	0.76	0.80	0.80
	PBIAS	-3.00	35.40	17.60	9.30	-5.80

Indices	Continuous statistical metrics	AEZs				
		Alpine	Desert	Sub-tropical	Temperate	Tropical
	NRMSE	5.23	5.53	7.97	7.48	7.26
	TSS	0.22	0.84	0.75	0.66	0.69
	Rank based on TSS	5	1	2	4	3
R95pTOT	PCC	0.41	0.72	0.78	0.74	0.71
	PBIAS	-16.90	52.80	44.70	39.00	22.30
	NRMSE	18.09	18.68	23.66	23.26	17.07
	TSS	0.28	0.64	0.79	0.73	0.76
	Rank based on TSS	5	4	1	3	2
R99pTOT	PCC	0.30	0.68	0.68	0.38	0.39
	PBIAS	-13.10	11.90	0.90	-3.10	-9.60
	NRMSE	10.35	7.57	6.22	7.35	9.06
	TSS	0.16	0.68	0.63	0.40	0.64
	Rank based on TSS	5	1	3	4	2
Rx1day	PCC	0.30	0.62	0.68	0.41	0.38
	PBIAS	-12.10	14.40	2.90	-0.40	-6.30
	NRMSE	10.15	8.11	6.22	7.38	8.64
	TSS	0.17	0.65	0.64	0.42	0.64
	Rank based on TSS	5	1	2	4	2
Rx5day	PCC	0.29	0.78	0.69	0.57	0.61
	PBIAS	7.60	34.40	24.70	17.80	4.70
	NRMSE	18.19	17.20	21.40	19.75	15.52
	TSS	0.20	0.79	0.69	0.54	0.71
	Rank based on TSS	5	1	3	4	2
R10	PCC	0.58	0.75	0.75	0.80	0.79
	PBIAS	-9.40	4.10	6.10	-7.30	-25.80
	NRMSE	2.45	1.81	3.49	3.81	3.85
	TSS	0.20	0.70	0.71	0.58	0.59
	Rank based on TSS	5	1	2	4	3
R20	PCC	0.15	0.37	0.61	0.62	0.69
	PBIAS	-31.80	5.60	-11.30	-21.40	-40.60
	NRMSE	2.11	0.77	1.79	1.75	2.17
	TSS	0.14	0.32	0.45	0.35	0.38
	Rank based on TSS	5	4	1	3	2
SDII	PCC	0.27	0.23	0.19	0.41	0.06
	PBIAS	-36.50	-39.80	-35.60	-37.90	-45.90
	NRMSE	4.44	4.60	4.31	4.41	6.18
	TSS	0.07	0.09	0.19	0.25	0.05
	Rank based on TSS	4	3	2	1	5

4.3.6 Trend analysis of extreme indices

Figure 4.15 and 4.16 summarize the trend analysis of seven extreme climate indices in the form of box-and-whisker plots over the period from 1981 to 2014 for the JJAS and FMAM seasons, respectively. As shown by the median values of the interquartile range for the JJAS season (Figure 5.15), the ENACTS dataset, EnseMean, and EnseMean_ALL revealed an increasing trend for PRCPTOT, Rx5day, R10, and SDII, while indicating a decreasing trends for CWD. For CDD, EnseMean and EnseMean_ALL show an increasing trend, whereas ENACTS displays a decreasing trend. Among the top-ranking models, all except NorESM2-LM show increasing trends for Rx5day, PRCPTOT, and SDII indices. Models such as E3SM-1-0, IPSL-CM6A-INCA, and NorESM2-MM exhibit an increasing trend for R10, while CESM2-WACCM-FV2, CMCC-ESM2, NESM3, and NorESM2-MM show decreasing trends. Additionally, ENACTS stands out with a larger intermodal range in simulating CWD, Rx5day, R10, and SDII compared with other models.

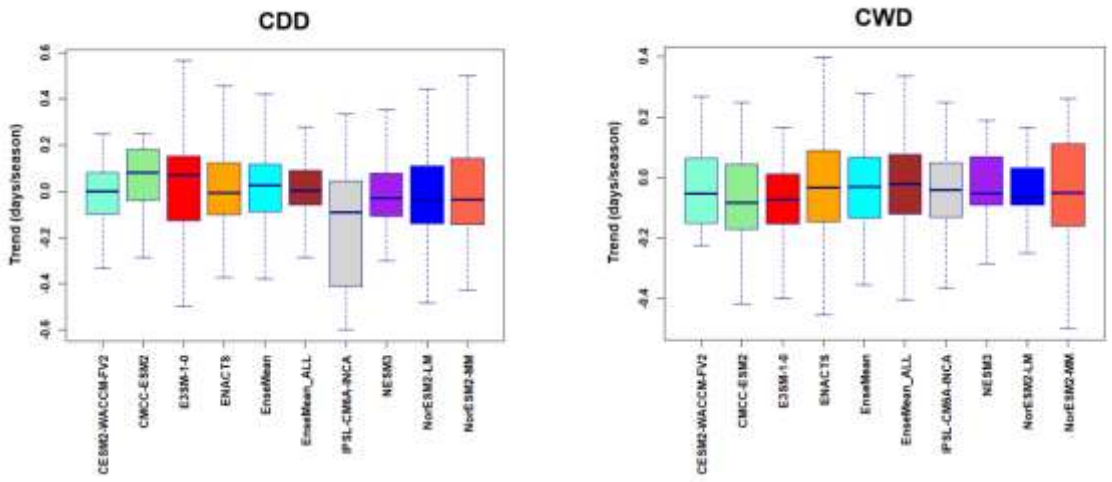

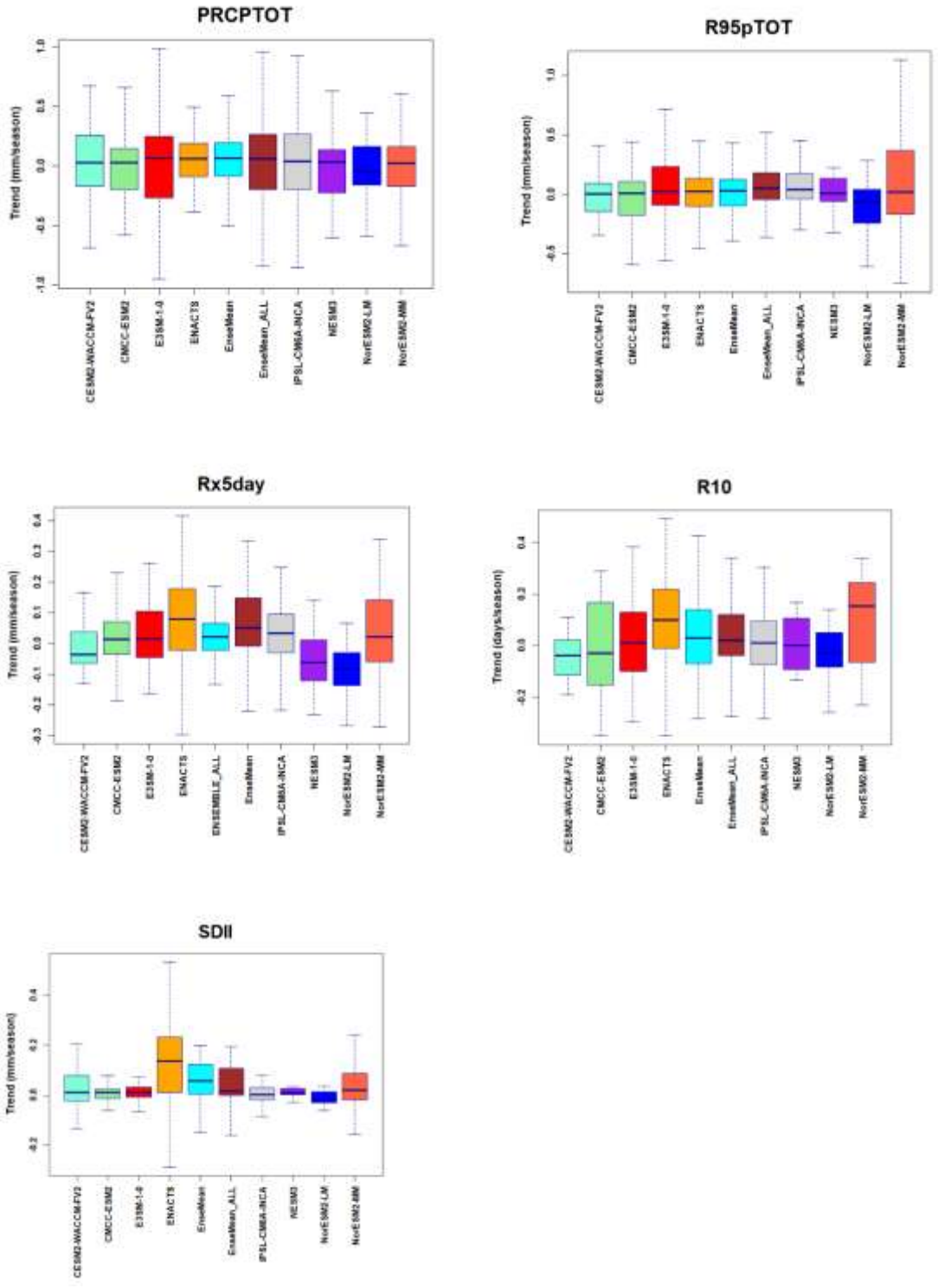

Figure 4.15: Box-and-whisker plots of trends for the ENACTS, top-ranking models, EnseMean, and EnseMean_ALL in simulating extreme precipitation indices (CDD, CWD, PRCPTOT, R95pTOT, Rx5day, R10, SDII) for the JJAS season over the period 1981–2014. The boxes

represent the interquartile range (spanning the 25th to 75th percentiles), with the thick black line inside each box indicating the median. The whiskers show the total intermodel range.

For the FMAM season (Figure 4.16), ENACTS and EnseMean show more alignment in the direction of trends across most extreme indices relative to ENACTS than EnseMean_ALL. Both ENACTS and EnseMean exhibit decreasing trends for CWD, PRCPTOT, R95pTOT, Rx5day, and R10. In contrast, EnseMean_ALL shows decreasing trends for CWD, PRCPTOT, and R95pTOT but reveals increasing trends for CDD, Rx5day, R10, and SDII. Notably, models such as BCC-ESM1-MR, GFDL-CM4, and GFDL-ESM4 display increasing trends for PRCPTOT, R95pTOT, and Rx5day. Furthermore, ENACTS, EnseMean, EnseMean_ALL, and all seven top-ranking models exhibit increasing trends for CDD and SDII. As in the JJAS season, ENACTS shows a greater intermodal range in simulating R10 and SDII compared to the other models.

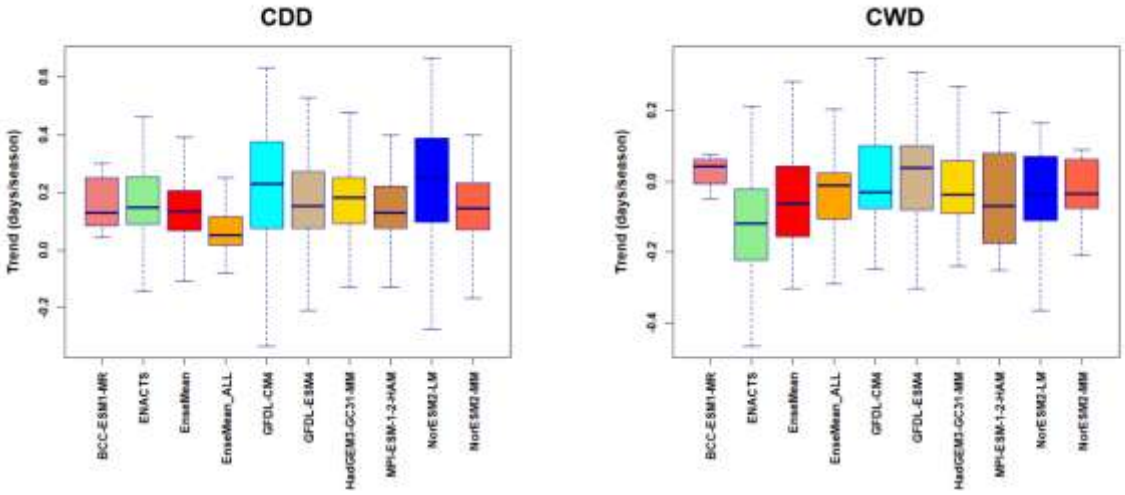

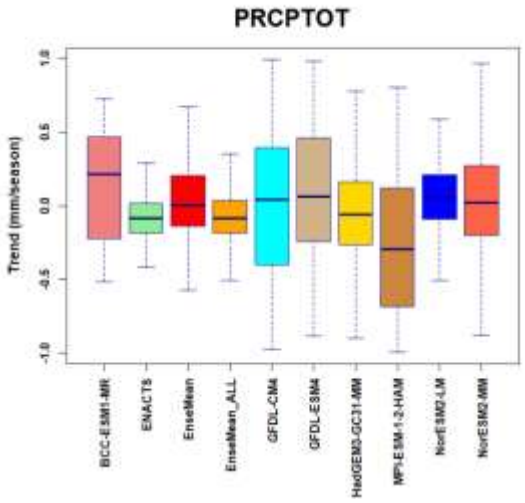
PRCPTOT
Trend (mm/season)
BCC-ESM1-MR
ENACTS
EnseMean
EnseMean_ALL
GFDL-CM4
GFDL-ESM4
HadGEM3-GC31-MM
MPI-ESM-1-2-HAM
NorESM2-LM
NorESM2-MM

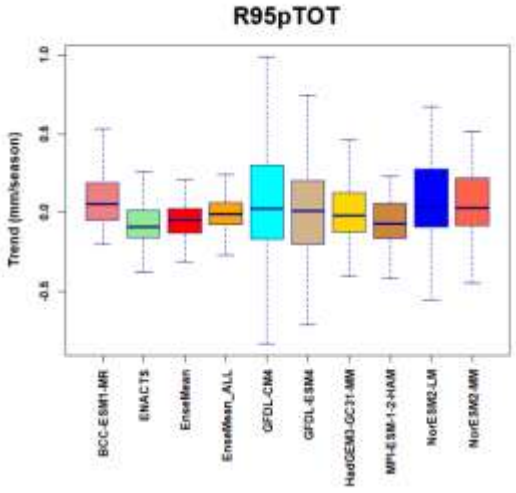
R95pTOT
Trend (mm/season)
BCC-ESM1-MR
ENACTS
EnseMean
EnseMean_ALL
GFDL-CM4
GFDL-ESM4
HadGEM3-GC31-MM
MPI-ESM-1-2-HAM
NorESM2-LM
NorESM2-MM

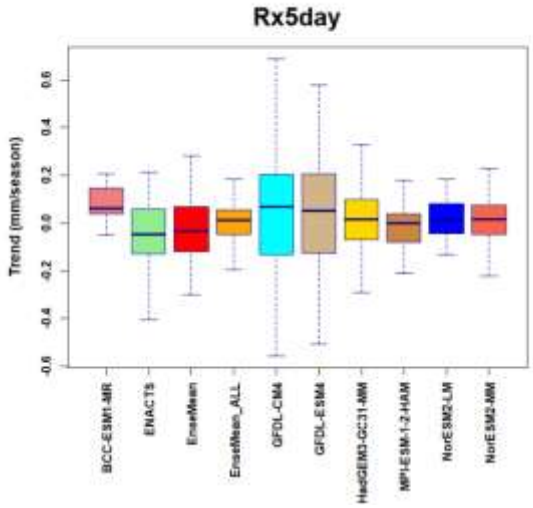
Rx5day
Trend (mm/season)
BCC-ESM1-MR
ENACTS
EnseMean
EnseMean_ALL
GFDL-CM4
GFDL-ESM4
HadGEM3-GC31-MM
MPI-ESM-1-2-HAM
NorESM2-LM
NorESM2-MM

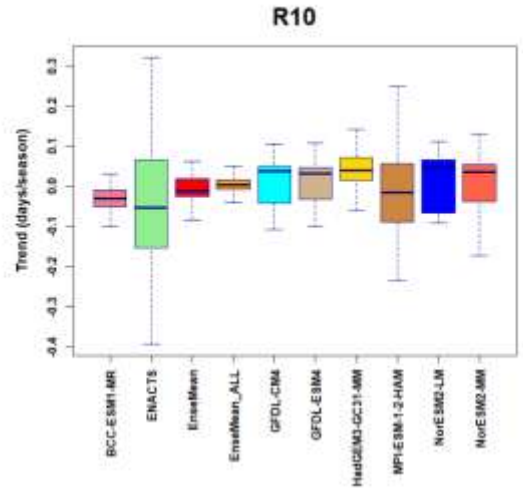
R10
Trend (days/season)
BCC-ESM1-MR
ENACTS
EnseMean
EnseMean_ALL
GFDL-CM4
GFDL-ESM4
HadGEM3-GC31-MM
MPI-ESM-1-2-HAM
NorESM2-LM
NorESM2-MM

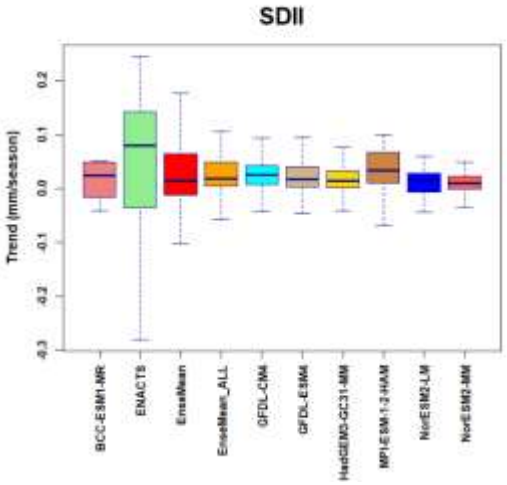
SDII
Trend (mm/season)
BCC-ESM1-MR
ENACTS
EnseMean
EnseMean_ALL
GFDL-CM4
GFDL-ESM4
HadGEM3-GC31-MM
MPI-ESM-1-2-HAM
NorESM2-LM
NorESM2-MM

Figure 4.16: Box-and-whisker plots of trends for the ENACTS, top-ranking models, EnseMean, and EnseMean_ALL in simulating extreme precipitation indices (CDD, CWD, PRCPTOT, Rx5day, R95pTOT, R10, SDII) for FMAM season over the period 1981–2014. The boxes represent the interquartile range (from the 25th to the 75th percentiles), with the thick black line inside each box indicating the median. The whiskers show the total intermodel range.

4.4 Discussion

Most CMIP6 models showed better skill in representing the spatial pattern of extreme precipitation indices during JJAS compared to FMAM in much of the country, but mostly with higher bias. This may be related to higher rainfall variability in the FMAM season relative to the JJAS season, which is often challenging to represent in GCMs (Kamruzzaman et al., 2022). Typically, the CMIP6 models performed better in reproducing the spatial pattern and magnitude of the extreme precipitation indices over the eastern Rift Valley and lowland areas of the country including the east and southeast parts of the country relative to the western Rift Valley and highland areas, covering west, northwest and central of the country. Additionally, EnseMean in the tropical and desert AEZs performs particularly better in simulating extreme indices compared to others AZEs. Its relative performance in other AEZs indicates a decreasing ability from the sub-tropical to alpine regions. The EnseMean declining performance from the Sub-tropical to the alpine AEZs suggests challenges in regions with more intricate topography and localized climatic phenomena. The temperate and alpine AEZs have more complex terrain, characterized by pronounced elevation gradients and rain-shadow effects.

Moreover, the majority of the models were generally poor in representing the magnitudes of extreme precipitation indices of the observational dataset across the country. The most significant bias of the extreme indices occurred over the high rainfall and highland areas of the country including the west, and northwest of the country. The high overestimation of CWD essentially displays the influence of topography on the spatial distribution of the indices over the study area. This noticeable bias may be due to greater variability in extremes, which is associated with topographic diversity, relief features, and large-scale climate variables (Gebrechorkos et al., 2019; Fer et al., 2017). Seasonal rainfall in Ethiopia is highly complex

and influenced mainly by the bi-annual migration of the Intertropical Convergence Zone (ITCZ), the El Ni˜ no–Southern Oscillation (ENSO), and the complex topography of the country, which results in strong inter-annual variability of rainfall across the country (Nicholson, 2017; Fazzini et al., 2015). Although the resolution of CMIP6 models has improved compared to CMIP5, the impact of topography has not yet been fully addressed in these models (Eyring et al., 2016). Most of the models fail to simulate accurately the ENSO characteristics (Beobide-Arsuaga et al., 2021) and the double-ITCZ (Tian and Dong, 2020). However, there are some modest changes in the basic characteristics of the IOD and ENSO from CMIP5 to CMIP6. Firstly, there is a slight shift in the seasonal cycle of IOD toward an earlier peak in September in CMIP6, compared with November in CMIP5. Secondly, inter-model spread in the frequency of ENSO and the IOD has reduced in CMIP6 relative to CMIP5 (McKenna et al., 2020).

A consistent bias was observed across most CMIP6 models, with an overestimation of CWD and an underestimation of most other indices (CDD, R10, R20, Rx5day, Rx1day, R95pTOT, R99pTOT, SDII, and PRCPTOT). Underestimation in most of extreme indices could indicate that the model is not fully capturing the frequency and intensity of extreme precipitation, which is critical for assessing flood risks and other hydrological impacts in a changing climate. Therefore, most models suggested that it rains too frequently but lower amount relative to the observational dataset. This may be due to the generally higher spatial resolution in CMIP6 models, thereby simulating light precipitation too frequently at a much finer scale by the high-resolution models. This indicates that drizzle biases in CMIP6 models over the study area have not been significantly improved relative to CMIP5 models (Dyer et al., 2022). Overall, a majority of the models showed higher skill scores in simulating most of the indices (CDD, Rx5day, Rx1day, R10, R95pTOT, and PRCPTOT) but lower scores for CWD and SDII indices as biases in CWD and SDII were generally larger than biases in the other indices. Nevertheless, there were significant magnitude discrepancies with the observational dataset across most models and seasons over the study area. It is more likely that the bias stems from a poor representation of the magnitude rather than patterns. Maraun et al. (2017) argue that bias correction operates under the assumption that the model delivers both skillful input for correction and a plausible representation of climate change. However, bias correction is not capable of addressing significant model errors. Our results aligne with the findings from

recent studies of CMIP6 models over East Africa, including Ethiopia (Akinsanola et al., 2021; Ayugi et al., 2021), West Africa (Klutse et al., 2021), and the Contiguous US regions (Srivastava et al., 2020).

Some studies indicate that the skill of GCMs for simulating observed rainfall over Ethiopia can be improved by increasing horizontal resolution (Li et al., 2016; Rettie et al., 2023). However, the majority of high-resolution CMIP6 models, including CNRM-CM6-1-HR, EC-Earth3, EC-Earth3, AWI-ESM-1-1-LR, and EC-Earth3-Veg showed lower performance in simulating extreme event indices of the observed dataset as compared to medium and low-resolution models such as NorESM2-MM, GFDL-CM4, NorESM2-LM, and GFDL-ESM4. Thus, the performance of CMIP6 models in representing the spatial patterns of extreme precipitation indices is largely independent of horizontal resolution across over the study area. Simply increasing the model's horizontal resolution may not adequately mitigate the biases, partially due to the inability of high-resolution global models to resolve convective processes in the tropics including East Africa (Akinsanola et al., 2021). Similar results have been observed in a recent study based on CMIP6 models over East Africa including Ethiopia (Akinsanola et al., 2021), Western North Pacific and East Asia (Chen et al., 2021), United States (Akinsanola et al., 2020) and regional climate models over the contiguous United States (Gibson et al., 2019). They found that the challenge of simulating extreme precipitation indices was primarily due to model parameterization, convective parametrization, and cloud microphysics.

NorESM2-LM and NorESM2-MM are the only models that showed better performance in both seasons (JJAS and FMAM) in representing the extreme indices of the observational dataset. Other models might have been accurate in one season but not the other, or failed to capture extremes properly. Likely reasons include Better representation of physical processes like convection, land–atmosphere interaction, or monsoon dynamics. Higher fidelity in capturing regional climate variability. Appropriate parameterizations for extreme events. The superior performance of NorESM2-LM and NorESM2-MM is likely due to their better representation of key physical processes, such as convection, land–atmosphere interactions, and monsoon dynamics, higher fidelity in simulating regional climate variability, and the use of appropriate parameterizations for extreme events (Zhang et. al., 2025.

However, the ensemble mean of the top-ranking models (EnseMean) showed a better representation of extreme precipitation compared to individual models and ensembles of all 47 models (EnseMean_ALL) when considering all metrics and seasons as it reduces biases in the different model members (Akinsanola and Zhou, 2019; Pour et al., 2018). EnseMean showed lower spatial variability in simulating most of extreme indices (CDD, PRCPTOT, R10, R20, R95pTOT and Rx5day) with higher PCC and lower RMSE and SD relative to EnseMean_ALL. The EnseMean can create a more complete representation of the observed data by combining the strengths of top-ranking models. Thus, EnseMean can improve the accuracy of climate models, as well as to provide a more accurate representation of the spatial patterns of extreme precipitation relative to EnseMean_ALL.

Biases and uncertainties in climate projections can also be reduced by generating ensembles based on better-performing GCMs identified through a ranking procedure rather than all of them (Hussain et al., 2020; Ahmed et al., 2020; Salman et al., 2020; Ali et al., 2023). Traditionally, in multimodel ensembles, each model is assigned the same weight, a practice known as "model democracy" (Eyring et al., 2016). Averaging the simulations is assumed to reduce the effect of internal variability, thereby highlighting the externally forced response (Knutti et al., 2010). However, the models are not independent; the ensemble includes model variants, and models share components and parameterizations. Recent literature has proposed that models should be weighted, but deriving an appropriate evaluation criterion or skill score remains raises challenges. For example, the Climate model Weighting by Independence and Performance (ClimWIP) applies a modelweighting approach based on historical performance, using multiple diagnostics, and consideration of model interdependence (Banner et al., 2020). Additionally, CMIP6 contains several "hot" models, which have a higher sensitivity to greenhouse gas forcing than is likely, based on physical evidence. Cannon (2024) recommended that regional assessments should weight or constrain the ensemble to moderate the influence of hot models. Moreover, emergent constraints can be used to reduce the spread in future climate projections. This approach considers the ensemble behaviors to identify an emergent relationship between a present-day/historical attribute for which observation data exist and a second attribute of the evolving climate system (Eyring et al., 2016; Huntingford et al., 2023). Moreover, weighting methods based on model structure can more effectively capture interdependencies among models compared to methods that rely solely on model

output. They suggest that family weighting, or a similar technique that selects a number of "independent" model branches based on the model code genealogy, could serve as a valuable and easily implementable method for weighting in MME studies (Kuma et al., 2023).

Evaluating trends at the grid-box scale is less effective as a performance indicator because small-scale trends are highly uncertain. This uncertainty arises because local trends are more susceptible to natural variability, making the spatial distribution of trends less useful for model evaluation (Li et al., 2016). The trend analysis reveals both seasonal and dataset-specific variations in the trends of extreme climate indices. During the JJAS season, the consistent upward trends in precipitation-related indices (e.g., PRCPTOT and Rx5day) suggest a potential intensification of heavy precipitation events. FMAM has an increase in CDD, SDII, and a decrease in CWD. Overall, during the FMAM season, the observed and models data indicates a tendency towards drier conditions with less frequent but potentially more intense rainfall events. This combination suggests an increase in dry spells interspersed with heavier rainfall events when they do occur. This increase in CDD, SDII and decrease of CWD during FMAM suggests a growing risk of prolonged dry periods, which could impact agricultural cycles and water availability. Rainfall during the long rainy season (March-April-May, MAM) is significantly reduced across East Africa (Liebmann et al., 2014; Lyon and DeWitt, 2012). The rapid warming of the Indian Ocean over the past 60 years, which has extended the tropical warm pool westward and shifted the western ascending branch of the Walker circulation, has been identified as a driver for the decline in MAM rainfall for East Africa, including Ethiopia (Williams and Funk, 2011). Moreover, the negative trends in MAM rainfall over East Africa have been linked to an enhanced east-west SST gradient in the western Pacific, caused by a warming process near Indonesia (Liebmann et al., 2014). Generally, despite declining historical trends, climate models project an increase covering East Africa including Ethiopia (Gebrechorkos et al., 2023). This phenomenon, known as the "East African Climate Paradox," including Ethiopia, highlights a complex interplay between climate projections and historical data (Souverijns et al., 2016; Nicholson, 2017).

4.5 Conclusion

The Ethiopian economy depends largely on rain-fed agriculture; therefore, it is crucial to adapt to climatic extreme precipitation events. This study has evaluated the performance of 45 CMIP6 models in simulating spatial and temporal characteristics of extreme precipitation indices for five AEZs over Ethiopia. In the context of the results, this research contributed to three key issues. First, it evaluates the performance of many models (45) against the most reliable gridded dataset of Enhancing National Climate Services (ENACTS) produced specifically for Ethiopia. Second, ten model indices are evaluated across five AEZs in Ethiopia. Third, this study also compares the ensemble of the top- ranking models with the ensemble of all models to assess the relative discrepancies between them. The findings revealed that a majority of the models found it challenging in reproducing the magnitudes of the observed extreme events, with underestimating over high rainfall and highland areas in the western half of the country, specifically west and northwest of tropical, sub-tropical, temperate and alpine of AEZs over the country. Most CMIP6 models could not adequately represent the diverse topography and relief features of the country over the above mentioned zones. However, extreme precipitation is better in parts of the eastern half of the desert and tropical AEZs of the country.

CESM2-WACCM-FV2, NESM3, NorESM2-LM, CMCC-ESM2, IPSL- CM6A-INCA, E3SM-1-0 and NorESM2-MM are regarded as the most skillful CMIP6 models for reproducing the ten eight extreme indices during JJAS season. NorESM2-MM, GFDL-CM4, HadGEM3-GC31-MM, Nor ESM2-LM, BCC-ESM1-MR, GFDL-ESM4, and MPI-ESM-1-2-HAM have been identified as the best performing CMIP6 models in reproducing the FMAM extreme rainfall indices. Moreover, the EnseMean of the top- ranking models showed better performance in capturing the extreme indices of the observational dataset relative to individual models and ensemble of all models.

In our current analysis, we have focused primarily on statistical performance metrics for evaluating 45 CMIP6 models' efficacy. The results provide useful informationextremes for national adaptation plans, while planning for adaptation to projected climate change. It is useful for identifying suitable CMIP6 models for future climate impact assessments for better adaptation and mitigation interventions in the country. However, future evaluations should incorporate the integration of diverse process-based emergent constraints with model-weighting approaches that

consider both model performance and interdependence, as this combination can yield more robust multimodel insights for a wide range of critical societal and environmental applications (Eyring et al. (2016)). Further in-depth studies including evaluation of teleconnections (ENSO or IOD), the influences of higher spatial resolution and improved model parameterization are needed to identify what modeling factors have contributed to the sources of systematic biases in extreme indices, particularly over the highland area.

Chapter 5. Historical Trend and Future Projection of Extreme Seasonal Precipitation over Ethiopia, East Africa

Abstract

East Africa is highly vulnerable to severe climate extremes due to its limited adaptive capacity and strong dependence on agriculture. Ethiopia, in East Africa, relies heavily on rainfall for livelihoods and productivity but faces significant challenges from droughts and floods. Thus, understanding historical climate trends and projecting precipitation extremes is crucial. This study examines historical (1981–2010) and future (2050s and 2080s) trends in extreme precipitation during JJAS (June–September) and FMAM (February–May) seasons using ten extreme indices and bias-corrected CMIP6 models under SSP245 and SSP585 scenarios. The ensemble means of bias-corrected top-ranking CMIP6 models is used to assess future extreme precipitation.

Results indicate increased PRCPTOT across much of Ethiopia in the future, with significant rises in R10, R20, R95p, R99p, and SDII in the northwest, west, and southwest parts of the country during JJAS. In FMAM, the north and northwest may see increases in PRCPTOT, despite historical declines. The northeast regions, particularly the Awash basin, are projected to experience more intense extreme precipitation events during the JJAS season, while a decrease is expected during the FMAM season. These changes may indicate a potential seasonal shift and extreme weather in these areas, particularly in the north (Tekeze basin), and the northeast parts of the country (Awash basin). However, uncertainty in future precipitation projections remains a major challenge, as demonstrated by the spread of results from top-performing models and the ensemble mean (EseMean) under SSP245 and SSP585 scenarios. The findings emphasize the importance of developing adaptive, flexible strategies that can effectively respond to a range of potential climate outcomes, rather than depending on any single projection. Recognizing and incorporating uncertainty into climate policy and planning is therefore essential for building long-term resilience. These insights are vital for guiding climate adaptation, resource allocation, and resilience planning in Ethiopia.

Key Words:

Extreme indices, historical trends, climate projection, CMIP6 models, Ethiopia, East Africa

5.1 Introduction

Climate change is expected to increase the frequency and intensity of both floods and droughts, leading to significant societal impacts such as property damage, injury, poverty, loss of life, and a decline in biodiversity (Zhang and Zhou 2020; IPCC, 2022). Extreme climate events have a more detrimental effect on the natural environment compared to average climate variability (Peterson & Manton, 2008; Tierney et al., 2015). East Africa is among the regions most vulnerable to current and projected climate, largely due to its low adaptive capacity, heavy reliance of economies and livelihoods on rain-fed systems, and the limited technological and resource capacity to adapt to climate-induced risks (Omondi et al., 2014; Endris et al., 2013). Extreme events in East Africa result in significant losses, livelihood disruption, and property destruction (Lyon and Dewitt 2012; Opiyo et al., 2015). These impacts necessitate response measures that cost millions of dollars annually (Martey et al., 2020).

Ethiopia, in East Africa, is especially vulnerable to climate change, experiencing extreme precipitation events (Viste et al., 2013; Maidment et al., 2015). Ethiopia has experienced eight major droughts over the past 15 years which have had severe negative impacts on the economy and livelihoods (World Bank, 2019). Climate change is also increasing flood risks in several basins, particularly in the Awash and Wabi-Shebelle Basins, as well as parts of the Great Rift Valley (World Bank, 2018). Floods caused 3,000 deaths, displaced 1.3 million people, and resulted in the loss of 250,000 cattle and half a million hectares of cropland from 1991 to 2019 (World Bank, 2019). Thus, the government of Ethiopia is currently implementing the National Adaptation Plan (NAP-ETH) as part of its broader Climate-Resilient Green Economy (CRGE) strategy to mitigate the impacts of climate change, including extreme events, and to foster economic growth (FDRE, 2019). The National Adaptation Plan (NAP-ETH) further elaborates on how Ethiopia will adapt to climate change and the country aims to actively and continuously incorporate climate change adaptation into its development policies and strategies. Thus, it is crucial to provide information on historical trends and expected future changes in precipitation extremes that can be used by governments for planning and designing appropriate adaptation strategies over the country.

Climate projections from General Circulation Models (GCMs) are essential for assessing the impacts of climate change and developing adaptation strategies at both global and regional scales to mitigate these effects (Eyring et al., 2016; Shiogama et al., 2021;Wainwright et al., 2019; Stouffer et al., 2017). Thus, a number of studies explore the future climate projection based on previous CMIP5 and RCM models (Daba & You, 2020; Fenta Mekonnen & Disse, 2018; Worku et al., 2020; Orkodjo et al., 2022; Musie et al., 2021; Gadissa et al., 2019; Daniel & Abate, 2022). Although CMIP5 models have generally performed well, they exhibit substantial biases in simulating seasonal and annual rainfall over Ethiopia (Jury, 2015; Li et al., 2016; Dyer et al., 2020).

Recently, a new set of coordinated climate experiments has been conducted as part of phase 6 of the Coupled Model Intercomparison Project (CMIP6). These experiments offer higher spatial resolution, incorporate new physical processes, feature improved parameterization schemes, and include larger ensemble sizes compared to CMIP5 (Eyring et al., 2016; Kim et al., 2020). CMIP6 uses the new scenarios, named Shared Socioeconomic Pathways (SSP), which are combined with the Representative Concentration Pathways (RCP) of CMIP5 (Eyring et al., 2016). Several CMIP6-based studies have investigated future mean precipitation over Ethiopia (Alaminie et al., 2021**;** Belay et al., 2024**;** Gebresellase et al., 2022**;** Desta & Belayneh, 2023**;** Feyissa et al., 2023**;** Gebrechorkos et al., 2023**;** Dyer et al., 2022**;** Fetene et al., 2022**;** Rettie et al., 2023). However, only a few studies have assessed the projections of extreme rainfall indices at the catchment scale (Bulti et al., 2021; Feyissa et al., 2023; Teshome et al., 2022). Thus, there is remains a lack of information regarding the projections of precipitation extremes under the new CMIP6 scenarios at a national level.

Therefore, there is a knowledge gap in previous studies regarding the understanding of extreme rainfall trends using high-resolution climate data and the projections of precipitation extremes under the new CMIP6 scenarios for Ethiopia (at a national level). To address the existing gap in the previous study, this research aims to examine the spatial and temporal variability of extreme precipitation in Ethiopia over the recent decades (1981-2010) and the next several decades (2041-2100). Thus, the objective of this study is to provide a comprehensive understanding of the climate trends in Ethiopia by integrating historical observations with future projections. By integrating historical observations with future projections, we aim to provide a holistic perspective on the

evolving climate dynamics in the country. Our comprehensive analysis utilizes high-resolution gridded observed data from Enhancing National Climate Services (ENACTS) to examine historical trend, with a spatial resolution of 4 km. This study is the first to use the top-ranking CMIP6 models to generate ensembles for future projections during the JJAS and FMAM seasons across Ethiopia. Moreover, the Ethiopian government launched a 10-year national plan titled "The Pathway to Prosperity" (2021–2030) (Tiruye et al., 2021), considering all sectors, including water, energy, and food. Hence, our findings focus on the non-studied years starting from 2041.

The findings of this study could serve as a valuable resource for the policy makers of East Africa countries in developing environmental and climate change plans from 2041 onward. Additionally, the research enhances understanding of climate variability and change in East Africa, providing critical insights for policymakers, researchers, and stakeholders on the risks of extreme precipitation and the importance of implementing effective adaptation strategies.

5.2 Data and Methodology

5.2.1 Study area

Ethiopia is situated between latitudes 3°N and 15°N and longitudes 33°E and 48°E (Figure 5.1a). The temporal distribution and amount of rainfall vary greatly across time and space (Gummadi et al., 2018; Van den Hende et al., 2021). Ethiopia has 12 major river basins that are vital to the country's water resources and play a key role in its economy, agriculture, and hydropower generation. These river basins vary in size, water volume, and geographical location, influencing the distribution of water resources across the country (Berhanu et al., 2014).

The highland regions (>1500 m a.s.l.) in the central, northwest, and southwestern parts of the country are known for receiving high rainfall and experiencing high humidity, whereas the lowland areas in the northeast, east, and southeast (<1500 m a.s.l.) receive lower rainfall and have a semiarid to arid agro-ecology (Figure 5.1a and b). Ethiopia's annual rainfall pattern is divided into three main seasons (Diro et al., 2011). The primary rainy season, Kiremt, spans from June to September and accounts for 50–80% of the country's total annual rainfall. The short rainy season, Belg, occurs from February to May, less rainfall in the central, northern, and southern regions. The Bega season, from October to December, is typically dry (Gizaw et al., 2017; Zegeye, 2018).

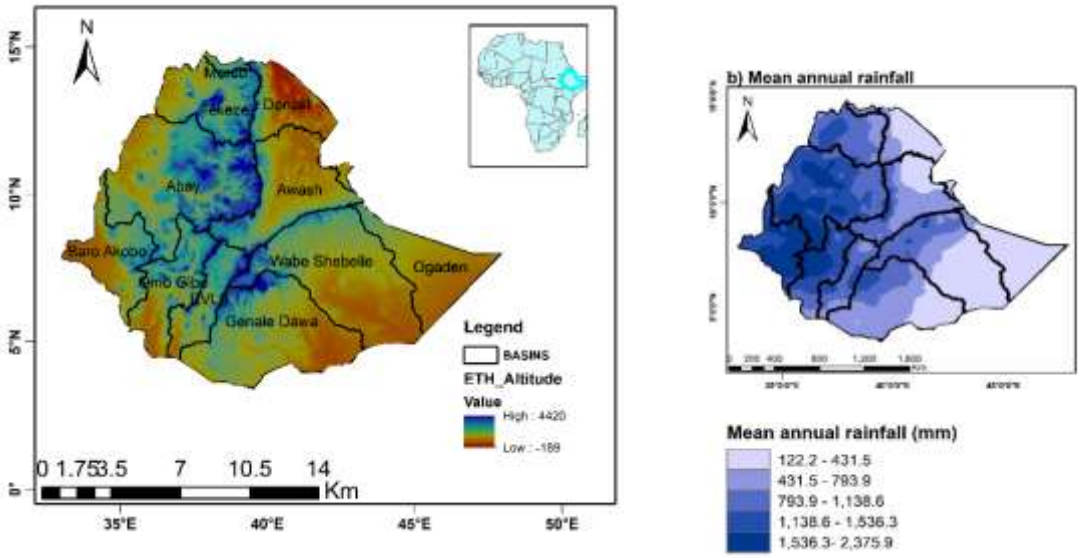

Figure 5.1**:** Location map of Ethiopia and its 12 river basins (a) and mean annual rainfall (b)

5.2.2 Data

High-resolution gridded data, such as the ENACTS dataset, are critical for understanding rainfall distribution in a data-scarce region like Ethiopia, where meteorological stations are sparse and not functioning. The ENACTS dataset is a hybrid combination of observed station data from Ethiopia's national network, managed by the National Meteorological Agency (NMA), and satellite data estimates from the US National Aeronautics and Space Administration (NASA) and the European Organization for the Exploitation of Meteorological Satellites (EUMETSAT) (Dinku et al., 2014). Satellite data were calibrated and validated using ground-based measurements to improve accuracy. The combined/hybrid dataset improves the quality of Ethiopia's national observations (Dinku, 2019). Furthermore, it contains no missing data. In this study, the ENACTS dataset, with a spatial resolution of 0.0375° × 0.0375°, used to derive observed precipitation extreme indices to analyze historical trends and assess potential future climate change. The daily precipitation ENACTS gridded dataset spanning from 1981 to 2010 was obtained from the Ethiopian Meteorological Institute (EMI).

The study used General Circulation Model (GCM) datasets from the CMIP6 project to assess changes in climate extremes. The performance of individual models varies depending on factors such as the season, extreme indices, and the choice of observed gridded datasets over East Africa

(Rettie et al., 2023; Akinsanola et al., 2021; Ayugi et al., 2021) and Ethiopia (Berhanu et al., 2023; Berhanu et al., 2025). Individual models excel at representing distinct aspects of precipitation characteristics, highlighting the need for model selection frameworks that evaluate performance across indices when generating future projections (Guputa et al., 2025). This selection process ensures that the most accurate models are used for specific seasons, thereby improving the reliability of the climate projections for the study area. Thus, in this study, different CMIP6 models were selected for season based on a comprehensive evaluation of model skill over Ethiopia, as conducted by Berhanu et al., (2023); Berhanu et al., (2025); Dyer et al., (2022) and; Alaminie et al., (2021) (Table 5.1). Selected CMIP6 models belonging to the 'r1i1p1f1' ensemble and featuring Shared Socioeconomic Pathways intermediate emission scenarios (SSP245) and high emission scenarios (SSP585) were chosen to maintain consistency across the models. The selected models were retrieved from the Earth Systems Grid Federation (ESGF; https://esgf-node.llnl.gov/projects/esgf-llnl/). In this study, we used 1981-2010 as the base period and two future time frames: the 2050s (2041-2070) and the 2080s (2071-2100).

Table 5.1: Selected models for projection of ten extreme precipitation indices for JJAS and FMAM seasons with respect to ENACTS

Parameters	JJAS	FMAM	Reference
Extreme indices	CESM2-WACCM-FV2, NESM3, NorESM2-LM, NorESM2-MM, CMCC-ESM2, IPSL-CM6A-INCA, and E3SM-1-0	NorESM2-MM, HadGEM3-GC31-MM, GFDL-CM4, NorESM2-LM, GFDL-ESM4, BCC-ESM1-MR, and MPI-ESM-1-2-HAM	(Berhanu et al., 2025, Akinsanola et al., 2021; Ayugi et al., 2021)

5.2.3 Methodology

5.2.3.1 Ensemble mean of CMIP6 models (EnseMean)

A consistent bias was observed across the majority of CMIP6 models (Berhanu et al., 2023; Akinsanola et al., 2021; Berhanu et al., 2025). Quantile mapping is a widely used bias-correction technique that helps improve the accuracy of climate model projections by aligning the statistical distribution of modeled data with observed data (Gudmundsson et al., 2012). Thus, this study employs the quantile mapping (QM) bias correction technique to minimize the biases in CMIP6 reported in recent studies over Ethiopia and also enhance the reliability of CMIP6 data in projecting extreme precipitation changes.

The Taylor skill score (TSS) was employed to evaluate the performance of both raw and bias-corrected outputs from the ensemble of top-ranked CMIP6 against the ENACTS datasets in replicating the spatial patterns of various extreme indices during the JJAS and FMAM seasons (Babaousmail et al., 2021; Ayugi et al., 2021). TSS is a comprehensive statistical measure that integrates three key metrics: The Pattern Correlation Coefficient (PCC), Root Mean Square Error (RMSE), and Standard Deviations (SD) (Taylor, 2001). PCC and TSS were calculated using Equation (5.1- 5.2).

$$\mathrm{TSS} = \frac{4(1+\mathrm{PCC})^2}{(\frac{\sigma_M}{\sigma_O}+\frac{\sigma_O}{\sigma_M})^2+(1+\mathrm{PCC_o})} \quad (5.1)$$

$$\mathrm{PCC} = \frac{\sum_{i=1}^{n}(O_i-\bar{O})(M_i-\bar{M})}{(\sigma_O*\sigma_M)} \quad (5.2)$$

Where TSS is Taylor skill score; PCC is the Pattern Correlation Coefficient between observational datasets and model outputs; σ_O and σ_M are the standard deviations of observational datasets and models respectively; n represents the number of observations; and PCC_0 is the highest achievable correlation coefficient, set at 1. M and O are model and observational datasets, respectively. The closer the value of TSS to 1, the better is the agreement between the simulation and observational datasets.

In this study, the ensemble mean of the bias-corrected top-ranking models (EnseMean) for ~~index and~~ season (as shown in Table 1) was generated to assess future extreme precipitation. Among the evaluated ensembles, the Multi-Model Ensemble (MME), MME8, and MME5 exhibited superior performance in reducing simulation uncertainty associated with downscaled GCM outputs (Guputa et al., 2025). Selective ensembling of top-performing models demonstrates superior predictive performance compared to full-model ensemble approaches (Iqbal et al., 2020; Yang et al., 2021; Patel et al., 2023; Rahman and Pekkat, 2024; Berhanu et al., 2023). Identifying optimal subsets of downscaled GCMs that accurately capture climate extremes is essential for enhancing the reliability of projections used in water resource planning and climate change adaptation strategies (Gupta and Chembolu, 2025).This approach enables a more robust and reliable projection by averaging the outputs of the best-performing models, which helps in reducing the effects of natural variability and systematic biases inherent in individual models(Akinsanola & Zhou, 2019; Pour et al., 2018).

5.2.3.2 Historical and future seasonal mean and extreme precipitation

This study employs ten extreme indices obtained from the Expert Team on Climate Change Detection and Indices (ETCCDI) to investigate patterns, trends, and future projections of extreme precipitation in Ethiopia. These indices provide a comprehensive framework for assessing various aspects of extreme precipitation events (Table 5.2). The extreme indices were computed using R-based software (RClimDex 1.1) for each grid point and season separately, namely JJAS (Kiremt) and FMAM (Belg).

Table 5.2: List of ten precipitation extreme indices used in the study (Zhang et al., 2011)

Index	Description	Definition	Unit
PRCPTOT	Total wet-day precipitation	Seasonal total precipitation during wet days	mm/season
SDII	Simple daily intensity index	Seasonal precipitation during wet days	mm/days
CDD	Consecutive dry days	Maximum number of consecutive days with precipitation <1 mm in season	Days/season
CWD	Consecutive wet days	Maximum number of consecutive days with precipitation >1 mm in season	Days/season
R10	Heavy precipitation days	Seasonal number of days with precipitation ≥10 mm	Days/season
R20	Very heavy precipitation days	Seasonal number of days with precipitation ≥20 mm	Days/season
R95pTOT	Very wet days	Seasonal total precipitation exceeding the 95th percentile	mm/season
R99pTOT	Extremely wet days	Seasonal total precipitation exceeding the 99th percentile	mm/season
Rx5day	Maximum consecutive five-day precipitation	Seasonal maximum 5-day precipitation amount	mm/season
Rx1day	Maximum one-day precipitation	Seasonal maximum 1-day precipitation amount	mm/season

The long-term average of all precipitation indices for the mid-future (2041 – 2070) and far future (2071 – 2100) periods was determined for both SSP245 and SSP585 scenarios. Various previous

studies have utilized these indices to assess changes in precipitation across diverse regions (Bobde et al., 2024; Tegegne et al., 2021; Huo et al., 2021; Han et al., 2021).

Prior to the statistical analysis, the indices derived from the native resolution of CMIP6 data and ENACTS were re-gridded to a common resolution of 1°×1° through the bilinear interpolation technique (Ayugi et al., 2021; Yang et al., 2023). A trend analysis for seasonal precipitation extremes was conducted using the Mann–Kendall (MK) test and Sen's slope estimator. These analyses were conducted using the "trend" package within the R statistical software (Pohlert, 2018). A significance level of 5% was employed to determine the statistical significance of the tests. Seasonal trend analyses were performed separately for each season to assess the trends in rainfall during the two primary rainy seasons of the study area, namely JJAS (Kiremt) and FMAM (Belg).

The projected relative changes in the precipitation extreme indices ($ETCCDI_{indices}$) are calculated based on the relative changes of the calculated ETCCDI indices for the projected periods ($ETCCDI_{proj}$) compared to the baseline period ($ETCCDI_{base}$) for each season (Eq.5.3)

$$\mathrm{ETTCDI}_{\mathrm{indices}} = \left(\frac{\mathrm{ETCCDI}_{\mathrm{proj}} - \mathrm{ETCCD}_{\mathrm{base}}}{\mathrm{ETCCD}_{\mathrm{base}}}\right) * 100 \qquad (5.3)$$

5.3 Results

5.3.1 Historical trends

5.3.1.1 Spatial distribution for extreme seasonal precipitation

Figure 5.2 and Figure 5.3 present the spatial variation of trends in ten extreme climate indices over a period of 30 years from 1981 to 2010 for the JJAS and FMAM seasons in Ethiopia, respectively. The significant trends for each extreme index with respect to ENACTS are presented in the supplementary material for JJAS (Appendix C1) and FMAM (Appendix C2). During JJAS, a non-significant increasing trend in PRCPTOT (Figure 5.2a and Appendix C1a) (up to 48 mm) is found in most parts of the country while a non-significant decreasing trend is observed during the FMAM season (Figure 5.3a and Appendix C2a). Most of the north, northwest, south, southwest, east, and southeast parts of the country (Tekeze, Abay, Omo Gibe, RVLB, Genale Dawa, Wabi Shebelle and Ogaden basins) show a non-significant increasing trend in PRCPTOT at different magnitudes (up to 20 mm/season) during JJAS while northeast, especially middle and lower parts of Awash

basin, show a decreasing trend (up to 12 mm). A weak rising trends in PRCPTOT (up to 4 mm/season) is observed in the south, southeast and east parts of the country near the Kenya and Somalia border during the JJAS season. In contrast, a strong increasing trend in PRCPTOT is evident in the northwest and southwest regions of the country, especially in the Abay and Omo Gibe basins. Additionally, the majority of areas in the western parts of the country, including the Baro Akobo basin, display a mixed trend during the JJAS season. During the FMAM season, a non-significant downward trend in PRCPTOT (Figure 5.3a and Appendix C2a) is observed across extensive areas in the north, east, southeast, south, northeast, and central parts of the country (including Tekeze, Ogaden, Awash, Wabi Shebelle, Genale Dawa, RVLB, and Dankali). Conversely, an upward trend (up to 6 mm/season) is noted in some parts of the northwest and southwest regions, particularly in the Abay and Omo Gibe basins, during the FMAM season. Generally, the northeast parts of the country, especially the middle and lower parts of the Awash basin, show a downward PRCPTOT trend for both seasons while most areas in the northwest parts of the country, particularly the middle and lower parts of the Abay basin, show an upward trend.

Throughout the JJAS season, the observed trend in CDD display a diverse pattern, encompassing both decreases and increases within the study area (Figure 5.2b). Conversely, during the FMAM season, there is a more widespread increase in the CDD trend, notably with a non-significant rise observed over more than 90% of the country's total area (Figure 5.3b and Appendix C2b). Non-significant rising trend in CDD is notable over large areas of the north, northwest, northeast, and central parts of the country, specifically most parts of Abay, Tekeze, Awash, and Dankali basins during the JJAS (Figure 5.2b and Appendix C1b) and FMAM seasons (Figure 5.3b and Appendix C2b). On the other hand, most parts of the east, south and southwest part of the country (Omo Gibe, RVLB, Ogaden, and Genale Dawa basins) experience more decreasing trend in CDD (up to 1 day/season) compared to other basins during the JJAS season. Moreover, the increase of CDD in the northeastern parts of the country (Dankali and lower parts of the Awash basin) is higher than in other parts of the country during the JJAS (up to 0.9 days/season) and FMAM (up to 2.8 days/season).

The higher increasing trend in CWD is observed during the JJAS season compared to the FMAM season. A non-significant increasing trend in CWD is revealed in areas with high rainfall receiving areas such as most parts of northwest, west, central and southwest parts of the country (Abay, Baro

Akob, Omo Gibe, RVLB, and most parts of the Awash basin) during the JJAS season (Figure 5.2c and Appendix C1c). In contrast, a decreasing trend in CWD is observed in low rainfall receiving areas, such as the east, southeast, and south lowlands of the country near East Africa countries (Kenya and Somalia) during JJAS and FMAM seasons. Moreover, a pronounced decrease in CWD (by up to 1 day/season) is observed in the northern and northwestern parts of the country near the Sudan border during the JJAS season. During FMAM season, a non-significant decreasing trend in CWD is observed across the majority of the country, including north, northeast, south, east, and southeast (Wabi Shebelle, Ogaden, Awash, Asayita, and Danakil basins) (Figure 5.3c and Appendix C2c). Conversely, some areas, particularly in the west and northwest parts of the country, specifically the Baro Akobo, most parts of the Abay and Omo-Gibe basins, exhibit a non-significant slight increasing trend during the FMAM season.

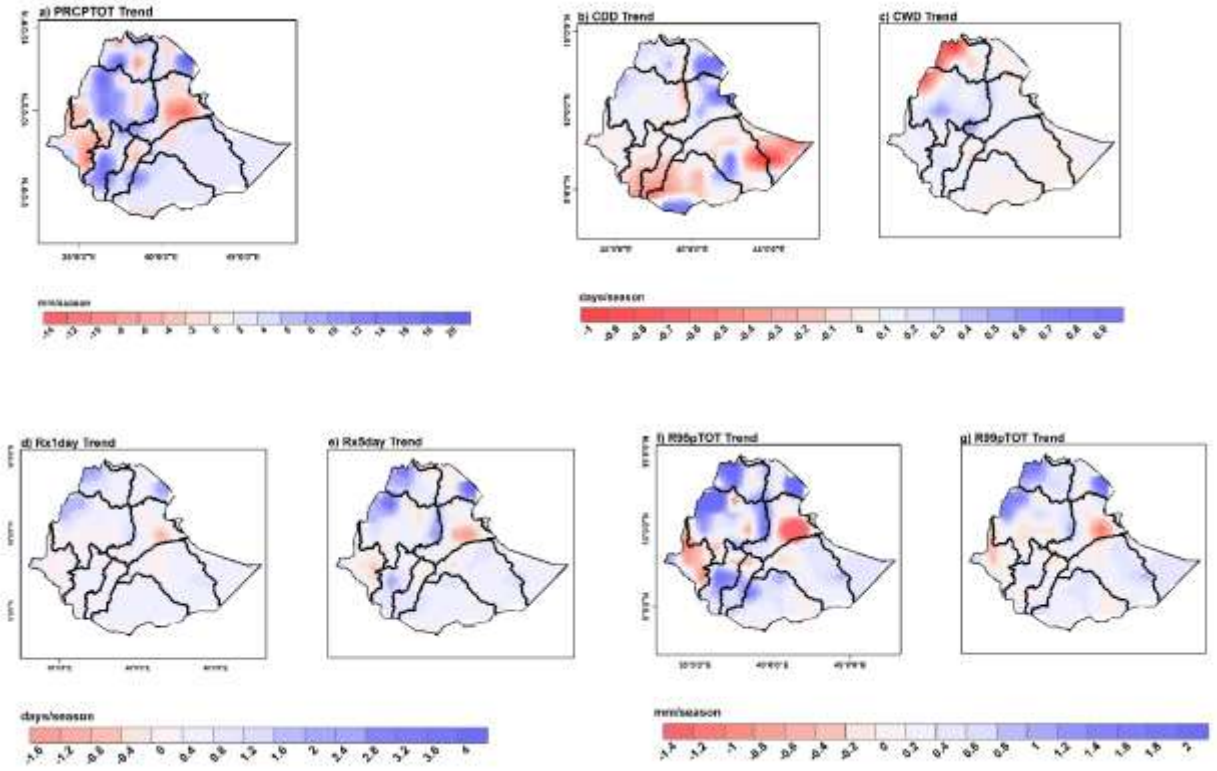

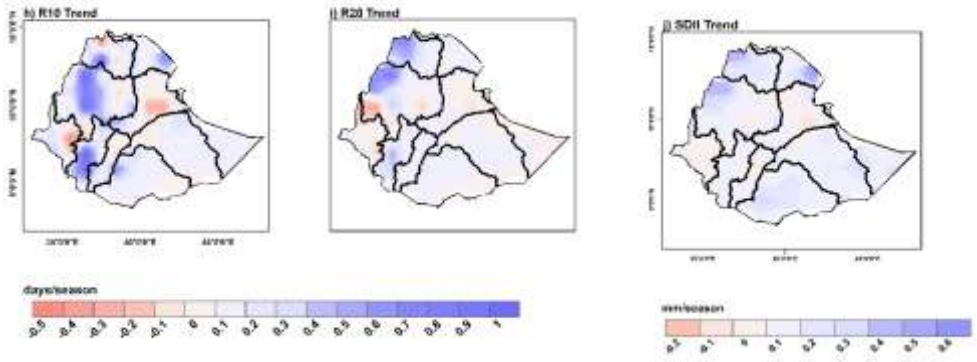

Figure 5.2**:** Spatial variation of trends in rainfall extreme indices over Ethiopia during the JJAS season for the period 1981–2010: (a) PRCPTOT, (b) CDD, (c) CWD, (d) Rx1day, (e) Rx5day, (f) R95pTOT, (g) R99pTOT, (h) R10, (i) R20, and (j) SDII.

Rx1day and Rx5day exhibit more similar spatial patterns across the study area during the JJAS season (Figure 5.2d and 5.2e) compared to the FMAM season (Figure 5.3d and 5.3e). During the FMAM season, a greater extent of decreasing trends is observed in Rx5day compared to Rx1day. A non-significant increase in Rx1day (by up to 2 days; Figure 5.2d and Appendix C1d) and Rx5day (by up to 4 days; Figure 5.2e and Appendix C1e) is observed across most parts of the country during the JJAS season, except in some regions of the northeast and west. In contrast, a divergent trend is observed during the FMAM season. A non-significant decreasing trend in Rx1day (up to 0.6 days; Figure 5.3d and Appendix C2d) and Rx5day (up to 0.8 days; Figure 5.3e and Appendix C2e) is observed in the northeast parts of the country, particularly over vast areas of the Awash basin, during the FMAM season while a non-significant increasing trend is observed in the south parts of the country.

A non-significant increasing trend in R95pTOT (Figure 5.2f and Appendix C1f) and R99pTOT (Figure 5.2g and Appendix C1g) is observed over a vast portion of the north, northwest, south, east, southeast, and southwest (Tekeze, Abay, Wabi Shebelle, Ogaden, Genale Dawa, and Omo Gibe basins) during the JJAS season. In the FMAM season, a more widespread decreasing trend is observed in R95pTOT than in R99pTOT. Furthermore, the south, southwest, east and southeast parts of the country showed contrasting trend in R95pTOT and R99pTOT during the FMAM season. For instance, a non-significant increasing trend in R99pTOT (up to 0.6 mm) is observed in those regions, specifically in the Wabi Shebelle, Genale Dawa, Omo Gibe and Ogaden) during

FMAM season (Figure 5.3g) while a decreasing trend in R95pTOT (up to 0.4 mm) is revealed (Figure 5.3f). Moreover, a non-significant decreasing trend in R95pTOT (Figure 5.3f and Appendix C2f) and R99pTOT (Figure 5.3g and Appendix C2g) indices (up to 1.6 mm) is noted over the majority of the northeast and central parts of the country (Awash basin) during the FMAM season.

A non-significant increasing trend in the R10 (Figure 5.2h and Appendix C1h) and R20 (Figure 5.2i and Appendix C1i) indices is observed over most of the north, northwest, northeast, and southwest parts of the country (Tekeze, Abay, Omo Gibe, and RVLB) during the JJAS season, despite some variations in other regions. In contrast, both R10 and R20 exhibit non-significant decreasing trends across most parts of the country during the FMAM season, with R10 showing a more widespread decline compared to R20. For instance, a non-significant decreasing trend in R10 is observed in the northeast, central, south, and southwest (Awash and RVLB basins) (Figure 5.3h and Appendix C2h), while a non-significant decreasing trend in R20 (Figure 5.3i and Appendix C2i) is evident in the north, west, and northeast during the FMAM season. Generally, the Awash basin shows a decreasing trend in R10 and R20 during the FMAM season. a non-significant increasing trend in SDII (up to 0.6 mm) is observed across most parts of the study area during the JJAS season (Figure 5.2j and Appendix C1j), except in the west and some northeast regions of the country. In contrast, non-significant decreasing trends in SDII (ranging from 0 to -0.4 mm) are observed during the FMAM season (Figure 5.3j and Appendix C2j). However, an increase in SDII trends is observed in the Genale Dawa and Baro Akob basins during the FMAM season (Figure 5.3j).

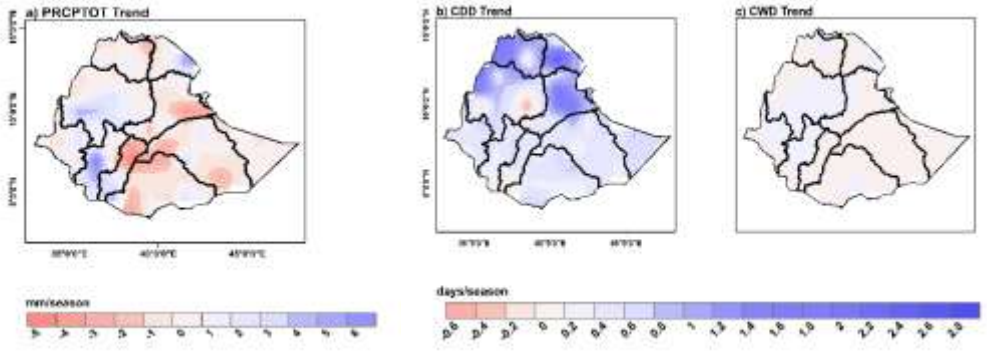

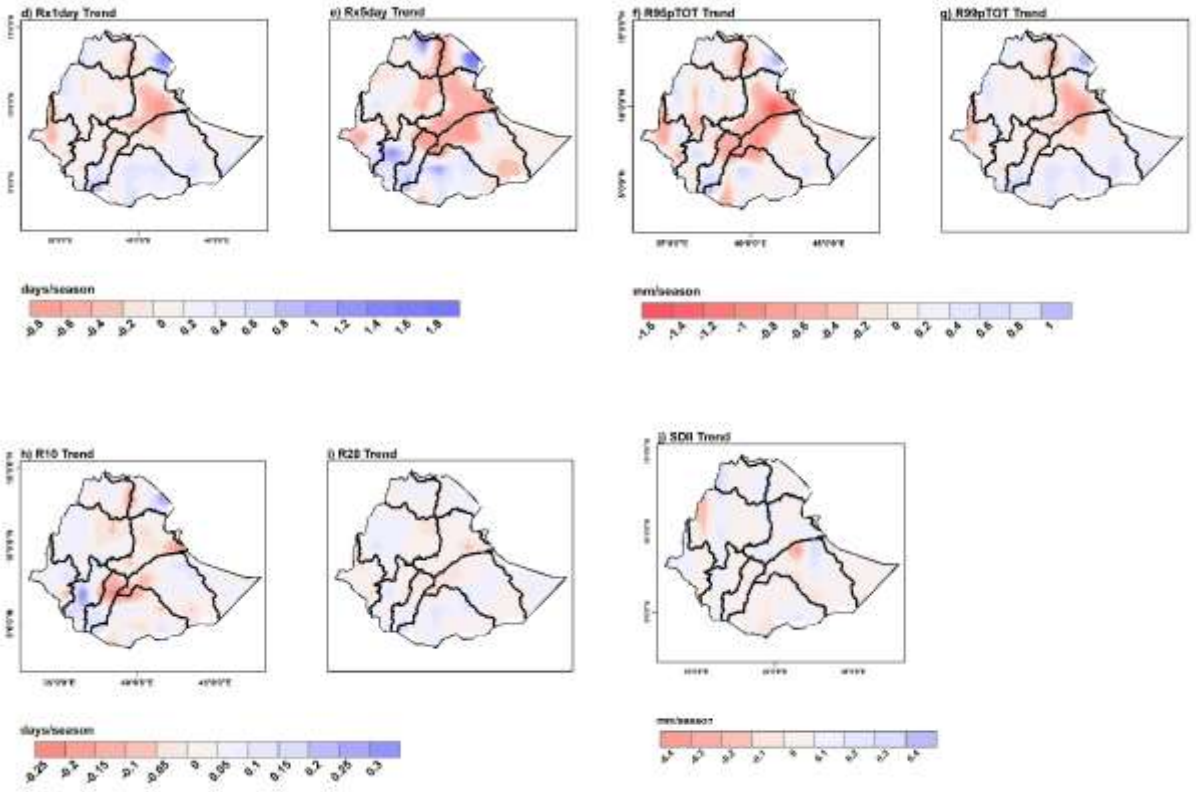

Figure 5.3: Spatial variation of trends in precipitation extreme indices over Ethiopia during the FMAM season for the period 1981–2010: (a) PRCPTOT, (b) CDD, (c) CWD, (d) Rx1day, (e) Rx5day, (f) R95pTOT, (g) R99pTOT, (h) R10, (i) R20, and (j) SDII.

5.3.1.2 Temporal analysis in extreme precipitation

Figure 5.4 displays boxplot trends of various extreme rainfall indices during the JJAS and FMAM seasons. The box plots summarize the distribution of trends for each index, where the central thick line represents the median trend, the box denotes the interquartile range (25th–75th percentiles), and the whiskers indicate the spread of the remaining values. During the JJAS season, the CDD index shows no significant change, with the median near zero, whereas the CWD index exhibits a slight increasing trend, indicated by a median slightly above zero. In contrast, during the FMAM season, CDD shows predominantly positive trends, whereas CWD displays a decreasing trend, with the median slightly below zero, during this season. PRCPTOT shows a positive skew, indicating an overall increase in total precipitation during the JJAS season while PRCPTOT shows a moderate negative trend, indicating an overall decrease in total precipitation during the FMAM season. R10 and R20 display positive trends, particularly R10**,** suggesting more heavy rainfall

events during the JJAS season. On the contrary, both indices display negative trends, which highlight a decrease in heavy rainfall events during the FMAM season. R95pTOT and R99pTOT indicate an increasing trend during JJAS season, while R95pTOT indicates a negative trend, with the median below zero, implying a decrease in extreme precipitation events during FMAM season. Rx1day and Rx5day suggest rising extreme rainfall over short durations during the JJAS season. However, Rx1day and Rx5day show a slight decreasing trend, suggesting a decrease in extreme rainfall events over short durations during FMAM season. SDII shows positive trends, reflecting increasing daily rainfall intensity during the JJAS and FMAM seasons.

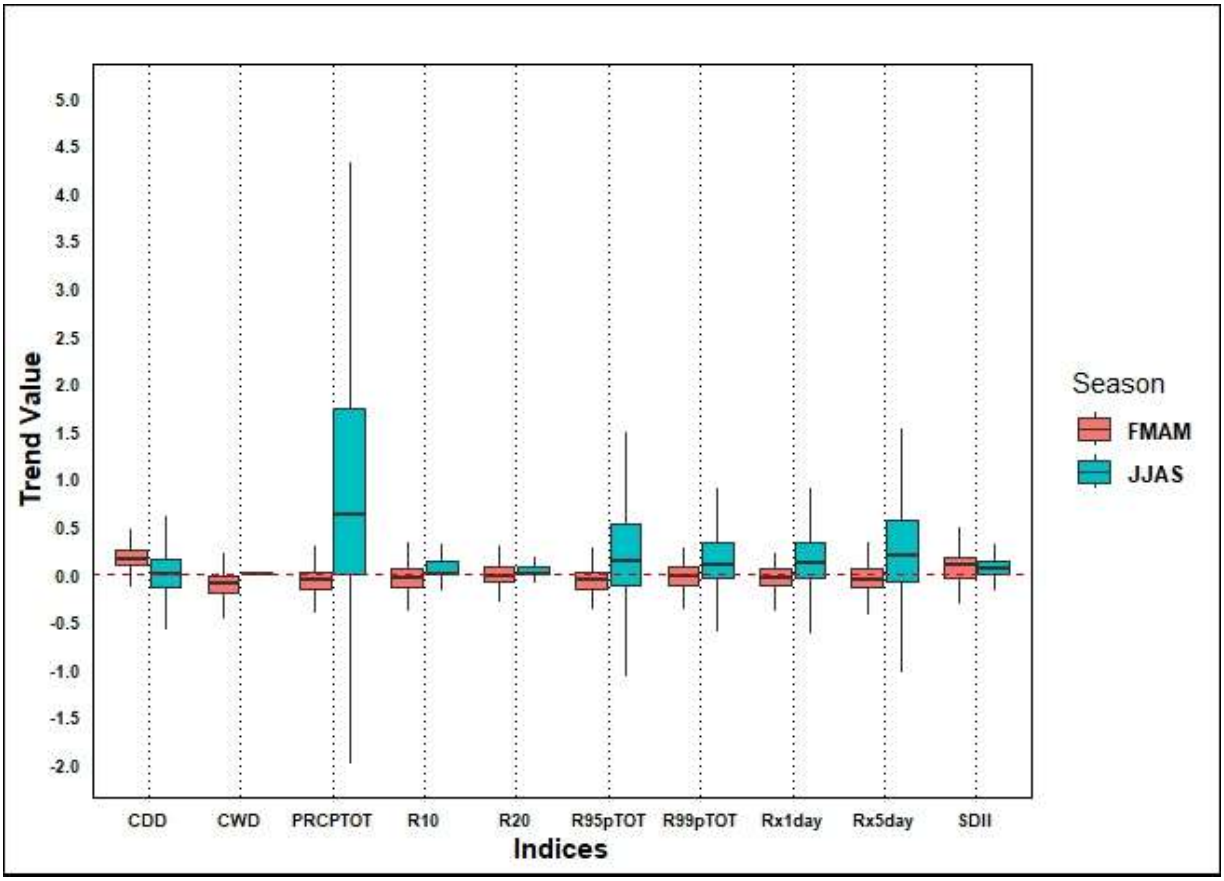

Figure 5.4**:** Box-and-whisker plots showing trends in precipitation extreme indices from the ENACTS dataset for the period 1981–2010 during the JJAS and FMAM seasons. Indices include: CDD (days), CWD (days), PRCPTOT (mm), R10 (days), R20 (days), R95pTOT (mm), R99pTOT (mm), Rx1day (mm), Rx5day (mm), and SDII (mm). The thick colored line within each box indicates the median value.

5.3.2 Future projection

Future projection of ten extreme indices during the JJAS and the FMAM seasons are shown in Figures 5.5–5.12. A comparison of raw and bias-corrected top-ranking models for extreme precipitation indices for the JJAS and FMAM seasons is presented in the supplementary material (Appendices C3 and C4). Bias correction enhances TSS values across various models and metrics, though the degree of improvement varies by model and metric (Appendix C3 and C4). Extreme precipitation metrics (R95P, R99P, Rx1day, Rx5day) shows significant improvement in all models, especially for GFDL-ESM4, MPI-ESM-1-2-HAM, and HadGEM3-GC31-MM (Appendix C3 and C4). Bias correction was more effective in improving PRCP in models like GFDL-ESM4 and MPI-ESM-1-2-HAM. CDD and SDII showed the smallest improvement across all models. Overall, all models benefit from bias correction for JJAS (Appendix C3) and FMAM (Appendix C4) seasons, with improvements ranging from 5% to 12%.

5.3.2.1 Projected changes in extreme precipitation in main rainy season (JJAS)

Figure 5.5a-t and 5.6a-t present the spatial distribution of projected extreme precipitation during the main rainy season (JJAS) under SSP245 and SSP585 for the periods 2041–2070 (2050s) and 2071–2100 (2080s), respectively, relative to 1981–2010. The country is projected to experience varying climate changes over the coming decades. Increases (up to 70%) are projected in the north, northwest, west, southwest, and northeast regions of the country, including the Tekeze, Abay, Baro Akob, Awash, Dankali, RVLB, and Omo Gibe basins in the 2050s under SSP245 (Figure 5.5a). However, a decrease is projected in north parts of the country (Tekeze basin) by the 2050s under SSP585 (Figure 5.5k) and by the 2080s under both scenarios (Figure 5.6a and k). Similarly, many of the northwest and west parts of the country, including the Abay and Baro Akobo basins, are projected to experience a slight increase in PRCPTOT in the 2050s under both scenarios and in the 2080s under SSP245, while a decrease is expected in the 2080s under SSP585. Additionally, areas with historically low rainfall, like the Dankali and lower Awash basins in the northeast, are expected to experience an increase in precipitation by the 2050s and 2080s in both scenarios. Generally, an increase of up to 40% in PRCPTOT is projected in the northeastern and central parts of the country, particularly in the Awash and Danakil basins, during the 2050s and 2080s under both scenarios. In contrast, a decrease in PRCPTOT (Wabi Shebelle and Ogaden basins) is

projected in the east and southeast in the 2050s and 2080s during the same periods and under both scenarios.

Both SSP245 and SSP585 scenarios project a consistent spatial pattern of decreasing CDD across Ethiopia in 2050s (Figures 5.5b and 5.5l) and 2080s (Figure 5.6b and l). During JJAS, a decrease in CDD is projected in the north, northwest, west, southwest, and northeast regions (such as the Abay, Baro Akobo, Omo Gibe, and Danakil basins) in the 2050s (Figure 5.5b) and 2080s (Figure 5.6b) under SSP245. In contrast, a consistent increase in CDD is projected for the eastern and southeastern parts of the country, particularly in the Ogaden and Wabi Shebelle basins, during both the 2050s and 2080s under both SSP245 and SSP585 scenarios. Additionally, a slight increase in CDD is projected in the north, west, and southeast parts of the country in the 2050s under SSP585 (Figure 5.5l), with this increase extending further into the southeast region by the 2080s (Figure 5.6l).

An increase in CWD is projected across more than 60% of the study area during the 2050s (Figures 5.5c and 5.5m) and 2080s (Figures 5.6c and 5.6m) under both scenarios. Most areas in the northwest, northeast, and central parts of the country, particularly the Abay, Awash, and Danakil basins, are projected to experience an increase in CWD during the 2050s (Figures 5.5c and 5.5m) and 2080s (Figures 5.6c and 5.6m) under both SSP245 and SSP585 scenarios. However, an exception is observed in much of the northwestern region (Abay basin), where CWD is projected to decrease during the 2080s under the SSP585 scenario (Figure 5.6m). Moreover, a decrease in CWD is projected for most of the east and southeast regions of the country, particularly in the Wabi Shebelle and Ogaden basins. A slight decrease is also projected in much of the northern and western regions, including the Tekeze and Baro Akobo basins, during the 2050s and 2080s under both SSP245 and SSP585 scenarios. Overall, the largest increase in CWD is projected in the Awash basin and in areas with historically low rainfall, such as the Danakil basin, under both scenarios. In contrast, the greatest decrease is expected in the east and southeast regions (Wabi Shebelle and Ogaden basins), with a slight decrease in the north (Tekeze basin) and in the western parts of the country, such as the Baro Akobo basin, which typically receive higher rainfall.

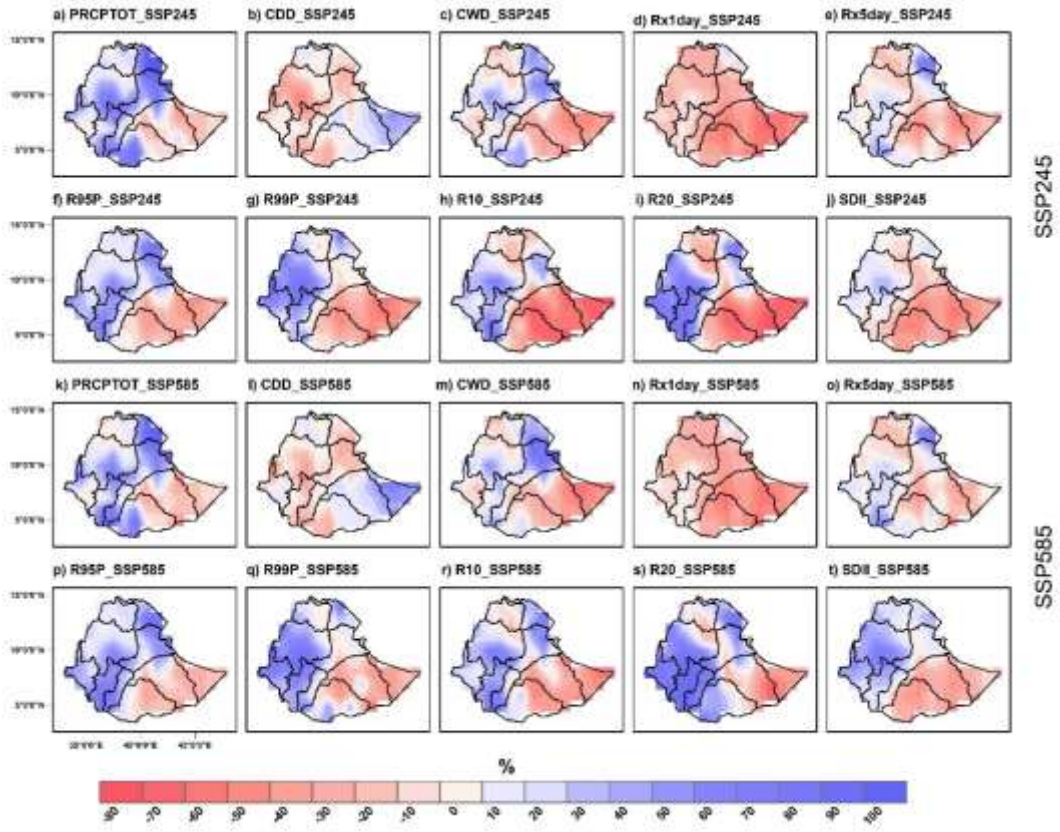

Figure 5.5: Projected change in extreme precipitation indices (a-t) (%), relative to the reference period (1981–2010), during JJAS for the 2050s under SSP245 and SSP585 scenarios. Indices include: CDD (days), CWD (days), PRCPTOT (mm), R10 (days), R20 (days), R95pTOT (mm), R99pTOT (mm), Rx1day (mm), Rx5day (mm), and SDII (mm).

More decreases in Rx1day are observed across most of the country compared to Rx5day in all future periods under both scenarios. A decrease in Rx1day is projected across more than 90% of the study area in the 2050s (Figures 5.5d and 5.5n) and 2080s (Figures 5.6d and 5.6n) under both scenarios, with more decline in the south and southeast parts of the country (up to 80%), especially in the Genale Dawa, Wabi Shebelle and Ogaden basins. A decrease projection in Rx5day is observed in most parts of north, south, southeast and east parts of the country in 2050s (Figures 5.5e and 5.5o) and 2080s under both scenarios (Figures 5.6e and 5.6o) while Rx5day in northeast (Dankali basin), southwest (Omo Gibe) and most parts of the northwest (Abay basin) show an increasing. Generally, greater increases in Rx5day are observed in low-rainfall areas, such as the northeast, particularly in the Dankali basin, across all future time periods and scenarios. More

increases in R95pTOT are projected across most parts of the country in the 2050s and 2080s under both scenarios, compared to R99pTOT. R95pTOT is expected to rise in more than 85% of the country, including the north, northwest, south, southwest, and northeast (Tekeze, Abay, Baro Akobo, RVLB, Omo-Gibe, and Dankali) by the 2050s under both scenarios (Figures 5.5f and 5.5p) and 2080s under SSP245 (Figure 5.6f).

Conversely, the eastern parts of the country especially the Wabi Shebelle and Ogaden basins are projected to decrease in both scenarios but slightly increase in some parts of the basins by the 2080s under SSP585. The projection indicates an increase in R99pTOT in the northwest, west, southwest, and northeast parts of the country (Abay, Baro Akobo, RVLB, and Dankali) in the 2050s under both scenarios (Figures 5.5g and 5.5q) and in the 2080s under SSP245 (Figure 5.6g). In the east and southeast (including Wabi Shebelle and Ogaden), a decrease in R99pTOT is expected by the 2050s and 2080s under both scenarios. Additionally, a further decrease in R99pTOT is projected across the entire Tekeze basin by the 2080s under the SSP585 scenario. Generally, extreme and heavy precipitation events (R95pTOT and R99pTOT) are projected to increase in the northwest, west, and southwest parts of Ethiopia by the 2050s and 2080s under both scenarios, while they are projected to decrease in the east and southeast parts of the country.

Compared to R10, more increases in R20 are expected across most of the country in all future periods under both scenarios. An increase in R10 is projected in the northwest, west and southwest (Abay, Baro Akobo, RVLB and most parts of the Awash basin) for both the 2050s (Figures 5.5h and 5.5r) and the 2080s (Figures 5.6h and 5.6r) under both scenarios. Conversely, the south, southeast, and east parts of the country (Wabi Shebelle, Genale Dawa and Ogaden basins) are expected to experience a decrease in the projection of R10 in all future time periods under both scenarios. An increase in R20 (up to 30%) is projected for the west, northwest, southwest, and northeast parts of the country, particularly in the Baro Akobo, RVLB, Dankali, Omo-Gibe, and much of the Abay basins, by the 2050s under SSP245 (Figure 5.5i). This increase is expected to extend into the south by the 2080s under SSP245 (Figure 5.5s) and the 2050s under SSP585 (Figure 5.6i), and further into the central and southeast regions by the 2080s under SSP585 (Figure 5.6s). In contrast, the east and southeast, especially the Wabi Shebelle and Ogaden basins, are projected to experience a decrease in R20 during the 2050s under both scenarios and the 2080s under SSP245.

Overall, the eastern and southeastern parts of the country (the Wabi Shebelle and Ogaden basins) are projected to experience the largest decreases in R10 and R20 during the 2050s and 2080s under both scenarios. Similarly, reductions in R10 and R20 are also expected across the entire Tekeze basin in the same periods. In contrast, the high rainfall areas, such as the northwest, west (Abay, Baro, Akobo, RVLB), and the low rainfall areas, such as the northeast (Dankali basin), are projected to increase in these indices. No significant changes in SDII are projected for the north, northwest, west, and southwest regions of the country, including the Tekeze, Abay, Baro Akobo, Omo Gibe, and Dankali basins, by the 2050s under SSP245 (Figure 5.5j). However, an increase of 10–30% in SDII is projected for these same areas by the 2050s under SSP585 (Figure 5.5t) and by the 2080s under both scenarios (Figure 5.6j and t). In contrast, the south and southeast regions, particularly the Genale Dawa, Wabi Shebelle, and Ogaden basins, are expected to experience a decrease in SDII across all time periods and scenarios, except for a slight increase in some parts of Ogaden basin in the 2080s under SSP585.

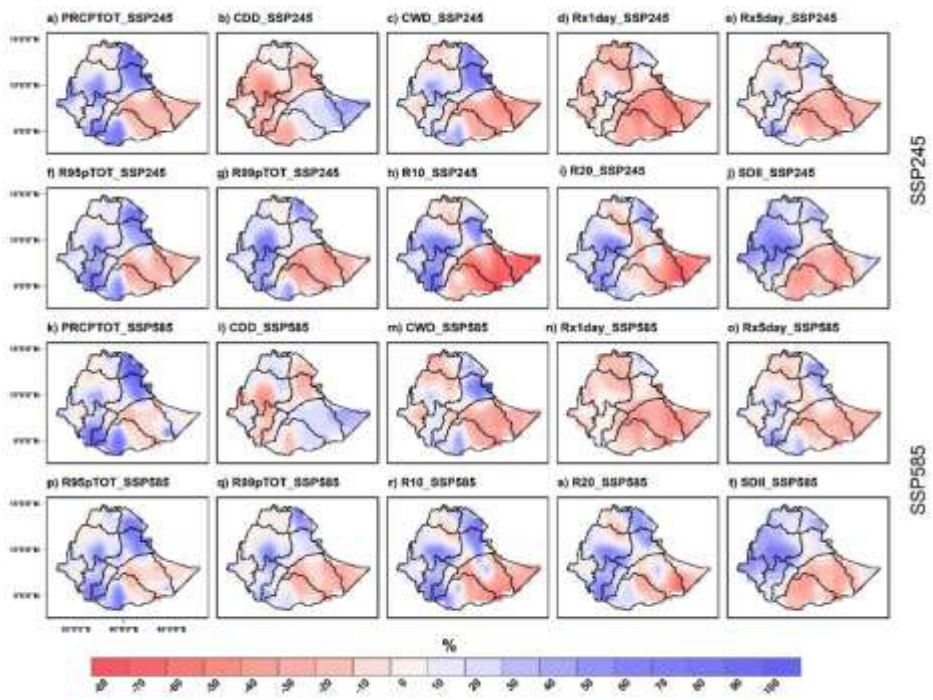

Figure 5.6: Projected change in extreme precipitation indices (a-t) (%), relative to the reference period (1981–2010), during JJAS for the 2080s under SSP245 and SSP585 scenarios. Indices include: CDD (days), CWD (days), PRCPTOT (mm), R10 (days), R20 (days), R95pTOT (mm), R99pTOT (mm), Rx1day (mm), Rx5day (mm), and SDII (mm).

5.3.2.2 Projected Changes in extreme precipitation in short rainy season (FMAM)

Figures 5.7a–t and 5.8a–t illustrate the spatial distribution of projected changes in extreme precipitation indices during the FMAM season under the SSP245 and SSP585 scenarios for the periods 2041–2070 (2050s) and 2071–2100 (2080s), respectively, relative to the baseline period 1981–2010. An increased PRCPTOT is projected across the north, northwest, west, and east regions of the country, including the Tekeze, Abay, Baro Akobo, Omo Gibe, and Ogaden basins, in the 2050s (Figures 5.7a and 5.7K) and 2080s (Figures 5.8a and 5.8K), under both scenarios. Under SSP585, this increase is expected to extend into the south and southeast regions by the 2050s (Figure 5.7k). By the 2080s, PRCPTOT is projected to rise in the south and southwest under SSP245 (Figure 5.8a), with a more pronounced increase in the southwest under SSP585 (Figure 5.8k). Moreover, an increase in PRCPTOT is projected across more than 95% of the study area by the 2080s under the SSP585 scenario. Conversely, most areas in the southern and southeastern parts of the country are expected to experience a decrease in PRCPTOT by the 2050s under SSP245, with slight increases (< 10%) projected for the 2080s under both scenarios (Figures 5.8a and 5.8k). Overall, the north and northwest regions of the country, particularly the Tekeze and Abay basins, are projected to experience an increase in PRCPTOT of more than 30% during both periods under both scenarios. In contrast, most of the Awash basin is expected to see a decrease of more than 10%.

Climate model projections indicate that more than 80% of the country is likely to experience a slight increase in the CDD, with a more pronounced increase projected for the 2050s under both scenarios (Figures 5.7b and 5.7l; Figures 5.8b and 5.8l). CDD is projected to increase by up to 10% during the 2050s and 2080s under both scenarios, particularly across the west, southwest, and northeast regions of the country, including the Baro Akobo, RVLB, Awash, and Ogaden basins in 2050s under both scenarios (Figures 5.7b and 5.7l). However, a slight decrease in CDD is expected in most northern areas, including the Tekeze basin, during the 2050s and 2080s under scenarios. This decrease is projected to extend further south (Genale Dawa basin), east (Ogaden basin) and northwest (most parts of the Abay basin), by the 2080s under both scenarios (Figures 5.8b and 5.8l).

The opposite patterns in CDD and CWD are projected over most parts of the country including the north, west, southwest, south, southeast and east parts of the country. The north, northwest, south, east, and northeast of the country (Tekeze, Abay, Wabi Shebelle, Danakil and lower parts the Awash basin) are anticipated to experience an increase in CWD with magnitude about 20% in 2050s under SSP24 (Figure 5.7c) and further extend in south and southeast under SSP585 scenario in 2050s (Figure 5.7m) and east in 2080s under SSP245 (Figure 5.8c). However, slight decreases in CWD (0%-10%) are projected over the northwest, west, and central parts of the country (including Baro Akobo and most parts of the Abay basins) in the 2080s under SSP585 (Figure 5.8m). Generally, the north and northwest regions, particularly the Tekeze and Abay basins, are projected to experience a 20% decrease in CDD and an increase in CWD across all future periods under both scenarios. In contrast, the western parts of the country, especially the Baro Akobo basin, are expected to exhibit an increase in CDD and a decrease in CWD.

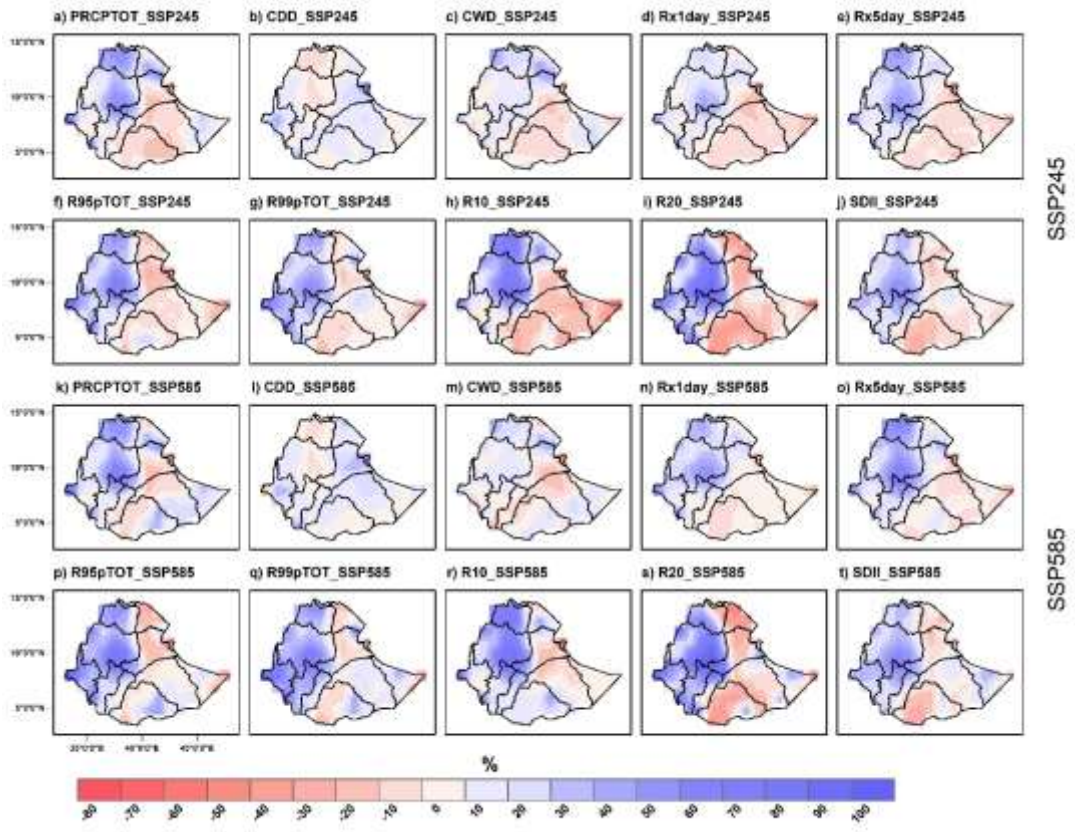

Figure 5.7: Projected change in extreme precipitation indices (a-t) (%), relative to the reference period (1981–2010), during FMAM for the 2050s under SSP245 and SSP585 scenarios. Indices

include: CDD (days), CWD (days), PRCPTOT (mm), R10 (days), R20 (days), R95pTOT (mm), R99pTOT (mm), Rx1day (mm), Rx5day (mm), and SDII (mm).

An increase in Rx1day and Rx5day is projected in the north, northwest, west, southwest, and central parts of the country, particularly in the Tekeze, Abay, Baro Akobo, Omo-Gibe, and RVLB basins during the 2050s (Figures 5.7d and 5.7n; Figures 5.7e and 5.7o) and 2080s (Figures 5.8d and 5.8n; Figures 5.8e and 5.8o) under both scenarios. In the case of Rx1day, this increase is projected to extend further south by the 2080s under SSP585 (Figure 5.8n). Conversely, a decrease in both Rx1day and Rx5day is observed in the southeast and east regions, particularly in the Wabi Shebelle and Ogaden basins, during both the 2050s and 2080s under both scenarios.

The R95pTOT and R95pTOT indices show similar increasing trends under both scenarios in most parts of the country during the 2050s and 2080s. Specifically, the north, northwest, west, and southwest regions, including the Tekeze, Abay, Baro Akobo, and Omo Gibe basins, are projected to increase up to a 60% in R95pTOT and R99pTOT by the 2050s (Figures 5.7f and 5.7p; Figures 5.7g and 5.7q.) and continuing into 2080s under both scenarios (Figures 5.8f and 5.8p; 5.8g and q). Under SSP585, a slight increase in R99pTOT is also projected to extend into the south, east, and southeast regions, particularly across the Wabi Shebelle, Ogaden, and Baro Akobo basins by the 2050s (Figures 5.7g and 5.7q) and 2080s (Figures 5.8g and 5.8q). Additionally, the R95pTOT index is projected to slightly increase in the southern region, particularly over the Genale Dawa basin, by the 2080s under both scenarios. Conversely, reductions in R95pTOT are expected in the northeast parts of the country, especially over the Dankali region and the middle to lower reaches of the Awash and Wabi Shebelle basins during the 2050s and 2080s under both scenarios. Similarly, a decrease in R99pTOT is projected in the south and northeast regions, particularly in much of the Genale Dawa and the Awash basin, during the 2050s under both scenarios (Figure 5.7g and q), and continuing into the 2080s under SSP245 (Figure 5.8g). Overall, an increase in the projection of both R95pTOT and R99pTOT indices is observed in the north, northwest, west, and southwest parts of the country under both scenarios during the 2050s and 2080s. In contrast, a reduction in R95pTOT and R99pTOT is projected in the northeast and central parts of the country.

Relative to the reference period, significant portions of north, and northwest Ethiopia (including Tekeze, and Abay basins) are projected to experience an increase in both R10 and R20 indices

during the 2050s (Figure 5.7 h and r; Figure 5.7i and s) and 2080s (Figure 5.8h and r; Figure 5.8i and s) under both scenarios. The projected increase in R10 extends further south, west, and southwest in the 2050s (Figure 5.7r) and 2080s (Figure 5.8r) under SSP585. A slight increase in R20 is also expected to extend into the eastern and southeastern parts of the country, particularly over the Wabi Shebelle and Ogaden basins, by the 2080s under SSP585 (Figure 5.8s). In contrast, the south and southeast parts of the country, including the Genale Dawa, most of the Wabi Shebelle, and central parts of the Awash basins, are projected to show a decreasing in R10 (Figure 5.7h and r; Figure 5.8h) and R20 (Figure 5.7i and s; Figure 5.8i) indices by the 2050s under both scenarios, and by the 2080s under SSP245. This decrease for R10 is expected to extend further into the eastern parts of the country, particularly the Ogaden basin, in future periods under both scenarios.

The north, northwest, west, and southwest parts of Ethiopia (including the Tekeze, Abay, Baro Akobo, Omo Gibe, RVLB, and Ogaden basins) are projected to experience a 0–40% increase in SDII during the 2050s (Figure 5.7j and t) and 2080s (Figure 5.8j and t) under both scenarios. Additionally, a slight increase in SDII (up to 10%) is projected to extend into the eastern parts of the country, particularly the Ogaden basin, during the 2050s under SSP585 and in the 2080s under both scenarios. In contrast, a decrease in SDII is projected in the south and northeast parts of the country, particularly in the Genale and middle and lower parts of the Awash basin, during the 2050s and 2080s under both scenarios.

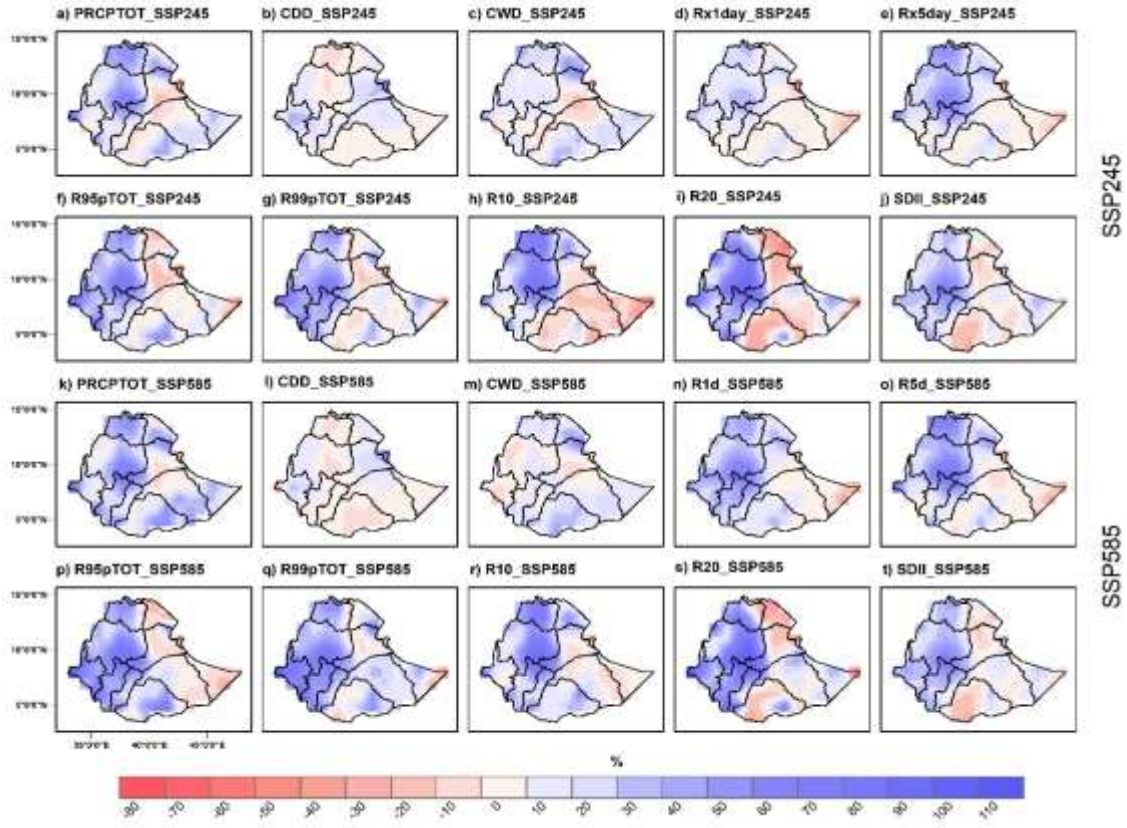

Figure 5.8: Projected change in extreme precipitation indices (a-t) (%), relative to the reference period (1981–2010), during FMAM for the 2080s under SSP245 and SSP585 scenarios. Indices include: CDD (days), CWD (days), PRCPTOT (mm), R10 (days), R20 (days), R95pTOT (mm), R99pTOT (mm), Rx1day (mm), Rx5day (mm), and SDII (mm).

5.3.2.3 Model uncertainty and trend analysis

Figure 5.9 shows box-and-whisker plots of trends for EnseMean and the top five models for simulating extreme indices under SSP245 for the 2050s for the JJAS season. However, significant variation exists among ensemble members. NorESM2-MM, CMCC-ESM2, and NESM3 closely align with the Ensemble Mean, all projecting a decrease in CDD, whereas NorESM2-LM shows a slight increase (Figure 5.9). The CMCC-ESM2 indicates a general greater increase in CWD, but NorESM2-MM diverges by projecting a decline. EnseMean, NorESM2-LM and NESM3 reveal a slight increase. All models consistently project an increase in PRCPTOT, in agreement with the EnseMean. EnseMean, CMCC-ESM2, and NorESM2-MM project an increasing trend in R10,

whereas NorESM2-LM indicates a decreasing trend. NESM3, on the other hand, shows no discernible trend for R10. For R20, neither the individual models nor the ensemble mean exhibits any significant trend. EnseMean projects increase in both R95pTOT and R99pTOT, with a more pronounced rising trend in R95pTOT. CMCC-ESM2, NESM3 and NorESM2-MM follow this trend, while NorESM2-LM deviates from the EnseMean projecting a decline (Figure 5.9). The EnseMean also suggests increases in Rx1day and Rx5day precipitation indices, with larger increases in Rx5day, and CMCC-ESM2 projects the strongest rise in Rx5day. Additionally, all models, including EnseMean, project a smaller increase in SDII.

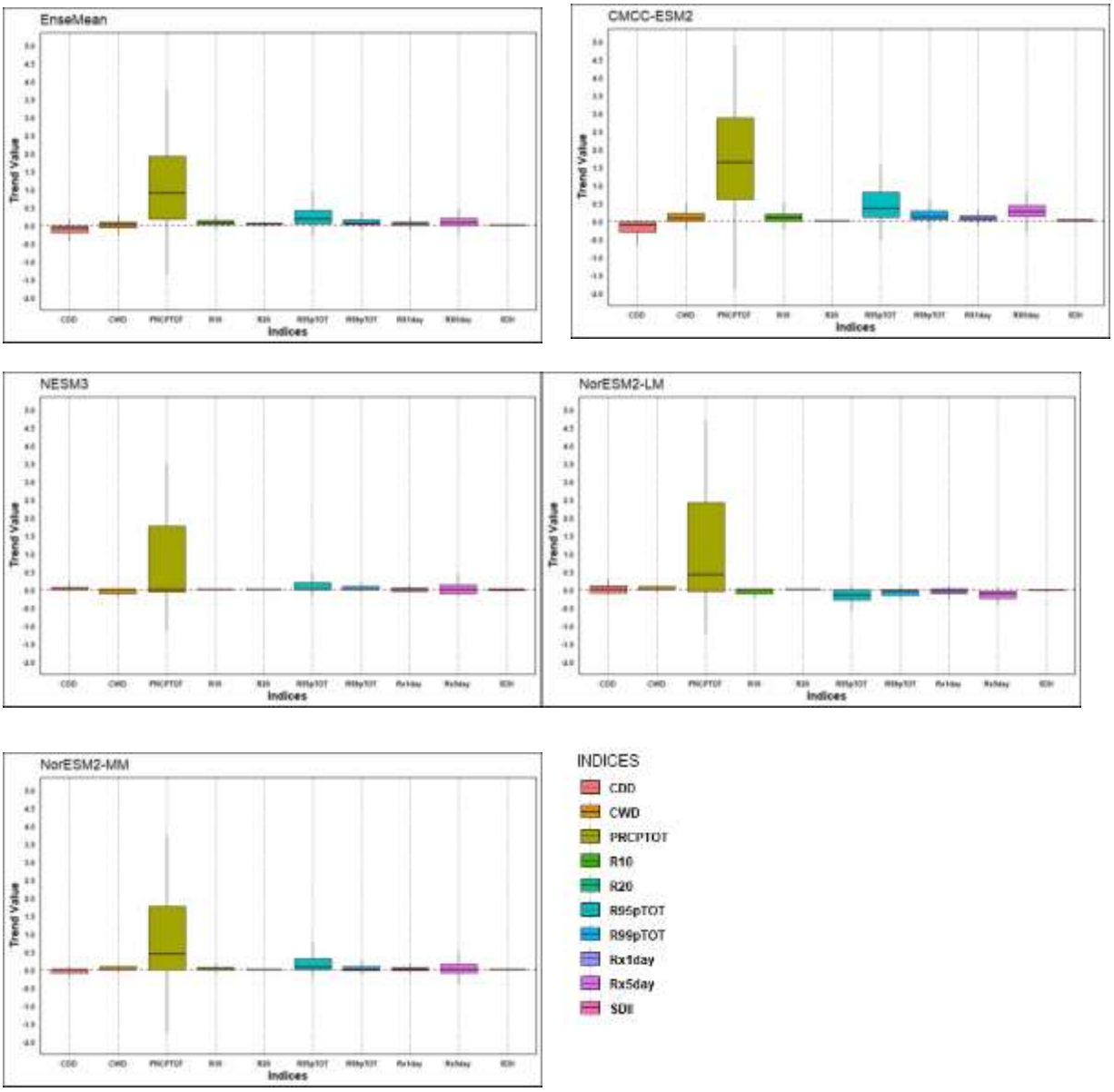

Figure 5.9: Box-and-whisker plots of trends for the EnseMean in simulating extreme precipitation indices: (CDD (days), CWD (days), PRCPTOT (mm), R10 (days), R20 (days), R95pTOT (mm), R99pTOT (mm), Rx1day (mm), Rx5day (mm), and SDII (mm)) for JJAS season for the 2050s under SSP245 scenario. The boxes represent the interquartile range (from the 25th to the 75th percentiles), with the thick black line within each box indicating the median. The whiskers show the total intermodal range.

Figure 5.10 shows box-and-whisker plots of trends for EnseMean and top-five models for simulating extreme indices under SSP245 for the 2080s for the JJAS season. The EnseMean projects a decreasing trend in CDD. This trend is supported by NESM3, NorESM2-MM, and CMCC-ESM2, while NorESM2-LM contrasts with the EnseMean by projecting an increase (Figure 5.10). Conversely, the EnseMean and CMCC-ESM2 indicate an increasing trend in CWD, with NESM3 projecting a smaller magnitude of increase, while NorESM2-LM shows no notable change. PRCPTOT is projected to increase more substantially than the other indices, although the projections exhibit considerable inter-model variability. EnseMean, CMCC-ESM2, NESM3, and NorESM2-MM show a stronger increasing trend in PRCPTOT, while NorESM2-LM projects a decline (Figure 5.10).

Both R10 and R20 show no significant trends in most models and in EnseMean, except for CMCC-ESM2, which projects an increase in R10. The EnseMean projects a moderate increase in both R95pTOT and R99pTOT. CMCC-ESM2 supports this with a stronger upward trend, while NESM3 and NorESM2-MM show comparatively weaker increases. In contrast, NorESM2-LM deviates by showing no trend in R95pTOT and only a slight increase in R99pTOT. The EnseMean suggests an increase in Rx1day and Rx5day, with CMCC-ESM2 projecting the strongest rise. However, NESM3, NorESM2-LM, and NorESM2-MM show a weaker rise in Rx1day and a decrease in Rx5day. Additionally, SDII exhibits no discernible trend across all individual models and the ensemble mean (Figure 5.10).

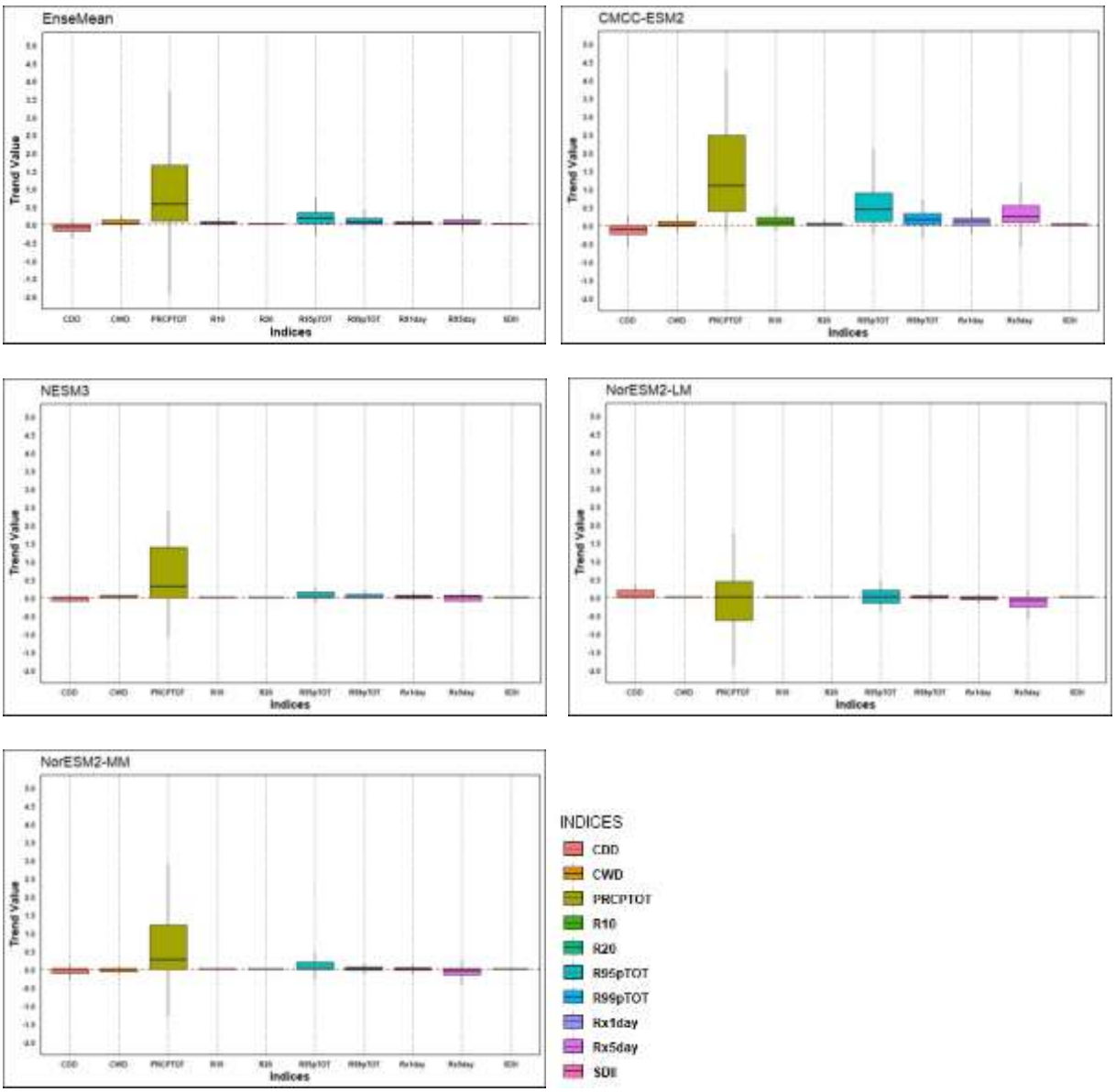

Figure 5.10: Box-and-whisker plots of trends for the EnseMean in simulating extreme precipitation indices: (CDD (days), CWD (days), PRCPTOT (mm), R10 (days), R20 (days), R95pTOT (mm), R99pTOT (mm), Rx1day (mm), Rx5day (mm), and SDII (mm)) for JJAS season for the 2080s under SSP245 scenario. The boxes represent the interquartile range (from the 25th to the 75th percentiles), with the thick black line within each box indicating the median. The whiskers show total intermodal range.

Figure 5.11 shows box-and-whisker plots of trends for EnseMean and top-five models for simulating extreme indices under SSP585 for the 2050s for the JJAS season. The EnseMean

projects a weak decreasing trend in CDD, suggesting a slight reduction in dry spell duration. NESM3 indicates a stronger decrease, reinforcing this signal. In contrast, NorESM2-MM projects an increasing trend, while CMCC-ESM2 shows no significant change. Notably, NorESM2-LM projects the most pronounced increase in CDD. For CWD, both the EnseMean and NESM3 project an increasing trend. CMCC-ESM2 shows the largest rise, whereas NorESM2-MM indicates a slight decline, and NorESM2-LM remains relatively stable (Figure 5.11). PRCPTOT is projected to rise moderately by the EnseMean, CMCC-ESM2, NorESM2-LM, and NorESM2-MM, while NESM3 projects an even stronger increasing trend.

R10 and R20 remain stable in both the ensemble mean and NorESM2-LM, while CMCC-ESM2 and NESM3 project a slight increasing trend in R10. R20, however, shows no significant change across all models and the EnseMean. R95pTOT is projected to increase across all models and the ensemble mean, with NESM3 exhibiting a particularly strong upward trend. R99pTOT is projected to increase slightly in the EnseMean, with CMCC-ESM2 and NorESM2-LM indicating stronger rises, although NorESM2-LM also exhibits a declining trend. Rx1day projections indicate a weaker rise in the EnseMean, and NorESM2-LM, while CMCC-ESM2 and NESM3 project stronger increases. CMCC-ESM2, NorESM2-LM and NESM3 project a higher rising trend for Rx5day, whereas while NorESM2-MM suggests a decline. SDII remains stable across all models, indicating no significant change in daily precipitation intensity. Overall, CMCC-ESM2 indicates the wettest conditions, with increases in both CWD and PRCPTOT. NESM3 projects stronger upward trends in R95pTOT, R99pTOT, Rx1day, and Rx5day (Figure 5.11).

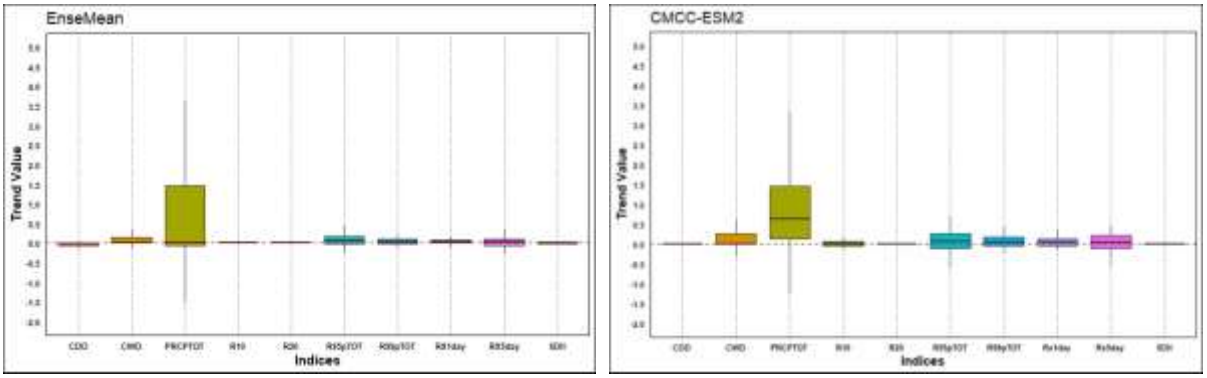

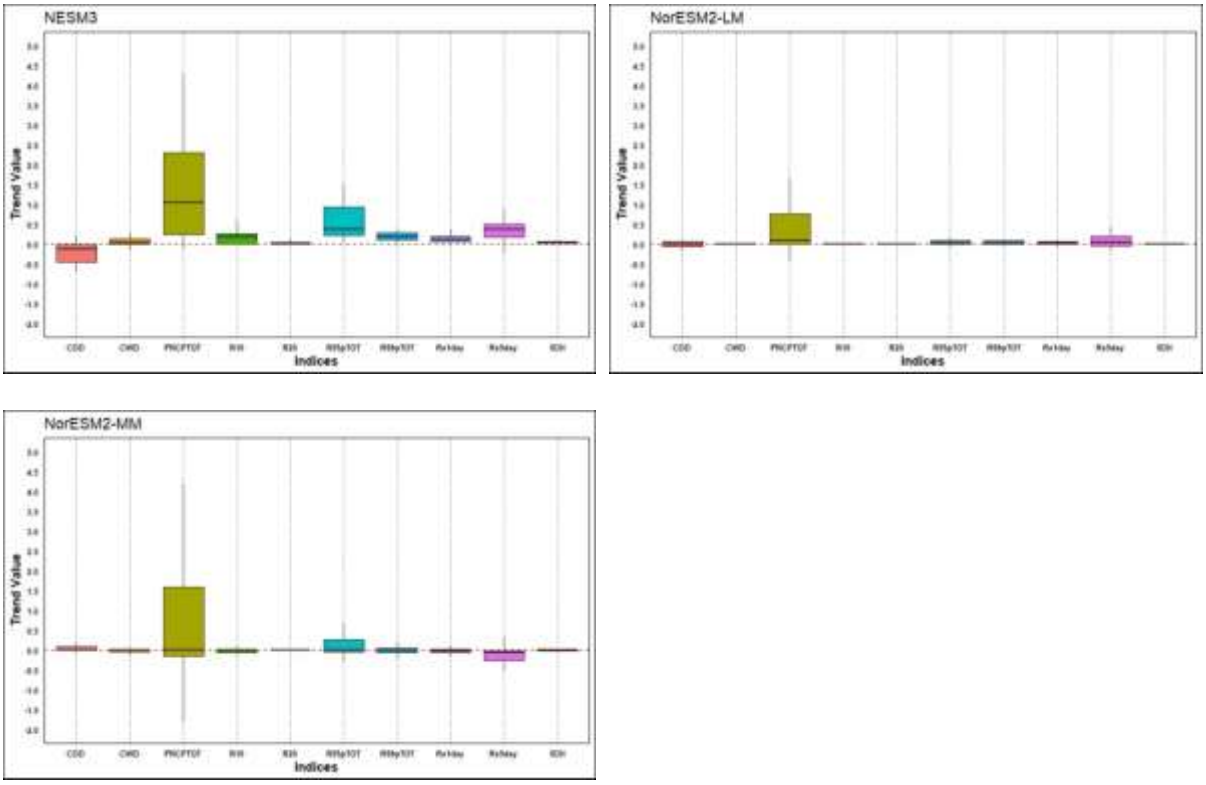

Figure 5.11: Box-and-whisker plots of trends for the EnseMean in simulating extreme precipitation indices: (CDD (days), CWD (days), PRCPTOT (mm), R10 (days), R20 (days), R95pTOT (mm), R99pTOT (mm), Rx1day (mm), Rx5day, and SDII (mm)) for JJAS season for the 2050s under SSP585 scenario. The boxes represent the interquartile range (spanning the 25th to 75th percentiles), with the thick black line inside each box indicating the median. The whiskers show total intermodal range.

Figure 5.12 shows box-and-whisker plots of trends for EnseMean and top five models for simulating extreme indices under SSP585 for the 2080s for JJAS season. The EnseMean, along with CMCC-ESM2, NorESM2-LM, and NorESM2-MM, projects a moderate decrease in CDD trends, whereas NESM3 shows an increase. EnseMean and NorESM2-MM project an increasing trend in CWD, while CMCC-ESM2, NorESM2-LM, and NESM3 indicate a slight increase. All four models are consistent with the EnseMean in projecting an overall rise in PRCPTOT, with NESM3 showing a more pronounced increase (Figure 5.12). The NESM3 and CMCC-ESM2 project a slight increase in R10, while EnseMean, NorESM2-LM and NorESM2-MM show no significant change. R20 remains stable across all models and EnseMean. All models, along with the EnseMean, project an increasing trend in R95pTOT. The EnseMean indicates a moderate rise

in projecting R95pTOT, with CMCC-ESM2 and NorESM2-LM showing stronger increases, while NESM3 and NorESM2-MM display weaker upward trends. The EnseMean projects an increasing trend in R99pTOT, closely followed by CMCC-ESM2. NorESM2-MM and NorESM2-LM show weaker increases, while NESM3 shows no significant change. All models, including EnseMean, project stronger increasing trends in Rx5day compared to Rx1day. An increasing trend in Rx1day is observed in the EnseMean and CMCC-ESM2, while the other models show no significant change. SDII remains stable across all models and the EnseMean, with no notable changes projected (Figure 5.12).

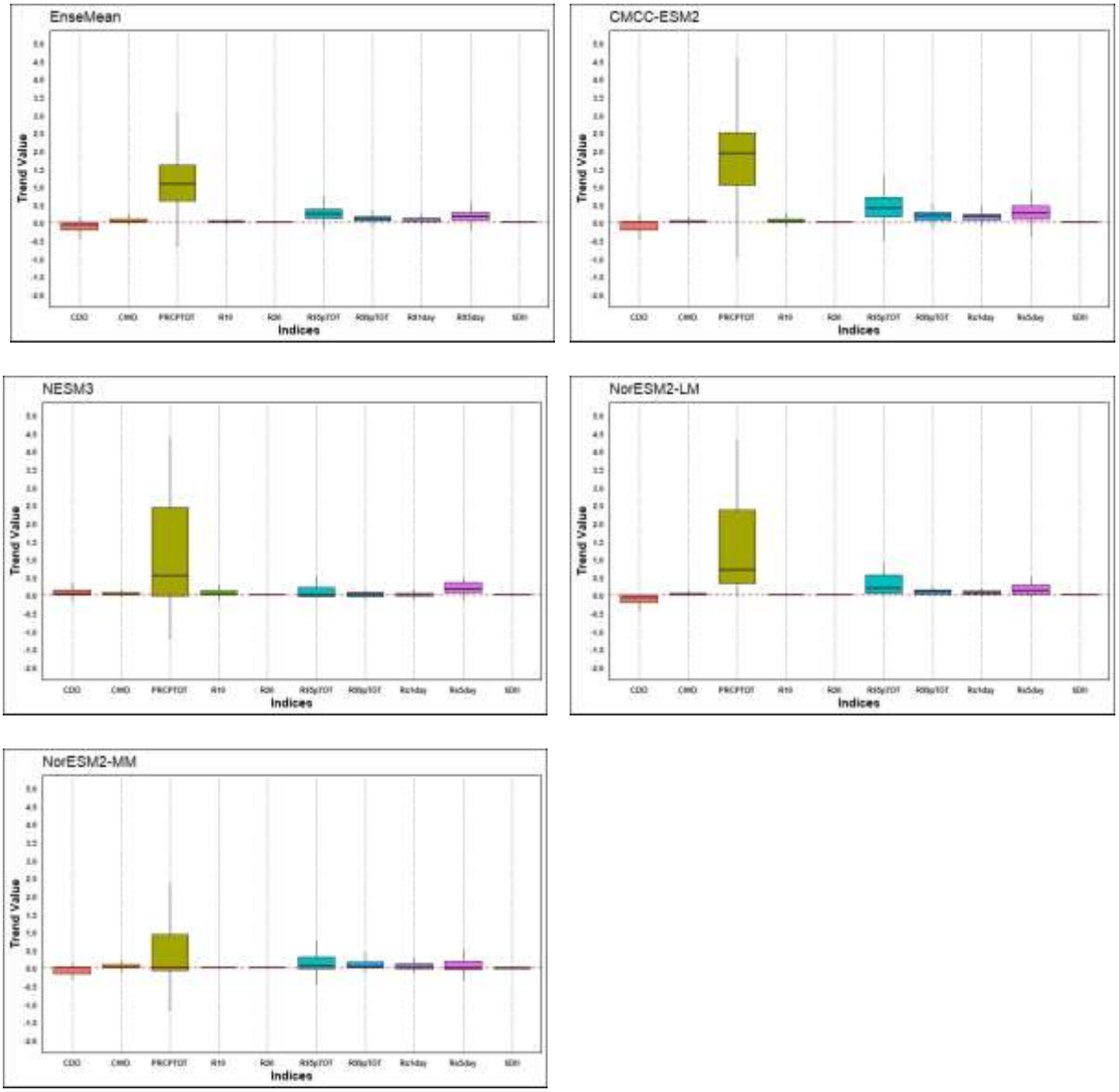

Figure 5.12: Box-and-whisker plots of trends for the EnseMean in simulating extreme precipitation indices: (CDD (days), CWD (days), PRCPTOT (mm), R10 (days), R20 (days), R95pTOT (mm), R99pTOT (mm), Rx1day (mm), Rx5day (mm), and SDII (mm)) for JJAS season for the 2080s under SSP585 scenarios. The boxes represent the interquartile range (from the 25th to the 75th percentiles), with the thick black line within each box indicating the median. The whiskers show total intermodal range.

The projected changes in extreme indices, averaged across five ensemble members for FMAM season (BCC-CSM2-MR, GFDL-CM4, GFDL-ESM4, NorESM2-LM, and NorESM2-MM), are provided in the supplementary material for FMAM season for 2050s and 2080s under both scenarios (Appendix C5–C8). BCC-CSM2-MR is the driest model with fewer wet days and lower extremes. GFDL-CM4 is moderate but aligns closely with EnseMean. GFDL-ESM4 is the wettest model with the highest extreme precipitation and intensity. NorESM2-LM projections showed the strongest increases in rainfall and wetter conditions.

5.4 Discussion

Understanding both historical trends and future projections of extreme precipitation is crucial for effective climate adaptation. Analyzing precipitation extremes across Ethiopia from 1981 to 2010 during the JJAS and FMAM seasons reveals significant regional and temporal variability, with implications for water resources and agriculture. Over the past three decades, most rainfall indices (except CDD) have shown non-significant increasing trends, particularly in high-rainfall areas (northwest, west, and southwest) and low-rainfall areas (south, southeast, and east) during the JJAS season. Conversely, during the FMAM season, non-significant decreasing trends are observed across most parts of the country in most indices.

Understanding future projections of extreme rainfall indices is essential, particularly due to Ethiopia's complex and diverse topography. Despite previous declines during the FMAM season, projections indicate a more pronounced increase in PRCPTOT during FMAM than durig JJAS across all timeframes and both scenarios in the north and northwest regions of Ethiopia. In these areas, the CWD is projected to increase and the CDD to decrease during FMAM. Overall, these patterns suggest a potential seasonal shift, with more rainfall occurring during FMAM than JJAS in the north and northwest, particularly in the Tekeze basin. This may require adjustments in

agricultural planning and water management. Moreover, the northeastern and central regions of the country, particularly the Awash Basin, are expected to experience increases in PRCPTOT and CWD during the JJAS season. In contrast, a decrease in PRCPTOT and CWD is anticipated during the February to May (FMAM) season, which aligns with the historical pattern of decreasing on PRCPTOT and CWD during this period. However, the rainfall pattern in the Awash basin is bimodal, with the main rainy season occurring from July to September (JAS) while small rains occur between March and May (Taye, et al., 2018). The anticipated reduction in FMAM rainfall, coupled with the projected increase in JJAS precipitation, suggests a potential shift from a bimodal to a more unimodal rainfall regime.

Overall, these potential seasonal shifts in north and northeast of the country, particularly in the Tekeze and the Awash basin, could have far-reaching implications. For agriculture, changes in rainfall timing and intensity may affect planting and harvesting cycles, crop yields, and food security. For water resource management, altered hydrological regimes could influence reservoir operations, irrigation planning, and flood risk. Additionally, ecosystem dynamics, including vegetation patterns and water availability for biodiversity, may also be affected. Proactive adaptation strategies will be crucial for managing the socio-economic and environmental impacts of these emerging rainfall trends.

High-rainfall areas in northwest, west, and southwest Ethiopia (Abay, Baro Akobo, Omo Gibe, and RVLB basins) are expected to see increased precipitation indices (PRCPTOT, CWD, R10, R20, R95P, R99P, and SDII) in both JJAS and FMAM seasons. This contrasts with historical trends, in which these regions saw increasing indices during JJAS but declining indices during FMAM. The projected rise in extreme rainfall events raises concerns about flooding, soil degradation, and agricultural losses. However, the hydropower sector, particularly Grand Ethiopian Renaissance Dam (GERD), Gibe II, and Gibe III, may benefit from increased water availability, reinforcing the need for strategic water management and infrastructure investments to mitigate risks while capitalizing on opportunities. Climate projections indicate a significant increase in extreme precipitation indices, with the exception of consecutive dry days (CDD), for the arid Danakil Basin in northeastern Ethiopia during the JJAS season of the 2050s and 2080s.While this could temporarily improve water availability for pastoralist communities, it also

heightens flood risks, threatening infrastructure, crops, and livelihoods. Developing flood control measures and early warning systems will be crucial to mitigate these impacts.

On the other hand, in the eastern parts of Ethiopia, the JJAS season is projected to see an increase in CDD, along with decreases in both CWD and PRCPTOT. In contrast, during the FMAM season, CWD and PRCPTOT are projected to increase, while CDD decreases. This projected pattern represents a shift from the historical rainfall trends in the region, indicating a potential reversal in seasonal precipitation behaviors. Knoben et al. (2019) identified a latitudinal shift in precipitation patterns across Africa, in which rainfall regimes transition from bimodal to unimodal with increasing latitude. Ethiopia's rainfall pattern is predominantly bimodal, but climate change could alter these latitudinal gradients, reshaping precipitation regimes across the continent (Sian, et al., 2025). In Ethiopia, such shifts could affect rainy season timing, distribution, and frequency, impacting water resources, agriculture, and ecosystem dynamics. The projected increases in extreme precipitation are consistent with previous studies on East Africa, including Ethiopia, using CMIP5 and RCMs (Onyutha et al., 2020; Fotso-Nguemo et al., 2019; Mariotti et al., 2014; Sylla et al., 2016; Shiferaw et al., 2018) as well as CMIP6 (Feyissa et al., 2023; Gebresellase et al., 2022; Balcha et al., 2022; IPCC, 2020; Gebrechorkos et al., 2023; Bobde et al., 2024).

The top-performing models and EnseMean for SSP245 and SSP585 scenarios indicate uncertainty in projecting precipitation indices, as some models often suggest divergent trends. Notably, the uncertainty in future PRCPTOT (total precipitation) is greater than that of other indices, with area-averaged projections ranging from −20% to +70%. The large spread in projected PRCPTOT (−20% to +70%) underscores the difficulty in drawing clear conclusions about future rainfall patterns, which are critical for sectors such as agriculture, water management, and disaster preparedness. This uncertainty makes it harder for policymakers to plan for future climate conditions. It suggests the need for flexible, adaptive strategies that can accommodate a range of possible futures, rather than relying on a single projected outcome.

Overall, climate projections suggest an increase in extreme rainfall events during JJAS. Despite historical declines, future projections indicate rising FMAM precipitation across most of Ethiopia, consistent with previous studies using statistically downscaled CMIP6 models for East Africa, including Ethiopia (Gebrechorkos et al., 2023). Future precipitation events, especially in western,

eastern, and central Africa, are expected to become more intense due to projected positive shifts (Bobde et al., 2024). This phenomenon, known as the "East African Climate Paradox," highlights the complex interplay between climate projections and historical data (Lyon and Vigaud, 2017; Nicholson, 2017). Possible reasons for this discrepancy include anthropogenic aerosol emissions, uncertainties in global climate models (GCMs), shifts in rainfall seasonality, and natural variability (Rowell et al., 2015; Wainwright et al., 2019). Belg (FMAM) rainfall, influenced by cyclonic activity and North Atlantic sea surface temperature anomalies, may also be affected by climate change, particularly due to warming patterns in the Indian and Pacific Oceans (Endris et al., 2019). The El Niño-Southern Oscillation (ENSO) remains a key driver of rainfall variability in Ethiopia, alongside local climatic factors, including diverse physiographic features (Zeleke et al., 2025; Palmer et al., 2023; Gitima and Mersha, 2020).

5.5 Conclusion

Considering Ethiopia's heavy reliance on rainfall for livelihoods and productivity and its vulnerability to the adverse effects of droughts and floods, understanding extreme precipitation trends and projections is essential for effective resource management and planning. Overall, despite historical declines in most extreme rainfall trends, projections indicate an increase in PRCPTOT during the FMAM season across much of the country in the coming decades. An increase in projection of extreme indices (PRCPTOT, CWD, Rx1day, Rx5day, R95pTOT, R99pTOT, R10 and R20) is observed during FMAM in the north and northwest, even though declining historical trends are observed in the above-mentioned areas. On the other hand, JJAS in the northwest, west, and southwest showed increases in R95pTOT, R99pTOT, R10, and R20, underscoring the need for region-specific strategies to manage water resources, mitigate flood risks, and adapt agricultural practices.

The potential seasonal shifts observed in the north (Tekeze basin), northwestern (upper parts Abay basin), northeast (Awash basin), and southern (Ogaden basin) regions of Ethiopia have significant implications for water resource management, agriculture, and climate resilience. These regions rely heavily on the timing and quantity of rainfall to sustain agricultural productivity and ensure water availability. Any alteration in the seasonal distribution of precipitation could impact planting schedules, crop growth cycles, and the reliability of water supplies, thereby posing risks to local

livelihoods and overall economic stability. Moreover, the projected increase in extreme rainfall across Ethiopia particularly in the northwest, west, and southwest, presents both opportunities and challenges. While enhanced rainfall offers potential benefits such as improved water availability for agriculture and hydroelectric power generation, the risks associated with extreme weather events, especially flooding, are a serious concern. Policymakers and stakeholders must consider these divergent patterns in their planning processes, ensuring that measures are in place to address both water scarcity and excess, depending on the time of year. Integrating climate projections into agricultural planning, infrastructure development, and disaster preparedness will be essential to enhance resilience against the anticipated changes in precipitation patterns. Generally, governmental and non-governmental bodies should consider these future predictions in their plans and programs when designing sustainable adaptation measures in the country. By doing so, they can implement precautionary measures that minimize the adverse impacts of climate-related hazards on agriculture. Effective planning and adaptation strategies, based on accurate climate predictions, are essential to ensure resilience against natural variability and potential future climate shifts.

Chapter 6. Historical Trends and Future Changes of Hydroclimate Extremes in Awash Basin, Ethiopia

Abstract

The Awash basin in Ethiopia faces severe water insecurity due to high climate variability, frequent droughts and floods, and excess water demand, all of which are expected to worsen with climate change. This study analyzes historical (1981–2010) and future (2020s, 2050s, 2080s) hydroclimatic changes in the basin under SSP245 and SSP585, focusing on precipitation, temperature, streamflow, drought, and flood characteristics, with a detailed assessment for the Mojo catchment. We employed outputs from ensembles of seven top-performing CMIP6 Global Climate Models (GCMs) and 1981–2010 is used as a reference period. The GCM outputs were statistically downscaled using bias-correction techniques—quantile mapping for precipitation and variance scaling for temperature to drive the hydrological model. The Soil and Water Assessment Tool Plus (SWAT+) hydrological model is used to simulate streamflow across the Mojo catchment in the Awash basin.

The results show strong spatial contrasts in historical precipitation indices. During the March-April-May (MAM) period, the Upper basin experiences minimal changes in PRCPTOT (less than 2 mm), accompanied by slight increases in CDD and a decline in both wet-day frequency and extreme rainfall events. In contrast, the Middle basin shows a decrease in PRCPTOT and CWD, while CDD increases by 1 to 4 days. The Lower basin displays more variable precipitation trends, with reductions in CWD and significant increases in CDD. In JAS, PRCPTOT rises in the Upper basin (+12 mm) but falls sharply in the Middle (−24 mm) and Lower basins. On the other hand, projections indicate MAM PRCPTOT increases in the Upper and Lower basins (up to +50% in Afar lowlands) but declines in the Middle basin. By the 2050s, JAS rainfall is projected to increase across most of the basin. CWD is projected to rise throughout the basin, with the largest increases occurring in the Lower basin during MAM (up to +50%) and in the Middle and Lower basins during JAS (+40–100%).CDD increases in the Middle basin during MAM (+40%) but declines in JAS. Extreme precipitation (R99pTOT, Rx5day) intensifies in the Upper basin, up to +70% by the 2080s under SSP585.

In the Mojo catchment, streamflow is expected to decline by 80%-100% during the MAM season, but to increase by up to 70% in July–August. This is because rainfall increases in July–August (+63%, +42%) but declines in March–May (−7% to −24%). Maximum and minimum temperatures are projected to increase by approximately +2.0 °C and +1.9 °C, respectively. Flood frequency (+48%) and drought severity (+36%) are projected to increase in the future. Overall, these findings emphasize the urgent need for climate-resilient integrated water resource management plans that account for both increasing deficits and surpluses throughout the year in the Awash basin and the Mojo catchment.

Key words: Awash River Basin, CMIP6 models, SWAT+, hydroclimate extreme indices, drought, flood, Mojo catchment

6.1 Introduction

Climate change is expected to profoundly affect the quantity, quality, and timing of river flows, groundwater recharge, and other critical hydrological processes (Jiménez Cisneros et al., 2014). Understanding and quantifying these impacts is essential for sustaining water security, preserving aquatic ecosystems, and maintaining the ecosystem services they provide (King et.al, 2024; Zhao et al., 2024). Hydrological impact assessments commonly rely on climate projections from General Circulation Models (GCMs) under various radiative forcing scenarios to modify meteorological inputs for hydrological models (Todd et al., 2011; Thompson et al., 2014).

Hydroclimate studies often focus on variables such as rainfall, temperature, and streamflow, whose variability strongly influences future water availability and hydrological extremes, including floods and droughts (Malede et al., 2024). Numerous studies have reported climate change effects on hydroclimatic systems, including changes in the intensity, frequency, and magnitude of hydrological extremes and their implications for agriculture (Sharma et al., 2020; Tadese et al., 2020; Andualem et al., 2020). Globally, water scarcity remains a pressing concern, with climate change projected to exacerbate this challenge through altered rainfall patterns and rising temperatures (Jiménez Cisneros et al., 2014; Malede et al., 2024). Thus, understanding long-term trends and future projections of hydroclimatic variables is critical for effective water resource management, especially in regions already experiencing water stress.

The Awash basin in Ethiopia faces acute water insecurity, primarily due to high climate variability, recurrent droughts and floods, and growing water demand—pressures that are expected to intensify under climate change (Adeba et al., 2015). As one of Ethiopia's most economically and socially critical basins, it supports agriculture, industry, hydropower, and urban water supply, yet its hydrological system is highly vulnerable to both seasonal variability and long-term climate shifts (Gedefaw et al., 2018; Mulugeta et al., 2019). Understanding spatiotemporal variations in precipitation and extreme rainfall indices across the basin is crucial, not only for anticipating future water availability but also for designing basin-wide adaptation strategies that address the dual risks of increasing drought severity and intensifying flood hazards. The Mojo catchment, one of the tributaries of the Awash River basin in Ethiopia, plays a vital role in the hydrology of the larger Awash River basin, influencing both the local ecosystems and agricultural activities. Given its

dependence on rainfall, the catchment is highly vulnerable to both meteorological drought (caused by prolonged precipitation deficits) and hydrological drought (resulting from reduced streamflow and water availability) (Alemu et al., 2023). In the Mojo watershed, reduced runoff during the dry season exacerbates the existing shortage of irrigation water and decreases hydropower generation from the Koka reservoir, which is located within this sub-basin (Tadese etal., 2019). Such conditions pose serious challenges to agricultural productivity, water resource management, and local livelihoods. In catchments such as Mojo, where rainfall variability strongly governs agricultural and hydrological processes, conducting a comprehensive drought and flood analysis is essential. This improves understanding of drought and flood frequency, intensity, and spatial distribution, thereby supporting early warning systems, water allocation planning, and strategies to build resilience in the agricultural sector.

Past research has largely relied on earlier CMIP5 climate projections and focused on mean rainfall patterns (Alemu et al., 2022; Emiru et al., 2021; Taye et al., 2018; Bekele et al., 2018), with limited analysis of hydroclimatic extremes. A few studies have used CMIP5 models with intermediate emission scenarios to examine climate extremes such as floods and droughts at spatiotemporal scales (Tola and Shetty 2023; Alemu et al., 2023). This gap underscores the need for updated assessments using CMIP6 projections and multiple emission pathways. Recent studies recommend incorporating the latest generation of climate models (CMIP6) and a multi-model ensemble mean to better capture basin-scale hydroclimatic dynamics and reduce uncertainties (Malede et al., 2024; Onyutha, 2024). Model uncertainties—stemming from GCM structure, emission scenario differences, and downscaling methods—can be reduced by using a multi-model ensemble mean (Hughes et al., 2013; Raju and Kumar 2020).

Accordingly, this study applies the ensemble mean from top-ranking CMIP6 models to enhance projection reliability. The novelty of this research lies in its combined analysis of historical (1981–2010) and future (2015–2100) trends, using the latest version of the Soil and Water Assessment Tool Plus (SWAT+) for assessing their potential impacts on hydrology and extreme events in the Awash basin of the Mojo catchment of impacts of climate change on hydrological extremes. The findings of this study serve as a basis for understanding the projected impacts of climate change on the Awash basin's hydrology and extremes, and provide critical evidence to support policy

makers in developing basin- and season-specific adaptation and integrated water resource management strategies.

6.2 Study area and datasets

6.2.1 Study area

The Awash basin, located between 7°53′–12°00′ N and 37°57′–43°25′ E, covers about 110,000 km² in central and northeastern Ethiopia (Figure 6.1a and b). Originating in the Ethiopian highlands near Ginchi (~3,000 m a.s.l.), the river flows northeastward into the Afar Depression, terminating in a chain of inland lakes (Bekele et al., 2017). The basin's climate ranges from humid subtropical in the highlands to semiarid and arid in the lowlands, with annual rainfall varying from >1,500 mm to <400 mm (figure 6.1b). Rainfall is seasonal, with Belg (March–May) providing short rains and Kiremt (July–September) serving as the main wet and crop-growing season (Taye et al., 2018).

Based on topography and climate, the basin is divided into three main zones. The Upper Awash Basin originates in the central highlands and includes Addis Ababa, Ethiopia's capital. This sub-basin is the most developed and economically significant, serving as the hub for industrial activities, major irrigation schemes (notably sugarcane cultivation), and hydropower projects, including the Koka Dam. The Middle Awash Basin, stretching from the Koka Reservoir to Gewane, has a semi-arid climate and is largely devoted to large-scale irrigated agriculture. The Lower Awash Basin, extending from Gewane to the Afar Depression (including the Tendaho Plain), is arid, characterized by very low rainfall, high evaporation, and limited water resources (Taddese et al., 2003; Edossa et al., 2010).

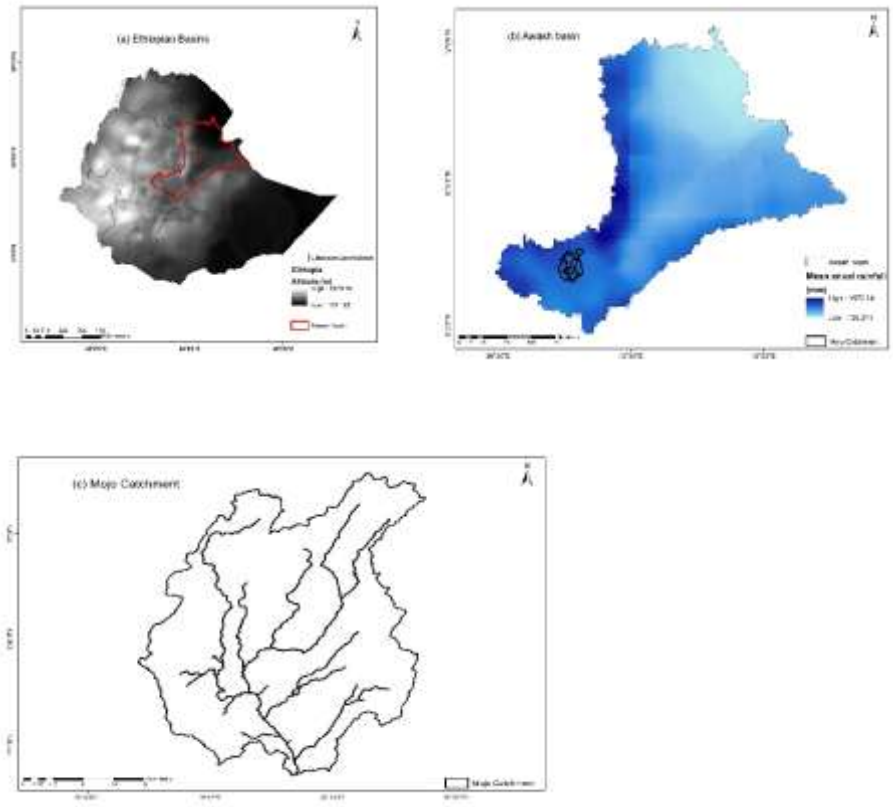

Figure 6.1: Location of the Awash basin and Mojo catchment within Ethiopian basins: (a) Ethiopian basins, (b) Awash basin, and (c) Mojo Catchment

The Mojo Catchment, located in the Upper Awash basin of central Ethiopia (8°34′30″ N–9°6′00″ N; 38°54′30″ E–39°17′30″ E), covers about 148,064 ha with elevations ranging from 1,719 m to 3,091 m above sea level (Figure 6.1c). Elevation ranges significantly from 1,719 m to 3,091 m above sea level, incorporating both highland and midland terrains. The Mojo River is a perennial tributary of the Awash River that passes through the town of Mojo, located about 43 km southeast of Addis Ababa. The river receives various effluents, while extensive agricultural activities and expanding human settlements have increasingly altered its catchment and riparian zones (Alemu et al., 2023). The watershed experiences both monomodal and bimodal rainfall patterns, reflecting varied seasonal distributions. More than 80% of the annual rainfall occurs during July to September (locally known as Kiremt), while the shorter rainy season, Belg, extends from March to May (Gonfa & Kumar, 2016). The area has an average annual rainfall of ~828 mm and mean temperatures between 11.1 °C and 26.3 °C. Dominant soils include vertic cambisols, pellic vertisols, and chromic luvisols. Land use is predominantly agricultural, though recent decades have

seen increased cultivation and urbanization, influencing streamflow patterns and water quality (Tufa et al., 2022).

6.2.2 Datasets

The high-resolution gridded data, such as the ENACTS dataset, is critical for understanding the rainfall distribution in a data scarce region like Ethiopia, where meteorological stations are sparse, dispersed and not functioning. In this study, the ENACTS dataset, with a resolution of 0.04° × 0.04°, is utilized for analyzing historical trends and assessing potential future climate changes. The daily precipitation and temperature ENACTS gridded dataset spanning from 1981 to 2010 was obtained from the Ethiopian Meteorological Institute (EMI).

Climate data from the CMIP6 models were utilized to evaluate changes in climate and climate extremes, as well as their impacts on hydrology and hydrological extremes. Different study indicate that the most accurate models are used for seasons, thereby improving the reliability of the climate projections for the study area (Guputa et al., 2025). Thus, in this study, different CMIP6 models were selected for extreme precipitation indices and temperature, based on a comprehensive evaluation of model skill over Ethiopia and Awash basin (Berhanu et al., 2023; Berhanu et al., 2025, Gebresellase et al., 2022; Alemu et al., 2023) (Table 6.1). In this study, two Shared Socioeconomic Pathways (SSPs) were employed: SSP245 and SSP585. SSP245 represents a future with medium challenges for both mitigation and adaptation, characterized by a continuation of fossil-fueled development, while SSP585 represents a pathway with high challenges to mitigation and relatively low challenges to adaptation to climate change. The selected models were retrieved from the Earth Systems Grid Federation (ESGF; https://esgf-node.llnl.gov/projects/esgf-llnl/). In this study, we selected the period from 1981 to 2010 as the base period, and two future time frames were selected: the 2050s (2041-2070) and the 2080s (2071-2100) to assess the future climate projection. The period from 2015 to 2040 (2020s) is only used for hydrological impact assessment.

Table 6.1: Selected models for projection of precipitation and temperature

	Model	Parameter	Time period	Referance
1.	CESM2-WACCM-FV2, NESM3, NorESM2-LM, CMCC-ESM2, IPSL-CM6A-INCA, E3SM-1-0, and NorESM2-MM	Precipitation	JAS	Gebresellase et al., 2022; Alemu et al., 2023; Berhanu et al., 2023; 2025.
2	NorESM2-MM, GFDL-CM4, HadGEM3-GC31-MM, NorESM2-LM, BCC-ESM1-MR, GFDL-ESM4, and MPI-ESM-1-2-HAM	Precipitation	MAM	Gebresellase et al., 2022; Alemu et al., 2023; Berhanu et al., 203; 2025.
3	EC-Earth3-veg, MRI-ESM2-0, MPI-ESM1-2-LR, ACCESS-ESM-1-5;	Temperature	MAM and JAS	Gebresellase et al., 2022

In addition to the climate data, daily observed streamflow data at the outlet of the Mojo catchment for the period 1981–2010 were obtained from the Ethiopian Ministry of Water Resources and used to calibrate and validate the SWAT+ model.

6.3 Methodology

6.3.1 Ensembles of CMIP6 models

The 1981–2010 period is used as a reference to assess changes in precipitation, Tmax, and Tmin during the 2020s (2014-2040), 2050s (2041–2070), and 2080s (2071–2100). The projected relative changes in precipitation extreme indices were calculated for the Awash Basin for the 2050s (2041–2070) and 2080s (2071–2100) under SSP245 and SSP585 scenarios, across all seasons. For the Mojo Catchment, projections also include the 2020s (2015–2040). This study employs five extreme indices obtained from the Expert Team on Climate Change Detection and Indices (ETCCDI) for historical and future periods. The selected indices were the total wet-day precipitation (PRCPTOT), consecutive dry days (CDD), consecutive wet days (CWD), maximum 5-day precipitation (Rx5day), and very wet days (R95pTOT). These indices provide a comprehensive framework for assessing high flows (flooding) and drought for historical and future periods (Gebrechorkos et al., 2023). The extreme indices were computed using R-based software (RClimDex 1.1) for each grid point and season separately, namely JAS (Kiremt) and MAM (Belg). Before conducting the statistical analysis, indices from the native resolutions of CMIP6 data and ENACTS were similarly interpolated to 1°×1° resolution using bilinear interpolation to facilitate computation and r comparison of results (Ayugi et al., 2021; Yang et al., 2023).

Most CMIP6 models exhibited a consistent systematic bias in Ethiopia and East Africa (Berhanu et al., 2023; Akinsanola et al., 2021; Berhanu et al., 2025).Thus, this study applies quantile mapping (QM) for precipitation and variance scaling for temperature to reduce systematic biases in individual models before generating ensembles (Gudmundsson et al., 2012). In this study, the ensemble mean of the bias-corrected selected models for index and season was generated to assess future climate extremes for the Awash basin and to drive a hydrological model to assess future hydrological changes in the Mojo catchment.

6.3.2 Hydrological model

6.3.2.1 Soil and Water Assessment Tool Plus (SWAT+)

The Soil and Water Assessment Tool Plus (SWAT+) (Bieger et al., 2017) was employed to evaluate the impacts of projected climate change on the hydrology of the Mojo catchment. The Soil and Water Assessment Tool (SWAT) modeling has recently been restructured to Soil and Water Assessment Tool Plus (SWAT+) (Bieger et al., 2017), which provides additional flexibility in routing water, nutrients, and sediment between watershed spatial objects (HRUs, aquifers, reservoirs, channels, routing units, wetlands). The SWAT+ is a next-generation, process-based, semi-distributed hydrological model developed to simulate the impacts of land management practices, climate variability, and other environmental changes on water, sediment, and agricultural chemical yields in large, complex watersheds over long periods. SWAT+ builds upon the original SWAT model by introducing a more flexible spatial representation of the landscape, allowing for the definition of multiple land use and management units within a subbasin and enhanced connectivity among hydrologic features such as channels, reservoirs, ponds, and wetlands. It incorporates modules for climate, hydrology, erosion, nutrient cycling, crop growth, and land management, enabling integrated watershed assessment under varying scenarios (Bieger et al., 2017).

6.3.2.2 Model input

SWAT+ requires a range of spatial and temporal datasets to simulate hydrology, sediment transport, and nutrient dynamics in a watershed. The input data for the SWAT model include climate data (daily precipitation, maximum and minimum temperature, solar radiation, relative humidity, wind speed), Digital Elevation Model (DEM), Land use/land cover, soil data and

streamflow data. The data type used in the development of the SWAT+ model of the Mojo and their sources are summarized in Table 6.2.

Table 6.2. Data sets utilized for SWAT+ to stimulate streamflow for Mojo catchment.

Datasets	Resolution	Source
Precipitation(ENACTS)	0.04° × 0.04°	EMI
Temperature (ENACTS)	0.04° × 0.04°	EMI
Wind speed	Simulated	Simulated from SWAT+ model
Solar radiation	Simulated	Simulated from SWAT+ model
Relative humidity	Simulated	Simulated from SWAT+ model
DEM		https:/www.asterweb.jpl.nasa.gov).
Land use and cover		FAO
Soil data		Water and Land Resource Center

6.3.2.3 Model calibration and validation

In this study, sensitivity analysis, calibration, and validation were performed using SWAT+ Toolbox Version 2.2. SWAT+ Toolbox is a specialized software tool designed to facilitate the calibration, validation, and sensitivity analysis of SWAT+ models. Before initiating the calibration process, a sensitivity analysis was performed to identify the most influential parameters affecting model output at the Mojo catchment, a sub-basin of the Awash basin. The purpose of this step is to determine which parameters significantly impact model behavior, allowing for a more focused and efficient calibration process. The analysis employed the Latin Hypercube-One Factor at a Time (LH-OAT) method, a global sensitivity analysis approach that systematically varies one parameter at a time across its defined range while holding others constant. Initial parameter ranges were selected based on existing literature (Gonfa and Kumar, 2016; Alemu et al., 2023; Onyutha et al., 2016; Bekele et al., 2018). A total of 14 parameters were chosen, and a first-order sensitivity analysis was conducted. A total of 1000 sample runs were executed on a Windows platform using four processing cores, ensuring comprehensive coverage of the parameter space and computational efficiency.

Following the sensitivity analysis, model calibration was carried out using daily streamflow observations. Both manual and automated approaches were employed to calibrate the SWAT simulations, followed by validation to assess the model's performance. The first one year of input data measurements was used for the "warming-up" of the models to estimate the initial state variables. The model was calibrated for 1982–2000 and validated for 2001–2010**.** The objective function used for calibration and validation across all scenarios is evaluated using statistical

metrics such as the Nash–Sutcliffe efficiency (NSE), Kling–Gupta Efficiency (KGE), percent bias (PBIAS), and root mean square error (RMSE). Further, we used SWAT+Editor to set up the project, edit SWAT+ inputs, run the model, and check the QSWAT+ model (Bieger et al., 2017).

6.3.2.4 Hydrological droughts and floods

Daily streamflow at the outlet of the Mojo catchment was estimated for both the historical period (1981–2010) and future period (2015–2100). To evaluate projected changes in streamflow across the rivers of the Mojo catchment within the Awash basin, the percentage change relative to the historical reference period was calculated for three future time slices: the 2020s (2015–2040), 2050s (2041–2070), and 2080s (2071–2100), under two climate scenarios, SSP245 and SSP585. The identification of hydrological extremes in this study used a percentile-based approach. Specifically, the hydrological drought (duration and severity) threshold was defined as the 20th percentile of the projected streamflow. The 20th percentile (i.e., flow exceeded 80% of the time) represents the flow value below which streamflow is unusually low and classified as a severe hydrological drought (Rivera et al., 2017). Flows below this threshold were considered to reflect periods of water scarcity that could impact ecological systems, water supply, and riverine management (Rivera et al., 2017; Gebrechorkos et al.,2023). Further, the frequency and duration of high flows (floods) are assessed. The flood threshold was defined as the 90th percentile of streamflow, representing flows above which conditions are considered unusually high. Streamflow exceeding this threshold was interpreted as an indicator of potential flood events (Gebrechorkos et al.,2023), which could pose risks to infrastructure, communities, and riverine ecosystems.

6.4 Results

6.4.1 Historical trends of precipitation extremes in the Awash basin

The spatial distribution of PRCPTOT, CWD, CDD, R99pTOT and Rx5days across the Awash basin during 1981–2010 reveals marked differences among the Upper, Middle, and Lower Awash basins. Figure 6.2 shows historical trends for PRCPTOT, CWD, CDD, R99pTOT and Rx5day for the period 1981–2010 during MAM for the Awash basin. The Upper Awash basin, which includes highland areas such as Addis Ababa and the surrounding mountainous regions, exhibits a mixed trend in PRCPTOT (Figure 6.2a) during the MAM season, with changes of less than 2 mm per season. A slight increase in CDD (up to 1 day per season) is observed (Figure 6.2c), while

decreasing trends are found in CWD (Figure 2b), Rx5day (Figure 6.2d), and R99pTOT (Figure 6.2e) across most parts of the Upper Awash basin. In contrast, the Middle Awash basin, a transitional zone between the highlands and the lowland Rift Valley, shows a decline in PRCPTOT, CWD, R99pTOT, and Rx5day values (Figure 6.2). However, CDD trends are increasing across the region, with values ranging from 1 to 4 days per season. The Lower Awash basin, situated in the arid Afar lowlands, exhibits a mixed trend in PRCPTOT (Figure 6.2a) over the study period. Meanwhile, the Lower Awash basin shows declining trends in CWD, R99pTOT, and Rx5day, accompanied by a strong and consistent increase in CDD across all areas.

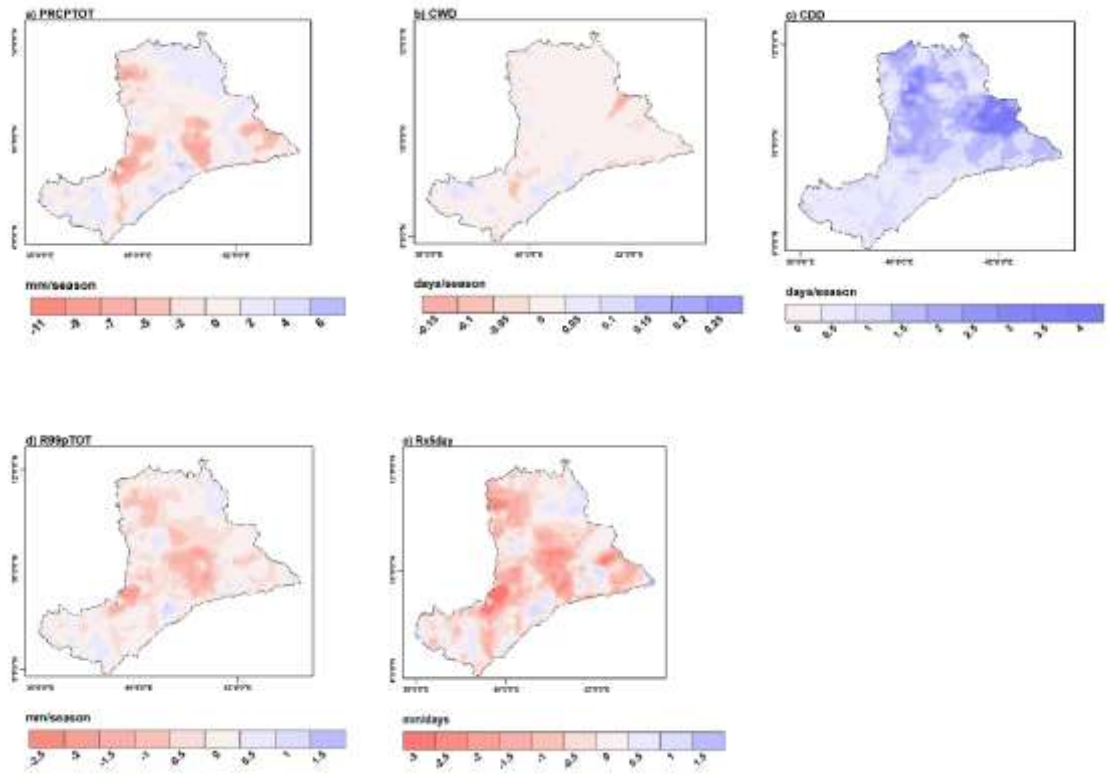

Figure 6.2: Historical trends for PRCPTOT (a), CWD (b), CDD (c), R99pTOT (d) and Rx5day (e) for the period 1981–2010 during MAM for the Awash basin.

Figure 6.3 shows historical trends for PRCPTOT (a), CWD (b), CDD (c), R99pTOT (d), and Rx5day (e) for the period 1981–2010 during the JAS season for the Awash basin. During the JAS season, the Upper Awash basin exhibits an increasing trend in PRCPTOT, with projected rises of up to 12 mm, while a mixing trends are observed across the Middle and Lower Awash basins

(Figure 6.3a). Notably, some parts of the Middle Awash basin experience the most substantial reduction, with declines reaching up to 24 mm. In terms of CWD (Figure 6.3b), the Upper basin shows an increase (up to 48 mm), whereas the Lower basin reveals a declining trend, and the Middle basin displays spatially mixed signals. A notable increase in CDD (Figure 6.3c) is observed across large parts of the Middle and Lower basins. In contrast, the Upper Awash basin shows a mixed pattern of change. For R99pTOT (Figure 6.3d), a mixed is detected in most areas of the Upper and Middle Awash basin, while the Lower basin experiences an increasing trend. Rx5day (Figure 63e) shows an increasing trend throughout much of the Awash basin, though some areas in the Middle basin exhibit notable localized decreases of up to 2.4 mm.

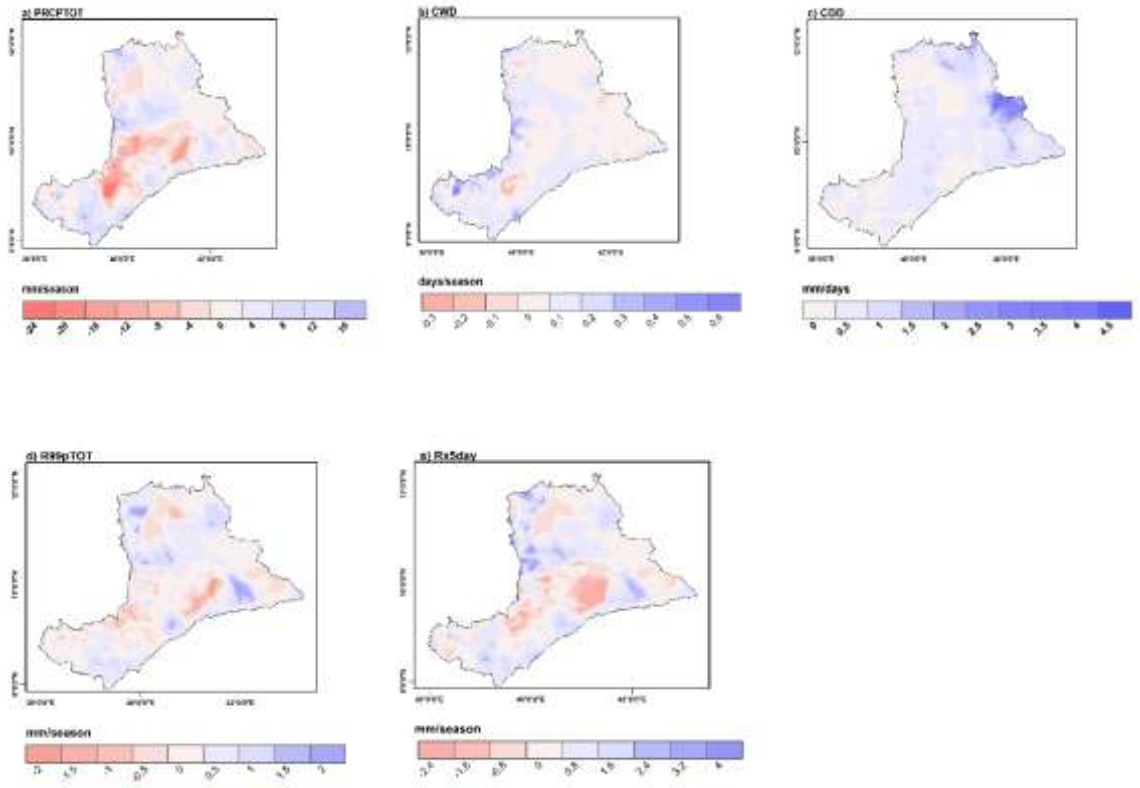

Figure 6.3: Historical trends for PRCPTOT (a), CWD (b), CDD (c), R99pTOT (d) and Rx5day (e) for the period 1981–2010 during JAS for the Awash basin.

6.4.2 Seasonal projection in precipitation extremes in the Awash basin

Figure 6.4 shows projected changes in PRCPTOT for two time periods (2050s and 2080s) and two scenarios (SSP245 and SSP585) during the MAM (March-May) and JAS seasons (July-

September). The projected relative changes in PRCPTOT are generally more consistent across both the 2050s and 2080s, under SSP245 and SSP585 during the MAM season than during the JAS season. An increase in PRCPTOT is projected for the Upper and Lower Awash basin during both time periods and scenarios, while a decrease is expected in the Middle Awash basin during the MAM season (Figure 6.4). A greater increase in projected PRCPTOT (up to 50%) is observed in the Upper Awash basin and in certain areas of the Lower Awash basin, particularly the Afar lowlands, during the MAM season (Figure 6.4 a-d). During the JAS season, PRCPTOT is projected toincrease substantially across all parts of the basin in the 2050s under both scenarios (Figures 6.4e and 6.4f). By the 2080s (Figures 6.4g, 6.4h), a continued increase in PRCPTOT is projected in the Middle and Lower Awash basins under SSP245 and SSP585, whereas a slight decrease is observed in some areas of the Upper Awash basin under SSP585.

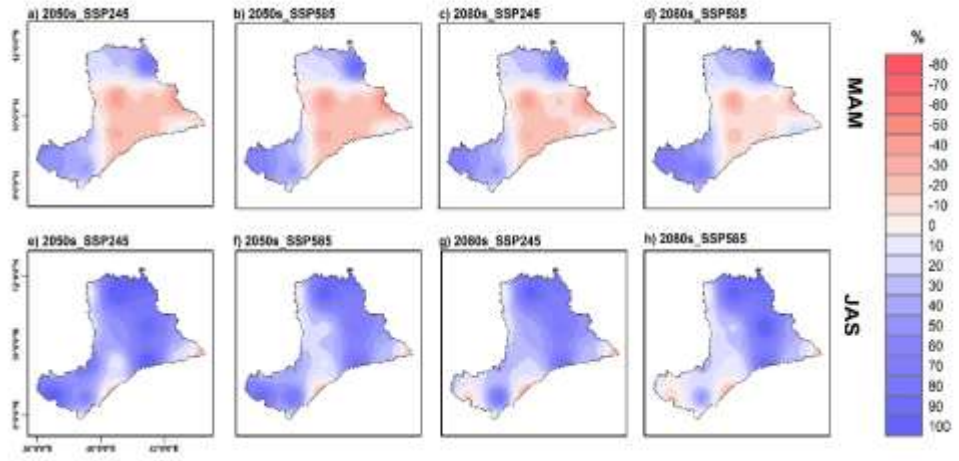

Figure 6.4: Projected change in PRCPTOT (%), relative to the reference period (1981–2010), during MAM (a-d) and JAS (e-h) for the 2050s and 2080s under SSP245 and SSP585 scenarios.

Figure 6.5 shows projected changes in the CWD (%) relative to the reference period (1981–2010) during the MAM and JAS seasons for the 2050s and 2080s, under SSP245 and SSP585, across the Upper, Middle, and Lower Awash basins. A slight increase in CWD (up to 10%) is projected in the Upper and Lower Awash basins during the MAM season for both the 2050s and 2080s under SSP245 and SSP585, with a more pronounced increase observed in the 2080s under both scenarios, particularly in the Lower Awash basin. Notably, the Afar lowlands within the lower basin show a higher increase in CWD (up to 50%) during MAM compared to other sub-regions (Figure 6.5a-d).

However, in the Middle Awash basin, a decline in CWD is projected during the MAM season across both scenarios and timeframes. During the JAS season, the entire Awash basin is projected to experience an increase in CWD across both future periods (2050s and 2080s) and under both scenarios (SSP245 and SSP585) (Figure 6.5e-h). A moderate to high increase in CWD (ranging from 40% to 100%) is projected in the Middle and Lower Awash basins in the 2050s and 2080s under both scenarios while a slight increase in CWD is projected in the Upper Awash basin. The highest increases are observed in the 2050s under SSP585 (Figure 5b) and in the 2080s under SSP245 (Figure 6.5c).

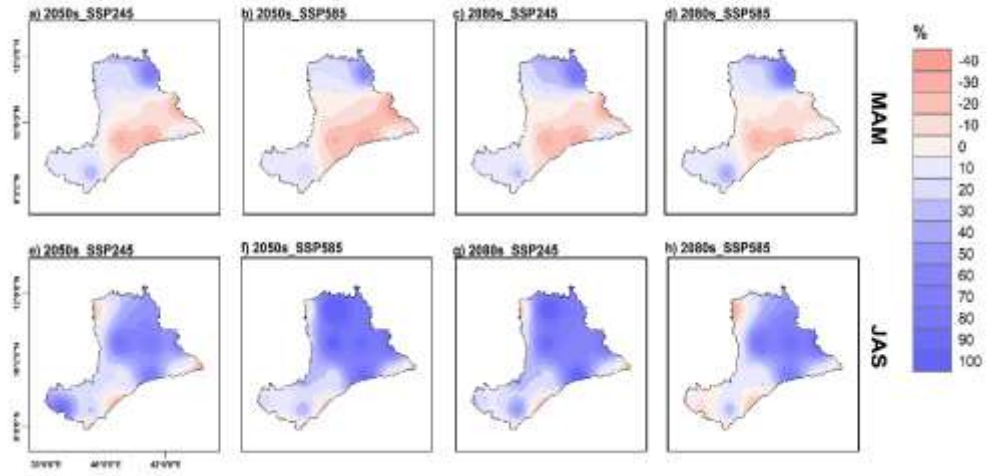

Figure 6.5: Projected change in CWD (%), relative to the reference period (1981–2010), during MAM (a-d) and JAS (e-h) for the 2050s and 2080s under SSP245 and SSP585 scenarios.

Figure 6.6 shows the projected changes in CDD relative to the 1981–2010 reference period across the Upper**,** Middle, and Lower parts of the Awash Basin for the MAM and JAS seasons, in the 2050s and 2080s, under SSP245 and SSP585 climate scenarios. During the MAM season, the Upper Awash basin shows a slight decrease in CDD (ranging from 0% to 10%) across both time periods and scenarios (Figure 6.6a-d). In contrast, the Middle Awash basin experiences a significant increase in CDD, with the highest rise (up to 40%) projected in the 2050s under SSP585 (Figure 6.6b) and in the 2080s under SSP245 (Figure 6.6c). The Lower Awash basin displays an increase in CDD during the 2050s under SSP245 (Figure 6.66a), while other periods and scenarios exhibit mixed trends. In the JAS season, projections show a slight to strong decrease in CDD across all parts of the basin for both time periods and scenarios (Figure 6.6e-h). An exception is observed

in the Upper Awash basin, where a slight increase in CDD is projected in the 2080s under SSP585 (Figure 6.6h).

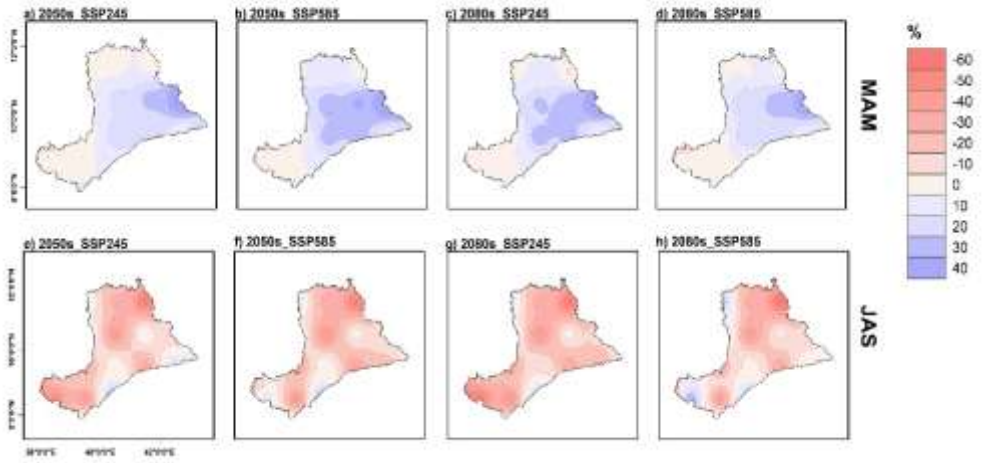

Figure 6.6: Projected change in CDD (%), relative to the reference period (1981–2010), during MAM (a-d) and JAS (e-h) for the 2050s and 2080s under SSP245 and SSP585 scenarios.

Figure 6.7 presents the projected changes in R99pTOT relative to the 1981–2010 reference period for the Upper, Middle, and Lower Awash basin during the MAM and JAS seasons, for the 2050s and 2080s, under SSP245 and SSP585 scenarios. During the MAM season (Figure 6.7a-d), the Upper Awash basin shows a consistent increase in R99pTOT across all scenarios and time periods, with a significant rise of up to 70% projected by the 2080s under SSP585 (Figure 6.7d). In contrast, the Middle Awash basin shows a moderate decrease in R99pTOT, particularly in the 2050s under SSP245 (Figure 6.7a), with reductions of up to 30%. The Lower Awash basin generally shows a decline in R99pTOT across most scenarios and periods, especially in the 2050s under SSP585 (Figure 6.7b) and the 2080s under both scenarios (Figure 6.8c, d), except for an increase observed in the 2050s under SSP245. Notably, the Afar lowlands exhibit an increase in R99pTOT during MAM in both timeframes and scenarios. In the JAS season, a similar pattern is observed in the Upper Awash Basin (Figure 6.7e-h). The Upper Awash Basin again shows a consistent increase in R99pTOT in both the 2050s and 2080s, with a particularly notable rise in the 2050s, where projections range from 20% to 50% under both SSP245 and SSP585 scenarios (Figure 6.7e, f). The Middle Awash basin shows a decrease in R99pTOT in the 2050s under both scenarios, followed by a slight to moderate increase (up to 20%) in the 2080s. In the Lower Awash Basin,

R99pTOT is projected to increase in the 2080s under both scenarios (Figure 6.7g, h), while a decrease is observed in the 2050s under SSP245 (Figure 7e), and mixed trends appear in the 2050s under SSP585 (Figure 6.7f).

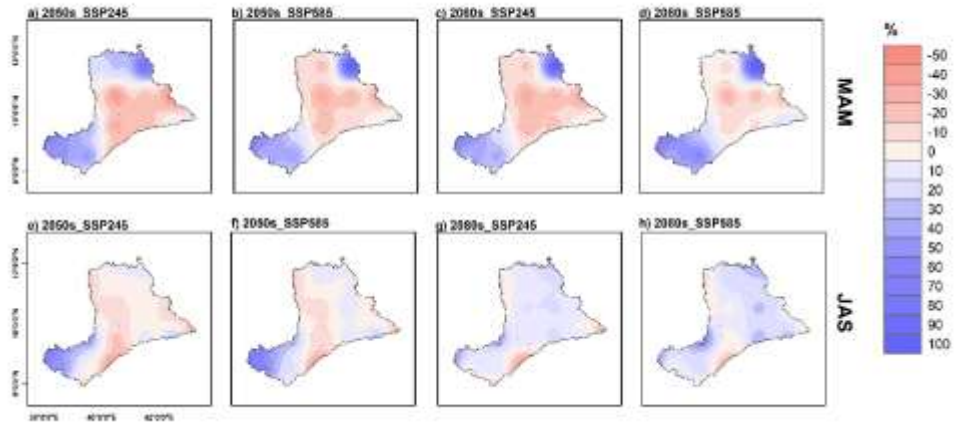

Figure 6.7: Projected change in R99pTOT (%), relative to the reference period (1981–2010), during MAM (a-d) and JAS(e-h) for the 2050s and 2080s under SSP245 and SSP585 scenarios.

Figure 6.8 presents the projected changes in Rx5day relative to the 1981–2010 reference period for the Upper, Middle, and Lower Awash basins, during the MAM and JAS seasons, in the 2050s and 2080s, under both SSP245 and SSP585 scenarios. During the MAM season (Figure 6.8 a-d), the Upper Awash basin shows a consistent increase in Rx5day, with projections rising from moderate increases in the 2050s to very large increases (up to 70%) by the 2080s, particularly under SSP585. In the Middle Awash basin, most areas exhibitdecreases in Rx5day, ranging from small to moderate, with the strongest declines in the 2050s under SSP245 (Figure 6.8a) and slightly weaker reductions by the 2080s (Figure 6.8c, 6.8d). The Lower Awash basin shows small to moderate increases, with the highest values (up to 50%) projected in the 2080s under both scenarios. During the JAS season, the Upper Awash basin displays a slight increase in Rx5day in the 2050s under both scenarios (Figure 6.8e, f), followed by a decrease in the 2080s under SSP585 (Figure 6.8h), and a mixed pattern under SSP245 (Figure 6.8g). The Middle Awash basin shows a decrease in the 2050s under both scenarios, but an increase by the 2080s under SSP245, with mixed trends under SSP585. In the Lower Awash basin, Rx5day is projected to increase in both the 2050s

and 2080s across all scenarios, with the largest increase occurring toward the 2080s (Figures 6.8 g, 6.8h).

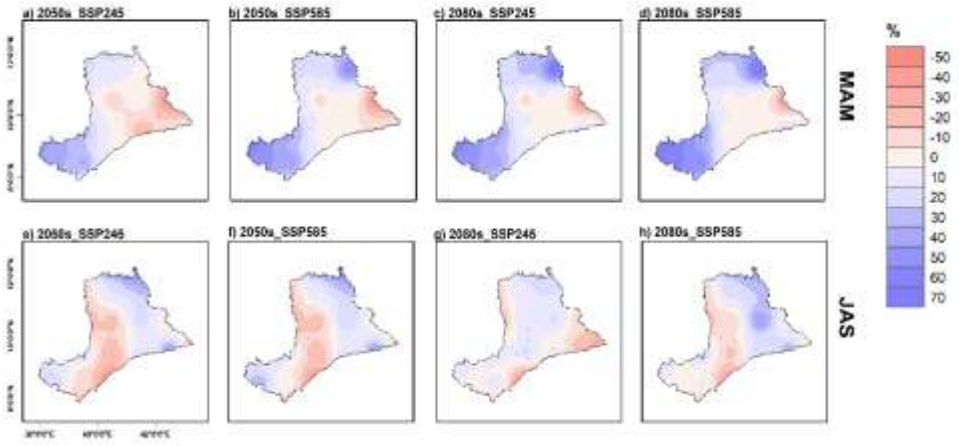

Figure 6.8: Projected change in Rx5day (%), relative to the reference period (1981–2010), during MAM (a-d) and JAS (e-h) for the 2050s and 2080s under SSP245 and SSP585 scenarios.

6.4.3 Projected changes in precipitation and temperature on the Mojo catchment

Figure 6.9 shows the projected percentage changes in monthly precipitation under SSP245 and SSP585 scenarios, compared to the historical reference period (1981–2010). The projections are categorized into three future periods: 2015–2040 (2020s), 2041–2070 (2050s), and 2071–2100 (2080s). During the near-term projection (2020s), both scenarios indicate significant seasonal variability. SSP245 projects the maximum increase in precipitation in August (+19%) and January (+16%). SSP585 shows a stronger response, with the greatest increases in January (+32%) and August (+30%). The largest decreases are observed in March and May, with precipitation reductions ranging from −22% to −24% under both scenarios (Figure 6.9).

In the mid-century period (2040s), the projected increases in precipitation become more pronounced. Mean annual precipitation is projected to rise by +20.72% under SSP245 and +25.13% under SSP585. Maximum monthly increases are projected for January (+37% under SSP245, +43% under SSP585) and August (+32% and +37%, respectively). March and May continue to show declines, although the magnitude of the decline is somewhat smaller than in the 2020s, ranging from −11% to −14% (Figure 6.9). By the late-century period (2070s), precipitation

changes are projected to be most extreme, particularly under the high-emission scenario (Figure 9). SSP245 projects a maximum increase of +59% in January and +39% in August. SSP585 shows further amplification, with January increasing by +63% and August by +42%. The intensity of reductions is relatively moderate, with March decreasing by −11% to −13% under SSP245, and by −7% under SSP585. April shows a small decline (−3%) under SSP585.Generally, increases in precipitation are expected in January, February, July, August, September, October, and November. Decreases are consistently projected for March, April, May, and June (Figure 6.9).

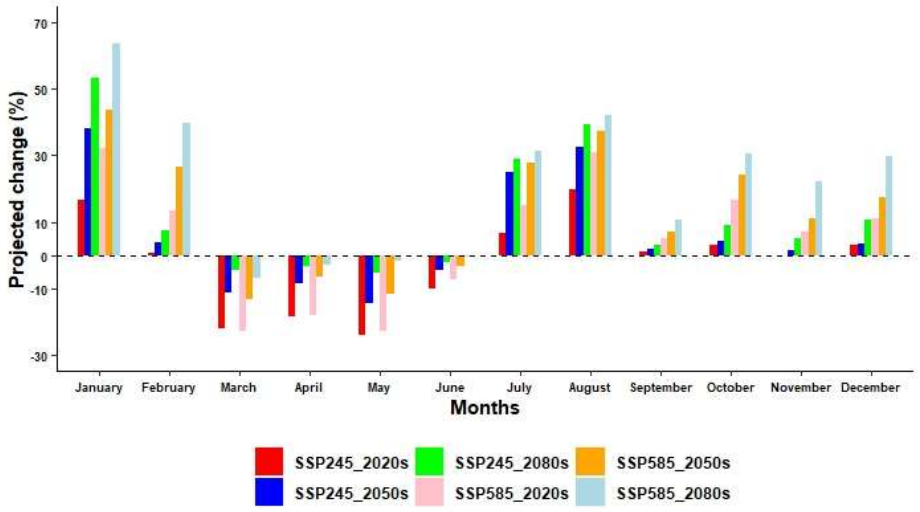

Figure 6.9: Projected monthly average precipitation change, relative to the reference period (1981-2010), for the 2020s, 2050s and 2080s under the SSP245 and SSP585 scenarios for the Mojo catchment.

Figure 6.10a presents the projected monthly average temperature cycle and percentage change for the maximum (Tmax) under the SSP245 and SSP585 scenarios across three future periods 2020s, 2040s, and 2070s. Overall, the results indicate a consistent warming trend under both scenarios, with Tmax expected to increase throughout the century. On average, the maximum temperature is projected to rise by approximately 0.7°C under SSP245 and 0.9°C under SSP585.

During the 2020s, Tmax under SSP245 is projected to increase modestly, ranging from 0.1°C in January to 0.4°C in March and June. Under SSP585, the increase is slightly greater, ranging from 0.2°C in July to 0.8°C in February and October. Although early-century warming is moderate, it shows variability across months. In the 2050s, the warming becomes more pronounced and evenly

distributed throughout the year. Under SSP245, Tmax increases are projected to range from 0.6°C in July and August to approximately 0.9°C in April, May, and June. Under SSP585, the increase ranges from 0.7°C in August and September to about 0.9°C in May and June, indicating a notable warming trend during the late spring and early summer months. By the 2080s, Tmax increases substantially under both scenarios. Under SSP245, the temperature rise ranges from approximately 1.0°C in July and August to 1.4°C in June. Under the high-emission scenario SSP585, projected Tmax increases range from around 1.2°C in August and September to a peak of 2.0°C in June. These projections reveal a strong seasonal signal, with the most significant warming occurring during the summer months, particularly from May to July (Figure 6.10a).

Notably, June consistently exhibits the highest projected temperature increase across all periods, especially under SSP585 in the 2070s, where it reaches around 2.0°C. Although the warming in July and August is slightly lower, it remains part of the overall increasing trend. The higher temperature increases under SSP585, compared to SSP245 (Figure 6.10a).

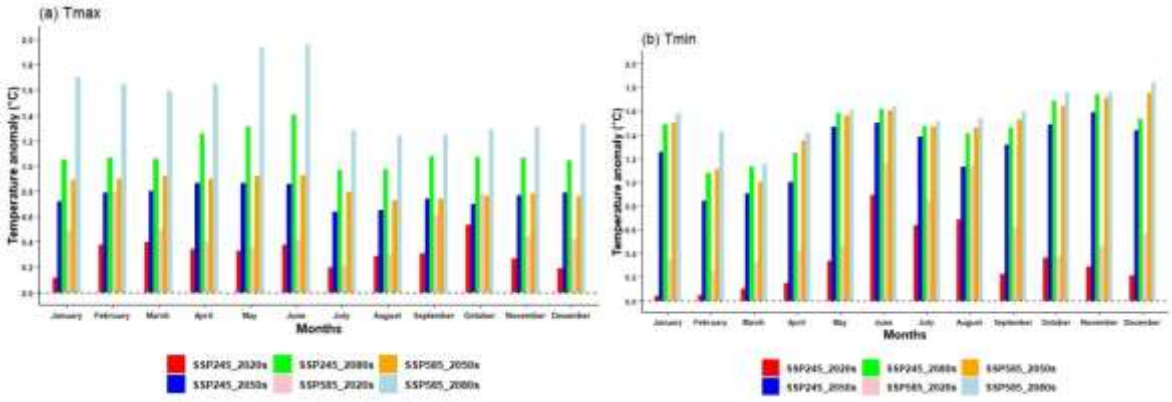

Figure 6.10: Projected monthly average temperature anomaly for Tmax (a) and Tmin (b), relative to the reference period (1981-2010), for 2020s, 2050s, and 2080s under the SSP245 and SSP585 scenarios for the Mojo catchment.

Figure 6.10b presents projected changes in monthly average minimum temperature (Tmin) under the SSP245 and SSP585 emission scenarios for the 2020s**,** 2040s, and 2070s. During the 2020s, Tmin is projected to increase under SSP245 from approximately 0.04°C in January to 0.9°C in June. Under SSP585, the warming is slightly higher, ranging from 0.2°C in February to 1.2°C in June. The smallest increases occur between February and April, with values gradually rising from

mid-year through December. For the 2040s, Tmin increases further, with SSP245 projecting a rise from 0.8°C in February to 1.6°C in November, while SSP585 shows a more substantial increase, ranging from ~1.2°C in March to 1.8°C in December. By the 2070s, Tmin increases become more pronounced. Under SSP245, projected increases range from ~1.1°C in February and March to 1.7°C in October and November. Under SSP585, Tmin increasesby up to ~1.9°C, with December exhibiting the largest increase. Overall, warming is persistent throughout all months and time periods, with the greatest increases occurring during the cooler months (e.g., December and January. Seasonally, summer months (June–August) exhibit moderate Tmin increases (~1.3–1.6°C) by the 2070s under both scenarios. The autumn to winter period (October–December) shows stronger increases under SSP585, particularly in December (~1.9°C). In contrast, the spring months (March–May) exhibit relatively smaller increases, though they still show a consistent warming trend over time.

6.4.4 Change in hydrological and hydrological extremes on the Mojo catchment

6.4.4.1 Sensitivity of model parameters

The sensitivity analysis for the Mojo Catchment identified nine parameters that exert the greatest influence on SWAT+ model performance. These parameters represent a wide range of model components, including the Hydrologic Response Unit (HRU), soil layer, aquifer, and basin processes, highlighting the integrated nature of hydrological responses within the catchment (Table 6.3).

Among the HRU-related parameters, CN2 (SCS runoff curve number) was found to be the most sensitive, with a fitted adjustment of 68.5%, underscoring its critical role in simulating surface runoff. Similarly, CN3_SWF, representing soil water retention adjustments, and CANMX (maximum canopy storage) strongly influenced evapotranspiration and interception processes. Parameters such as ESCO (soil evaporation compensation factor) and PERCO (percolation coefficient) further emphasize the importance of soil–water interactions in driving hydrological dynamics. Soil-related processes were significantly affected by K (saturated hydraulic conductivity) and AWC (available water capacity), both of which govern infiltration and water-holding capacity. From the aquifer group, REVAP_CO (revap coefficient) was highly influential in regulating upward water transfer from shallow aquifers to the root zone. At the basin scale,

SURLAG (surface runoff lag coefficient) emerged as a key control parameter, affecting runoff timing and streamflow response.

Overall, the analysis indicates that parameters governing runoff generation (CN2, CN3_SWF, SURLAG), soil–water processes (K, AWC, PERC0, ESCO, CANMX), and groundwater interactions (REVAP_CO) are critical for accurate hydrological simulation in the Mojo Catchment. These findings provide a strong basis for targeted calibration, ensuring that the most influential processes are well-constrained to improve model reliability.

Table 6.3: List of top 9 sensitive parameters at the Mojo catchment at the locations of the Awash basin.

ID	Name	Unit	Group	Change Type	Set Min	Set Max	Fit Value Manual
1	CN2	-	hru	Percent	0	100	68.515
2	CN3_SWF	-	hru	Replace	0	1	0.012
3	CANMX	mm	hru	Percent	0	100	13.374
4	PERCO	-	hru	Replace	0	1	0.01
5	K	mm hr^{-1}	sol	Replace	0	2000	1380.6
6	REVAP_CO	-	aqu	Replace	0.02	0.2	0.027
7	ESCO	-	hru	Replace	0	1	0.07
8	SURLAG	days	bsn	Replace	0.05	24	2.843
9	AWC	mm mm^{-1}	sol	Replace	0.01	10	0.02

6.4.4.2. Hydrological model calibration and validation

Figure 6.11 illustrates the comparison between observed and simulated streamflow during the calibration and validation period. The performance of the SWAT+ model was evaluated in a two-phase process: calibration and validation using observed discharge data from the Mojo catchment within the Awash Basin. The blue dashed line represents the observed discharge, while the orange dotted line indicates the simulated discharge from the SWAT+ model. From Figure 6.11, it is evident that the model successfully captures the overall seasonal and interannual variability in streamflow. The hydrological model performs reasonably well for low and medium flows, but less so for high flows. Additionally, the timing of peak flows is generally well-represented, although there are instances in which the model slightly underestimates or overestimates the magnitude of peak discharges. Despite these discrepancies, the simulated discharge closely aligns with observed values for the majority of the period.

During the calibration period, the model achieved an NSE of 0.692 and increased to 0.731 during validation. This suggested that the model maintained robust predictive performance even when tested with independent data. Similarly, the KGE values were 0.743 and 0.752 for the calibration and validation periods, respectively. These values fall within the "good" to "very good" performance range, demonstrating that the model effectively captured the temporal variability and magnitude of observed flows. The RMSE was 15.297 m^3/s during calibration and decreased to 11.198 m^3/s during validation. This reduction indicates improved accuracy in flow simulation over time. Furthermore, the Pbias values were -5.487% for calibration and -0.523% for validation. The slightly negative PBIAS indicates a minor tendency toward overestimation, but it remains within acceptable limits. Overall, these results affirm the model's suitability for hydrological simulations of future hydrological extremes and for water resource management in the study area.

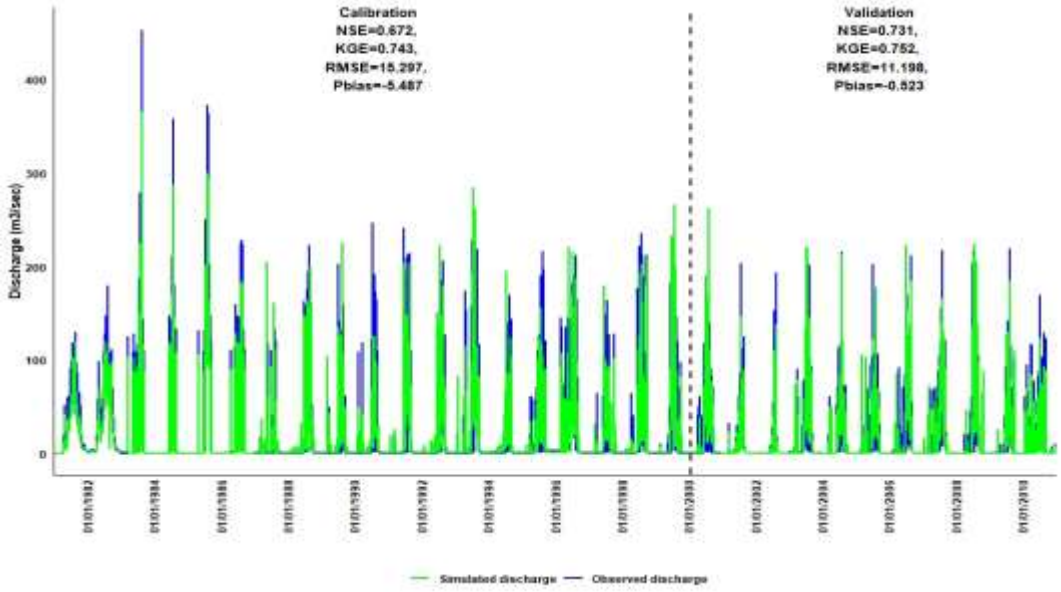

Figure 6.11: Measured and simulated daily stream flow for SWAT+ models for river gauge station at Mojo catchment.

6.4.4.3 Projected change in seasonal streamflow

The future behavior of streamflow in the Mojo catchment under climate change was analyzed by comparing the monthly relative change in discharge (%) to a historical baseline under two SSP245 and SSP585 for the 2020s, 2050s, and 2080s (Figure 6.12). A positive percentage indicates an

increase in streamflow relative to the historical average, whereas a negative percentage indicates a decline. A distinct seasonal pattern is observed across all scenarios and time periods, with strong contrasts between the dry/short rainy seasons and the main rainy season. During January and February, which typically mark the early rainy season, discharge is projected to decline modestly across all scenarios. Reductions range from approximately 10% to 30%, with larger declines under SSP585.

The most critical reduction in discharge occurs during the short rainy season (March to May). In this period, discharge decreases by 80% to nearly 100%, especially under SSP585 for the 2050s and 2080s projections. In contrast, the long rainy season (July–September) shows a consistent and significant increase in discharge across all future scenarios. The most notable changes occur in July and August, where streamflow increases by up to 60–70% under SSP585 by 2080s. September also shows a sustained increase, albeit more moderate than in July and August, further suggesting a prolonged wet season under future conditions. During the post-rainy dry season (October–December), streamflowchanges are relatively small, generally within ±20% across all scenarios and time periods. Overall, increases in absolute discharge are more pronounced during the wet season than in the dry season.

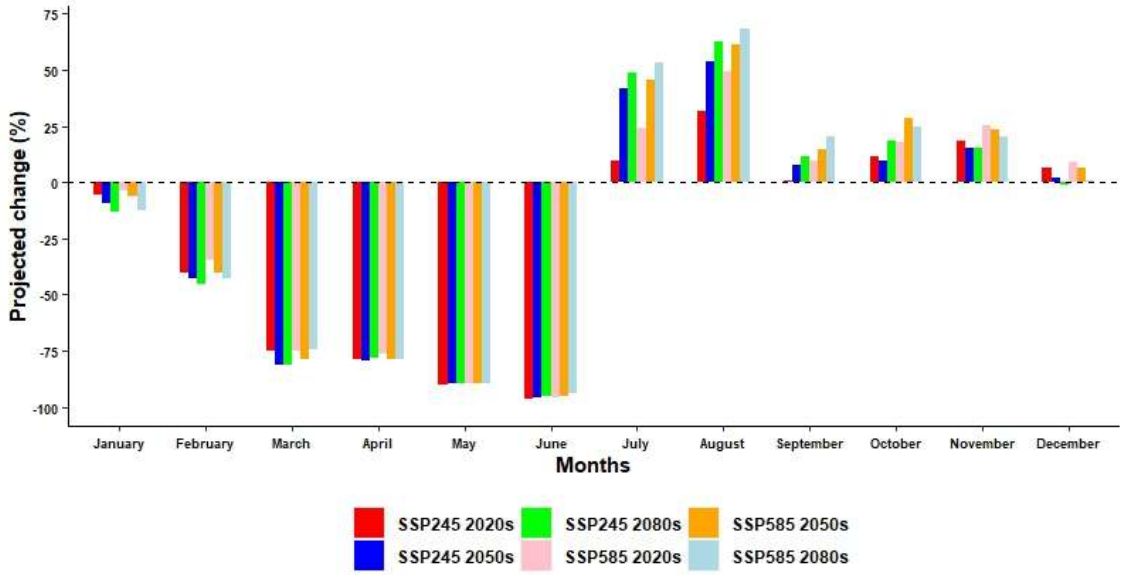

Figure 6.12: Projected change in mean monthly streamflow (%), relative to the reference period (1981-2010) for the 2020s, 2050s, and 2080s under SSP245 and SSP585.

6.4.4.4 Projected change in hydrological extremes

Figure 6.13 presents the projected drought duration day and severity (%) for the 2020s, 2050s, and 2080s relative to the 1981–2010 baseline under SSP245 and SSP585. In both scenarios, drought duration and severity are expected to be greater in the 2080s than in the 2020s or 2050s. In the Mojo catchment, drought duration under SSP245 is projected to increase by approximately 20%, 26%, and 29% in the 2020s, 2050s, and 2080s, respectively, compared to the reference period. Under SSP585, drought duration is projected to increase by about 22%, 27%, and 34% in the 2020s, 2050s, and 2080s, respectively. Similarly, drought severity follows a similar trend, climbing from 22% in the 2020s to 36% by the 2080s. Drought severity under SSP245 is projected to increase by around 22%, 27%, and 36% in the 2020s, 2050s, and 2080s, respectively, whereas under SSP585, the corresponding increases are about 25%, 30%, and 35%. In both scenarios, severity in the 2080s is higher than in the 2050s. Overall, the results indicate that drought duration and severity in the Moo catchment tend to intensify throughout the 21st century (Figure 6.13).

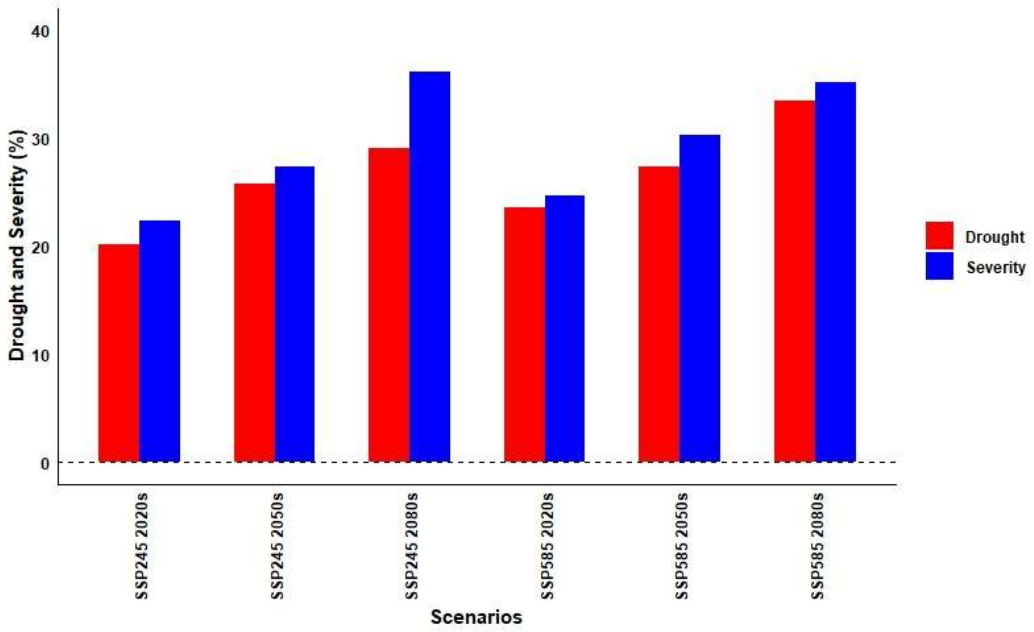

Figure 6.13: Projected change in drought duration days and severity (%), relative to the reference period (1981–2010), for the 2020s, 2050s, and 2080s under SSP245 and SSP585.

Figure 6.14 examines the projected percentage change in the number and frequency of flood events for three future time horizons (2020s, 2050s, 2080s) relative to the historical baseline period of

1981–2010. Under the SSP245 scenario, the number of flood events shows a slight decrease of about 8% in the 2020s relative to the baseline, followed by a marked increase of approximately 20% in the 2050s and a further rise to around 33% in the 2080s. This indicates a steady upward trendsince the mid-20th century. Flood frequency under SSP245 increases modestly by about 2% in the 2020s, then rises significantly by roughly 28% in the 2050s and reaches around 39% in the 2080s. Under the high-emission SSP585 scenario, the number of flood events shows a small decrease of about 4% in the 2020s, followed by a strong increase of approximately 30% in the 2050s and a substantial rise to around 39% in the 2080s, exceeding SSP245 projections for the same period. Flood frequency increases notably by about 10% in the 2020s, rises strongly by roughly 32% in the 2050s, and reaches a very large increase of around 48% in the 2080s. Generally, across both scenarios, projections indicate a general increase in both the number of flood events and their frequency as the century progresses. The magnitude of change is greater for the high-emission SSP585 scenario, especially toward the latter part of the century (2080s).

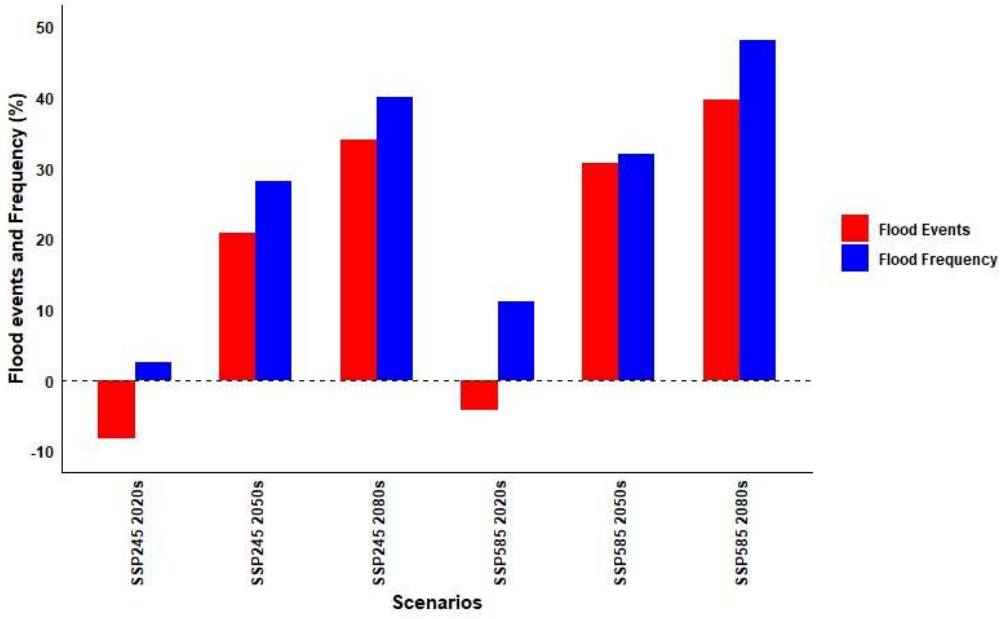

Figure 6.14: Projected change in number and frequency of flood events (%), relative to 1981–2010, for the 2020s, 2050s, and 2080s under SSP245 and SSP585.

6.5 Discussion

The spatial and temporal variability of precipitation and extreme rainfall indices across the Awash basin reflect the complex interactions between topography, atmospheric circulation, and regional moisture dynamics. Historical observations reveal clear contrasts between the Upper, Middle, and Lower basins, indicating that localized climatic drivers strongly influence rainfall behavior in each sub-basin. During the March–May (MAM) season, the Upper Awash basin exhibited mixed changes in total precipitation (PRCPTOT), with marginal fluctuations of less than 2 mm per season. Concurrent declines in Rx5day, CWD, and R99pTOT suggest a tendency toward reduced wet spell intensity, despite a slight rise in CDD. In contrast, the Middle basin displayed more consistent drying trends during MAM, with decreases in PRCPTOT, CWD, R99pTOT, and Rx5day, accompanied by notable increases in CDD (up to 4 days). This pattern indicates more frequent dry spells and heightened drought vulnerability.

The arid Lower basin experienced pronounced increases in CDD alongside declines in wet-spell indices, reflecting intensifying water stress. Seasonal reversals were observed during July–September (JAS), however, with the Upper basin showing gains in PRCPTOT and CWD, indicative of wetter conditions and prolonged wet spells. Meanwhile, the Middle and Lower basins continued to experience declines in PRCPTOT and increased CDD, which may indicate persistent dryness. Nevertheless, an increase in Rx5day trends across much of the basin during JAS indicates a shift toward more intense, short-duration rainfall events, which may raise flood risks even in regions where total seasonal rainfall is projected to decrease. These observations align with previous studies reporting non-significant increases in rainfall during the major rainy season (JAS) and significant declines during the minor rainy season (MAM) (Duguma et al., 2021; Bekele et al., 2017; Tadese et al., 2019). Precipitation in the Awash Basin is projected to increase over the course of the century, with the largest increases occurring in the mid-future period. Although areas of maximum precipitation—particularly in the upper parts of the basin expand spatially over time, these high-precipitation events occur less frequently while exhibiting higher rainfall intensity (Legass et al., 2025).

Future projections reveal strong seasonal and spatial dependencies. During MAM, both SSP245 and SSP585 scenarios suggest increasing PRCPTOT in the Upper and Lower basins, with the most

pronounced gains (up to 50%) occurring in the Afar lowlands by the 2080s. These increases coincide with higher CWD, particularly in the Lower basin, where wet spell durations may increase by up to 50%, potentially enhancing water availability but simultaneously increasing flood hazard potential. Conversely, the Middle basin is projected to experience declining PRCPTOT and CWD, coupled with rising CDD, highlighting prolonged dry spells and increased drought risk. Extreme rainfall indices, particularly R99pTOT and Rx5day, indicate intensification of heavy precipitation events, especially in the Upper basin during MAM, where R99pTOT could increase by up to 70% under SSP585 by the 2080s. Such trends suggest that rainfall will not only become more frequent but also more intense, exacerbating flood potential. In contrast, the Middle basin often shows reductions in these extremes during MAM, which worsens dry-season water scarcity. The observed decrease in precipitation projection during MAM across most parts of the basin aligns with historical trends (Alemu et al., 2023; Duguma et al., 2021; Taye et al., 2018; Daba et al., 2015; Eshetu et al., 2020). Contrary to those findings, previous studies showed an increase in precipitation during MAM in Ethiopia, Kenya, and Uganda throughout the 21st century (Gebrechorkos et al., 2019; 2022; ICPAC, 2016; Tierney et al., 2015). These discrepancies likely stem from differences in the climate models employed, emission scenarios, spatial resolution, and the representation of regional climate dynamics, highlighting the inherent uncertainties in rainfall projections (Taguela et al., 2025; Choi et al., 2023).

During JAS, projections indicate basin-wide increases in CWD, particularly in the Middle and Lower basins, which may rise by 40–100%. This shift toward more persistent wet spells could exacerbate runoff and erosion risks in flood-prone lowlands. Conversely, CDD generally declines across the basin, except in the Upper basin under SSP585 in the 2080s, suggesting localized intensification of dry spells. The divergence of trends between the Upper, Middle, and Lower basins underscores the need for geographically targeted adaptation strategies. Flood management infrastructure and early-warning systems will be critical in the Upper basin, especially during MAM when heavy rainfall events are expected to intensify. The Middle basin faces dual challenges of water scarcity in MAM and potential flooding in JAS, necessitating flexible management approaches. In the Lower basin, projected increases in PRCPTOT and CWD may improve water supply but heighten the risks of flash floods and sediment transport, particularly given the fragile soils of the Afar lowlands.

Projected rainfall and temperature changes in the Mojo catchment demonstrate strong coupling between seasonal climate variability and hydrological extremes. Precipitation shows consistent increases during the main rainy season (July–September) but persistent declines during the short rainy season (March–May). Under SSP585, rainfall is projected to rise by up to 42% in July and August, reflecting intensified extreme rainfall events. Streamflow projections closely follow precipitation trends, with flows increasing by 60–70% in July and August by the 2080s. Such patterns indicate a greater risk of flash flooding, river overflow, and soil erosion, emphasizing the need for improved flood control infrastructure, early warning systems, and catchment protection measures.

On the contrary, drying trends during the short rainy season (MAM) could reduce river discharge by nearly 24%, affecting early-season planting, irrigation, and water storage. Models project substantial reductions in river discharge from February to May, raising concerns for agriculture, water supply, and ecosystem health during critical low-flow periods. This is due to the fact that the short rainy season (March–May) is expected to experience a decline in rainfall which limitwater availability before the main rainy season and reduces aquifer recharge. Additionally, both maximum (Tmax) and minimum (Tmin) temperatures are projected to rise steadily, amplifying evapotranspiration and further stressing water availability. Several studies on streamflow and runoff projections under CMIP5 models and RCP climate scenarios report declines in streamflow, surface runoff, and water availability, driven by decreasing precipitation and rising temperatures (Alemu et al., 2023; Taye et al., 2020; Bekele et al., 2019; Ghosh et al., 2010; Lemann et al., 2016). Consequently, water availability will be limited during dry periods when irrigation demand is highest, while more water will be available during the rainy season when demand is lower. Mitigation measures such as rainwater harvesting, groundwater recharge, water recycling, and efficient irrigation practices could help alleviate seasonal water scarcity.

Both drought duration and severity are projected to increase throughout the century in the Mojo catchment under both SSP245 and SSP585, with the most significant impacts occurring by the 2080s. Droughts lengthen and intensify, with duration increasing up to 34% and severity up to 36% by the 2080s under both scenarios, while Flood events also grow more frequent (up to +48%) in the high-emission scenario. The co-occurrence of intensified wet-season rainfall and prolonged dry periods suggests a growing tendency toward hydrological extremes, challenging water storage,

distribution, and agricultural planning. Additionally, flood risk projections indicate a steady increase in both the number and frequency of flood events, with the strongest increases under SSP585. By the 2080s, flood frequency could increase by nearly 50% under SSP585, reflecting the impacts of intensified extreme rainfall events and seasonal runoff concentration. This dual threat of more severe droughts alongside more frequent floods will challenge water resource management, agricultural planning, and infrastructure resilience in the Mojo catchment. Dry-season water scarcity may threaten agricultural productivity, domestic water supply, and ecological balance. Wet-season flood risks will require targeted investments in infrastructure (e.g., reservoirs, diversion channels), land-use planning, and community preparedness. Thus, the divergence in seasonal flow patterns emphasizes the need for climate-resilient water management strategies that account for both increasing deficits and surpluses throughout the year.

6.6 Summary and Conclusion

Understanding spatiotemporal variations in precipitation and extreme rainfall indices across the Awash basin is critical for guiding future water management. Such knowledge not only enhances the ability to anticipate changes in water availability but also provides a foundation for developing geographically tailored adaptation strategies. The spatial and seasonal variability in precipitation and hydrological extremes across the Awash basin and the Mojo catchment indicates a future climate characterized by increased variability and contrasting trends. Historical and projected data highlight distinct patterns: the Upper basin tends toward increased heavy rainfall and flood risk, particularly during the main rainy season (JAS), whereas the Middle basin faces prolonged dry spells and heightened drought vulnerability during the short rainy season (MAM). The Lower basin shows potential gains in wet spell duration but with amplified flood and erosion hazards, especially in fragile lowlands. In the Mojo catchment, climate change drives sharper wet -dry season contrasts, with substantial increases in wet-season rainfall and severe early-season drying, exacerbated by rising temperatures that intensify evapotranspiration and water stress. This study reveals a clear difference in the seasonal distribution of water availability in the Mojo catchment under future climate scenarios. The model predicts substantial reductions in discharge during the dry season particularly from February to May, which could pose challenges for agriculture, water supply, and ecosystem health during critical low-flow periods. Conversely, the wet season is expected to intensify, increasing the risk of flooding and soil erosion if not properly managed.

This dual risk creates a challenging "hydrological extremes paradox," in which floods and droughts both become more frequent and severe in the Mojo catchment. This will challenge water resource management, agricultural planning, and infrastructure resilience in the Mojo catchment. Adaptation strategies will need to address both ends of the climate risk spectrum. In agricultural systems, this may involve adopting drought-resilient crop varieties and expanding irrigation efficiency measures. In water resource management, enhanced flood protection infrastructure, and improved seasonal forecasting will be critical. These findings highlight the need for adaptive, integrated water resource management planning capable of addressing both prolonged dry spells and extreme wet-season flows in the coming decades. By addressing these interconnected risks, policymakers and stakeholders can better safeguard water security, sustain ecosystem services, and support livelihoods across the basin under a changing climate. In general, we recommend adopting adaptive, flexible strategies capable of responding to a spectrum of possible climate futures, rather than relying on any single projection. Since uncertainty is inherent in all climate projections, explicitly acknowledging and incorporating it into climate policy and water resource planning should be viewed not as a limitation but as a strength. Such an approach enhances long-term resilience by promoting robust adaptation measures, including diversified water management options, flexible agricultural practices, and adaptive infrastructure planning.

Chapter 7. Synthesis, and Overall Conclusion

7.1 Synthesis of the overall findings of the study

This study evaluated 45 CMIP models for simulating mean and extreme precipitation, and used these simulations to project 10 extreme indices at both national and basin scales, as well as hydroclimate extremes specifically for the Awash basin. The study had four main objectives: (1) evaluate CMIP6 models in capturing Ethiopia's rainfall patterns during JJAS and FMAM using ENACTS and identify an optimal ensemble, (2) assess their ability to simulate 10 extreme precipitation indices at national and agro-ecological levels, (3) generate historical trends and future projections of precipitation extremes under different emission scenarios using top-performing models at national and basin scale, and (4) assess climate change impacts on streamflow, droughts, and floods in key basins, particularly the Upper Awash (Mojo catchment), using the SWAT+ hydrological model.

Most models better represented the short rainy season (FMAM) than the main rainy season (JJAS), with many failing to capture the crucial August peak that supports rain-fed agriculture. Persistent dry biases were observed across both seasons, particularly in high-rainfall regions, reflecting challenges inherited from CMIP5. Model performance varied considerably, and weighted ensembles of the top-performing models reproduced rainfall patterns more accurately than individual models or full-model averages.

Most CMIP6 models showed better skill in capturing the spatial patterns of extreme precipitation indices during JJAS than FMAM, though often with higher biases, reflecting challenges in simulating rainfall variability in Ethiopia's complex topography and climate system. Models performed relatively well over the eastern Rift Valley and lowlands but poorly over high-rainfall highland regions. They consistently overestimated CWD and underestimated other indices, such as CDD, R10, R20, and Rx5day. This reflects drizzle biases and the difficulty of simulating extreme magnitudes. Performance varied across agro-ecological zones. EnseMean outperformed individual and full-model ensembles, particularly in tropical and desert zones, by reducing biases and capturing spatial patterns more accurately. Additionally, improving performance solely through model resolution was not feasible, as high-resolution models often struggled with convective processes. This suggests that parameterization remains a key limitation. Ranking based

on Taylor Skill Scores (TSS) and Comprehensive Rating Metrics (RM) identified CESM2-WACCM-FV2, NESM3, NorESM2-LM, NorESM2-MM, CMCC-ESM2, IPSL-CM6A-INCA, and E3SM-1-0 as the most reliable models for Ethiopia during the JJAS season. During the FMAM season, NorESM2-MM performed the best, followed by HadGEM3-GC31-MM, GFDL-CM4, NorESM2-LM, GFDL-ESM4, BCC-ESM1-MR, and MPI-ESM-1-2-HAM.

This study shows that Ethiopia's rainfall extremes exhibit significant spatial and temporal variability. Historical records from 1981 to 2010 indicate an overall increase in JJAS rainfall indices in high-rainfall areas and a decrease in FMAM rainfall in most regions. Future projections under SSP245 and SSP585 indicate a seasonal shift in some areas with important implications for agriculture and water management. During the FMAM season, PRCPTOT and CWD are expected to increase in the northern regions, especially in the Tekeze basin. Meanwhile, CDD is expected to decrease. This indicates wetter conditions, which could benefit early-season crops but also increase the risk of flooding and soil erosion. Conversely, the JJAS season is projected to experience reduced PRCPTOT and CWD, which suggests that the main rainy season may shift from JJAS to FMAM. This change could disrupt traditional cropping calendars, reduce irrigation water availability, and increase vulnerability to drought during the main rainy season. This emphasizes the need for adaptive water and agricultural management strategies.

The north, west, and southwest regions of the country, particularly the Abay, Baro Akobo, and Omo Gibe basins, are expected to experience more intense rainfall, which could increase the risk of flooding and soil erosion within the basins and in neighboring countries, such as Sudan and Kenya. However, this could also enhance opportunities for hydropower generation. This dual outcome highlights the complexity of climate impacts, where benefits in one sector may be offset by severe risks in others. Given these dynamics, there is an urgent need to strengthen infrastructure, including the development of efficient drainage systems and the construction or expansion of large-capacity dams, to manage the anticipated rise in extreme rainfall. Arid basins such as the Danakil may experience wetter JJAS conditions, improving water availability but increasing flood risk. Eastern Ethiopia may experience a reversal of historical patterns, with drier JJAS and wetter FMAM conditions. Despite consistent signals, substantial uncertainty remains, particularly for PRCPTOT. These findings emphasize the need for flexible, adaptive strategies to safeguard agriculture, water resources, and livelihoods under changing climate extremes.

Climate extremes in Ethiopia's Awash basin and Mojo catchment are projected to intensify, with major implications for water management, agriculture, and disaster preparedness. Historical patterns already show increasing drought frequency during the short rainy season (March–May) and rising flood risk during the main rainy season (July–September). Future projections suggest that this dual challenge will intensify. Wetter and more intense rainfall events in some areas, especially the Upper and Lower Awash, will increase flooding and erosion risks, while persistent drying in the Middle Awash will worsen drought and water scarcity. In the Mojo watershed, seasonal contrasts are even more pronounced. By the 2080s, rainfall and streamflow could increase by up to 70% from July to September, greatly amplifying flood hazards. Meanwhile, declines of over 20% from March to May could threaten irrigation, water supply, and recharge. Rising temperatures exacerbate water stress through increased evapotranspiration, and droughts and floods are expected to become more frequent and severe. Overall, these findings call for geographically tailored adaptation strategies. Flood-prone areas require stronger infrastructure, early warning systems, and land-use planning, while drought-affected zones need improved irrigation efficiency, rainwater harvesting, and groundwater recharge. Building resilience will require balancing water deficits and surpluses across seasons to secure livelihoods, ecosystems, and development goals.

7.2 Implications of the study for climate-resilient integrated water resource management

This study underscores the critical importance of integrating climate change considerations into Ethiopia's water resource management framework. The evaluation of 45 CMIP6 models shows that a subset of bias-corrected, top-performing models can reliably simulate Ethiopia's rainfall variability and extremes, providing a sound scientific foundation for climate-informed decision-making. The findings reveal significant spatial and temporal variability in precipitation. Wet conditions are projected during the FMAM season in northern Ethiopia, whereas the Tekeze Basin experiences fewer wet spells during the JJAS season. There are also sharp seasonal extremes in the Awash Basin and the Mojo catchment area. These shifts signal major challenges for agriculture, water storage, and disaster risk management, including heightened flood hazards in the Upper and Lower Awash and intensified drought risks in the Middle Awash. Similarly, in the Mojo catchment, projected increases in wet-season streamflow and declines during dry months highlight the dual risks of floods and water scarcity.

For integrated water resource management (IWRM), these results imply that adaptation strategies must be tailored geographically and seasonally. Flood-prone regions require stronger investment in infrastructure (dams, reservoirs, diversion channels), improved land-use planning, and real-time flood forecasting systems. Drought-vulnerable areas demand efficient irrigation technologies, rainwater harvesting, groundwater recharge, and demand-side water management. The intensification of evapotranspiration under rising temperatures further underscores the need to balance water supply among agriculture, energy, ecosystems, and domestic use. This study provides a foundation for embedding climate resilience within Ethiopia's IWRM by linking robust climate projections with a comprehensive evaluation of CMIP6 models. This foundation supports sustainable water security, agricultural productivity, and adaptive capacity to future climate extremes.

7.3 Methodological contributions and applicability

This study makes several methodological contributions by systematically integrating the evaluation of CMIP6 models, climate projection and hydrological modeling approaches to assess climate extremes and their impact in Ethiopia. First, it establishes a rigorous evaluation framework for 45 CMIP6 models by combining statistical metrics and graphical tools with high-resolution reference datasets (ENACTS) to identify top-performing models and construct reliable ensembles. Second, it advances the use of bias correction techniques such as quantile mapping and variance scaling to improve the reliability of climate projections and enhance the representation of both mean and extreme precipitation. Third, it uses ensembles of the bias-corrected top-ranking models for future climate projection of extreme indices. It also integrates historical observations with future projections to provide a holistic perspective on the evolving climate dynamics in the country. Fourth, it employs a multi-scale assessment at national, regional (five agro-ecological zones), and basin levels. Finally, by coupling climate model ensembles with the SWAT+ hydrological model, the study provides a robust framework for quantifying future changes in streamflow, floods, and droughts under different emission scenarios.

This methodology is applicable beyond Ethiopia because it offers a transferable framework for other data-scarce regions in Africa and globally. These regions need robust climate projections for water resource planning, agricultural management, and climate adaptation strategies.

Policymakers, practitioners, and researchers can adopt this integrated approach to improve climate risk assessments, support evidence-based decision-making, and strengthen resilience against hydroclimate extremes.

7.4 Overall Conclusions

On the basis of the findings of this study, the following conclusions were synthesized:

- The findings demonstrate that, although CMIP6 models accurately represent Ethiopia's seasonal rainfall patterns and extreme precipitation indices, significant biases remain, especially in regions with high rainfall and complex topography. Raw model outputs are unreliable for direct use in impact studies, but careful model evaluation and selective ensemble approaches can substantially improve confidence. Weighted ensembles of the best-performing models are a more reliable basis for future projections than equal-weight multimodel ensembles. This supports their use in climate impact studies. Thus, this study confirms the importance of model evaluation and selection for regional climate applications.

- The findings reveal clear evidence of shifting rainfall regimes in Ethiopia, with increasing risks of extreme precipitation events and possible seasonal shifts in some regions. These shifts are expected to reshape agricultural calendars, water resource availability, and flood risk profiles. These changes will have significant implications for food security, hydropower, and the health of ecosystems. The "East African Climate Paradox," where models project wetter conditions despite historical declines, highlights the complexity of rainfall variability and the need for basin-specific assessments. Overall, the results emphasize the importance of integrating robust climate information into national adaptation strategies.

- The study concludes that climate change is intensifying hydroclimatic extremes in Ethiopia's Awash basin and Mojo catchment. Rainfall is becoming more variable, with longer wet spells in some regions and increasingly intense heavy rainfall events. These shifts indicate a transition toward hydrological extremes, in which droughts and floods co-occur with increasing frequency. The Middle Awash emerges as particularly vulnerable to prolonged droughts, while the Upper and Lower Awash face greater flood hazards. Similarly, in the Mojo catchment, seasonal drying in MAM and intensified JAS flooding

reflect widening disparities between water deficits and surpluses. Rising temperatures will further exacerbate these extremes by elevating evapotranspiration and reducing dry-season water availability. These findings underscore the need for basin-specific and seasonally adaptive integrated water management approaches, as uniform strategies are unlikely to address the divergent challenges of floods and droughts.

- Effective and sustainable management plans will be essential for addressing the projected basin-specific extreme conditions. Such plans should integrate investments in social infrastructure, strengthen climate resilience, and promote adaptation policies tailored to local contexts. At the same time, long-term strategies must include greenhouse gas mitigation measures to limit further intensification of climate extremes. A balanced approach that combines local adaptation with global mitigation efforts will therefore be critical to safeguarding livelihoods, ecosystems, and water security in the affected basins.

7.5 Recommendations

The following recommendations are provided from the perspectives of CMIP6 model selection, generating ensembles, drought and flood risk mitigation, climate-resilient integrated water resource management, policy and governance, and future research directions:

- Model evaluation and use of ensembles: Future work should focus on evaluating climate models and prioritizing the use of top-performing ensembles for impact studies, rather than relying on simple all-model averages.

- Bias correction and downscaling: Regional climate assessments should combine bias correction with dynamical or statistical downscaling to better capture local topographic influences on rainfall.

- Climate-resilient water management: Integrated strategies should be adopted to balance flood control during the wet season with water storage and conservation during the dry season. Measures should include dams, reservoirs, diversion structures, groundwater recharge, and improved irrigation efficiency.

- Agricultural adaptation: Cropping calendars, crop varieties, and planting strategies should be

adjusted in response to shifting rainfall patterns, particularly in the Tekeze, Awash, and other high-rainfall basins.

- Flood and disaster risk reduction: Early warning systems should be strengthened, and investments should be made in flood control infrastructure and watershed management in flood-prone areas, such as the Abay, Baro Akobo, Omo Gibe, Upper Awash, and Lower Afar lowlands. Rainwater harvesting should be enhanced, small-scale irrigation expanded, and drought-tolerant crops promoted, particularly in the Middle Awash and Mojo catchments.

- Ecosystem and catchment protection: Soil and water conservation practices, afforestation, and watershed rehabilitation should be implemented to reduce erosion, enhance groundwater recharge, and stabilize hydrological responses.

- Policy and institutional integration: Climate extremes should be mainstreamed into national and regional water, agriculture, and disaster risk policies, ensuring alignment with basin-level realities.

- Future research: Future evaluations should integrate diverse process-based emergent constraints with model-weighting strategies that consider both model performance and interdependence. Such an approach can provide more robust multimodel insights across a wide range of critical societal and environmental applications. Additionally, further work is needed to improve the representation of large-scale drivers (ENSO, ITCZ, IOD) in climate models, and to test high-resolution regional climate models for better capture of convective processes and local extremes. This study recommends evaluating multiple CMIP6 models across Ethiopia's homogeneous rainfall zones to generate more robust insights into their performance. Such an approach would allow researchers to identify spatial differences in model skill, account for regional climate variability, and improve the reliability of projections. By tailoring model evaluation to distinct rainfall regimes, future studies can better capture localized hydroclimatic extremes and provide more accurate information for basin-scale planning and adaptation. This would not only reduce uncertainty in climate projections but also strengthen the scientific basis for water resource management, agricultural planning, and disaster risk reduction in Ethiopia.

References

Abdulahi, S.D., Abate, B., Harka, A.E. and Husen, S.B., 2022. Response of climate change impact on streamflow: the case of the Upper Awash sub-basin, Ethiopia. Journal of Water and Climate Change, 13(2), pp.607-628. https://doi.org/10.2166/wcc.2021.251

Adeba, D.; Kansal, M.; Sen, S. 2015. Assessment of water scarcity and its impacts on sustainable development in Awash basin, Ethiopia. Sustain. Water Res. Manag. 1, 71–87. https://doi.org/10.1007/s40899-015-0006-7.

Ahmed, K., Sachindra, D.A., Shahid, S., Iqbal, Z., Nawaz, N., Khan, N., 2020. Multi-model ensemble predictions of precipitation and temperature using machine learning algorithms. Atmos. Res. 236, 104806. https://doi.org/10.1016/j.atmosres.2019.104806.

Akinsanola, A. A., Zhou, W,. 2019. Projections of West African summer monsoon rainfall extremes from two CORDEX models. Climate Dynamics, 52(3–4), 2017–2028. https://doi.org/10.1007/s00382-018-4568-6.

Akinsanola, A.A. and Zhou, W., 2019. Ensemble-based CMIP5 simulations of West African summer monsoon rainfall: current climate and future changes. Theoretical and Applied Climatology, 136, pp.1021-1031. https://doi.org/10.1007/s00704-018-2516-3.

Akinsanola, A.A., Kooperman, G.J., Pendergrass, A.G., Hannah, W.M., Reed, K.A., 2020. Seasonal representation of extreme precipitation indices over the United States in CMIP6 present-day simulations. Environ. Res. Lett. 15, 94003. https://doi.org/10.1088/1748-9326/ab92c.

Akinsanola, A.A., Ongoma, V., Kooperman, G.J., 2021. Evaluation of CMIP6 models in simulating the statistics of extreme precipitation over Eastern Africa. Atmos. Res. 254, 105509. https://doi.org/10.1016/j.atmosres.2021.105509.

Alaminie, A. A., Tilahun, S. A., Legesse, S. A., Zimale, F. A., Tarkegn, G. B. & Jury, M. R., 2021 Evaluation of past and future climate trends under CMIP6 scenarios for the UBNB (Abay), Ethiopia. Water 13 (15), 2110. https://doi.org/10.3390/w13152110

Alemu, M.G., Wubneh, M.A. and Worku, T.A., 2022. Impact of climate change on hydrological response of Mojo river catchment, Awash river basin, Ethiopia. Geocarto International, p.2152497. https://doi.org/10.1080/10106049.2022.2152497

Ali, Z., Hamed, M.M., Muhammad, M.K.I., Iqbal, Z. and Shahid, S., 2023. Performance evaluation of CMIP6 GCMs for the projections of precipitation extremes in Pakistan. Climate Dynamics, pp.1-16. https://doi.org/10.1007/s00382-023-06831-6

Andualem, T.G., Malede, D.A. and Ejigu, M.T., 2020. Performance evaluation of integrated multi-satellite retrieval for global precipitation measurement products over Gilgel Abay watershed, Upper Blue Nile Basin, Ethiopia. Modeling Earth Systems and Environment, 6(3), pp.1853-1861. https://doi.org/10.1007/s40808-020-00795-w

Ayugi, B., Zhihong, J., Zhu, H., Ngoma, H., Babaousmail, H., Rizwan, K., Dike, V., 2021. Comparison of CMIP6 and CMIP models in simulating mean and extreme precipitation over East Africa. Int. J. Climatol. 41, 6474–6496. https://doi.org/10.1002/joc.7207.

Babaousmail, H., Hou, R., Ayugi, B., Ojara, M., Ngoma, H., Karim, R., Rajasekar, A., Ongoma, V., 2021. Evaluation of the Performance of CMIP6 Models in Reproducing Rainfall Patterns over North Africa. Atmosphere (Basel). 12, 475. https://doi.org/10.3390/atmos12040475.

Bala, A., Aliu, A.M., Wan, L.S., 2023. Evaluation of CMIP6 Models Skill in Representing Annual Extreme Precipitation over Northern and Southern Nigeria. J. Geogr. Environ. Earth Sci. Int. 27, 49–61. https://doi.org/10.3390/rs15092376.

Balcha, Y. A., Malcherek, A., Alamirew, T., 2022. Understanding future climate in the upper awash basin (UASB) with selected climate model outputs under CMIP6. Climate, 10(12), 185. https://doi.org/10.3390/cli10120185.

Bedasa, Y., Bedemo, A., 2023. The effect of climate change on food insecurity in the Horn of Africa. GeoJournal 88, 1829–1839. https://doi.org/10.1007/s10708-022-10733-1.

Bekele, D., Alamirew, T., Kebede, A., Zeleke, G. & Melese, A. M., 2017 Analysis of rainfall trend and variability for agricultural water management in Awash River Basin, Ethiopia. *Journal of Water and Climate Change* 8 (1), 127–141.

Bekele, D., Alamirew, T., Kebede, A., Zeleke, G. and M. Melesse, A., 2018. Modeling climate change impact on the Hydrology of Keleta watershed in the Awash River basin, Ethiopia. Environmental Modeling & Assessment, 24(1), pp.95-107. https://doi.org/10.1007/s10666-018-9619-1

Bekele, D.; Alamirew, T.; Kebede, A.; Zeleke, G.; Melesse, A.M.,2017. Analysis of rainfall trend and variability for agricultural water management in Awash River Basin, Ethiopia. J. Water Clim. Chang. 8, 127–141.

Belay, B., Amha, Y., Ambaw, G., Demissie, T., Solomon, D., 2024. Climate Risk Management for Agricultural Extension: Processes, Experiences, And Lessons Learnt from Ethiopia. https://hdl.handle.net/10568/148724

Beobide-Arsuaga, G., Bayr, T., Reintges, A., Latif, M., 2021. Uncertainty of ENSO-amplitude projections in CMIP5 and CMIP6 models. Clim. Dyn. 56, 3875–3888. https://doi.org/10.1007/s00382-021-05673-4.

Berhanu, D., Alamirew, T., Bewket, W., Tarkegn, T.G., Zeleke, G., Haileslassie, A., O'Donnell, G., Walsh, C.L. and Gebrehiwot, S., 2025. Evaluation of CMIP6 models in simulating seasonal extreme precipitation over Ethiopia. Weather and Climate Extremes. https://doi.org/10.1016/j.wace.2025.100752.

Berhanu, D., Alamirew, T., Taye, M.T., Tibebe, D., Gebrehiwot, S., Zeleke, G., 2023. Evaluation of CMIP6 models in reproducing observed rainfall over Ethiopia. J. Water Clim. Chang. 14, 2583–2605. https://doi.org/10.2166/wcc.2023.502.

Bieger, K., Arnold, J., Rathjens, H., White, M. J., et al. ,2017. Introduction to SWAT+, a completely restructured version of the Soil and Water Assessment Tool. Journal of the American Water Resources Association, 53(1), 115–130. DOI:10.1111/1752-1688.12482.

Bobde, V., Akinsanola, A. A., Folorunsho, A. H., Adebiyi, A. A., Adeyeri, O. E., 2024. Projected regional changes in mean and extreme precipitation over Africa in CMIP6 models. Environmental Research Letters. https://doi.org/10.1088/1748-9326/ad545c.

Brunner, L., Pendergrass, A. G., Lehner, F., Merrifield, A. L., Lorenz, R., and Knutti, R.2020.,

Reduced global warming from CMIP6 projections when weighting models by performance and independence, Earth Syst. Dynam., 11, 995–1012, https://doi.org/10.5194/esd-11-995-2020.

Bulti, D. T., Abebe, B. G., Biru, Z., 2021. Analysis of the changes in historical and future extreme precipitation under climate change in Adama city, Ethiopia. Modeling Earth Systems and Environment, 7, 2575–2587. https://doi.org/10.1007/s40808-020-01019-x.

Chadwick, R., Wu, P., Good, P. & Andrews, T., 2013 Asymmetries in tropical rainfall and circulation patterns in idealised CO2 removal experiments. Climate Dynamics 40, 295–316.

Champion, A. J., Hodges, K. I., Bengtsson, L. O., Keenlyside, N. S. & Esch, M., 2011 Impact of increasing resolution and a warmer climate on extreme weather from Northern Hemisphere extratropical cyclones. Tellus A: Dynamic Meteorology and Oceanography 63 (5), 893–906. https://doi.org/10.1111/j.1600-0870.2011.00538.x.

Chen, C.-A., Hsu, H.-H., Liang, H.-C., 2021. Evaluation and comparison of CMIP6 and CMIP5 model performance in simulating the seasonal extreme precipitation in the Western North Pacific and East Asia. Weather Clim. Extrem. 31, 100303. https://doi.org/10.1016/j.wace.2021.100303.

Chen, J., Brissette, F. P., Zhang, X. J., Chen, H., Guo, S. & Zhao, Y., 2019 Bias correcting climate model multi-member ensembles to assess climate change impacts on hydrology. Climatic Change 153 (3), 361–377. https://doi.org/10.1007/s10584-019-02393-x.

Cherinet, A., Tadesse, C., Abebe, T., 2022. Drought and Flood Extreme Events and Management Strategies in Ethiopia. J Geogr Nat Disast 12, 248. https://doi.org/10.35248/2167-0587.22.12.248.

Choi, YW., Campbell, D., Eltahir, E.,2023. Near-term regional climate change in East Africa. Clim Dyn 61, 961–978. https://doi.org/10.1007/s00382-022-06591-9.

Daba, M. H., You, S., 2020. Assessment of climate change impacts on river flow regimes in the upstream of Awash Basin, Ethiopia: based on IPCC fifth assessment report (AR5) climate change scenarios. Hydrology, 7(4), 98. https://doi.org/10.3390/hydrology7040098.

Daba, M.; Tadele, K.; Shemalis, A., 2015. Evaluating potential impacts of climate change on surface water resource availability of upper Awash Sub-Basin, Ethiopia. Open Water J. 2015, 3, 22.

Daniel, H., Abate, B., 2022. Effect of climate change on streamflow in the Gelana watershed, Rift valley basin, Ethiopia. Journal of Water and Climate Change, 13(5), 2205–2232. https://doi.org/10.2166/wcc.2022.059.

Desta, L. J., Belayneh, M., 2023. Analysis of Climatic Change and Variability and Its Effect on Coffee Production in Mattu District, Southwest Ethiopia. Sustainability and Climate Change, 16(6), 461–479. https://doi.org/10.1089/scc.2023.0091.

Dinku, T., 2019. Challenges with availability and quality of climate data in Africa. In Extreme Hydrology and Climate Variability. Elsevier. https://doi.org/10.1016/B978-0-12-815998-9.00007-5.

Dinku, T., Block, P., Sharoff, J., Hailemariam, K., Osgood, D., del Corral, J., Cousin, R. & Thomson, M. C., 2014. Bridging critical gaps in climate services and applications in Africa. Earth Perspectives 1 (1), 15. https://doi.org/10.1186/2194-6434-1-15.

Dinku, T., Thomson, M. C., Cousin, R., del Corral, J., Ceccato, P., Hansen, J. & Connor, S. J., 2018. Enhancing national climate services (ENACTS) for development in Africa. Climate and Development 10 (7), 664–672. https://doi.org/10.1080/17565529.2017.1405784.

Diro, G. T., Toniazzo, T., Shaffrey, L., 2011. Ethiopian Rainfall in Climate Models. 51–69. https://doi.org/10.1007/978-90-481-3842-5_3.

Donat, M.G., Delgado-Torres, C., De Luca, P., Mahmood, R., Ortega, P., Doblas-Reyes, F.J., 2023. How credibly do CMIP6 simulations capture historical mean and extreme precipitation changes? Geophys. Res. Lett. 50, e2022GL102466. https://doi.org/10.1029/2022GL102466.

Duguma, F.A., Feyessa, F.F., Demissie, T.A. and Januszkiewicz, K., 2021. Hydroclimate trend analysis of upper awash basin, Ethiopia. Water, 13(12), p.1680. https://doi.org/10.3390/w13121680.

Dyer, E., Hirons, L. & Taye, M. T., 2022. July–September rainfall in the Greater Horn of Africa: the combined influence of the Mascarene and South Atlantic highs. Climate Dynamics 59 (11–12), 1–21.

Dyer, E., Washington, R. & Teferi Taye, M., 2020. Evaluating the CMIP5 ensemble in Ethiopia: creating a reduced ensemble for rainfall and temperature in Northwest Ethiopia and the Awash basin. International Journal of Climatology 40 (6), 2964–2985. https://doi.org/ 10.1002/joc.6377.

Edossa, D.C., Babel, M.S., Gupta, A.D,.2010. Drought analysis in the Awash river basin, Ethiopia. Water Resour. Manag. 24, 1441–1460.

Emiru, N.C., Recha, J.W., Thompson, J.R., Belay, A., Aynekulu, E., Manyevere, A., Demissie, T.D., Osano, P.M., Hussein, J., Molla, M.B. and Mengistu, G.M., 2021. Impact of climate change on the hydrology of the Upper Awash River Basin, Ethiopia. Hydrology, 9(1), p.3. https://doi.org/10.3390/hydrology9010003.

Endris, H.S., Omondi, P., Jain, S., Lennard, C., Hewitson, B., Chang'a, L., Awange, J.L., Dosio, A., Ketiem, P., Nikulin, G. and Panitz, H.J., 2013. Assessment of the performance of CORDEX regional climate models in simulating East African rainfall. Journal of Climate, 26(21), pp.8453-8475. https://doi.org/10.1175/JCLI-D-12-00708.1.

Eshetu, M., 2022. Hydro-climatic variability and trend analysis of Modjo river watershed, Awash River Basin of Ethiopia. Journal of Environment and Earth Science.

Eyring, V., Bony, S., Meehl, G. A., Senior, C. A., Stevens, B., Stouffer, R. J., Taylor, K. E., 2016. Overview of the Coupled Model Intercomparison Project Phase 6 (CMIP6) experimental design and organization. Geoscientific Model Development, 9(5), 1937–1958. https://doi.org/10.5194/gmd-9-1937-2016.

Faye, A. & Akinsanola, A. A., 2022. Evaluation of extreme precipitation indices over West Africa in CMIP6 models. Climate Dynamics.58 (3–4), 925–939. https://doi.org/10.1007/s00382-021-05942-2.

FDRE-Federal Democratic Republic of Ethiopia. 2019. Ethiopia's National Adaptation Plan (NAP-ETH). Addis Ababa, Ethiopia.

Feng, T., Zhu, X., Dong, W., 2023. Historical assessment and future projection of extreme precipitation in CMIP6 models: Global and continental. Int. J. Climatol. 43, 4119-4135. https://doi.org/10.1002/joc.8077.

Fenta Mekonnen, D., Disse, M., 2018. Analyzing the future climate change of Upper Blue Nile River basin using statistical downscaling techniques. Hydrology and Earth System Sciences, 22(4), 2391–2408. https://doi.org/10.5194/hess-22-2391-2018

Fer, I., Tietjen, B., Jeltsch, F., Wolff, C., 2017. The influence of El Niño–Southern Oscillation regimes on eastern African vegetation and its future implications under the RCP8. 5 warming scenario. Biogeosciences 14, 4355–4374. https://doi.org/10.5194/bg-14-4355-2017.

Fetene, Z. A., Zaitchik, B. F., Zeleke, T. T., Yeshita, B. D. & Vashisht, A., 2022. Coupled model intercomparison project phase 5 and 6 representation of peak and end of rainy season over Upper Blue Nile basin. International Journal of Climatology 42 (16), 8489–8508.

FEWS NET ,2022. Extreme food insecurity persists in the north while outcomes deteriorate in the south amid historic drought. Available at: https://reliefweb.int/report/ ethiopia/ethiopia-food-security-outlook-june-2021-january-2022.

Feyissa, T. A., Demissie, T. A., Saathoff, F., Gebissa, A., 2023. Evaluation of general circulation models CMIP6 performance and future climate change over the omo river basin, Ethiopia. Sustainability, 15(8), 6507. https://doi.org/10.3390/su15086507.

Flato G, Marotzke J, Abiodun B, Braconnot P, Chou SC, Collins W, Cox P, Driouech F, Emori S, Eyring V, Forest C. 2013.Evaluation of climate models. InClimate change. the physical science basis. Contribution of Working Group I to the Fifth Assessment Report of the Intergovernmental Panel on Climate Change 2014 Jun (pp. 741-866). Cambridge University Press.

Fotso-Nguemo, T. C., Diallo, I., Diakhaté, M., Vondou, D. A., Mbaye, M. L., Haensler, A., Gaye, A. T., Tchawoua, C., 2019. Projected changes in the seasonal cycle of extreme rainfall events from CORDEX simulations over Central Africa. Climatic Change, 155(3), 339–357. https://doi.org/10.1007/s10584-019-02492-9.

Funk, C., Peterson, P., Landsfeld, M., Pedreros, D., Verdin, J., Shukla, S., Husak, G., Rowland, J., Harrison, L., Hoell, A., Michaelsen, J., 2015. The climate hazards infrared precipitation with stations—a new environmental record for monitoring extremes. Sci. Data 2, 150066. https://doi.org/10.1038/sdata.2015.66.

Gadissa, T., Nyadawa, M., Behulu, F., Mutua, B., 2019. Assessment of catchment water resources availability under projected climate change scenarios and increased demand in Central Rift Valley Basin. In Extreme hydrology and climate variability (pp. 151–163). Elsevier. https://doi.org/10.1016/B978-0-12-815998-9.00013-0.

Gebisa, B.T., Dibaba, W.T. and Kabeta, A., 2023. Evaluation of historical CMIP6 model simulations and future climate change projections in the Baro River Basin. Journal of Water and Climate Change, 14(8), pp.2680-2705. https://doi.org/10.2166/wcc.2023.032.

Gebrechorkos, S. H., Hülsmann, S., & Bernhofer, C. ,2019. Regional climate projections for impact assessment studies in East Africa. Environ mental Research Letters, 14(4), 044031. https://doi.org/10.1088/1748-9326/ab055a.

Gebrechorkos, S. H., Pan, M., Lin, P., Anghileri, D., Forsythe, N., Pritchard, D. M. W., et al. (2022). Variability and changes in hydrological drought in the Volta Basin, West Africa. Journal of Hydrology: Regional Studies, 42, 101143. https://doi.org/10.1016/j.ejrh.2022.101143

Gebrechorkos, S. H., Taye, M. T., Birhanu, B., Solomon, D., & Demissie, T. ,2023. Future changes in climate and hydroclimate extremes in East Africa. Earth's Future, 11(2), e2022EF003011. https://doi.org/10.1029/2022EF003011

Gebrechorkos, S.H., Hülsmann, S., Bernhofer, C., 2019. Changes in temperature and precipitation extremes in Ethiopia, Kenya, and Tanzania. Int. J. Climatol. 39, 18–30. https://doi.org/10.1002/joc.5777.

Gebresellase, S. H., Wu, Z., Xu, H., Muhammad, W. I., 2022. Evaluation and selection of CMIP6 climate models in Upper Awash Basin (UBA), Ethiopia: Evaluation and selection of CMIP6 climate models in Upper Awash Basin (UBA), Ethiopia. Theoretical and Applied Climatology, 149(3–4), 1521–1547. https://doi.org/10.1007/s00704-022-04056-x

Gedefaw, M., Wang, H., Yan, D., Song, X., Yan, D., Dong, G., Wang, J., Girma, A., Ali, B.A., Batsuren, D. and Abiyu, A., 2018. Trend analysis of climatic and hydrological variables in the Awash river basin, Ethiopia. Water, 10(11), p.1554. https://doi.org/10.3390/w10111554.

Ghosh, S. and Misra, C., 2010. Assessing hydrological impacts of climate change: modeling techniques and challenges. Open Hydrology Journal, 4(1), pp.115-121. https://doi.org/10.2174/1874378101004010115

Gibson, P.B., Waliser, D.E., Lee, H., Tian, B., Massoud, E., 2019. Climate model evaluation in the presence of observational uncertainty: precipitation indices over the contiguous United States. J. Hydrometeorol. 20, 1339–1357. https://doi.org/ 10.1175/JHM-D-18-0230.1

Gissila, T., Black, E., Grimes, D. I. F. & Slingo, J. M., 2004 Seasonal forecasting of the Ethiopian summer rains. International Journal of Climatology 24 (11), 1345–1358. https://doi.org/10.1002/joc.1078.

Gitima, G. and Mersha, M., 2020. The impacts of El-Niño-Southern Oscillation (ENSO) on agriculture and coping strategies in rural communities of Ethiopia: systematic review article. Asian Journal of Geographical Research, 3(4), pp.56-69. https://doi.org/10.9734/ajgr/2020/v3i430117.

Gizaw, M.S., Biftu, G.F., Gan, T.Y., Moges, S.A. and Koivusalo, H., 2017. Potential impact of climate change on streamflow of major Ethiopian rivers. Climatic Change, 143, pp.371-383. https://doi.org/10.1007/s10584-017-2021-1.

Gonfa ZB, Kumar D., 2016. Application of soil and water assessment tool model to estimate runoff and sediment yield from Mojo watershed. Int J Innov Res Sci Eng Technol. 5(2):2081–2091. https://doi.org/10.15680/IJIRSET.2016.0502058.

Gudmundsson, L., Bremnes, J. B., Haugen, J. E., Engen-Skaugen, T., 2012. Downscaling RCM precipitation to the station scale using statistical transformations–a comparison of methods. Hydrology and Earth System Sciences, 16(9), 3383–3390. https://doi.org/10.5194/hess-16-3383-2012.

Gummadi, S., Rao, K.P.C., Seid, J., Legesse, G., Kadiyala, M.D.M., Takele, R., Amede, T. and Whitbread, A., 2018. Spatio-temporal variability and trends of precipitation and extreme rainfall events in Ethiopia in 1980–2010. Theoretical and Applied Climatology, 134, pp.1315-1328. https://doi.org/10.1007/s00704-017-2340-1

Gupta, R., Prakash, P. Chembolu, V., 2025. Multi criteria evaluation of downscaled CMIP6 models in predicting precipitation extremes. Atmospheric Research, 315, p.107921. https://doi.org/10.1016/j.atmosres.2025.107921.

Han, Z., GAO, X., XU, Y., 2021. Mean and extreme precipitation projection over land area of East Asia based on multiple regional climate models. Chinese Journal of Geophysics, 64(6), 1869–1884. https://doi.org/10.6038/cjg2021O0103.

Hughes, D.A., Mantel, S. and Mohobane, T., 2014. An assessment of the skill of downscaled GCM outputs in simulating historical patterns of rainfall variability in South Africa. Hydrology Research, 45(1), pp.134-147. https://doi.org/10.2166/nh.2013.027.

Huo, R., Li, L., Chen, H., Xu, C.-Y., Chen, J., Guo, S., 2021. Extreme precipitation changes in Europe from the last millennium to the end of the twenty-first century. Journal of Climate, 34(2), 567–588. https://doi.org/10.1175/JCLI-D-19-0879.1.

Hussain, J., Khaliq, T., Asseng, S., Saeed, U., Ahmad, A., Ahmad, B., Ahmad, I., Fahad, M., Awais, M., Ullah, A. and Hoogenboom, G., 2020. Climate change impacts and adaptations for wheat employing multiple climate and crop modelsin Pakistan. Climatic Change, 163, pp.253-266. https://doi.org/10.1007/s10584-020-02855-7.

ICPAC. (2016). Projected changes in rainfall and temperature over Greater Horn of Africa (GHA) in different scenarios. IGAD Climate Predic tion and Applications Centre. Retrieved from http://rcc.icpac.net/wp-content/uploads/Progress_Report_March_Hussen.pdf

IPCC, 2022. The Physical Science Basis. Contribution of Working Group I to the Sixth Assessment Report of the Intergovernmental Panel on Climate Change [Masson-Delmotte, V., P. Zhai, A. Pirani, S. L. Connors, C. Péan, S. Berger, N. Caud, Y. Chen, L. Goldfarb, M. I. G. Cambridge University Press. In Press.

IPCC. 2021. Climate Change 2021: The Physical Science Basis. Contribution of Working Group I to the Sixth Assessment Report of the Intergovernmental Panel on Climate Change. Cambridge University Press.

Iqbal, Z., Shahid, S., Ahmed, K., Ismail, T., Khan, N., Virk, Z.T., Johar, W., 2020. Evaluation of global climate models for precipitation projection in sub-Himalaya region of Pakistan. Atmospheric Research, 245, p.105061. https://doi.org/10.1016/j.atmosres.2020.105061.

Jiang, Z., Li, W., Xu, J., Li, L., 2015. Extreme precipitation indices over China in CMIP5 models. Part I: Model evaluation. J. Clim. 28, 8603–8619. https://doi.org/10.1175/JCLI-D-15-0099.1.

Jiménez Cisneros, B. E., Oki, T., Arnell, N. W., Benito, G., Cogley, J. G., Döll, P., Jiang, T., & Mwakalila, S. ,2014. Freshwater resources. In C. B. Field, V. R. Barros, D. J. Dokken, K. J. Mach, M. D. Mastrandrea, T. E. Bilir, M. Chatterjee, et al. (Eds.), Climate Change 2014: Impacts, Adaptation, and Vulnerability. Part A: Global and Sectoral Aspects. Contribution of Working Group II to the Fifth Assessment Report of the Intergovernmental Panel on Climate Change (pp. 229–269). Cambridge University Press.

Jury, M. R., 2015. Statistical evaluation of CMIP5 climate change model simulations for the Ethiopian highlands. International Journal of Climatology 35 (1), 37–44. https://doi.org/10.1002/joc.3960.

Kamruzzaman, M., Shahid, S., Roy, D. K., Islam, A. R. M. T., Hwang, S., Cho, J., Zaman, M. A. U., Sultana, T., Rashid, T. & Akter, F., 2022. Assessment of CMIP6 global climate models

in reconstructing rainfall climatology of Bangladesh. International Journal of Climatology 42 (7), 3928–3953.

Kim, Y.H., Min, S.K., Zhang, X., Sillmann, J. and Sandstad, M., 2020. Evaluation of the CMIP6 multi-model ensemble for climate extreme indices. Weather and Climate Extremes, 29, p.100269. https://doi.org/10.1016/j.wace.2020.100269.

King, J. A., Weber, J., Lawrence, P., Roe, S., Swann, A. L. S., & Val Martin, M. ,2024. Global and regional hydrological impacts of global forest expansion. Biogeosciences, 21(17). https://doi.org/10.5194/bg-21-3883-2024

Klutse, N.A.B., Quagraine, K.A., Nkrumah, F., Quagraine, K.T., Berkoh-Oforiwaa, R., Dzrobi, J.F., Sylla, M.B., 2021. The Climatic Analysis of Summer Monsoon Extreme Precipitation Events over West Africa in CMIP6 Simulations. Earth Syst. Environ. 5, 25–41. https://doi.org/10.1007/s41748-021-00203-y.

Knutti, Reto, Reinhard Furrer, Claudia Tebaldi, Jan Cermak, and Gerald A. Meehl., 2010. 'Challenges in Combining Projections from Multiple Climate Models', Journal of Climate, 23: 2739-58. https://doi.org/10.1175/2009JCLI3361.1.

Korecha, D. & Barnston, A. G., 2007. Predictability of June–September Rainfall in Ethiopia. Monthly Weather Review 135 (2), 628–650. https://doi.org/10.1175/MWR3304.1.

Kuma, P., Bender, F. A.-M., & Jönsson, A. R., 2023. Climate model code genealogy and its relation to climate feedbacks and sensitivity. Journal of Advances in Modeling Earth Systems, 15, e2022MS003588. https://doi. org/10.1029/2022MS003588

Lemann, T., Zeleke, G., Amsler, C., Giovanoli, L., Suter, H. and Roth, V., 2016. Modelling the effect of soil and water conservation on discharge and sediment yield in the upper Blue Nile basin, Ethiopia. Applied geography, 73, pp.89-101. http://dx.doi.org/10.1016/j.apgeog.2016.06.008.

Lewis, K., 2017. Understanding climate as a driver of food insecurity in Ethiopia. Clim. Change 144, 317–328. https://doi.org/10.1007/s10584-017-2036-7.

Li, L., Li, W., Ballard, T., Sun, G., Jeuland, M., 2016. CMIP5 model simulations of Ethiopian Kiremt-season precipitation: current climate and future changes. Climate Dynamics, 46(9–10), 2883–2895. https://doi.org/10.1007/s00382-015-2737-4.

Liebmann, B., Hoerling, M.P., Funk, C., Bladé, I., Dole, R.M., Allured, D., Quan, X., Pegion, P. and Eischeid, J.K., 2014. Understanding recent eastern Horn of Africa rainfall variability and change. Journal of Climate, 27(23), pp.8630-8645. https://doi.org/10.1175/JCLI-D-13-00714.1.

Lyon B., DeWitt, D.G., 2012. A recent and abrupt decline in the East African long rains. Geophys Res Lett 39, L02702. http://doi.org/10.1029/2011GL050337.

Lyon, B. and Vigaud, N., 2017. Unraveling East Africa's climate paradox. Climate extremes: Patterns and mechanisms, pp.265-281. https://doi.org/10.1002/9781119068020.ch16.

Maidment, R.I.; Allan, R.P.; Black, E.,2015. Recent observed and simulated changes in precipitation over Africa. Geophys. Res. Lett., 42, 8155–8164. https://doi.org/10.1002/2015GL065765.

Makula, E. K. & Zhou, B., 2022. Coupled Model Intercomparison Project phase 6 evaluation and projection of East African precipitation. Int. J. Climatol. 42, 2398–2412. https://doi.org/10.1002/joc.7373.

Malede, D. A., Andualem, T. G., Yibeltal, M., Alamirew, T., Demeke, G. G., & Mekonnen, Y. G. ,2024. Climate change impacts on hydroclimatic variables over Awash basin, Ethiopia: A systematic review. Discover Applied Sciences, 6, Article 27. https://doi.org/10.1007/s42452-024-05640-8

Maraun, D., Shepherd, T., Widmann, M. et al. Towards process-informed bias correction of climate change simulations. Nature Clim Change 7, 764–773 (2017). https://doi.org/10.1038/nclimate3418

Mariotti, L., Diallo, I., Coppola, E., Giorgi, F., 2014. Seasonal and intraseasonal changes of African monsoon climates in 21st century CORDEX projections. Climatic Change, 125, 53–65. https://doi.org/10.1007/s10584-014-1097-0.

Martey E., Etwire PM., Kuwornu J.K., 2020. Economic impacts of smallholder farmers' adoption of drought-tolerant maize varieties. Land Use Policy 94, 104524. https://doi.org/10.1016/j.landusepol.2020.104524.

Mera, G.A., 2018. Drought and its impacts in Ethiopia. Weather Clim Extrem 22: 24–35. https://doi.org/10.1016/j.wace.2018.10.002.

MoA. Minister of Agriculture, 1998. Agro-Ecological Zones of Ethiopia. Natural Resources Management and Regulatory Department. With Support of German Agency for Technical Cooperation (GTZ); MoA: Addis Ababa, Ethiopia.

Moges, D.M. and Bhat, H.G., 2021. Climate change and its implications for rainfed agriculture in Ethiopia. journal of Water and Climate Change, 12(4), pp.1229-1244. https://doi.org/10.2166/wcc.2020.058.

Mohammed, J.A., Gashaw, T., Worku Tefera, G., Dile, Y.T., Worqlul, A.W. and Addisu, S., 2022. Changes in observed rainfall and temperature extremes in the Upper Blue Nile Basin of Ethiopia. Weather Clim Extremes 37: 100468. https://doi.org/10.1016/j.wace.2022.100468

Mulugeta, S., Fedler, C. and Ayana, M., 2019. Analysis of long-term trends of annual and seasonal rainfall in the Awash River Basin, Ethiopia. Water, 11(7), p.1498. https://doi.org/10.3390/w1107 1498.

Musie, M., Momblanch, A., Sen, S., 2021. Exploring future global change-induced water imbalances in the Central Rift Valley Basin, Ethiopia. Climatic Change, 164(3), 47. https://doi.org/10.1007/s10584-021-03035-x.

Ngoma, H., Ayugi, B., Onyutha, C., Babaousmail, H., Lim Kam Sian, K.T., Iyakaremye, V., Mumo, R. & and Ongoma, V., 2022. Projected changes in rainfall over Uganda based on CMIP6 models. Theoretical and Applied Climatology, 149(3-4), 1117–1134.

Ngoma, H., Wen, W., Ayugi, B., Babaousmail, H., Karim, R. & Ongoma, V. 2021. Evaluation of precipitation simulations in CMIP6 models over Uganda. International Journal of Climatology 41 (9), 4743–4768. https://doi.org/10.1002/joc.7098.

Nicholson, S. E. 2018. Climate of the Sahel and West Africa. In: Oxford Research Encyclopedia of Climate Science. Oxford University Press. https://doi.org/10.1093/acrefore/9780190228620.013.510

Nicholson, S.E., 2017. Climate and climatic variability of rainfall over eastern Africa. Rev. Geophys. 55, 590–635. https://doi.org/10.1002/2016RG000544.

Omay, P.O., Muthama, N.J., Oludhe, C., Kinama, J.M., Artan, G., Atheru, Z., 2023. Evaluation of CMIP6 Historical Simulations over IGAD region of Eastern Africa. Discov Environ 1, 11. https://doi.org/10.1007/s44274-023-00012-2.

Omondi, P., Awange, J., Forootan, E., Ogallo, L. A., Barakiza, R., Girmaw, G. B., Fesseha, I., Kululetera, V., Kilembe, C., Mbati, M. M., 2014. Changes in temperature and precipitation extremes over the Greater Horn of Africa region from 1961 to 2010. International Journal of Climatology, 34(4), 1262–1277. https://doi.org/10.1002/joc.3763.

Ongoma, V., Chen, H. & Gao, C., 2019. Evaluation of CMIP5 twentieth century rainfall simulation over the equatorial East Africa. Theoretical and Applied Climatology 135 (3–4), 893–910.

Ongoma, V., Chen, H., Gao, C., 2018. Projected changes in mean rainfall and temperature over East Africa based on CMIP5 models. Int. J. Climatol. 38, 1375–1392. https://doi.org/10.1007/s11069-017-3079-9.

Onyutha, C., Acayo, G., Nyende, J., 2020. Analyses of precipitation and evapotranspiration changes across the Lake Kyoga Basin in east Africa. Water, 12(4), 1134. https://doi.org/10.3390/w12041134.

Onyutha, C., Tabari, H., Rutkowska, A., Nyeko-Ogiramoi, P. and Willems, P., 2016. Comparison of different statistical downscaling methods for climate change rainfall projections over the Lake Victoria basin considering CMIP3 and CMIP5. Journal of hydro-environment research, 12, pp.31-45. https://doi.org/10.1016/j.jher.2016.03.001

Opiyo F., Wasonga O., Nyangito M., Schilling. J, Munang R., 2015. Drought adaptation and coping strategies among the Turkana pastoralists of norther n Kenya. Int J Disaster Risk Sci 6:b295–309. http://doi.org/10.1007/s13753-015-0063-4.

Orkodjo, T. P., Kranjac-Berisavijevic, G., Abagale, F. K., 2022. Impact of climate change on future precipitation amounts, seasonal distribution, and streamflow in the Omo-Gibe basin, Ethiopia. Heliyon, 8(6). https://doi.org/10.1016/j.heliyon.2022.e09711.

Palmer, P.I., Wainwright, C.M., Dong, B., Maidment, R.I., Wheeler, K.G., Gedney, N., Hickman, J.E., Madani, N., Folwell, S.S., Abdo, G. and Allan, R.P., 2023. Drivers and impacts of Eastern African rainfall variability. Nature Reviews Earth & Environment, 4(4), pp.254-270. https://doi.org/10.1038/s43017-023-00397-x.

Patel, G., Das, S. Das, R., 2023. Identification of Best CMIP6 Global Climate Model for Rainfall by Ensemble Implementation of MCDM Methods and Statistical Inference. Water Resour Manage 37, 5147–5170. https://doi.org/10.1007/s11269-023-03599-6.

Peterson, T. C., Manton, M. J., 2008. Monitoring changes in climate extremes: a tale of international collaboration. Bulletin of the American Meteorological Society, 89(9), 1266–1271. https://doi.org/10.1175/2008BAMS2501.1

Philip, S., Kew, S. F., Jan van Oldenborgh, G., Otto, F., O'Keefe, S., Haustein, K., King, A., Zegeye, A., Eshetu, Z., Hailemariam, K., Singh, R., Jjemba, E., Funk, C. & Cullen, H., 2018 Attribution Analysis of the Ethiopian Drought of 2015. Journal of Climate 31 (6), 2465–2486. https://doi.org/10.1175/JCLI-D-17-0274.1

Philip, S., Kew, S.F., Jan van Oldenborgh, G., Otto, F., O'Keefe, S., Haustein, K., King, A., Zegeye, A., Eshetu, Z., Hailemariam, K., Singh, R., Jjemba, E., Funk, C., Cullen, H., 2018. Attribution Analysis of the Ethiopian Drought of 2015. J. Clim. 31, 2465–2486. https://doi.org/10.1175/JCLI-D-17-0274.1.

Pohlert, Torsten., 2016. The Trend Package. R Package Version 1.1. https://CRAN.R-project.org/package=trend.

Pour, S. H., Shahid, S., Chung, E.-S., Wang, X.-J., 2018. Model output statistics downscaling using support vector machine for the projection of spatial and temporal changes in rainfall of Bangladesh. Atmospheric Research, 213, 149–162. https://doi.org/10.1016/j.atmosres.2018.06.006.

Rahman, A., Pekkat, S., 2024. Identifying and ranking of CMIP6-global climate models for projected changes in temperature over Indian subcontinent. Sci Rep 14, 3076. https://doi.org/10.1038/s41598-024-52275-1.

Raju, K.S. and Kumar, D.N., 2020. Review of approaches for selection and ensembling of GCMs. Journal of Water and Climate Change, 11(3), pp.577-599. https://doi.org/10.2166/wcc.2020.128

Reddy, N.M., Saravanan, S., 2023. Extreme precipitation indices over India using CMIP6: a special emphasis on the SSP585 scenario. Environ. Sci. Pollut. Res. 30, 47119–47143. https://doi.org/10.1007/s11356-023-25649-7.

Reinman, S. L., 2012 Intergovernmental panel on climate change (IPCC). Reference Reviews 26 (2), 41–42.

Rettie, F. M., Gayler, S., Weber, T. K. D., Tesfaye, K., Streck, T., 2023. High-resolution CMIP6 climate projections for Ethiopia using the gridded statistical downscaling method. Scientific Data, 10(1), 442. https://doi.org/10.3389/fenvs.2023.1127265.

Rivera, J. A., Araneo, D. C., & Penalba, O. C., 2017. Threshold level approach for streamflow drought analysis in the Central Andes of Argen tina: A climatological assessment. Hydrological Sciences Journal, 62(12), 1949–1964. https://doi.org/10.1080/02626667.2017.1367095

Rivera, J.A., Arnould, G., 2020. Evaluation of the ability of CMIP6 models to simulate precipitation over Southwestern South America: Climatic features and long-term trends (1901–2014). Atmos. Res. 241, 104953. https://doi.org/10.1016/j.atmosres.2020.104953.

Rowell, D.P., Booth, B.B., Nicholson, S.E. and Good, P., 2015. Reconciling past and future rainfall trends over East Africa. Journal of Climate, 28 (24), pp.9768-9788. https://doi.org/10.1175/JCLI-D-15-0140.1.

Salman, S.A., Nashwan, M.S., Ismail, T., Shahid, S., 2020. Selection of CMIP5 general circulation model outputs of precipitation for peninsular Malaysia. Hydrol. Res. 51, 781–798. https://doi.org/10.2166/nh.2020.154.

Şen, Z., 2012. Innovative trend analysis methodology. Journal of Hydrologic Engineering, 17(9), 1042–1046.

Sharma, T., Vittal, H., Karmakar, S. and Ghosh, S., 2020. Increasing agricultural risk to hydro-climatic extremes in India. Environmental Research Letters, 15(3), p.034010. https://doi.org/10.1088/1748-9326/ab63e1

Shiferaw, A., Tadesse, T., Rowe, C., Oglesby, R., 2018. Precipitation extremes in dynamically downscaled climate scenarios over the greater horn of Africa. Atmosphere, 9(3), 112. https://doi.org/10.3390/atmos9030112.

Shiogama, H., Ishizaki, N. N., Hanasaki, N., Takahashi, K., Emori, S., Ito, R., Nakaegawa, T., Takayabu, I., Hijioka, Y., Takayabu, Y. N., 2021. Selecting CMIP6-based future climate scenarios for impact and adaptation studies. Sola, 17, 57–62. https://doi.org/10.2151/sola.2021-009.

Sian, K.T.C.L.K., Ayugi, B.O., Onyutha, C., Sagero, P. and Ait Brahim, Y., 2025. Rainfall variability across Africa. In Climate Change and Rainfall Extremes in Africa (pp. 3-26). Elsevier. https://doi.org/10.1016/B978-0-443-28867-8.00001-0.

Souverijns, N., Thiery, W., Demuzere, M. and Van Lipzig, N.P., 2016. Drivers of future changes in East African precipitation. Environmental research letters, 11(11), p.114011. https://doi.org/10.1088/1748-9326/11/11/114011

Srivastava, A., Grotjahn, R., Ullrich, P.A., 2020. Evaluation of historical CMIP6 model simulations of extreme precipitation over contiguous US regions. Weather Clim. Extrem. 29, 100268. https://doi.org/10.1016/j.wace.2020.100268.

Stouffer, R. J., Eyring, V., Meehl, G. A., Bony, S., Senior, C., Stevens, B., Taylor, K. E., 2017. CMIP5 Scientific Gaps and Recommendations for CMIP6. Bulletin of the American Meteorological Society, 98(1), 95–105. https://doi.org/10.1175/BAMS-D-15-00013.1.

Sylla, M. B., Nikiema, P. M., Gibba, P., Kebe, I., Klutse, N. A. B., 2016. Climate change over West Africa: Recent trends and future projections. Adaptation to Climate Change and Variability in Rural West Africa, 25–40. https://doi.org/10.1007/978-3-319-31499-0_3.

Tadese MT, Kumar L, Koech R, Science R., 2020. Climate change projections in the Awash River basin of Ethiopia using global and regional climate models. Int J Climatol. 2020. https://doi.org/10.1002/ joc.6418.

Tadese, M.T., Kumar, L., Koech, R. and Zemadim, B., 2019. Hydro-climatic variability: a characterisation and trend study of the Awash River Basin, Ethiopia. Hydrology, 6(2), p.35. https://doi.org/10.3390/hydrology6020035

Taguela, T.N., Akinsanola, A.A., Adeliyi, T.E., Rhoades, A. and Nazarian, R.H., 2025. Understanding drivers and uncertainty in projected African precipitation. npj Climate and Atmospheric Science, 8(1), p.222. https://doi.org/10.1038/s41612-025-01123-8

Taye, M.T., Dyer, E., Hirpa, F.A. and Charles, K.,2018. Climate change impact on water resources in the Awash basin, Ethiopia. Water, 10(11), p.1560.https://doi.org/10.3390/w10111560

Taylor, K.E., 2001. Summarizing multiple aspects of model performance in a single diagram. J. Geophys. Res. Atmos. 106, 7183–7192. https://doi.org/10.1029/2000JD900719.

Tegegne, G., Melesse, A. M., Alamirew, T., 2021. Projected changes in extreme precipitation indices from CORDEX simulations over Ethiopia, East Africa. Atmospheric Research, 247, 105156. https://doi.org/10.1016/j.atmosres.2020.105156.

Teshome, A., Zhang, J., Demissie, T., Ma, Q., 2022. Observed and future spatiotemporal changes of rainfall extreme characteristics and their dynamic driver in June-August season over Africa. Atmospheric and Climate Sciences, 12(2), 358–382. https://doi.org/10.4236/acs.2022.122022.

Thompson, J.R., Green, A.J. and Kingston, D.G., 2014. Potential evapotranspiration-related uncertainty in climate change impacts on river flow: An assessment for the Mekong River basin. Journal of Hydrology, 510, pp.259-279. https://doi.org/10.1016/j.jhydrol.2013.12.010.

Tian, B., Dong, X., 2020. The double-ITCZ bias in CMIP3, CMIP5, and CMIP6 models based on annual mean precipitation. Geophys. Res. Lett. 47, e2020GL087232. https://doi.org/10.1029/2020GL087232.

Tierney, J. E., Ummenhofer, C. C., Demenocal, P. B., 2015. Past and future rainfall in the Horn of Africa. Science Advances, 1(9), e1500682. https://doi.org/10.1126/sciadv.1500682.

Tiruye, G. A., Besha, A. T., Mekonnen, Y. S., Benti, N. E., Gebreslase, G. A., Tufa, R. A., 2021. Opportunities and Challenges of Renewable Energy Production in Ethiopia. Sustainability 2021, 13, 10381. https://doi.org/10.3390/su131810381.

Todd, M. C., Taylor, R. G., Osborn, T. J., Kingston, D. G., Arnell, N. W., & Gosling, S. N. ,2011. Uncertainty in climate change impacts on basin scale freshwater resources – preface to the special issue: the QUEST GSI methodology and synthesis of results. Hydrology and Earth System Sciences, 15, 1035–1046. https://doi.org/10.5194/hess 15 1035 2011

Tola, S.Y. and Shetty, A., 2023. Extreme hydroclimatic variability and impact of local and global climate system anomalies on extreme flow in the Upper Awash River basin: SY Tola, A. Shetty. Theoretical and Applied Climatology, 153(3), pp.1117-1137. https://doi.org/10.1007/s00704-023-04510-4.

Tufa, D. F., Soromessa, T., & Meshesha, D. T. ,2022. Impact of land-use and land-cover change on watershed hydrology: A case study of Mojo watershed, Ethiopia. Environmental Systems Research, 11(1), 1–15. https://doi.org/10.1186/s40068-022-00260-y

Van den Hende, C., Van Schaeybroeck, B., Nyssen, J., Van Vooren, S., Van Ginderachter, M., and Termonia, P., 2021. Analysis of rain-shadows in the Ethiopian Mountains using climatological model data. Clim. Dyn. 56, 1663–1679. https://doi.org/10.1007/s00382-020-05554-2.

Viste, E., Korecha, D., Sorteberg, A., 2013. Recent drought and precipitation tendencies in Ethiopia. Theor. Appl. Climatol. 112, 535–551. https://doi.org/10.1007/s00704-012-0746-3.

Wainwright, C. M., Marsham, J. H., Keane, R. J., Rowell, D. P., Finney, D. L., Black, E., Allan, R. P., 2019. 'Eastern African Paradox' rainfall decline due to shorter not less intense Long Rains. Npj Climate and Atmospheric Science, 2(1), 1–9. https://doi.org/10.1038/s41612-019-0091-7.

Williams, A.P., Funk, C., 2011. A westward extension of the warm pool leads to a westward extension of the Walker circulation, drying eastern Africa. Clim Dyn 37, 2417–2435. https://doi.org/10.1007/s00382-010-0984-y.

Worku, G., Teferi, E., Bantider, A., Dile, Y. T., 2019. Observed changes in extremes of daily rainfall and temperature in Jemma Sub-Basin, Upper Blue Nile Basin, Ethiopia. Theoretical and Applied Climatology, 135, 839–854.Worku, G., Teferi, E., Bantider, A., Dile, Y. T., 2020. Statistical bias correction of regional climate model simulations for climate change projection in the Jemma sub-basin, upper Blue Nile Basin of Ethiopia. Theoretical and Applied Climatology, 139, 1569–1588. https://doi.org/10.1007/s00704-018-2412-x.

World Bank 2018. Climate Change Profile: Ethiopia. Available online at: https:// reliefweb.int/sites/reliefweb.int/files/resources/Ethiopia_4.pdf (accessed January 15, 2021).

World Bank 2019. Disaster Risk Profile: Ethiopia. Washington, DC.

Yang, B., Qin, C., Bräuning, A., Osborn, T.J., Trouet, V., Ljungqvist, F.C., Esper, J., Schneider, L., Grießinger, J., Büntgen, U. Rossi, S., 2021. Long-term decrease in Asian monsoon rainfall and abrupt climate change events over the past 6,700 years. Proceedings of the National Academy of Sciences, 118(30), p.e2102007118. http://doi/10.1073/pnas.2102007118.

Yang, W., Seager, R., Cane, M. A. & Lyon, B., 2015. The rainfall annual cycle bias over east Africa in CMIP5 coupled climate models. Journal of Climate 28 (24), 9789–9802. https://doi.org/10.1175/JCLI-D-15-0323.1.

Yang, X., Zhou, B., Xu, Y. et al., 2023. CMIP6 Evaluation and Projection of Precipitation over Northern China: Further Investigation. Adv. Atmos. Sci. 40, 587–600. https://doi.org/10.1007/s00376-022-2092-4.

Zegeye, H., 2018. Climate change in Ethiopia: impacts, mitigation and adaptation. International Journal of Research in Environmental Studies, 5(1), pp.18-35. https://doi.org/10.13140/RG.2.2.16782.46408.

Zeleke, E.B., Melesse, A.M., Zhu, P., Burgman, R. and Gann, D., 2025. Spatial variability and relative influence of seasonal rainfall drivers in Ethiopia. Theoretical and Applied Climatology, 156(2), p.131. https://doi.org/10.1007/s00704-025-05368-4.

Zhang, W.X, Zhou T.J., 2020. Increasing impacts from extreme pre cipitation onpopulation ver China with global warming. Sci Bull 65(3):243–252. https://doi.org/10.1016/j.scib.2019.12.002.

Zhang, X., Alexander, L., Hegerl, G.C., Jones, P., Tank, A.K., Peterson, T.C., Trewin, B., Zwiers, F.W., 2011. Indices for monitoring changes in extremes based on daily temperature and precipitation data. Wiley Interdiscip. Rev. Clim. Chang. 2, 851–870. https://doi. org/10.1002/wcc.147.

Zhang, X., Yang, F., 2004. RClimDex (1.0) user manual. Clim. Res. Branch Environ. Canada 22, 13–14.

Zhao, J., Zhang, N., Liu, Z., Zhang, Q., & Shang, C., (2024). SWAT model applications: From hydrological processes to ecosystem services. Science of the Total Environment, 172605. https://doi.org/10.1016/j.scitotenv.2024.172605.

Zhu, Y.-Y. & Yang, S., 2020. Evaluation of CMIP6 for historical temperature and precipitation over the Tibetan Plateau and its comparison with CMIP5. Advances in Climate Change Research 11 (3), 239–251. https://doi.org/10.1016/j.accre.2020.08.001.

Appendix

A1: Percent Bias over time for GFDL-CM4, GFDL-ESM4, ESM-1-0, MPI-ES3M1-2-HR, NESM3, CESM2, CESM2-WACCM, CESM2-WACCM-FV2, MPI-ESM1-2-LR and BCC-CSM2-MR models with respect to ENACTS from 1981-2014

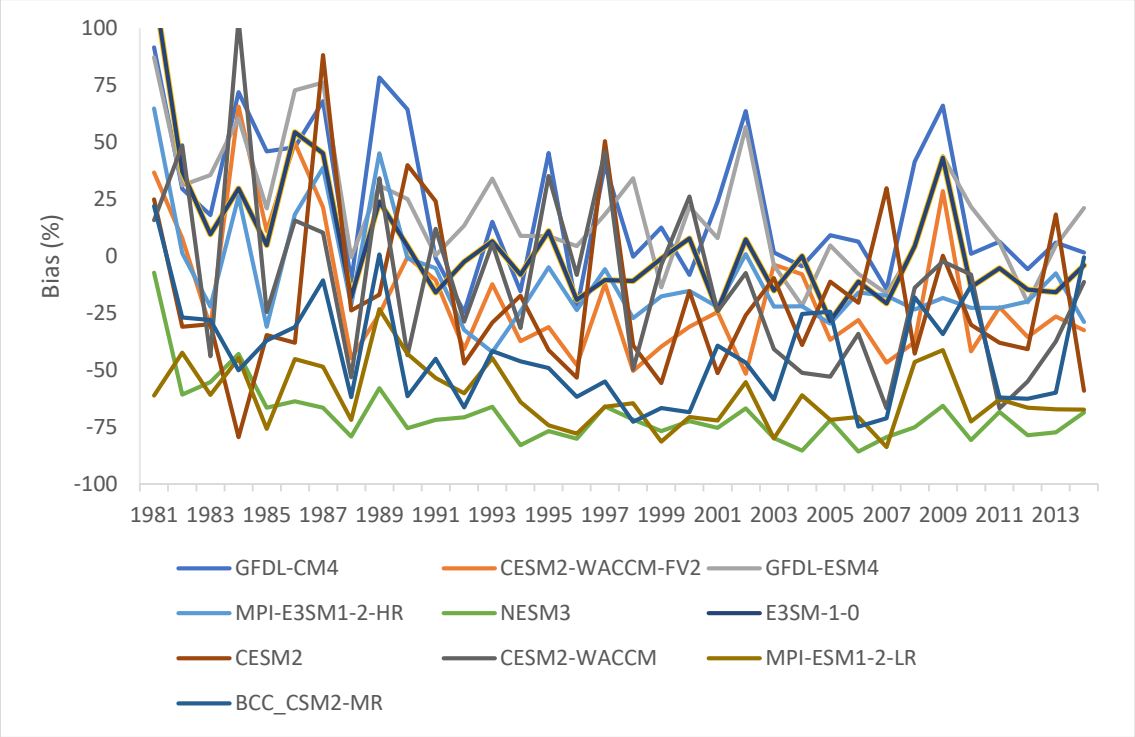

A2: Bias for mean monthly, JJAS and FMAM for weighted and simple average of ensembles with respect to ENACTS

BIAS						
	MEAN MONTHLY		JJAS		FMAM	
Ensembles	Simple average	Weighted average	Simple average	Weighted average	Simple average	Weighted average
ENSEMB_4	8.03	1.81	-0.74	-0.16	6.66	1.49
ENSEMB_8	-1.88	0.59	-1.95	-2.43	-16.28	0.01
ENSEMB_10	-0.79	-0.3	-3.87	-1.79	-11.26	-4.7
ENSEMB_16	-1.79	-0.72	-2.04	-1.08	-15.93	-6.96
ENSEMB_20	-1.21	-0.51	-1.98	-1.09	-14.5	-6.55
ENSEMB_27	-1.25	-0.56	-3.48	-1.73	-14.42	-6.84
ENSEMB_ALL	-7.8	-1.95	-21.77	-6.64	-14.68	-6.85

A3: RMSE for mean monthly, JJAS and FMAM for weighted and simple average of ensembles with respect to ENACTS

RMSE						
	MEAN MONTHLY		JJAS		FMAM	
Ensembles	Simple average	Weighted average	Simple average	Weighted average	Simple average	Weighted average
ENSEMB_4	38.62	20.23	39.86	25.09	30.27	16.12
ENSEMB_8	40.26	22.45	42.47	27.55	35.03	19.47
ENSEMB_10	41.32	30.26	45.46	39.52	34.37	26.32
ENSEMB_16	40.39	30.52	42.62	38.93	35.23	27.65
ENSEMB_20	40.90	31.02	44.12	39.94	34.98	27.76
ENSEMB_27	41.09	31.70	43.93	40.51	33.92	27.88
ENSEMB_ALL	44.27	36.74	52.23	50.41	32.60	29.06

A4: TSS for mean monthly, JJAS and FMAM for weighted and simple average of ensembles with respect to ENACTS

TSS						
	MEAN MONTHLY		JJAS		FMAM	
Ensembles	Simple average	Weighted average	Simple average	Weighted average	Simple average	Weighted average
ENSEMB_4	0.88	0.88	0.9	0.9	0.84	0.84
ENSEMB_8	0.86	0.88	0.88	0.91	0.78	0.82
ENSEMB_10	0.86	0.86	0.87	0.87	0.78	0.78
ENSEMB_16	0.86	0.86	0.87	0.88	0.78	0.78
ENSEMB_20	0.86	0.86	0.87	0.87	0.78	0.78
ENSEMB_27	0.85	0.85	0.86	0.86	0.78	0.79
ENSEMB_ALL	0.83	0.82	0.77	0.81	0.77	0.78

A5: RM values and overall ranking of 37 CMIP6 models,weighted average of 7 ensembles and CHIRPS based on RM values of bias (RM_BIAS), RMSE (RM_RMSE),PCC (RM_PCC) and TSS (RM_TSS) for the period 1981-2014 over Ethiopia DanielB54325662

MODELS	RM_BIAS (Rank)	RM_RMSE (Rank)	RM_PCC (Rank)	RM_TSS (Rank)
CHIRPS	0.79	0.96	0.98	0.98
ACCESS-CM2	0.12(41)	0.23(36)	0.19(38)	0.08(41)
ACCESS-ESM1-5	0.26(32)	0.11(40)	0.32(31)	0.30(33)
BCC_CSM2-MR	0.61(14)	0.55(20)	0.45(26)	0.58(15)
BCC-ESM1	0.75(8)	0.41(25)	0.31(33)	0.42(26)
CAMS-CSM1-0	0.24(34)	0.51(21)	0.50(18)	0.11(39)
CanESM5	0.53(23)	0.31(31)	0.26(36)	0.45(25)
CESM2	0.62(15)	0.62(14)	0.74(9)	0.76(9)
CESM2-WACCM	0.61(16)	0.57(19)	0.83(7)	0.75(10)
CESM2-WACCM-FV2	0.30(31)	0.35(28)	0.27(35)	0.35(30)
CMCC-CM2-HR4	0.70(10)	0.11(41)	0.15(40)	0.29(34)
CMCC-CM2-SR5	0.65(13)	0.38(27)	0.45(22)	0.47(23)
CMCC-ESM2	0.57(17)	0.33(29)	0.44(23)	0.42(27)
CNRM-CM6-1	0.10(42)	0.09(42)	0.01(44)	0.01(44)
CNRM-CM6-1-HR	0.17(38)	0.16(38)	0.07(42)	0.10(40)
CNRM-ESM2-1	0.07(43)	0.09(43)	0.05(43)	0.07(42)
E3SM-1-0	0.55(21)	0.76(10)	0.65(13)	0.72(13)
EC-Earth3	0.57(18)	0.42(24)	0.46(25)	0.55(17)
EC-Earth3-Veg	0.5(26)	0.39(26)	0.44(28)	0.48(21)
EC-Earth3-Veg-LR	0.56(20)	0.45(23)	0.48(23)	0.52(18)
ENSEMB_10	0.87 (2)	0.89(4)	0.64(14)	0.77(8)
ENSEMB_16	0.81 (6)	0.88(5)	0.67(11)	0.82(6)
ENSEMB_20	0.85(3)	0.84(6)	0.65(14)	0.81(7)
ENSEMB_27	0.83(5)	0.82(7)	0.66(12)	0.73(12)
ENSEMB_4	0.88(1)	0.96(1)	0.89(4)	0.93(3)
ENSEMB_8	0.84(4)	0.94(2)	0.83(8)	0.92(4)
ENSEMB_ALL	0.69(11)	0.75(11)	0.51(17)	0.65(15)
FGOALS-f3-L	0.13(40)	0.30(33)	0.45(27)	0.05(43)
FGOALS-g3	0.57(19)	0.12(39)	0.30(34)	0.27(35)
GFDL-CM4	0.69(12)	0.79(8)	0.94(1)	0.97(1)
GFDL-ESM4	0.74(9)	0.93(3)	0.91(2)	0.95(2)
HadGEM3-GC31-LL	0.26(33)	0.62(15)	0.47(20)	0.37(28)
IITM-ESM	0.55(22)	0.24(35)	0.18(39)	0.15(38)
INM-CM4-8	0.39(29)	0.30(34)	0.15(41)	0.23(36)
INM-CM5-0	0.52(24)	0.47(22)	0.35(30)	0.45(24)
IPSL-CM6A-LR	0.37(30)	0.33(30)	0.32(32)	0.48(22)
MIROC6	0.01(44)	0.04(44)	0.47(24)	0.19(37)

MODELS	RM_BIAS (Rank)	RM_RMSE (Rank)	RM_PCC (Rank)	RM_TSS (Rank)
MPI-ESM1-2-HR	0.17(39)	0.60(17)	0.70(10)	0.50(19)
MPI-ESM1-2-LR	0.19 (37)	0.69(12)	0.90(3)	0.66(14)
MRI-ESM2-0	0.43(28)	0.22(37)	0.22(37)	0.35(31)
NESM3	0.22(36)	0.64(13)	0.88(6)	0.74(11)
NorESM2-MM	0.79(7)	0.77(9)	0.89(5)	0.85(5)
SAM0-UNICON	0.44(27)	0.58(18)	0.46(21)	0.35(32)
TaiESM1	0.51(25)	0.31(32)	0.36(29)	0.49(20)
UKESM1-0-LL	0.22(35)	0.62(16)	0.55(16)	0.36(29)

B1: Mean consecutive dry days (CDD) (days/season) from observational dataset, CHIRPS, 45 CMIP6 models, and EnseMean over Ethiopia for JJAS season from 1981–2014

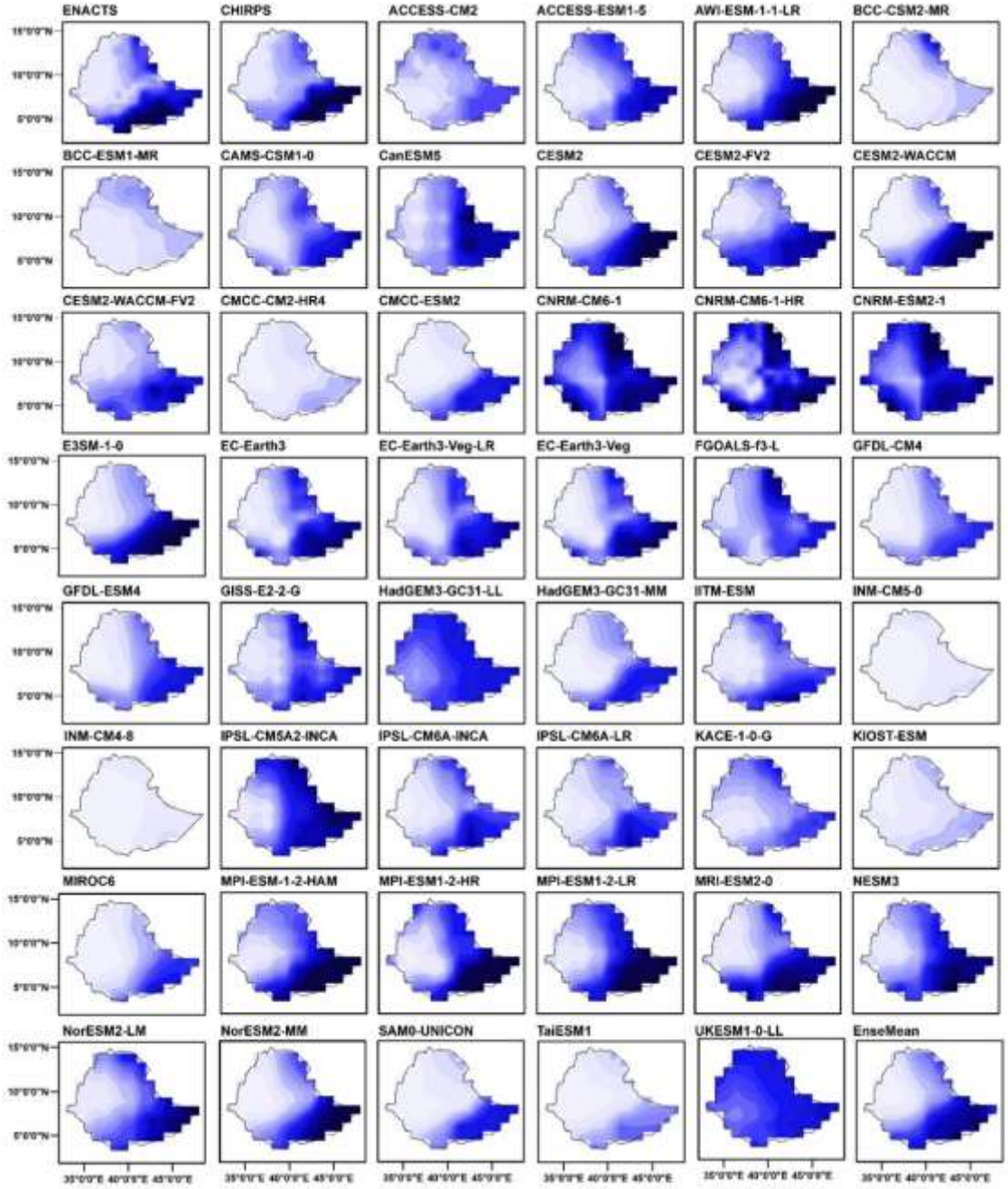

JJAS CDD (days/season)

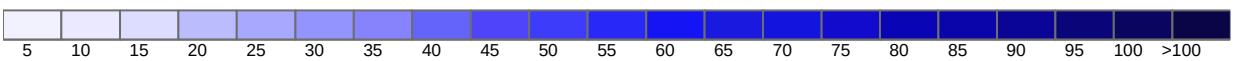

B2: Mean consecutive dry days (CDD) (days/season) from observational dataset, CHIRPS, 45 CMIP6 models, and EnseMean over Ethiopia for FMAM season from 1981–2014

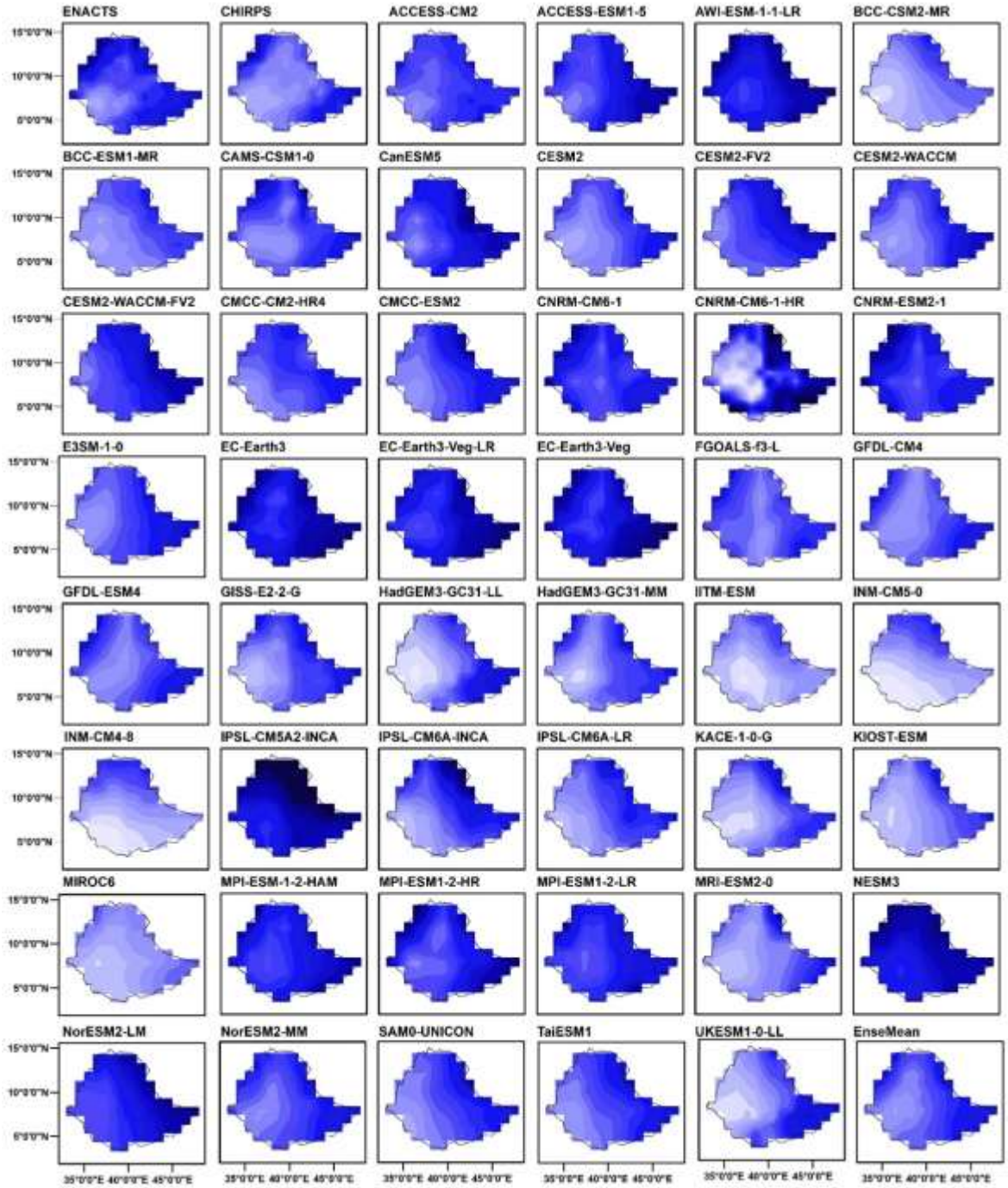

FMAM CDD (days/season)

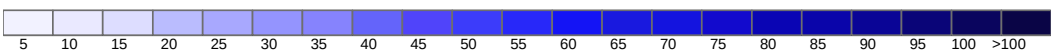

B3: Mean very heavy precipitation days (R20) (days/season) from observational dataset, CHIRPS, 45 CMIP6 models, and EnseMean over Ethiopia for JJAS season from 1981–2014.

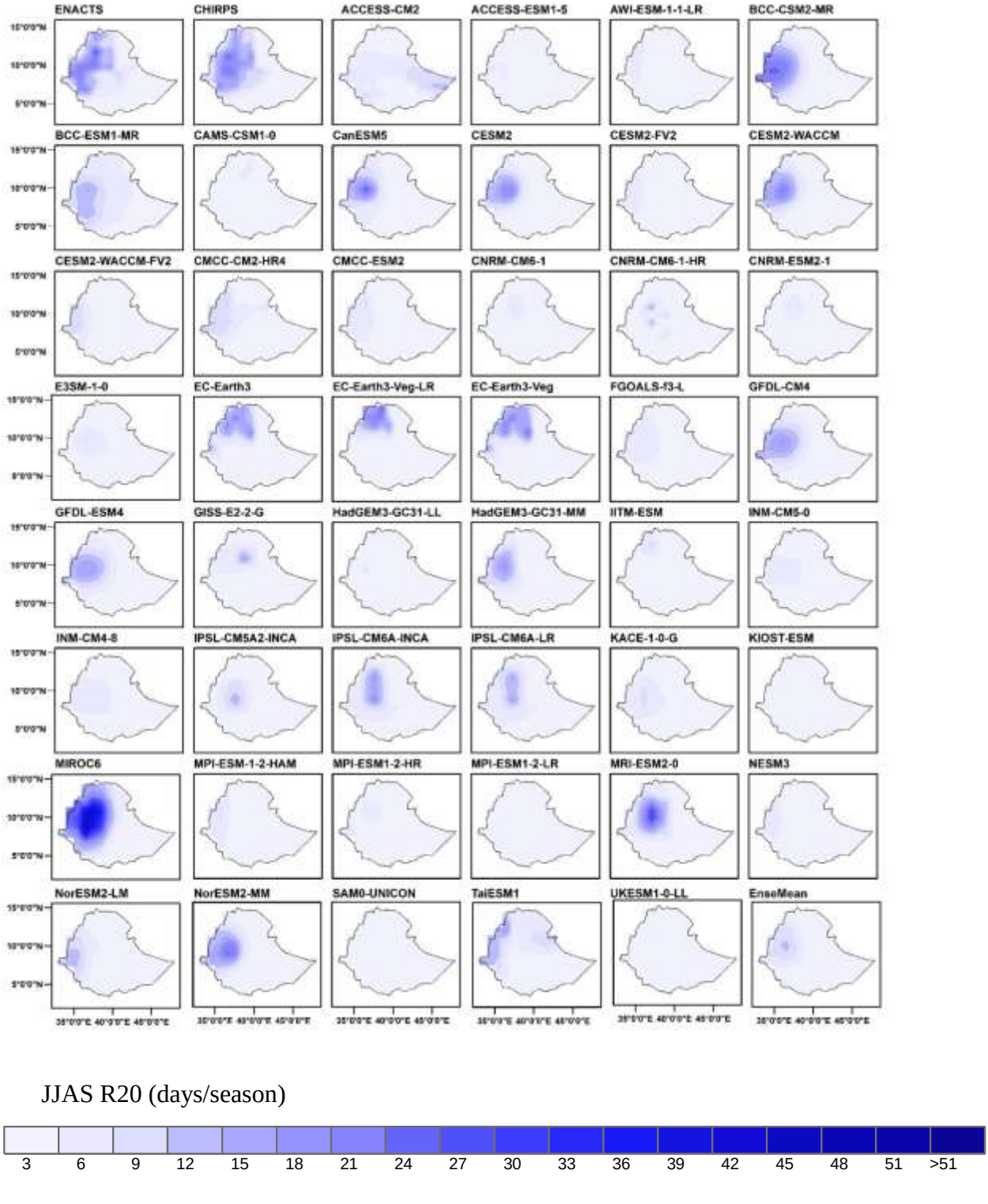

B4: Mean very heavy precipitation days (R20) (days/season) from observational dataset, CHIRPS, 45 CMIP6 models, and EnseMean over Ethiopia for FMAM season from 1981–2014.

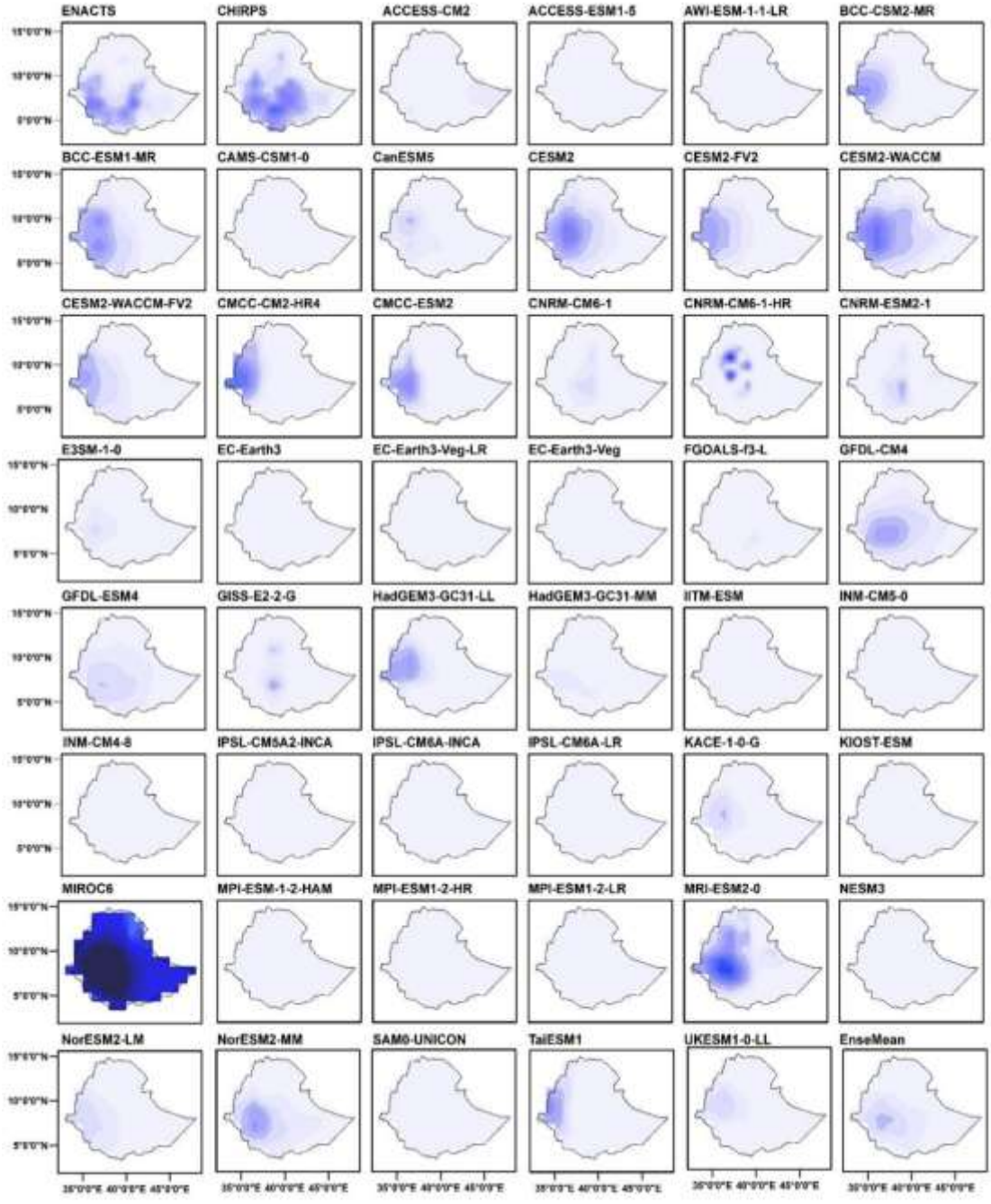

FMAM R20 (days/season)

B5: Mean seasonal precipitation over extremely wet days (R99pTOT) (mm/season) from observational dataset, CHIRPS, 45 CMIP6 models and, EnseMean over Ethiopia for JJAS season from 1981–2014.

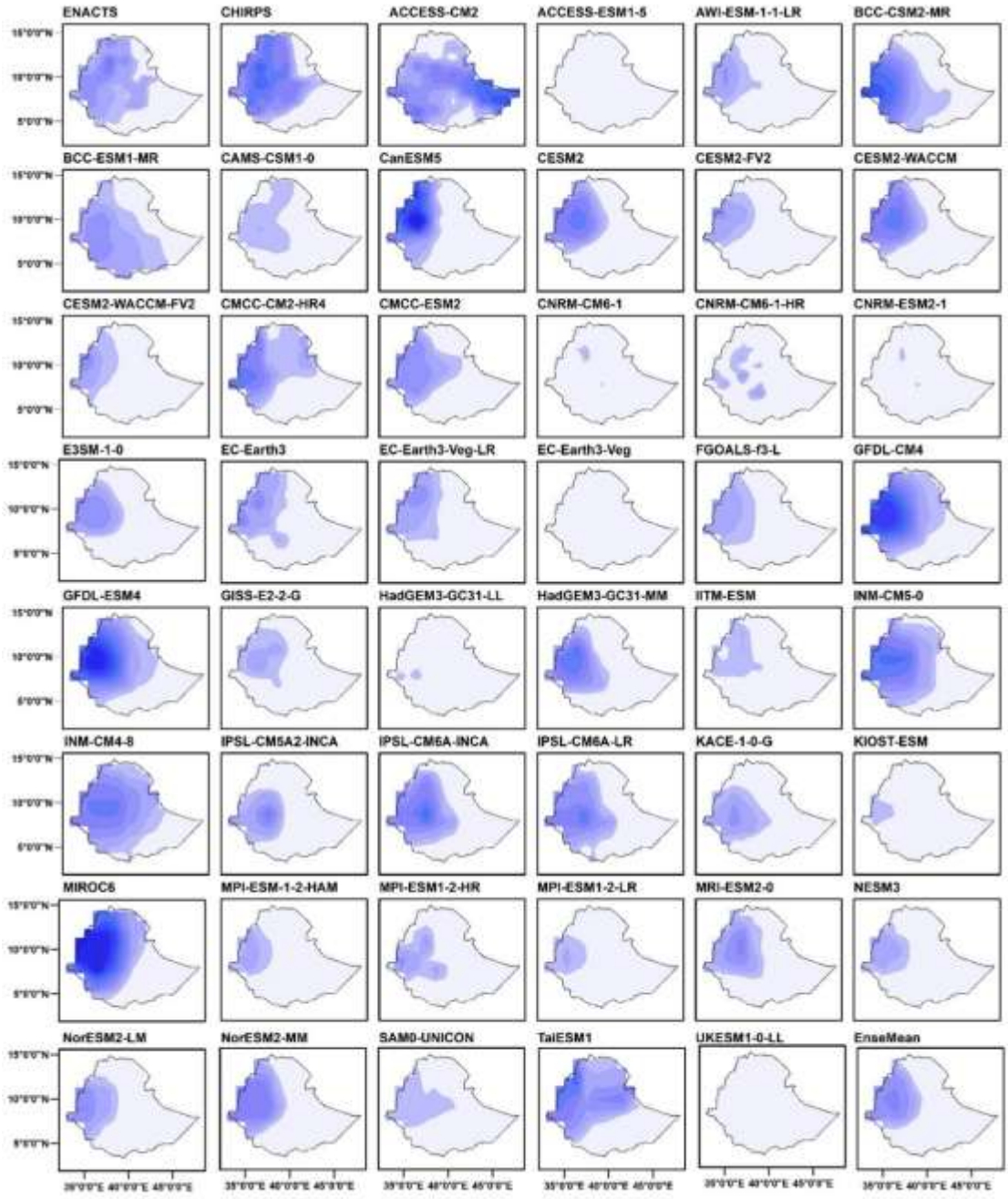

JJAS R99pTOT

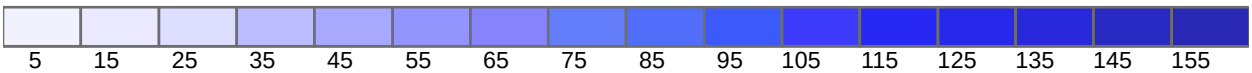

B6: Mean seasonal precipitation over extremely wet days (R99pTOT) (mm/season) from observational dataset, CHIRPS, 45 CMIP6 models and, EnseMean over Ethiopia for FMAM season from 1981–2014.

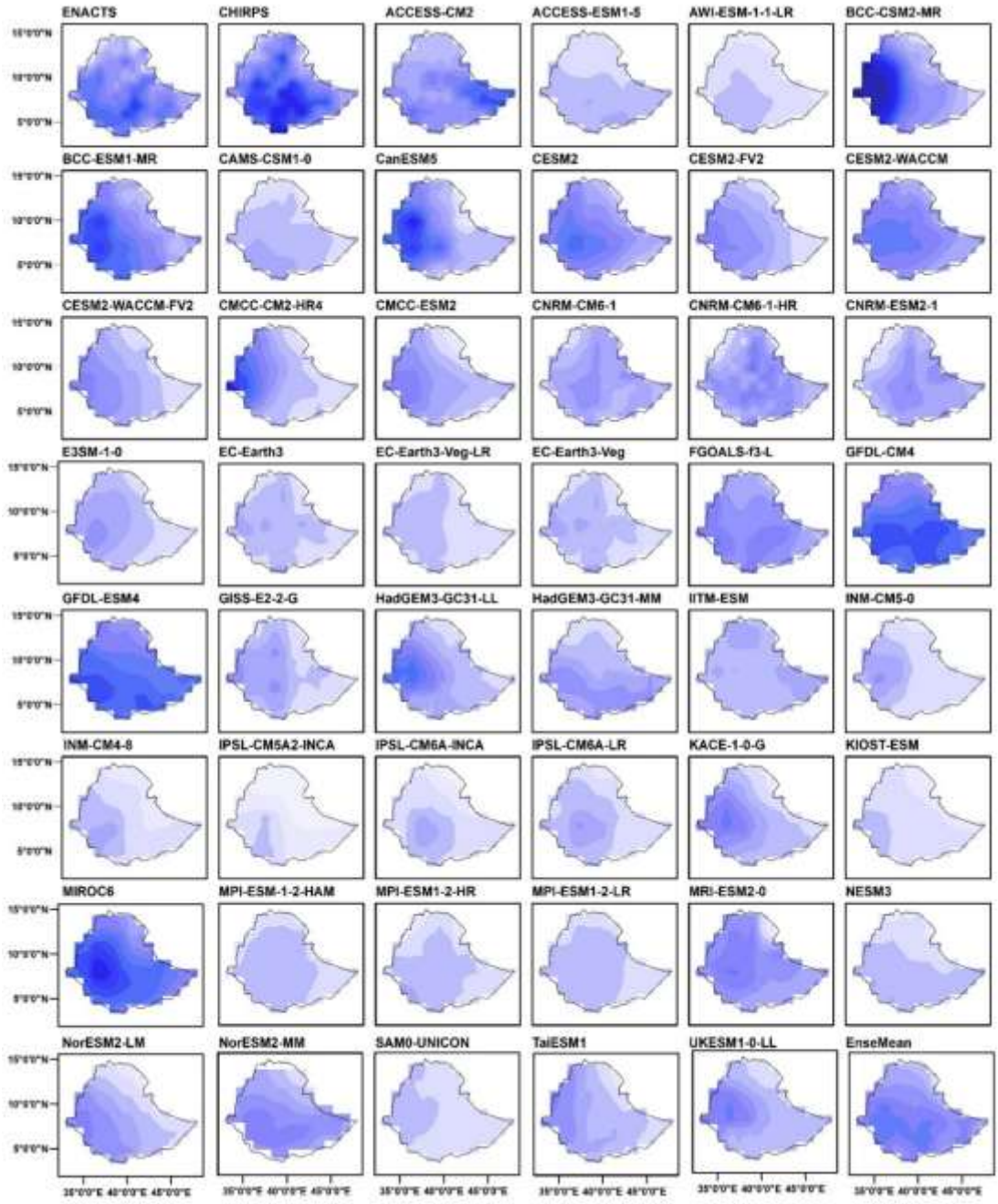

FMAM R99pTOT

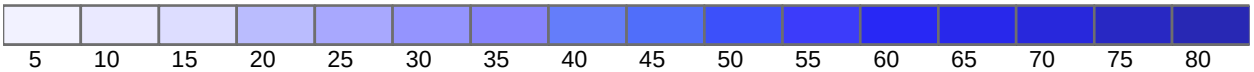

B7: Mean maximum one day rainfall (Rx1day) (mm/season) from observational dataset, CHIRPS, 45 CMIP6 models and, EnseMean over Ethiopia for JJAS season from 1981-2014

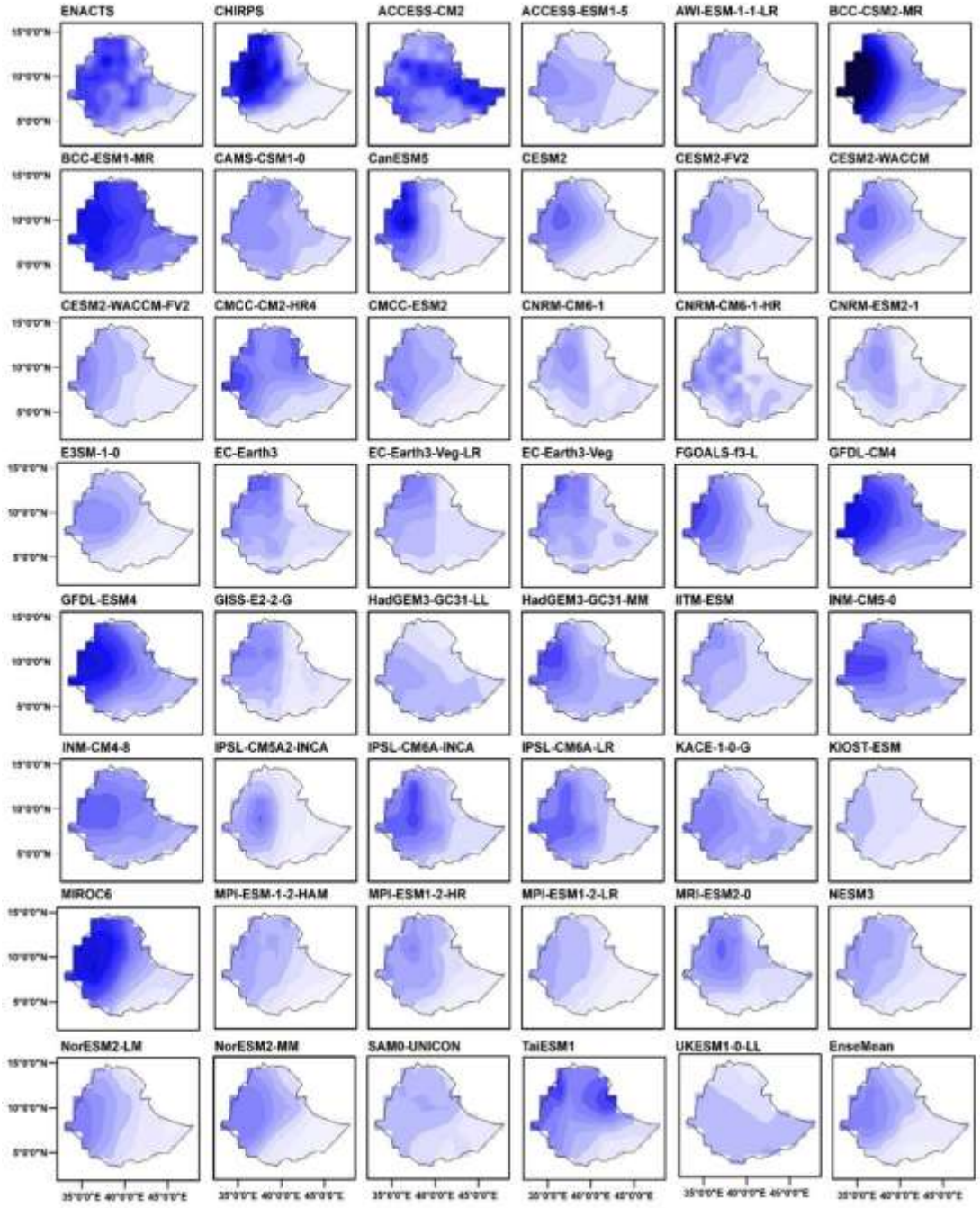

JJAS Rx1day (mm/season)

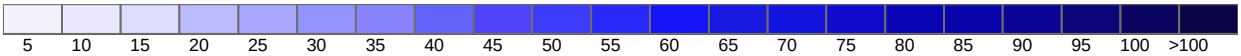

B8: Mean maximum one day rainfall (Rx1day) from observational dataset, CHIRPS, 45 CMIP6 models and, EnseMean over Ethiopia for FMAM season from 1981-2014

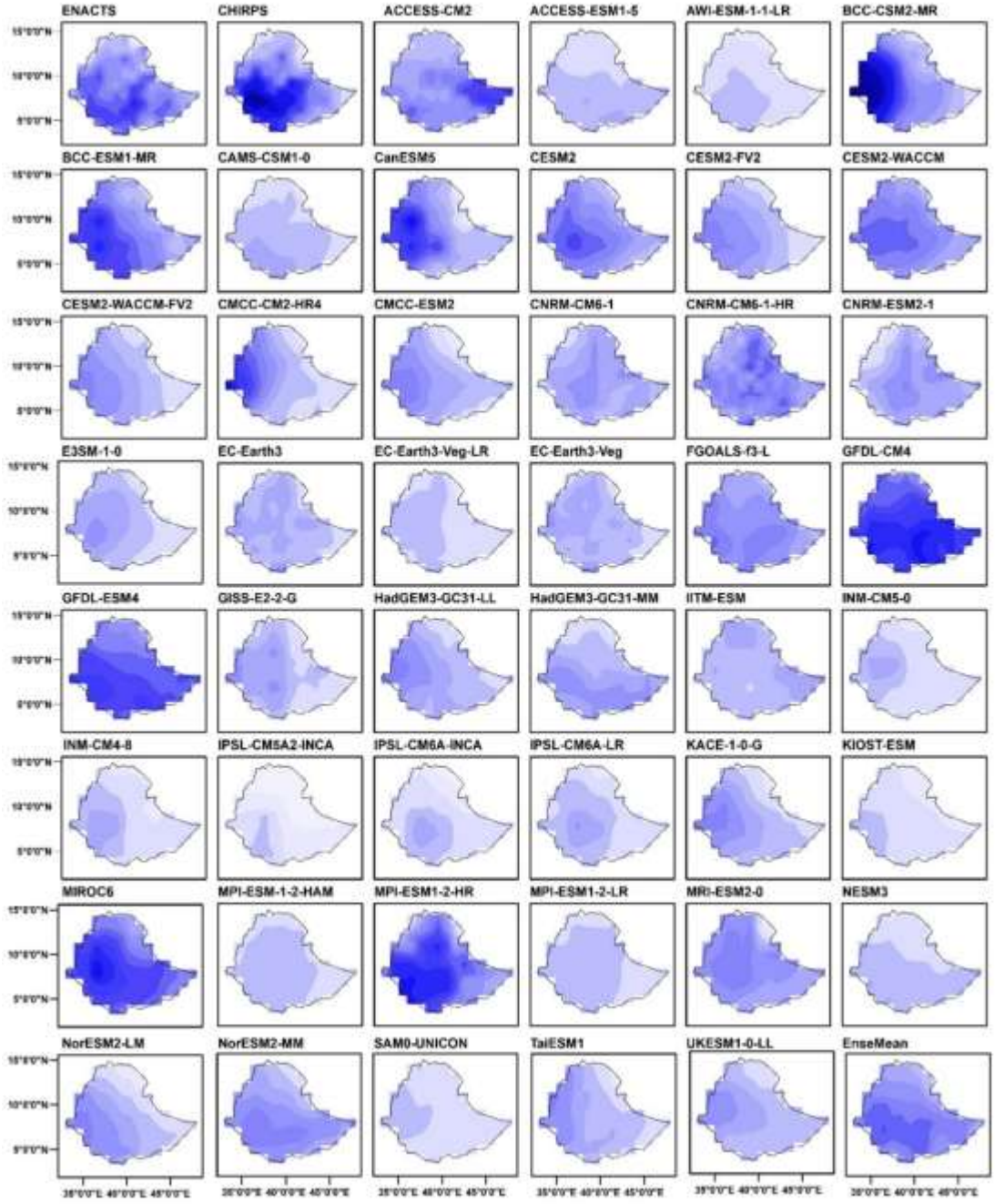

FMAM Rx1day (mm/season)

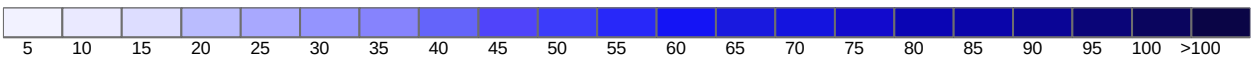

B9: TSS values and overall ranks of CMIP6 models based on RM of TSS values for 45 CMIP6 models for the period 1981-2014 during JJAS season over Ethiopia with respect to observational dataset. Numbers within brackets represent the rank of CMIP6 model for each extreme index with respect to TSS values.

	TSS Values (Rank)											
Models	CDD	CWD	R10	R20	R95p T0T	R99p TOT	PRCP TOT	SDII	Rx 5day	Rx 1day	RM_ TSS	Over all ranks
ACCESS-CM2	0.28 (39)	0.38 (15)	0.19 (43)	0.17 (35)	0.26 (42)	0.21 (42)	0.26 (43)	0.16 (40)	0.32 (39)	0.30 (40)	0.16	42
ACCESS-ESM1-5	0.60 (26)	0.31 (18)	0.37 (36)	0.11 (39)	0.02 (45)	0.02 (45)	0.52 (36)	0.12 (42)	0.37 (38)	0.31 (39)	0.19	41
AWI-ESM-1-1-LR	0.83 (7)	0.41 (13)	0.75 (13)	0.17 (34)	0.76 (21)	0.74 (6)	0.84 (12)	0.55 (11)	0.74 (18)	0.60 (20)	0.66	10
BCC_CSM2-MR	0.15 (41)	0.38 (14)	0.80 (11)	0.63 (7)	0.61 (31)	0.51 (32)	0.71 (27)	0.51 (19)	0.59 (30)	0.30 (41)	0.44	29
BCC-ESM1-MR	0.08 (43)	0.56 (4)	0.58 (27)	0.61 (9)	0.43 (36)	0.43 (35)	0.64 (32)	0.42 (26)	0.82 (9)	0.82 (1)	0.51	23
CAMS-CSM1-0	0.69 (24)	0.64 (2)	0.26 (41)	0.08 (41)	0.56 (32)	0.46 (34)	0.47 (38)	0.11 (43)	0.50 (33)	0.45 (34)	0.28	36
CanESM5	0.55 (29)	0.11 (40)	0.65 (22)	0.71 (6)	0.54 (34)	0.27 (41)	0.71 (26)	0.52 (15)	0.64 (29)	0.57 (26)	0.40	31
CESM2	0.84 (5)	0.11 (39)	0.68 (18)	0.72 (4)	0.88 (4)	0.67 (20)	0.81 (16)	0.58 (7)	0.86 (5)	0.79 (3)	0.73	7
CESM2-FV2	0.81 (9)	0.57 (3)	0.72 (16)	0.21 (32)	0.76 (20)	0.64 (24)	0.81 (15)	0.43 (23)	0.69 (26)	0.52 (31)	0.56	19
CESM2-WACCM	0.85 (4)	0.11 (41)	0.67 (19)	0.76 (1)	0.88 (5)	0.68 (19)	0.80 (18)	0.56 (10)	0.31 (40)	0.79 (2)	0.65	11
CESM2-WACCM-FV2	0.76 (16)	0.54 (5)	0.86 (2)	0.50 (14)	0.93 (1)	0.75 (5)	0.94 (2)	0.58 (5)	0.82 (8)	0.69 (10)	0.85	1
CMCC-CM2-HR4	0.11 (42)	0.53 (7)	0.80 (10)	0.54 (13)	0.81 (13)	0.70 (11)	0.80 (19)	0.45 (21)	0.72 (21)	0.62 (18)	0.61	16
CMCC-ESM2	0.78 (11)	0.20 (28)	0.86 (3)	0.37 (20)	0.88 (3)	0.78 (2)	0.88 (5)	0.52 (17)	0.81 (10)	0.66 (16)	0.74	5
CNRM-CM6-1	0.50 (32)	0.29 (19)	0.29 (39)	0.14 (37)	0.35 (39)	0.37 (36)	0.31 (41)	0.28 (34)	0.46 (34)	0.40 (36)	0.23	39
CNRM-CM6-1_HR	0.45 (33)	0.44 (11)	0.31 (38)	0.23 (27)	0.40 (37)	0.36 (38)	0.34 (40)	0.25 (37)	0.42 (37)	0.38 (38)	0.25	37
CNRM-ESM2-1	0.51 (30)	0.29 (20)	0.27 (40)	0.12 (38)	0.33 (40)	0.37 (37)	0.30 (42)	0.27 (35)	0.45 (35)	0.40 (37)	0.21	40
E3SM-1-0	0.89 (2)	0.13 (36)	0.79 (12)	0.22 (30)	0.88 (6)	0.77 (3)	0.89 (4)	0.54 (12)	0.84 (6)	0.67 (14)	0.72	8
EC-Earth3	0.73 (21)	0.14 (33)	0.62 (23)	0.49 (15)	0.81 (12)	0.69 (14)	0.77 (21)	0.52 (14)	0.19 (43)	0.56 (28)	0.50	24
EC-Earth3-Veg	0.76 (17)	0.12 (38)	0.59 (26)	0.47 (17)	0.06 (44)	0.69 (13)	0.74 (24)	0.51 (18)	0.73 (20)	0.53 (30)	0.45	28
EC-Earth3-Veg-LR	0.77 (13)	0.11 (42)	0.53 (30)	0.41 (18)	0.81 (11)	0.70 (12)	0.72 (25)	0.44 (22)	0.72 (24)	0.46 (33)	0.49	25
FGOALS-f3-L	0.39	0.67	0.46	0.34	0.74	0.69	0.54	0.42	0.74	0.71	0.51	22

Models	TSS Values (Rank)											
	CDD	CWD	R10	R20	R95p T0T	R99p TOT	PRCP TOT	SDII	Rx 5day	Rx 1day	RM_ TSS	Over all ranks
	(36)	(1)	(32)	(22)	(24)	(16)	(35)	(25)	(19)	(9)		
GFDL-CM4	0.51	0.16	0.81	0.74	0.74	0.51	0.86	0.41	0.86	0.78	0.62	12
	(31)	(32)	(8)	(2)	(23)	(31)	(9)	(28)	(3)	(4)		
GFDL-ESM4	0.64	0.17	0.82	0.74	0.72	0.47	0.88	0.37	0.86	0.76	0.62	13
	(25)	(31)	(6)	(3)	(27)	(33)	(6)	(31)	(4)	(6)		
GISS-E2-2-G	0.73	0.50	0.44	0.29	0.68	0.68	0.55	0.38	0.72	0.68	0.48	26
	(22)	(9)	(35)	(25)	(28)	(17)	(34)	(30)	(23)	(12)		
HadGEM3-GC31-LL	0.29	0.48	0.21	0.10	0.27	0.16	0.23	0.07	0.14	0.13	0.13	44
	(38)	(10)	(42)	(40)	(41)	(43)	(44)	(44)	(44)	(44)		
HadGEM3-GC31-MM	0.75	0.28	0.73	0.55	0.85	0.69	0.80	0.41	0.68	0.66	0.60	18
	(19)	(21)	(15)	(12)	(9)	(15)	(20)	(27)	(28)	(15)		
IITM-ESM	0.74	0.13	0.44	0.22	0.75	0.57	0.76	0.39	0.68	0.44	0.37	32
	(20)	(37)	(33)	(29)	(22)	(28)	(22)	(29)	(27)	(35)		
INM_CM4-8	0.03	0.06	0.62	0.32	0.74	0.76	0.68	0.36	0.51	0.58	0.37	33
	(45)	(44)	(24)	(23)	(25)	(4)	(30)	(32)	(32)	(24)		
INM-CM5-0	0.03	0.06	0.51	0.21	0.78	0.63	0.67	0.33	0.55	0.61	0.32	35
	(44)	(45)	(31)	(31)	(18)	(25)	(31)	(33)	(31)	(19)		
IPSL-CM5A2-INCA	0.55	0.09	0.60	0.36	0.67	0.63	0.68	0.62	0.75	0.57	0.46	27
	(27)	(43)	(25)	(21)	(29)	(26)	(29)	(3)	(17)	(25)		
IPSL-CM6A-INCA	0.80	0.23	0.74	0.56	0.86	0.72	0.87	0.53	0.78	0.73	0.74	6
	(10)	(23)	(14)	(11)	(8)	(8)	(8)	(13)	(13)	(7)		
IPSL-CM6A-LR	0.78	0.18	0.66	0.61	0.80	0.61	0.82	0.45	0.71	0.69	0.60	17
	(12)	(30)	(20)	(8)	(14)	(27)	(13)	(20)	(25)	(11)		
KACE-1-0-G	0.43	0.43	0.44	0.29	0.64	0.55	0.47	0.25	0.42	0.53	0.33	34
	(34)	(12)	(34)	(24)	(30)	(30)	(37)	(36)	(36)	(29)		
KIOST-ESM	0.35	0.35	0.06	0.00	0.37	0.36	0.36	0.13	0.23	0.19	0.14	43
	(37)	(16)	(45)	(44)	(38)	(40)	(39)	(41)	(42)	(43)		
MIROC6	0.55	0.14	0.54	0.29	0.56	0.36	0.56	0.52	0.77	0.72	0.42	30
	(28)	(34)	(29)	(26)	(33)	(39)	(33)	(16)	(14)	(8)		
MPI-ESM-1-2-HAM	0.87	0.31	0.81	0.21	0.74	0.66	0.87	0.25	0.75	0.51	0.55	20
	(3)	(17)	(7)	(33)	(26)	(22)	(7)	(38)	(16)	(32)		
MPI-ESM1-2-HR	0.82	0.20	0.83	0.14	0.77	0.65	0.85	0.57	0.80	0.56	0.61	15
	(8)	(27)	(4)	(36)	(19)	(23)	(11)	(8)	(11)	(27)		
MPI-ESM1-2-LR	0.77	0.23	0.80	0.04	0.78	0.73	0.89	0.63	0.83	0.60	0.68	9
	(14)	(24)	(9)	(42)	(17)	(7)	(3)	(2)	(7)	(21)		
MRI-ESM2-0	0.91	0.20	0.57	0.41	0.79	0.66	0.69	0.42	0.72	0.60	0.53	21
	(1)	(29)	(28)	(19)	(15)	(21)	(28)	(24)	(22)	(23)		
NESM3	0.76	0.22	0.95	0.23	0.89	0.78	0.96	0.63	0.87	0.60	0.78	2
	(15)	(26)	(1)	(28)	(2)	(1)	(1)	(1)	(1)	(22)		
NorESM2-LM	0.75	0.53	0.83	0.48	0.83	0.70	0.86	0.58	0.78	0.67	0.76	3
	(18)	(8)	(5)	(16)	(10)	(9)	(10)	(6)	(12)	(13)		
NorESM2-MM	0.83	0.14	0.66	0.72	0.88	0.70	0.80	0.59	0.86	0.77	0.75	4
	(6)	(35)	(21)	(5)	(7)	(10)	(17)	(4)	(2)	(5)		
SAMO-UNICON	0.72	0.22	0.31	0.00	0.53	0.57	0.76	0.17	0.30	0.23	0.25	38
	(23)	(25)	(37)	(45)	(35)	(29)	(23)	(39)	(41)	(42)		
TaiESM1	0.40	0.27	0.71	0.60	0.78	0.68	0.81	0.56	0.76	0.66	0.62	14
	(35)	(22)	(17)	(10)	(16)	(18)	(14)	(9)	(15)	(17)		
UKESM1-0-LL	0.18	0.54	0.12	0.03	0.17	0.08	0.15	0.03	0.06	0.05	0.11	45

Models	TSS Values (Rank)											
	CDD	CWD	R10	R20	R95pTOT	R99pTOT	PRCPTOT	SDII	Rx5day	Rx1day	RM_TSS	Overall ranks
	(40)	(6)	(44)	(43)	(43)	(44)	(45)	(45)	(45)	(45)		

B10: TSS values and overall ranks of CMIP6 models based on RM of TSS values for 45 CMIP6 models for the period 1981-2014 over Ethiopia with respect to observational dataset during FMAM season. Numbers within brackets represent the rank of CMIP6 model for each extreme index with respect to TSS values.

Models	TSS Values(Rank)										RM_TSS	Overall ranks
	CDD	CWD	R10	R20	R95PTOT	R99PTOT	PRCPTOT	SDII	Rx5day	Rx1day		
ACCESS-CM2	0.46 (41)	0.57 (1)	0.75 (1)	0.12 (28)	0.27 (44)	0.33 (22)	0.32 (42)	0.06 (39)	0.34 (37)	0.32 (24)	0.31	39
ACCESS-ESM1-5	0.58 (22)	0.49 (2)	0.19 (40)	0.03 (35)	0.35 (38)	0.13 (41)	0.32 (43)	0.05 (42)	0.25 (42)	0.13 (40)	0.24	44
AWI-ESM-1-1-LR	0.74 (5)	0.31 (13)	0.12 (44)	0.00 (45)	0.47 (24)	0.40 (13)	0.03 (45)	0.49 (2)	0.67 (4)	0.40 (14)	0.62	12
BCC_CSM2-MR	0.50 (36)	0.24 (18)	0.60 (10)	0.44 (10)	0.15 (45)	0.21 (36)	0.55 (29)	0.17 (22)	0.36 (34)	0.28 (25)	0.43	27
BCC-ESM1-MR	0.76 (3)	0.41 (4)	0.60 (8)	0.49 (8)	0.41 (31)	0.49 (5)	0.66 (12)	0.25 (8)	0.52 (19)	0.47 (7)	0.76	6
CAMS-CSM1-0	0.75 (4)	7.00 (5)	0.58 (12)	0.04 (32)	0.67 (6)	0.47 (6)	0.70 (8)	0.16 (25)	0.61 (9)	0.47 (6)	0.71	8
CanESM5	0.68 (16)	0.19 (24)	0.35 (32)	0.38 (12)	0.32 (41)	0.38 (16)	0.62 (16)	0.29 (7)	0.38 (31)	0.37 (21)	0.56	16
CESM2	0.67 (18)	0.17 (26)	0.56 (17)	0.52 (5)	0.55 (13)	0.41 (12)	0.61 (20)	0.18 (17)	0.60 (10)	0.42 (12)	0.67	10
CESM2-FV2	0.38 (43)	0.18 (25)	0.53 (21)	0.51 (7)	0.49 (21)	0.42 (10)	0.56 (27)	0.30 (6)	0.53 (17)	0.44 (10)	0.59	15
CESM2-WACCM	0.71 (11)	0.21 (20)	0.51 (23)	0.55 (2)	0.59(11)	0.35 (20)	0.64 (13)	0.18 (18)	0.55 (14)	0.37 (20)	0.68	9
CESM2-WACCM-FV2	0.51 (34)	0.20 (23)	0.56 (19)	0.51 (6)	0.52 (20)	0.37 (17)	0.62 (17)	0.23 (10)	0.54 (16)	0.39 (16)	0.60	14
CMCC-CM2-HR4	0.48 (40)	0.12 (31)	0.50 (24)	0.31 (18)	0.32 (40)	0.25 (30)	0.43 (36)	0.17 (23)	0.32 (38)	0.26 (29)	0.32	38
CMCC-ESM2	0.57 (25)	0.05 (41)	0.35 (30)	0.52 (4)	0.52 (18)	0.36 (19)	0.44 (34)	0.23 (9)	0.57 (12)	0.38 (19)	0.53	18
CNRM-CM6-1	0.63 (19)	0.22 (19)	0.30 (35)	0.24 (23)	0.48 (23)	0.26 (28)	0.47 (33)	0.12 (29)	0.37 (32)	0.26 (31)	0.43	28
CNRM-CM6-1_HR	0.26 (45)	0.07 (39)	0.41 (26)	0.25 (22)	0.53 (15)	0.55 (2)	0.35 (40)	0.19 (16)	0.50 (23)	0.51 (5)	0.53	19

Models	TSS Values(Rank)										RM_TSS	Overall ranks
	CDD	CWD	R10	R20	R95PTOT	R99PTOT	PRCPTOT	SDII	Rx 5day	Rx 1day		
CNRM-ESM2-1	0.57 (24)	0.20 (22)	0.28 (36)	0.30 (19)	0.46 (25)	0.39 (15)	0.43 (35)	0.18 (20)	0.36 (35)	0.38 (17)	0.42	29
E3SM-1-0	0.54 (29)	0.12 (32)	0.38 (28)	0.34 (15)	0.53 (16)	0.18 (40)	0.60 (22)	0.12 (28)	0.46 (26)	0.19 (38)	0.43	26
EC-Earth3	0.72 (8)	0.26 (17)	0.57 (15)	0.11 (29)	0.42 (29)	0.19 (39)	0.60 (23)	0.18 (19)	0.17 (45)	0.15 (39)	0.44	25
EC-Earth3-Veg	0.72 (7)	0.27 (15)	0.60 (9)	0.12 (27)	0.44 (27)	0.22 (33)	0.61 (21)	0.21 (12)	0.50 (22)	0.21 (34)	0.55	17
EC-Earth3-Veg-LR	0.71 (10)	0.33 (11)	0.59 (11)	0.04 (33)	0.31 (42)	0.10 (42)	0.51 (30)	0.13 (27)	0.40 (29)	0.10 (42)	0.37	35
FGOALS-f3-L	0.49 (37)	0.36 (8)	0.47 (25)	0.13 (26)	0.46 (26)	0.31 (25)	0.27 (44)	0.07 (37)	0.36 (36)	0.33 (23)	0.34	36
GFDL-CM4	0.70 (12)	0.34 (9)	0.16 (43)	0.53 (3)	0.72 (2)	0.53 (3)	0.76 (3)	0.12 (30)	0.64 (5)	0.57 (3)	0.84	3
GFDL-ESM4	0.76 (2)	0.40 (6)	0.68 (4)	0.40 (11)	0.77 (1)	0.43 (8)	0.74 (5)	0.04 (43)	0.62 (7)	0.44 (9)	0.77	5
GISS-E2-2-G	0.62 (20)	0.15 (27)	0.58 (13)	0.24 (24)	0.40 (34)	0.25 (32)	0.49 (31)	0.17 (21)	0.37 (33)	0.25 (32)	0.39	33
HadGEM3-GC31-LL	0.53 (31)	0.04 (43)	0.40 (27)	0.34 (16)	0.30 (43)	0.32 (24)	0.37 (39)	0.11 (31)	0.45 (27)	0.28 (26)	0.32	37
HadGEM3-GC31-MM	0.70 (14)	0.27 (16)	0.34 (33)	0.37 (13)	0.66 (7)	0.60 (1)	0.80 (1)	0.20 (14)	0.72 (2)	0.59 (2)	0.84	2
IITM-ESM	0.58 (23)	0.11 (35)	0.73 (2)	0.04 (31)	0.52 (17)	0.07 (44)	0.58 (26)	0.06 (38)	0.25 (43)	0.07 (44)	0.26	41
INM_CM4-8	0.56 (26)	0.03 (44)	0.26 (38)	0.01 (43)	0.54 (14)	0.20 (38)	0.62 (18)	0.05 (41)	0.30 (41)	0.19 (37)	0.25	42
INM-CM5-0	0.55 (27)	0.05 (42)	0.18 (42)	0.01 (41)	0.52 (19)	0.20 (37)	0.64 (15)	0.05 (40)	0.31 (40)	0.12 (41)	0.25	43
IPSL-CM5A2-INCA	0.51 (33)	0.08 (38)	0.05 (45)	0.02 (39)	0.43 (28)	0.33 (21)	0.60 (24)	0.39 (4)	0.55 (13)	0.34 (22)	0.47	23
IPSL-CM6A-INCA	0.36 (44)	0.06 (40)	0.51 (22)	0.03 (36)	0.68 (4)	0.41 (11)	0.62 (19)	0.41 (3)	0.73 (1)	0.41 (13)	0.62	13
IPSL-CM6A-LR	0.55 (28)	0.14 (28)	0.64 (6)	0.06 (30)	0.62 (8)	0.21 (35)	0.69 (11)	0.08 (36)	0.53 (18)	0.22 (33)	0.49	21
KACE-1-0-G	0.41 (42)	0.11 (33)	0.63 (7)	0.34 (14)	0.38 (35)	0.40 (14)	0.56 (28)	0.20 (13)	0.54 (15)	0.40 (15)	0.51	20
KIOST-ESM	0.48 (38)	0.11 (34)	0.56 (18)	0.02 (40)	0.67 (5)	0.25 (31)	0.74 (6)	0.10 (32)	0.50 (21)	0.27 (28)	0.40	30
MIROC6	0.48 (39)	0.14 (29)	0.20 (39)	0.16 (25)	0.36 (37)	0.43 (9)	0.34 (41)	0.16 (24)	0.46 (25)	0.42 (11)	0.40	31
MPI-ESM-1-2-HAM	0.71 (9)	0.20 (21)	0.27 (37)	0.02 (37)	0.60 (9)	0.37 (18)	0.80 (2)	0.50 (1)	0.63 (6)	0.38 (18)	0.73	7
MPI-ESM1-2-HR	0.81 (1)	0.39 (7)	0.58 (14)	0.04 (34)	0.56 (12)	0.32 (23)	0.69 (10)	0.00 (45)	0.57 (11)	0.59 (1)	0.66	11
MPI-ESM1-2-LR	0.68 (17)	0.31 (12)	0.57 (16)	0.01 (42)	0.41 (30)	0.08 (43)	0.70 (9)	0.09 (34)	0.31 (39)	0.08 (43)	0.38	34

Models	TSS Values(Rank)										RM_TSS	Over all ranks
	CDD	CWD	R10	R20	R95PTOT	R99PTOT	PRCPTOT	SDII	Rx 5day	Rx 1day		
MRI-ESM2-0	0.70 (13)	0.14 (30)	0.31 (34)	0.28 (20)	0.40 (33)	0.26 (26)	0.38 (38)	0.14 (26)	0.40 (28)	0.26 (30)	0.40	32
NESM3	0.73 (6)	0.43 (3)	0.55 (20)	0.02 (38)	0.41 (32)	0.22 (34)	0.64 (14)	0.09 (33)	0.51 (20)	0.20 (36)	0.49	22
NorESM2-LM	0.51 (32)	0.34 (10)	0.65 (5)	0.44 (9)	0.60 (10)	0.51 (4)	0.71 (7)	0.39 (5)	0.62 (8)	0.52 (4)	0.80	4
NorESM2-MM	0.69 (15)	0.29 (14)	0.70 (3)	0.61 (1)	0.71 (3)	0.44 (7)	0.76 (4)	0.21 (11)	0.67 (3)	0.45 (8)	0.85	1
SAMO-UNICON	0.54 (30)	0.10 (36)	0.18 (41)	0.00 (44)	0.37 (36)	0.03 (45)	0.60 (25)	0.02 (44)	0.20 (44)	0.04 (45)	0.15	45
TaiESM1	0.59 (21)	0.09 (37)	0.35 (31)	0.33 (17)	0.49 (22)	0.26 (29)	0.49 (32)	0.19 (15)	0.48 (24)	0.27 (27)	0.45	24
UKESM1-0-LL	0.51 (35)	0.03 (45)	0.37 (29)	0.27 (21)	0.33 (39)	0.26 (27)	0.40 (37)	0.08 (35)	0.39 (30)	0.21 (35)	0.28	40

B11: TSS values and overall ranks of CMIP6 models, EnseMean_ALL and EnseMean based on RM of TSS values for the period 1981-2014 during JJAS season over Ethiopia with respect to observational dataset

Models	TSS Values											
	CDD	CWD	R10	R20	R95pTOT	R99pTOT	PRCPTOT	SDII	Rx 5day	Rx 1day	RM_TSS	Over all ranks
ACCESS-CM2	0.28	0.38	0.19	0.17	0.26	0.21	0.26	0.16	0.32	0.30	0.16	44
ACCESS-ESM1-5	0.60	0.31	0.37	0.11	0.02	0.02	0.52	0.12	0.37	0.31	0.19	43
AWI-ESM-1-1-LR	0.83	0.41	0.75	0.17	0.76	0.74	0.84	0.55	0.74	0.60	0.64	11
BCC_CSM2-MR	0.15	0.38	0.80	0.63	0.61	0.51	0.71	0.51	0.59	0.30	0.43	31
BCC-ESM1-MR	0.08	0.56	0.58	0.61	0.43	0.43	0.64	0.42	0.82	0.82	0.50	25
CAMS-CSM1-0	0.69	0.64	0.26	0.08	0.56	0.46	0.47	0.11	0.50	0.45	0.28	38
CanESM5	0.55	0.11	0.65	0.71	0.54	0.27	0.71	0.52	0.64	0.57	0.40	33
CESM2	0.84	0.11	0.68	0.72	0.88	0.67	0.81	0.58	0.86	0.79	0.72	8
CESM2-FV2	0.81	0.57	0.72	0.21	0.76	0.64	0.81	0.43	0.69	0.52	0.55	21
CESM2-WACCM	0.85	0.11	0.67	0.76	0.88	0.68	0.80	0.56	0.31	0.79	0.64	12
CESM2-WACCM-FV2	0.76	0.54	0.86	0.50	0.93	0.75	0.94	0.58	0.82	0.69	0.85	1
CMCC-CM2-HR4	0.11	0.53	0.80	0.54	0.81	0.70	0.80	0.45	0.72	0.62	0.60	16
CMCC-ESM2	0.78	0.20	0.86	0.37	0.88	0.78	0.88	0.52	0.81	0.66	0.73	7
CNRM-CM6-1	0.50	0.29	0.29	0.14	0.35	0.37	0.31	0.28	0.46	0.40	0.22	41

	TSS Values											
Models	CDD	CWD	R10	R20	R95p TOT	R99p TOT	PRCP TOT	SDII	Rx 5day	Rx 1day	RM_ TSS	Over all ranks
CNRM-CM6-1_HR	0.45	0.44	0.31	0.23	0.40	0.36	0.34	0.25	0.42	0.38	0.24	39
CNRM-ESM2-1	0.51	0.29	0.27	0.12	0.33	0.37	0.30	0.27	0.45	0.40	0.21	42
E3SM-1-0	0.89	0.13	0.79	0.22	0.88	0.77	0.89	0.54	0.84	0.67	0.71	9
EC-Earth3	0.73	0.14	0.62	0.49	0.81	0.69	0.77	0.52	0.19	0.56	0.49	26
EC-Earth3-Veg	0.76	0.12	0.59	0.47	0.06	0.69	0.74	0.51	0.73	0.53	0.44	30
EC-Earth3-Veg-LR	0.77	0.11	0.53	0.41	0.81	0.70	0.72	0.44	0.72	0.46	0.48	27
EnseMean	0.83	0.25	0.86	0.43	0.88	0.77	0.92	0.52	0.86	0.68	0.80	2
EnseMean_ALL	0.69	0.46	0.70	0.59	0.76	0.73	0.77	0.36	0.67	0.61	0.57	20
FGOALS-f3-L	0.39	0.67	0.46	0.34	0.74	0.69	0.54	0.42	0.74	0.71	0.50	24
GFDL-CM4	0.51	0.16	0.81	0.74	0.74	0.51	0.86	0.41	0.86	0.78	0.61	13
GFDL-ESM4	0.64	0.17	0.82	0.74	0.72	0.47	0.88	0.37	0.86	0.76	0.61	15
GISS-E2-2-G	0.73	0.50	0.44	0.29	0.68	0.68	0.55	0.38	0.72	0.68	0.47	28
HadGEM3-GC31-LL	0.29	0.48	0.21	0.10	0.27	0.16	0.23	0.07	0.14	0.13	0.13	46
HadGEM3-GC31-MM	0.75	0.28	0.73	0.55	0.85	0.69	0.80	0.41	0.68	0.66	0.59	19
IITM-ESM	0.74	0.13	0.44	0.22	0.75	0.57	0.76	0.39	0.68	0.44	0.36	34
INM_CM4-8	0.03	0.06	0.62	0.32	0.74	0.76	0.68	0.36	0.51	0.58	0.36	35
INM-CM5-0	0.03	0.06	0.51	0.21	0.78	0.63	0.67	0.33	0.55	0.61	0.30	37
IPSL-CM5A2-INCA	0.55	0.09	0.60	0.36	0.67	0.63	0.68	0.62	0.75	0.57	0.44	29
IPSL-CM6A-INCA	0.80	0.23	0.74	0.56	0.86	0.72	0.87	0.53	0.78	0.73	0.73	6
IPSL-CM6A-LR	0.78	0.18	0.66	0.61	0.80	0.61	0.82	0.45	0.71	0.69	0.59	18
KACE-1-0-G	0.43	0.43	0.44	0.29	0.64	0.55	0.47	0.25	0.42	0.53	0.32	36
KIOST-ESM	0.35	0.35	0.06	0.00	0.37	0.36	0.36	0.13	0.23	0.19	0.14	45
MIROC6	0.55	0.14	0.54	0.29	0.56	0.36	0.56	0.52	0.77	0.72	0.41	32
MPI-ESM-1-2-HAM	0.87	0.31	0.81	0.21	0.74	0.66	0.87	0.25	0.75	0.51	0.54	22
MPI-ESM1-2-HR	0.82	0.20	0.83	0.14	0.77	0.65	0.85	0.57	0.80	0.56	0.60	17
MPI-ESM1-2-LR	0.77	0.23	0.80	0.04	0.78	0.73	0.89	0.63	0.83	0.60	0.66	10
MRI-ESM2-0	0.91	0.20	0.57	0.41	0.79	0.66	0.69	0.42	0.72	0.60	0.52	23
NESM3	0.76	0.22	0.95	0.23	0.89	0.78	0.96	0.63	0.87	0.60	0.78	3
NorESM2-LM	0.75	0.53	0.83	0.48	0.83	0.70	0.86	0.58	0.78	0.67	0.75	4
NorESM2-MM	0.83	0.14	0.66	0.72	0.88	0.70	0.80	0.59	0.86	0.77	0.74	5
SAMO-UNICON	0.72	0.22	0.31	0.00	0.53	0.57	0.76	0.17	0.30	0.23	0.24	40
TaiESM1	0.40	0.27	0.71	0.60	0.78	0.68	0.81	0.56	0.76	0.66	0.61	14
UKESM1-0-LL	0.18	0.54	0.12	0.03	0.17	0.08	0.15	0.03	0.06	0.05	0.11	47

B12: TSS values and overall ranks of CMIP6 models, EnseMean_ALL and EnseMean based on RM of TSS values for the period 1981-2014 during FMAM season over Ethiopia with respect to observational dataset

	TSS Values											
Models	CDD	CWD	R10	R20	R95p TOT	R99p TOT	PRCP TOT	SDII	Rx 5day	Rx 1day	RM_ TSS	Over all ranks
EnseMean	0.72	0.28	0.78	0.53	0.66	0.62	0.81	0.32	0.70	0.61	0.89	1
NorESM2-MM	0.69	0.29	0.70	0.61	0.71	0.44	0.76	0.21	0.67	0.45	0.83	2
HadGEM3-GC31-MM	0.70	0.27	0.73	0.37	0.66	0.60	0.80	0.20	0.72	0.59	0.83	3
GFDL-CM4	0.70	0.34	0.68	0.53	0.72	0.53	0.76	0.12	0.64	0.57	0.82	4
EnseMean_ALL	0.23	0.23	0.67	0.36	0.71	0.55	0.78	0.47	0.71	0.58	0.77	5
NorESM2-LM	0.51	0.34	0.65	0.44	0.60	0.51	0.71	0.39	0.62	0.52	0.77	6
GFDL-ESM4	0.76	0.40	0.58	0.40	0.77	0.43	0.74	0.04	0.62	0.44	0.75	7
BCC-ESM1-MR	0.76	0.41	0.58	0.49	0.41	0.49	0.66	0.25	0.52	0.47	0.74	8
MPI-ESM-1-2-HAM	0.71	0.20	0.75	0.02	0.60	0.37	0.80	0.50	0.63	0.38	0.71	9
CAMS-CSM1-0	0.75	0.40	0.35	0.04	0.67	0.47	0.70	0.16	0.61	0.47	0.69	10
CESM2-WACCM	0.71	0.21	0.56	0.55	0.59	0.35	0.64	0.18	0.55	0.37	0.65	11
CESM2	0.67	0.17	0.53	0.52	0.55	0.41	0.61	0.18	0.60	0.42	0.63	12
MPI-ESM1-2-HR	0.81	0.39	0.58	0.04	0.56	0.32	0.69	0.00	0.57	0.59	0.63	13
AWI-ESM-1-1-LR	0.74	0.31	0.60	0.00	0.47	0.40	0.03	0.49	0.67	0.40	0.60	14
IPSL-CM6A-INCA	0.36	0.06	0.64	0.03	0.68	0.41	0.62	0.41	0.73	0.41	0.59	15
CESM2-WACCM-FV2	0.51	0.20	0.50	0.51	0.52	0.37	0.62	0.23	0.54	0.39	0.57	16
CESM2-FV2	0.38	0.18	0.51	0.51	0.49	0.42	0.56	0.30	0.53	0.44	0.56	17
CanESM5	0.68	0.19	0.56	0.38	0.32	0.38	0.62	0.29	0.38	0.37	0.53	18
EC-Earth3-Veg	0.72	0.27	0.59	0.12	0.44	0.22	0.61	0.21	0.50	0.21	0.52	19
CMCC-ESM2	0.57	0.05	0.30	0.52	0.52	0.36	0.44	0.23	0.57	0.38	0.50	20
KACE-1-0-G	0.41	0.11	0.56	0.34	0.38	0.40	0.56	0.20	0.54	0.40	0.48	21
NESM3	0.73	0.43	0.55	0.02	0.41	0.22	0.64	0.09	0.51	0.20	0.46	22
IPSL-CM6A-LR	0.55	0.14	0.63	0.06	0.62	0.21	0.69	0.08	0.53	0.22	0.46	23
CNRM-ESM2-1	0.57	0.20	0.38	0.30	0.46	0.39	0.43	0.18	0.36	0.38	0.45	24
CNRM-CM6-1_HR	0.26	0.07	0.28	0.25	0.53	0.55	0.35	0.19	0.50	0.51	0.44	25
IPSL-CM5A2-INCA	0.51	0.08	0.51	0.02	0.43	0.33	0.60	0.39	0.55	0.34	0.44	26
TaiESM1	0.59	0.09	0.35	0.33	0.49	0.26	0.49	0.19	0.48	0.27	0.42	27
EC-Earth3	0.72	0.26	0.60	0.11	0.42	0.19	0.60	0.18	0.17	0.15	0.41	28
BCC_CSM2-MR	0.50	0.24	0.60	0.44	0.15	0.21	0.55	0.17	0.36	0.28	0.40	29
E3SM-1-0	0.54	0.12	0.57	0.34	0.53	0.18	0.60	0.12	0.46	0.19	0.40	30
CNRM-CM6-1	0.63	0.22	0.41	0.24	0.48	0.26	0.47	0.12	0.37	0.26	0.40	31
KIOST-ESM	0.48	0.11	0.20	0.02	0.67	0.25	0.74	0.10	0.50	0.27	0.38	32

	TSS Values											
Models	CDD	CWD	R10	R20	R95p TOT	R99p TOT	PRCP TOT	SDII	Rx 5day	Rx 1day	RM_ TSS	Over all ranks
MIROC6	0.48	0.14	0.27	0.16	0.36	0.43	0.34	0.16	0.46	0.42	0.37	33
MRI-ESM2-0	0.70	0.14	0.31	0.28	0.40	0.26	0.38	0.14	0.40	0.26	0.37	34
GISS-E2-2-G	0.62	0.15	0.40	0.24	0.40	0.25	0.49	0.17	0.37	0.25	0.36	35
MPI-ESM1-2-LR	0.68	0.31	0.57	0.01	0.41	0.08	0.70	0.09	0.31	0.08	0.36	36
EC-Earth3-Veg-LR	0.71	0.33	0.47	0.04	0.31	0.10	0.51	0.13	0.40	0.10	0.34	37
FGOALS-f3-L	0.49	0.36	0.16	0.13	0.46	0.31	0.27	0.07	0.36	0.33	0.31	38
HadGEM3-GC31-LL	0.53	0.04	0.34	0.34	0.30	0.32	0.37	0.11	0.45	0.28	0.29	39
CMCC-CM2-HR4	0.48	0.12	0.35	0.31	0.32	0.25	0.43	0.17	0.32	0.26	0.29	40
ACCESS-CM2	0.46	0.57	0.19	0.12	0.27	0.33	0.32	0.06	0.34	0.32	0.29	41
UKESM1-0-LL	0.51	0.03	0.37	0.27	0.33	0.26	0.40	0.08	0.39	0.21	0.25	42
IITM-ESM	0.58	0.11	0.26	0.04	0.52	0.07	0.58	0.06	0.25	0.07	0.24	43
INM_CM4-8	0.56	0.03	0.18	0.01	0.54	0.20	0.62	0.05	0.30	0.19	0.23	44
ACCESS-ESM1-5	0.58	0.49	0.12	0.03	0.35	0.13	0.32	0.05	0.25	0.13	0.22	45
INM-CM5-0	0.55	0.05	0.05	0.01	0.52	0.20	0.64	0.05	0.31	0.12	0.22	46
SAMO-UNICON	0.54	0.10	0.18	0.00	0.37	0.03	0.60	0.02	0.20	0.04	0.13	47

B13: RM values of bias (RM_Pbias), RMSE (RM_NRMSE),PCC (RM_PCC), TSS (RM_TSS) and overall ranks of CMIP6 models, EnseMean and EnseMean_ALL for the period 1981-2014 over Ethiopia during JJAS season with respect to observational dataset

Models	RM_Pbias	RM_NRMSE	RM_PCC	RM_TSS
	(Rank)	(Rank)	(Rank)	(Rank)
ACCESS-CM2	0.51(22)	0.23(43)	0.04(47)	0.16(44)
ACCESS-ESM1-5	0.32(38)	0.29(40)	0.16(42)	0.19(43)
AWI-ESM-1-1-LR	0.64(8)	0.68(6)	0.58(21)	0.64(11)
BCC_CSM2-MR	0.45(32)	0.43(29)	0.37(31)	0.43(31)
BCC-ESM1-MR	0.35(37)	0.37(33)	0.36(33)	0.50(25)
CAMS-CSM1-0	0.62(12)	0.64(9)	0.29(39)	0.28(38)
CanESM5	0.56(18)	0.15(47)	0.59(19)	0.40(33)
CESM2	0.65(7)	0.57(20)	0.78(8)	0.72(8)
CESM2-FV2	0.51(24)	0.74(3)	0.74(11)	0.55(21)
CESM2-WACCM	0.62(11)	0.54(23)	0.82(5)	0.64(12)
CESM2-WACCM-FV2	0.40(35)	0.63(10)	0.83(2)	0.85(1)
CMCC-CM2-HR4	0.63(10)	0.61(15)	0.50(24)	0.60(16)
CMCC-ESM2	0.54(19)	0.67(7)	0.77(9)	0.73(7)
CNRM-CM6-1	0.18(46)	0.19(45)	0.09(44)	0.22(41)
CNRM-CM6-1_HR	0.28(41)	0.30(37)	0.08(45)	0.24(39)
CNRM-ESM2-1	0.17(47)	0.17(46)	0.07(46)	0.21(42)
E3SM-1-0	0.53(21)	0.62(12)	0.76(10)	0.71(9)
EC-Earth3	0.60(14)	0.49(25)	0.41(27)	0.49(26)
EC-Earth3-Veg	0.59(16)	0.45(27)	0.31(37)	0.44(30)
EC-Earth3-Veg-LR	0.58(17)	0.40(32)	0.38(29)	0.48(27)
EnseMean	0.69(3)	0.88(1)	0.82(4)	0.80(2)
EnseMean_ALL	0.66(5)	0.81(2)	0.79(7)	0.57(20)
FGOALS-f3-L	0.48(30)	0.55(22)	0.60(16)	0.50(24)
GFDL-CM4	0.51(25)	0.59(18)	0.64(13)	0.61(13)
GFDL-ESM4	0.49(28)	0.59(17)	0.65(12)	0.61(15)
GISS-E2-2-G	0.49(29)	0.58(19)	0.33(35)	0.47(28)
HadGEM3-GC31-LL	0.29(40)	0.29(38)	0.16(41)	0.13(46)
HadGEM3-GC31-MM	0.71(2)	0.71(4)	0.50(25)	0.59(19)
IITM-ESM	0.39(36)	0.42(31)	0.41(28)	0.36(34)
INM_CM4-8	0.45(33)	0.36(34)	0.37(30)	0.36(35)
INM-CM5-0	0.41(34)	0.36(35)	0.33(36)	0.30(37)
IPSL-CM5A2-INCA	0.50(26)	0.26(41)	0.31(38)	0.44(29)
IPSL-CM6A-INCA	0.61(13)	0.62(14)	0.59(20)	0.73(6)
IPSL-CM6A-LR	0.60(15)	0.57(21)	0.46(26)	0.59(18)
KACE-1-0-G	0.63(9)	0.48(26)	0.18(40)	0.32(36)
KIOST-ESM	0.19(45)	0.29(39)	0.35(34)	0.14(45)
MIROC6	0.27(43)	0.23(44)	0.63(14)	0.41(32)

Models	RM_Pbias	RM_NRMSE	RM_PCC	RM_TSS
MPI-ESM-1-2-HAM	0.47(31)	0.59(16)	0.57(22)	0.54(22)
MPI-ESM1-2-HR	0.51(23)	0.63(11)	0.62(15)	0.60(17)
MPI-ESM1-2-LR	0.28(42)	0.43(30)	0.83(3)	0.66(10)
MRI-ESM2-0	0.75(1)	0.44(28)	0.37(32)	0.52(23)
NESM3	0.50(27)	0.67(8)	0.93(1)	0.78(3)
NorESM2-LM	0.68(4)	0.70(5)	0.60(17)	0.75(4)
NorESM2-MM	0.66(6)	0.62(13)	0.81(6)	0.74(5)
SAMO-UNICON	0.29(39)	0.35(36)	0.60(18)	0.24(40)
TaiESM1	0.53(20)	0.53(24)	0.54(23)	0.61(14)
UKESM1-0-LL	0.24(44)	0.25(42)	0.13(43)	0.11(47)

B14: RM values of bias (RM_Pbias), RMSE (RM_NRMSE),PCC (RM_PCC), TSS (RM_TSS) and overall ranks of CMIP6 models, EnseMean and EnseMean_ALL for the period 1981-2014 over Ethiopia during FMAM season with respect to observational dataset

Models	RM_Pbias	RM_NRMSE	RM_PCC	RM_TSS
	(Rank)	(Rank)	(Rank)	(Rank)
ACCESS-CM2	0.60(11)	0.53(16)	0.23(39)	0.29(41)
ACCESS-ESM1-5	0.30(41)	0.33(37)	0.64(14)	0.22(45)
AWI-ESM-1-1-LR	0.23(44)	0.50(21)	0.75(10)	0.60(14)
BCC_CSM2-MR	0.47(27)	0.24(44)	0.39(27)	0.40(29)
BCC-ESM1-MR	0.66(7)	0.59(14)	0.69(13)	0.74(8)
CAMS-CSM1-0	0.36(36)	0.67(9)	0.87(2)	0.69(10)
CanESM5	0.62(9)	0.44(27)	0.55(19)	0.53(18)
CESM2	0.58(16)	0.62(12)	0.57(18)	0.63(12)
CESM2-FV2	0.76(3)	0.66(10)	0.39(28)	0.56(17)
CESM2-WACCM	0.53(22)	0.63(11)	0.62(16)	0.65(11)
CESM2-WACCM-FV2	0.60(12)	0.40(33)	0.38(29)	0.57(16)
CMCC-CM2-HR4	0.72(5)	0.29(41)	0.11(47)	0.29(40)
CMCC-ESM2	0.55(19)	0.48(22)	0.50(22)	0.50(20)
CNRM-CM6-1	0.59(15)	0.46(23)	0.19(41)	0.40(31)
CNRM-CM6-1_HR	0.61(10)	0.41(31)	0.25(38)	0.44(25)
CNRM-ESM2-1	0.50(23)	0.36(34)	0.19(42)	0.45(24)
E3SM-1-0	0.62(8)	0.59(13)	0.37(32)	0.40(30)
EC-Earth3	0.45(31)	0.42(28)	0.37(31)	0.41(28)
EC-Earth3-Veg	0.37(35)	0.52(17)	0.45(25)	0.52(19)
EC-Earth3-Veg-LR	0.33(37)	0.41(30)	0.38(30)	0.34(37)
EnseMean	0.75(2)	0.97(1)	0.89(1)	0.89(1)
EnseMean_ALL	0.76(4)	0.89(2)	0.78(9)	0.77(5)
FGOALS-f3-L	0.66(6)	0.83(4)	0.51(21)	0.31(38)
GFDL-CM4	0.56(18)	0.58(15)	0.80(8)	0.82(4)
GFDL-ESM4	0.57(17)	0.71(8)	0.82(6)	0.75(7)

Models	RM_Pbias	RM_NRMSE	RM_PCC	RM_TSS
GISS-E2-2-G	0.54(21)	0.45(25)	0.17(44)	0.36(35)
HadGEM3-GC31-LL	0.46(29)	0.32(38)	0.21(40)	0.29(39)
HadGEM3-GC31-MM	0.59(14)	0.80(5)	0.86(3)	0.83(3)
IITM-ESM	0.44(32)	0.29(40)	0.15(46)	0.24(43)
INM_CM4-8	0.22(46)	0.16(46)	0.30(35)	0.23(44)
INM-CM5-0	0.23(45)	0.20(45)	0.27(36)	0.22(46)
IPSL-CM5A2-INCA	0.16(47)	0.16(47)	0.51(20)	0.44(26)
IPSL-CM6A-INCA	0.32(39)	0.51(18)	0.72(12)	0.59(15)
IPSL-CM6A-LR	0.38(34)	0.36(36)	0.47(24)	0.46(23)
KACE-1-0-G	0.50(24)	0.51(19)	0.34(33)	0.48(21)
KIOST-ESM	0.24(43)	0.36(35)	0.58(17)	0.38(32)
MIROC6	0.27(42)	0.25(43)	0.43(26)	0.37(33)
MPI-ESM-1-2-HAM	0.49(25)	0.72(7)	0.73(11)	0.71(9)
MPI-ESM1-2-HR	0.47(26)	0.51(20)	0.85(4)	0.63(13)
MPI-ESM1-2-LR	0.44(33)	0.45(24)	0.47(23)	0.36(36)
MRI-ESM2-0	0.46(30)	0.41(29)	0.25(37)	0.37(34)
NESM3	0.32(38)	0.41(32)	0.84(5)	0.46(22)
NorESM2-LM	0.59(13)	0.77(6)	0.63(15)	0.77(6)
NorESM2-MM	0.77(1)	0.84(3)	0.82(7)	0.83(2)
SAMO-UNICON	0.32(40)	0.26(42)	0.18(43)	0.13(47)
TaiESM1	0.54(20)	0.44(26)	0.34(34)	0.42(27)
UKESM1-0-LL	0.47(28)	0.31(39)	0.15(45)	0.25(42)

C1: Spatial variations of mean and extreme indices of precipitation significant trends a) PRCPTOT (mm), b) Mean (mm), c) CDD (days), d) CWD (days), e) Rx1day (days), f) Rx5day (days), g) R95pTOT (mm), h) R99PTOT (mm), i) R10 (days), j) R20 (days) and k) SDII (mm) over Ethiopia for the duration of 1981-2020 during JJAS season.

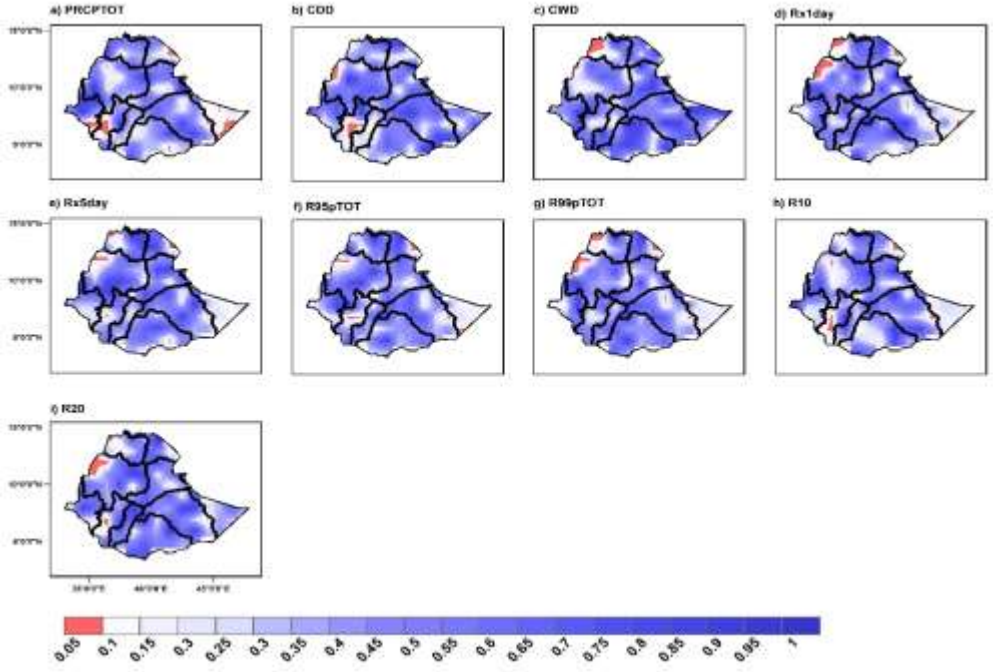

C2: Spatial variations of mean and extreme indices of precipitation significant trends a) PRCPTOT (mm), b) Mean (mm), c) CDD (days), d) CWD (days), e) Rx1day (days), f) Rx5day (days), g) R95pTOT (mm), h) R99PTOT (mm), i) R10 (days), j) R20 (days) and k) SDII (mm) over Ethiopia for the duration of 1981-2020 during FMAM season.

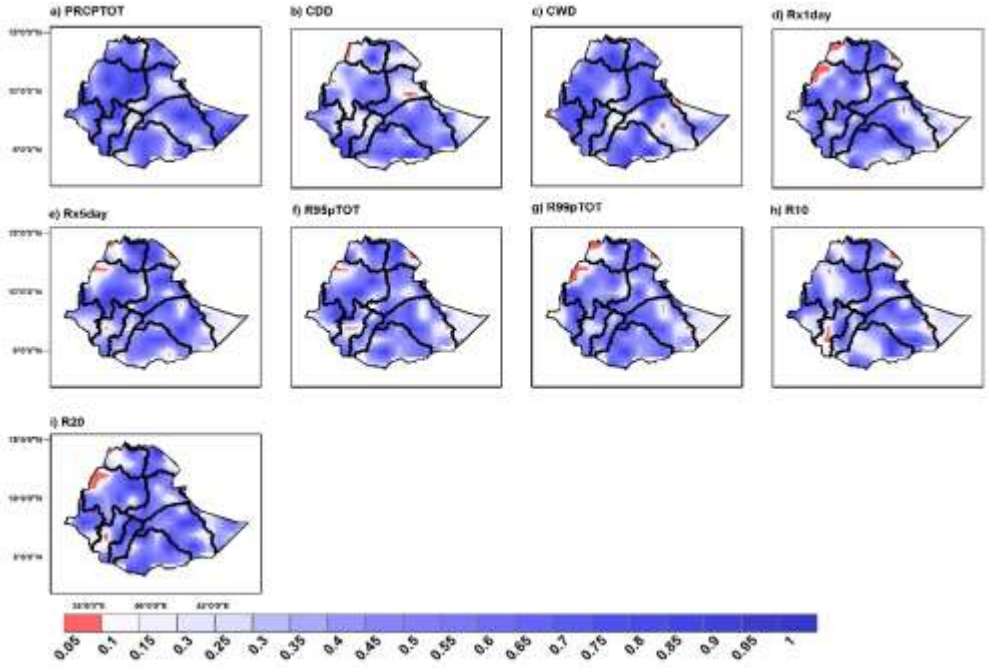

C3: Comparison of raw and bias-corrected outputs for the top-ranking models in simulating extreme precipitation indices during JJAS season

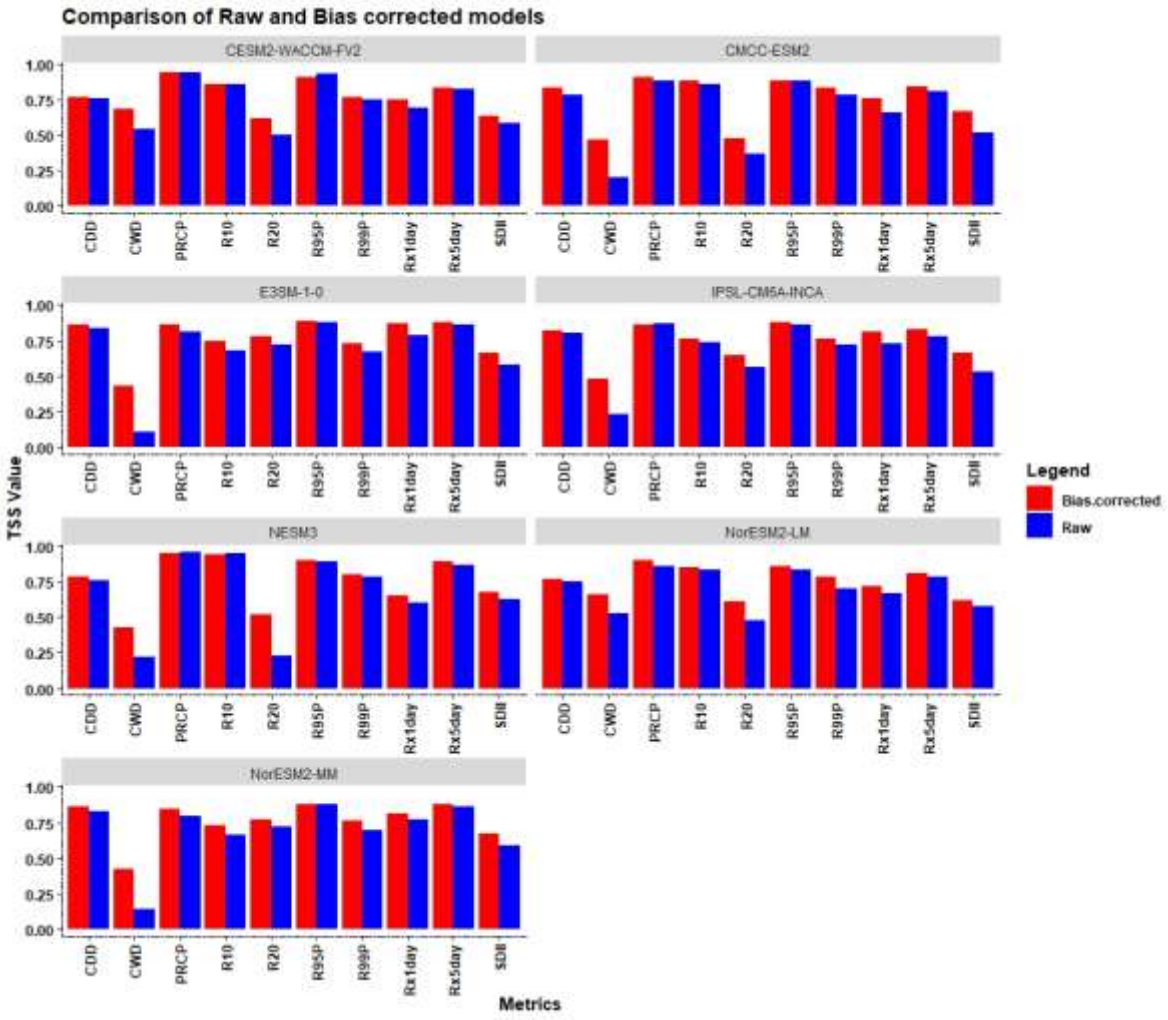

C4: Comparison of raw and bias-corrected outputs for the top-ranking models in simulating extreme precipitation indices during FMAM season

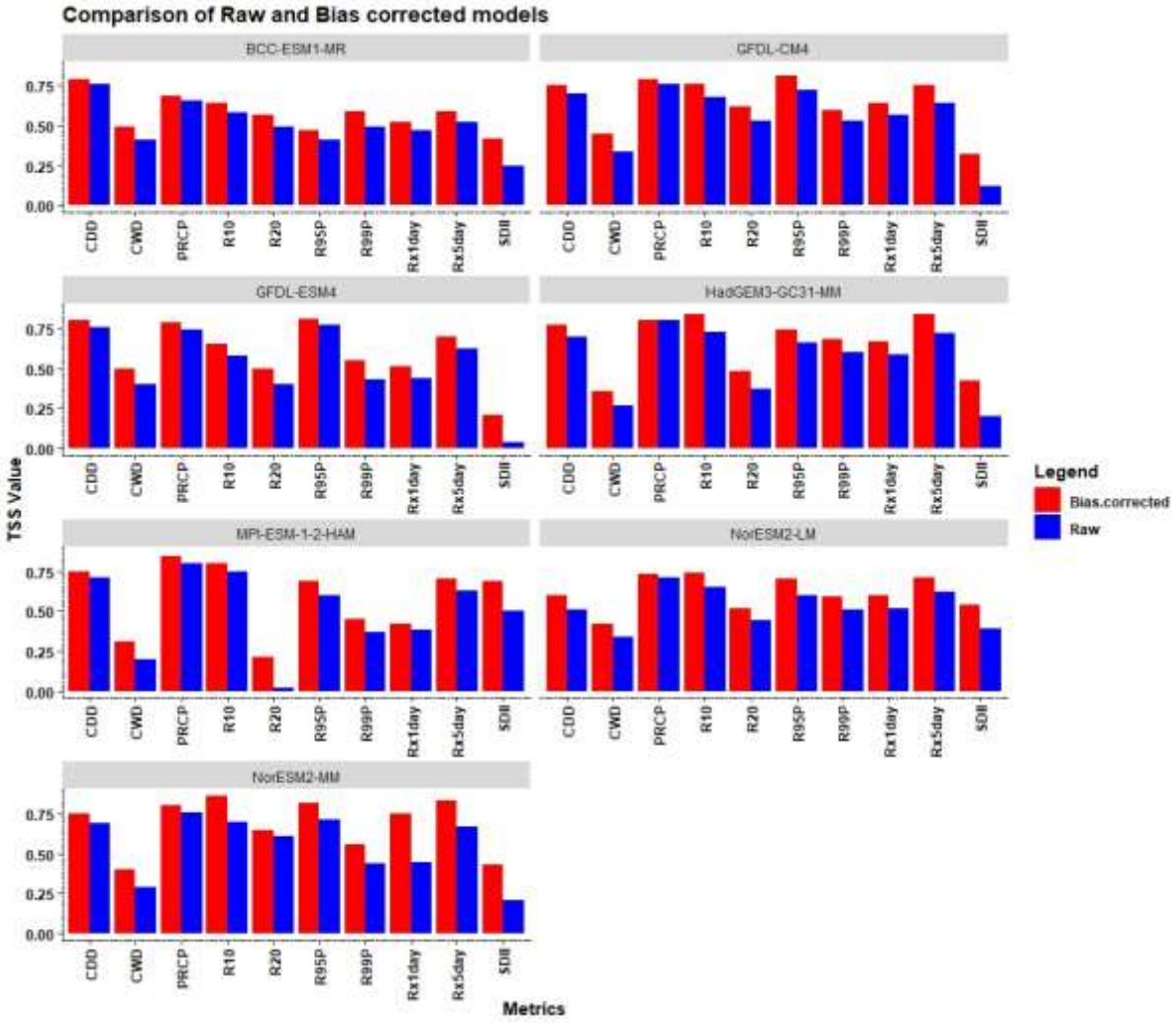

C5: Box-and-whisker plots of trends for the EnseMean in simulating extreme precipitation indices (CDD (days), CWD (days), MEAN (mm), PRCPTOT (mm), R10 (days), R20 (days), R95Ptot (mm), R99Ptot (mm), Rx1day (mm), Rx5day (mm), SDII (mm)) for FMAM season for the 2040s under SSP245 scenario. The boxes represent the interquartile range (spanning the 25th to 75th percentiles), with the thick black line inside each box indicating the median. The whiskers show total intermodel range.

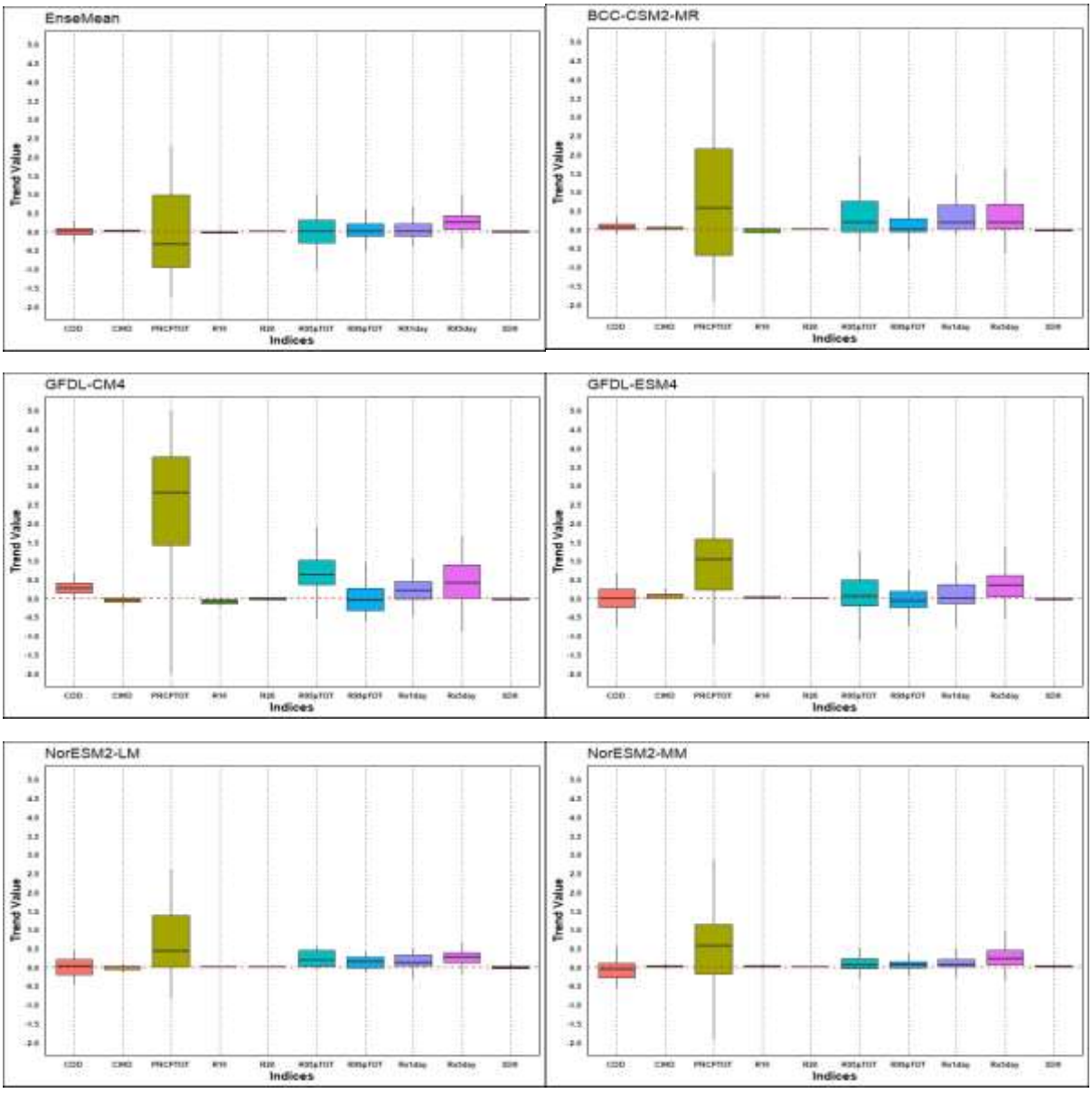

C6: Box-and-whisker plots of trends for the EnseMean in simulating extreme precipitation indices (CDD (days), CWD (days), MEAN (mm), PRCPTOT (mm), R10 (days), R20 (days), R95Ptot (mm), R99Ptot (mm), Rx1day (mm), Rx5day (mm), SDII (mm)) for FMAM season for the 2070s under SSP245 scenario. The boxes represent the interquartile range (spanning the 25th to 75th percentiles), with the thick black line inside each box indicating the median. The whiskers show total intermodel range.

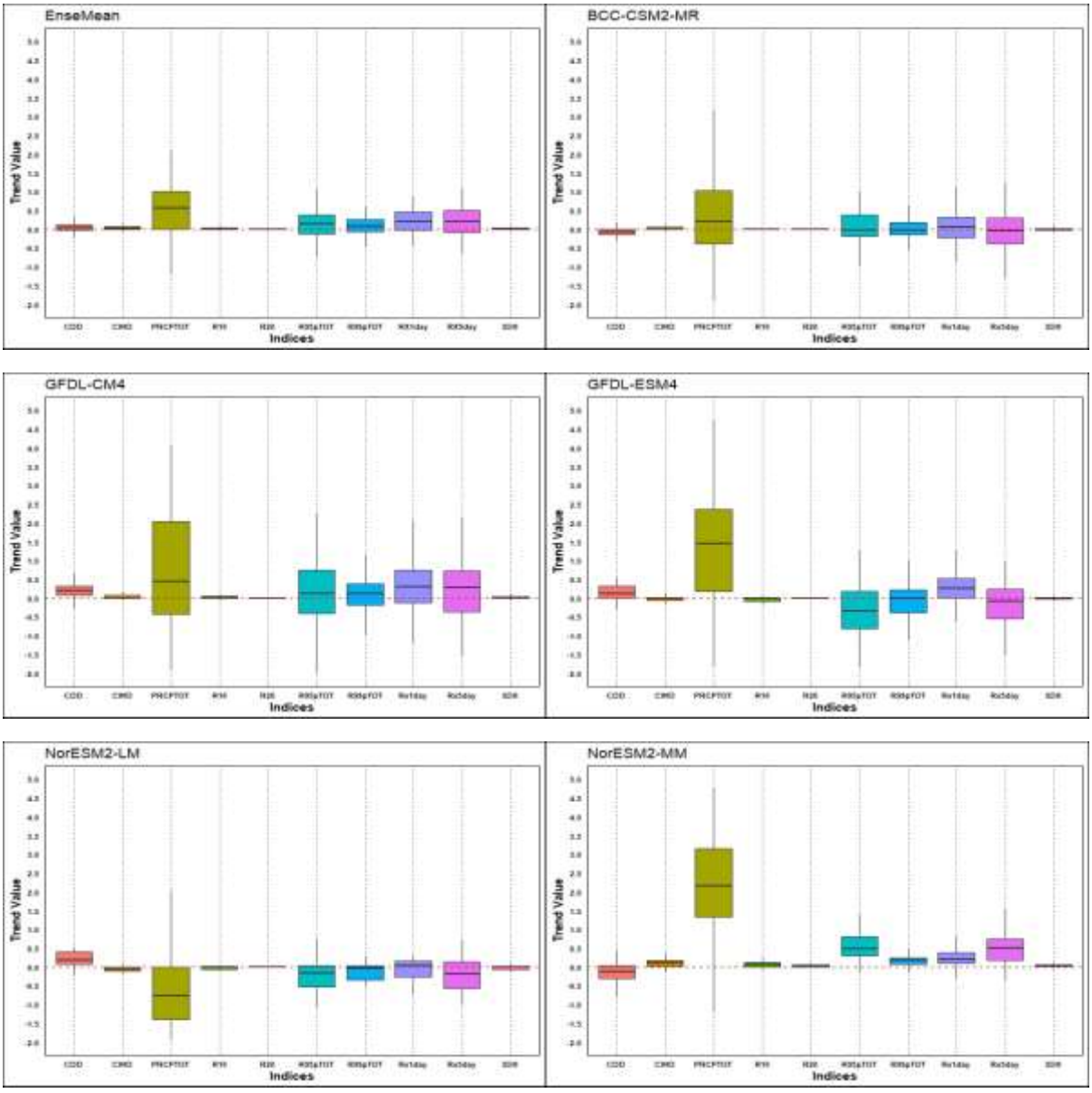

C7: Box-and-whisker plots of trends for the EnseMean in simulating extreme precipitation indices (CDD (days), CWD (days), MEAN (mm), PRCPTOT (mm), R10 (days), R20 (days), R95Ptot (mm), R99Ptot (mm), Rx1day (mm), Rx5day (mm), SDII (mm)) for FMAM season for the 2040s under SSP585 scenario. The boxes represent the interquartile range (spanning the 25th to 75th percentiles), with the thick black line inside each box indicating the median. The whiskers show total intermodel range.

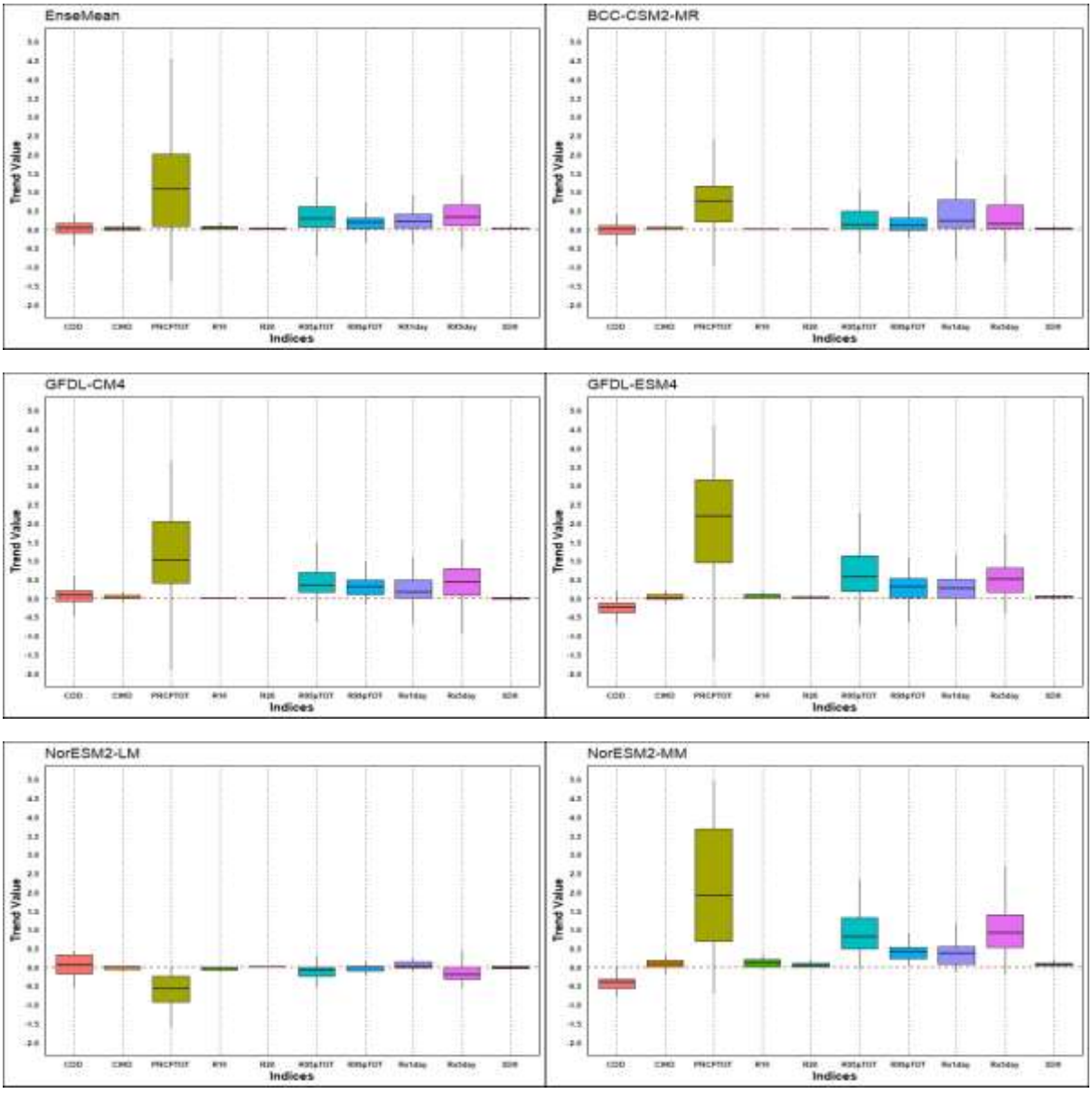

C8: Box-and-whisker plots of trends for the EnseMean in simulating extreme precipitation indices (CDD (days), CWD (days), MEAN (mm), PRCPTOT (mm), R10 (days), R20 (days), R95Ptot (mm), R99Ptot (mm), Rx1day (mm), Rx5day (mm), SDII (mm)) for FMAM season for the 2070s under SSP585 scenario. The boxes represent the interquartile range (spanning the 25th to 75th percentiles), with the thick black line inside each box indicating the median. The whiskers show total intermodel range.